Nano-sized Transition Metal Oxide Negative Electrode Materials for Lithium-ion Batteries

Mechthild Lübke

A thesis submitted to
University College London

in partial fulfilment of the requirements for the degree of
Doctor of Philosophy

Supervised by Professor Jawwad A. Darr

2018

Christopher Ingold Laboratories
Department of Chemistry
20 Gordon Street
London WC1H 0AJ
United Kingdom

Declaration

I, Mechthild Lübke, confirm that the work presented in this thesis is my own. Where information has been derived from other sources, I confirm that this has been indicated in the thesis.

Mechthild Lübke

Abstract

This thesis focuses on the synthesis, characterization and electrochemical evaluation of various nano-sized materials for use in high power and high energy lithium-ion batteries. The materials were synthesised via a continuous hydrothermal flow synthesis (CHFS) process, which is a single step synthesis method with many advantages including screening processes (chapter 5).

Electrochemical energy storage is introduced in chapter 1, with a focus on high power and high energy negative electrode materials for lithium-ion batteries (and capacitors). Many different classes of materials are discussed with associated advantages and disadvantages. This is followed by an experimental section in chapter 2.

Chapter 3 deals with the main question regarding why some high power insertion materials show a wider operational potential window than expected. The nature of this electrochemical performance is discussed and classified towards battery-like and supercapacitor-like behaviour. Chapter 4 deals with Nb-doped anatase TiO_2, which was tested for high power insertion materials. The role of the dopant was discussed in a comprehensive study.

Chapter 5 gives an excellent example how CHFS processes can help accurately answer a scientific question. In this case the question dealt with the impact of transition metal dopants on the electrochemical performance of SnO_2. Since CHFS enables similar materials properties despite doping, the real impact could be investigated in a fair manner. Finally, chapter 6 shows a strategy of achieving higher energy simultaneously with high cycle life. Insertion materials are combined with alloying materials in a simple, single step synthesis and this showed increased capacity, which is essential for high energy.

Acknowledgements

First, I would like to thank UCL, ASTAR and EPSRC for funding my PhD project. There were many people contributing in making the project so enjoyable during past three years, who are highlighted in the following:

I would like to thank my supervisor Jawwad Darr, who did an amazing job in controlling my "messy" thoughts and directing them into something useful. I got lots of support and degree of freedom during the past three years. Jawwad always helped me to get the most of the science I investigated and supported me in any possible way. Thanks for all endless discussions during the past three years, Jawwad!

Moreover, I would like to thank my other supervisors Dan Brett and Zhaolin Liu for supporting me as much as possible during any tricky challenges. Same applies for all the hidden geniuses at UCL and IMRE who always had an open mind for fruitful discussions, which include Martin Vickers, Jeremy Cockcroft, Steve Firth, Ding Ning, Afriyanti Sumboja, Michael Powell and so many more.

Our group at UCL was very supportive during the past years, no matter how far I was away. Therefore, I would like to thank Neel, Liam, Pete, Marco, Clement (TEM images in chapter 6.4.1), Ian, Dustin (electrochemical characterization for Figure 83a), Adrian, Tom, Kalyani, Charles, Carlos, Alistair, Paul, Jess, Eva and the guys from UCell. Dougal helped me during the lab movement of IMRE and supported me with needed scientific measurements and discussions (see XPS, BET and TEM analysis in chapter 6.4.2 and 6.4.3). Thanks Dougal, for all the help and input. Moreover, Juhun Shin is thanked for electrochemical characterizations for the results in chapter 3.

I would like to thank all the other helpful colleagues I met at ASTAR, which include Ceilidh, Ola (XPS analysis in chapter 3 and 6), Aled, Diana (SEM image in chapter 6.4.3), LP,

Davide, Andy, Sam, Will (I + II), Lizzy and so many more. Thank you all for the inspiring discussions and heads ups, when I got lost.

Being part of an exchange program was quite easy, simply because of all the helpful people organizing it. I would like to thank Zhimei Du, Jadranka Butorak and Yi Wen Teo for their endless efforts during the past three years.

Next, I would like to thank all the nice people I met during my PhD. Being part of a foreign society for only a few years can be a tricky adventure. Fortunately, I met so many kind and open people along the way in both UK and Singapore who made my stay very pleasant. Singapore was a great place to live and will always have a place in my heart. Special thanks to the lovely team mates from Football Plus and SMU.

Finally, “Danke an die Wehmer Fraktion”, who always got me back to reality. Also thanks to my second family, the Grevers. The “Ciao Bellas” should not be missed as well as most of my friends including Andrea, Sebastian, Stefan, Ruth, Anne and so many more. I want to thank my family, which got a new, tiny member since my stay in Singapore. Heiner, Tina, Rita, Smita, Astrid and my dear lovely mum, simply thanks for all the support during the past years.

List of Publications

Publications related to the work presented in this thesis:

M. Lübke, D. Ning, C.F. Armer, D. Howard, D.J.L. Brett, Z. Liu, J.A. Darr, "Evaluating the Potential Benefits of Metal Ion Doping in SnO_2 Negative Electrodes for Lithium Ion Batteries", Electrochimica Acta, 242, (2017) 400-407.

M. Lübke, D. Howard, C.F. Armer, A.J. Gardecka, A. Lowe, M.V. Reddy, Z. Liu, J.A. Darr, "High energy lithium ion battery electrode materials; enhanced charge storage via both alloying and insertion processes", Electrochimica Acta, 231, (2017) 247-254.

M. Lübke, N. Ding, M.J. Powell, D.J. Brett, P.R. Shearing, Z. Liu, J.A. Darr, "VO_2 nano-sheet negative electrodes for lithium-ion batteries", Electrochemistry Communications, 64, (2016) 56-60.

M. Lübke, A. Sumboja, I.D. Johnson, D.J. Brett, P.R. Shearing, Z. Liu, J.A. Darr, "High power nano-Nb_2O_5 negative electrodes for lithium-ion batteries", Electrochimica Acta, 192, (2016) 363-369.

M. Lübke, P. Marchand, D.J. Brett, P. Shearing, R. Gruar, Z. Liu, J.A. Darr, "High power layered titanate nano-sheets as pseudocapacitive lithium-ion battery anodes", Journal of Power Sources, 305, (2016) 115-121.

M. Lübke, J. Shin, P. Marchand, D.J. Brett, P. Shearing, Z. Liu, J.A. Darr, "Highly pseudocapacitive Nb-doped TiO_2 high power anodes for lithium-ion batteries", Journal of Materials Chemistry A, 3, (2015) 22908-22914.

M. Lübke, I. Johnson, N.M. Makwana, D.J. Brett, P. Shearing, Z. Liu, J.A. Darr, "High Power TiO_2 and High Capacity Sn-doped TiO_2 Nanomaterial Anodes for Lithium-ion Batteries", Journal of Power Sources, 294, (2015) 94-102.

Other Publications:

M. Lübke, A. Sumboja, L. McCafferty, C.F. Armer, A.D. Handoko, Y. Du, K McColl, F. Cora, D. Brett, Z. Liu, J.A. Darr, "Transition metal doped α-MnO_2 nanorods as bifunctional catalysts for efficient oxygen reduction and evolution reactions" ChemistrySelect (2018).

A. Sumboja, M. Lübke, Y. Wang, T. An, Y. Zong, Z. Liu, "All-Solid-State, Foldable, and Rechargeable Zn-Air Batteries based on Manganese Oxide Grown on Graphene Coated Carbon Cloth Air Cathode" Advanced Energy Materials, (2017) 1700927.

C.F. Armer, M. Lübke, M.V. Reddy, J.A. Darr, X. Li, A. Lowe, "Phase change effect on the structural and electrochemical behaviour of pure and doped vanadium pentoxide as positive electrodes for lithium ion batteries", Journal of Power Sources, 353, (2017) 40-50.

I.D. Johnson, M. Lübke, O.Y. Wu, N.M. Makwana, G.J. Smales, H.U. Islam, R.Y. Dedigama, R.I. Gruar, C.J. Tighe, D.O. Scanlon, F. Corà, J.A. Darr, " Pilot-scale continuous synthesis of a vanadium-doped $LiFePO_4$/C nanocomposite high-rate cathodes for lithium-ion batteries", Journal of Power Sources, 302, (2015) 410-418.

M. Lübke, N.M. Makwana, R. Gruar, C. Tighe, D. Brett, P. Shearing, Z. Liu, J.A. Darr, “High capacity nanocomposite $F_{e3}O_4$/Fe anodes for Li-ion batteries”, Journal of Power Sources, 291, (2015) 102-107.

List of Abbreviations

AC	Activated Carbon
BET	Brunauer Emmett Teller
CV	Cyclic voltammetry
CHFS	Continuous Hydrothermal Flow Synthesis
CJM	Confined jet mixer
DEC	Diethyl carbonate
DFT	Density functional theory
DMC	Dimethyl carbonate
EC	Ethylene carbonate
EDLC	Electrochemical double layer capacitor
EDX	Energy dispersive X-ray
EIS	Electrochemical impedance spectroscopy
ESW	Electrochemical stability window
LCO	Lithium cobalt oxide
LFP	Lithium iron phosphate
LiB	Lithium-ion battery
LiC	Lithium-ion capacitor
LFP	Lithium iron phosphate
NCM	Lithium nickel cobalt manganese oxide
PXRD	Powder X-ray diffraction
SEI	Solid electrolyte interphase
SEM	Scanning electron microscopy
TEM	Transmission electron microscopy
TGA	Thermogravimetric analysis
XPS	X-ray photoelectron spectroscopy
XRF	X-ray fluorescence

Table of Contents

1. Introduction

1.1 Motivation

There are currently high motivations for drastic changes in the energy market. The increasing population (corresponding to an increasing demand of energy), global warming and the decreasing availability of natural resources pose a big challenge for humanity. In 2007, approximately 68 % of the electrical energy was supplied from fossil fuels (coal 42 %, natural gas 21 %, oil 5 %), 14 % from nuclear, 15 % from hydro, and the remaining 3 % was supplied by renewable energy tech [1]. One strategy towards sustainable energy markets is the increased use of renewable energy sources (solar and wind energy). But the sun does not shine overnight (or with the same intensity every day) and wind does not blow every day with the same speed (Figure 1a).

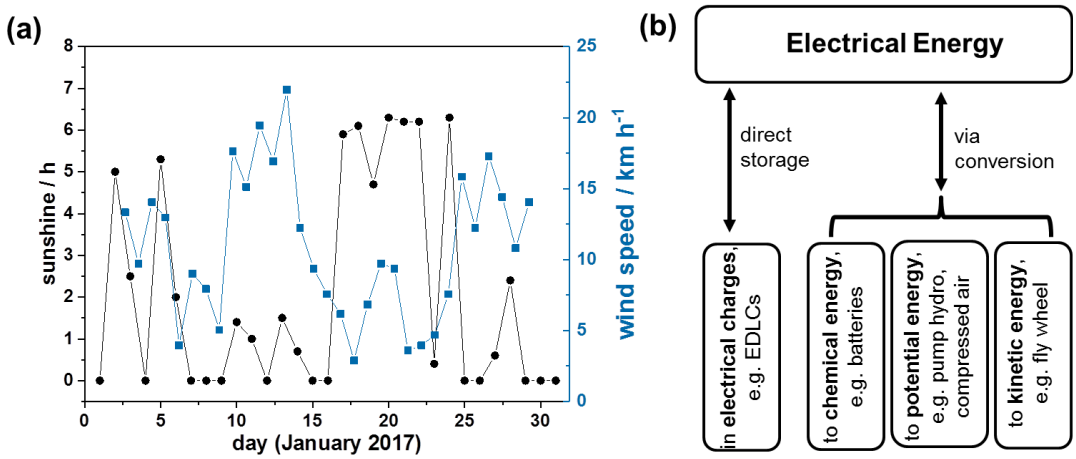

Figure 1: a) Daily profiles of average sun light in hours and average wind speed in km h^{-1} per day (January 2017, data obtained at London Heathrow Airport; weatheronline.co.uk). b) Classifications of potential electrical storage mechanisms for stationary applications.

Therefore, smart grid solutions have to be established including efficient energy storage systems in terms of cost, power, long-life and so on. Electrical energy can be stored directly via physical double layer charges in electrochemical double layer capacitors (EDLC) or indirectly via conversion in kinetic, potential or chemical energy (Figure 1b). Batteries seem to be very promising for the storage of electrical energy when considering high energy efficiencies and densities. Because of their high specific energy, lithium-ion batteries (LiBs) are considered to be the most promising solution for many kinds of energy storage applications.

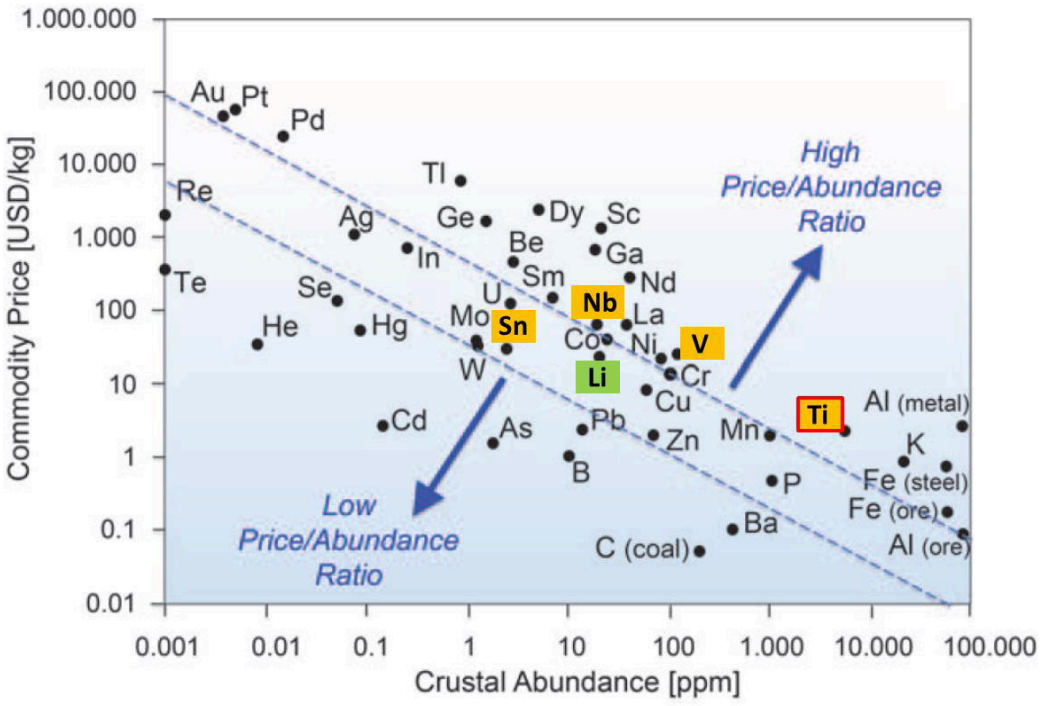

Figure 2: Relationship between metal price and its relative abundance in the Earth's upper continental crust (based on abundance of Si: 10^6 atoms). The metal price data from 2013. Modified taken from ref [2].

Although LiBs are established commercial products, further research and development is still needed to improve the performance in terms of energy density, cost, rate capability and safety; especially considering that LiBs are expected to play a key role in electric vehicles. In addition to safety issues with the electrolyte, current commercial LiBs (ca. 200 Wh kg^{-1}), would exceed a weight of 800 kg for 1000 km. New electrode materials with far higher specific capacities need to be investigated in order to decrease such high weight to less than 400 kg. Moreover, energy storage needs to be affordable.

In Figure 2, the metal prices from April 2015 are plotted. E.g. for the negative electrode of a LiB, graphite is still used due to its high theoretical capacity (372 mAh g^{-1}), high electronic conductivity and low price. But there are several issues such as high lithium-ion loss during the initial cycles, low safety due to lithium plating and also poor power performance, which force the development of alternative safe electrode materials. The plot indicates why elements like titanium are interesting simply due to high abundance and low costs. Herein, various metal oxides are investigated for different applications towards high power and high energy devices.

High power is very important, as the customer does not want to charge their car or phone for many hours (which would be a huge drawback compared to conventional fuel based cars; please note that many current, conventional battery packs for electric vehicles show a continuous charge power capability of less than 1C) and high energy is also important, as the customer does not want to recharge the phone or car after a short period of usage time. Moreover, there are also different applications needing only high power or high energy. Thus, even for LiBs, the variety of possible combinations is huge and will be introduced during chapter 1. The cost of each material should be kept in mind.

1.2 Electrochemical Basics for Electrochemical Energy Storage

Energy can be stored physically and chemically in electrochemical energy storage devices. For the electrochemical energy storage, the reaction Gibbs energy ΔG [J mol^{-1}] represents the useful energy available from a reaction and can be seen as the maximum work an electrochemical device can deliver.

$$\Delta G = -nF\Delta E \quad (1)$$

ΔG is related to the potential difference ΔE, the Faraday constant F ($F = 96485 \frac{\mathrm{C}}{\mathrm{mol}}$) and the numbers n of transferred electrons per mol (Equation 1). A negative ΔG represents a spontaneous reaction like an electrochemical discharge step. The reaction Gibbs energy ΔG can be related to other parameters, such as temperature or pressure (Equation 2).

$$\Delta G = \Delta G^0 + \mathrm{R}T \ln\left(\frac{a_p}{a_R}\right) \quad (2)$$

ΔG^0 is the maximum work under standard conditions, R the gas constant ($R = 8.3145 \frac{\mathrm{J}}{\mathrm{mol\,K}}$), T the temperature, a_p the activity of the product and a_R the activity of the reactants. The combination of Equation 1 and Equation 2 gives the Nernst equation (Equation 3). The Nernst equation allows the calculation of the potential E [V], where the standard potential E^0 of each material can be found in literature.

$$E = E^0 - \frac{RT}{zF} \ln\left(\frac{a_p}{a_R}\right) \quad (3)$$

When the potential of the positive and negative electrode is known, the cell potential can be calculated (Equation 4).

$$\Delta E = E_{positive} - E_{negative} \tag{4}$$

The theoretical specific capacity $Q_{th}\left[\frac{\mathrm{mAh}}{\mathrm{g}}\right]$ of each electrode material is a very important parameter for the energy of a full cell. A high specific capacity material results from a low molar mass M combined with a high number of transferred electrons z (Equation 5), note 1 C = 1 As.

$$Q_{th} = \frac{zF}{3.6\ M} \tag{5}$$

Finally, the theoretical specific energy of an ideal battery $W\ [\frac{\mathrm{Wh}}{\mathrm{kg}}]$ is the product of the cell potential ΔE and the theoretical specific capacity Q_{th} (Equation 6). Therefore, the increase of the cell voltage and the specific capacity results in higher energy densities [3].

$$W = \int_{q=0}^{Q_{th}} \Delta E\ \mathrm{d}q \approx Q_{th}\ \Delta E \tag{6}$$

The specific power is in addition to the specific energy a very important characteristic for many applications. This can be described as the maximum energy a device can store and release within very short time.

1.3 Electrochemical Energy Storage Devices

An ideal energy storage device provides a long cycle life, high specific power and energy (which means the mass of the device is very low), environmental compatibility, high safety and low costs. So far, there are four main electrochemical energy storage systems (redox-flow batteries are not considered herein, as the focus is set on non-continuous charge storage). Capacitors and electrochemical capacitors store the charge physically (electrochemical pseudocapacitors store the charge also chemically) at the surface and these are high power devices with a high cycle life (up to 1,000,000 cycles). These devices show low specific energy compared to batteries and fuel cells. Batteries store the charge chemically and have medium cycle life (up to 10,000 cycles depending on the electrode materials, see discussion later) and less specific power [4].

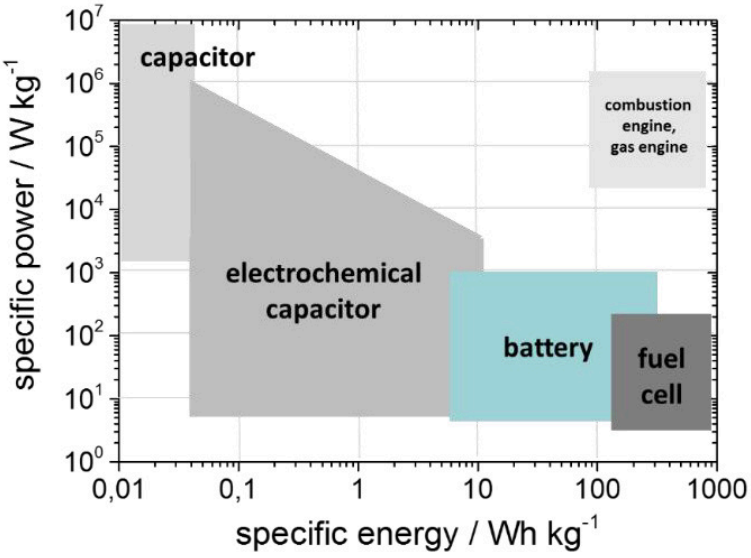

Figure 3: Specific power versus specific energy for different energy storage devices (Ragone plot modified taken from [3, 5]).

Specific power and specific energy are often inversely related. The specific energy decreases with higher specific power and vice versa. Reaching higher specific power and specific energy under acceptable cycle life conditions at once is still a challenge (see Ragone plot in Figure 3).

1.3.1 Lithium-ion Batteries (LiBs)

Compared to other battery systems, LiBs show higher gravimetric and volumetric energy density due to the low atomic weight of lithium-ions (Figure 4). Moreover, using lithium results in large cell potentials, because of its very low standard potential, which therefore increases the energy density (see chapter 1.2). Besides the high worldwide abundance of Li (e.g. two times higher than Pb), all these characteristics make LiBs an attractive secondary energy storage system.

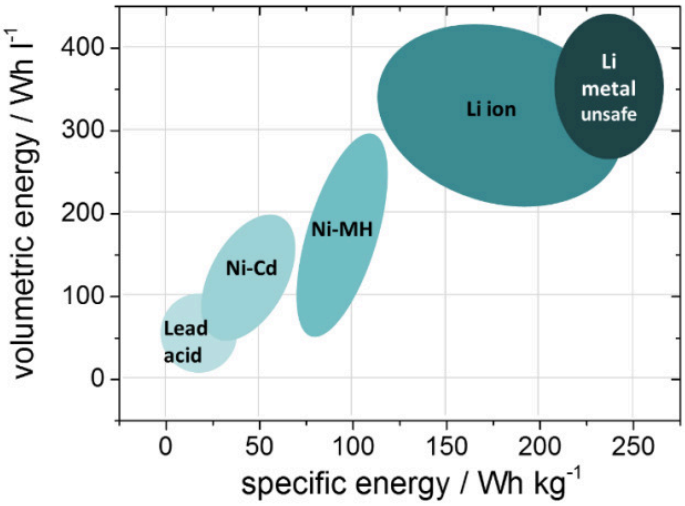

Figure 4: Comparison of the different battery technologies in terms of volumetric and gravimetric energy density (modified taken from [6]).

The first commercial rechargeable LiBs on the market were sold by Sony in 1991 [7]. A typical LiB consists of graphite as negative electrode and a layered transition metal oxide [such as $LiCoO_2$, (LCO) previously and more recently $LiNi_{1/3}Co_{1/3}Mn_{1/3}O_2$, (NCM)] as the positive electrode. The charge is stored via lithium-ions which move during charge from the positive to the negative electrode and intercalate between the graphene layers (Figure 5). Theoretically, one lithium-ion can be intercalated for every six carbon atoms.

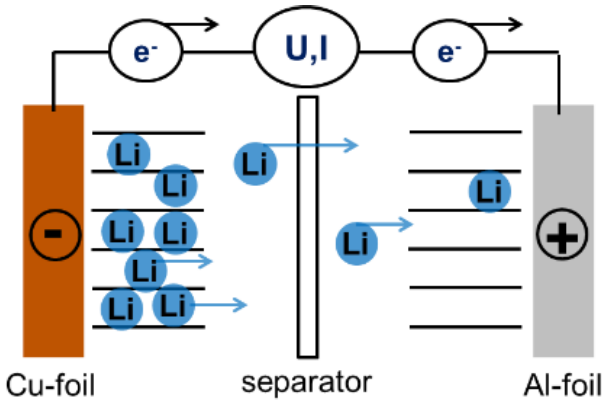

Figure 5: The principle of operation of the first commercialized LiBs. Lithium-ions move from the negative to the positive electrode during discharging (it is vice versa for charge).

Note: An anode and a cathode are defined according to oxidation and reduction reactions, respectively. During discharge of a LiB, these terminologies are correct. As soon the battery is charged, these terminologies are incorrect, because the anode and cathode switch roles. The first batteries were all primary, which explains why the incorrect terminologies of “anode” and “cathode” for secondary batteries are still used by the majority of electrochemists [8].

The negative and positive electrodes are separated by a separator soaked with an organic electrolyte containing lithium-ion salt. The electrolyte should show high lithium-ion conductivity and also good safety performance such as low vapour pressure and high flash point. Mixtures of

ethylene carbonate (EC) and dimethyl carbonate (DMC) can exhibit some of these characteristics best, but they are flammable. Lithium hexafluorophosphate ($LiPF_6$) is used as lithium salt in the electrolyte, because it still possesses the best compromise in terms of solubility, electrochemical stability and also the ability to inhibit anodic dissolution at the aluminium current collector at the positive electrode side. $LiPF_6$ is thermally (>60 °C) and chemically (with H_2O traces) unstable causing safety issues. In combination with the EC solvent, $LiPF_6$ is also able to form an effective Solid Electrolyte Interphase (SEI), which was the key development for the use of graphite in LiBs. The SEI layer acts as a protection layer, which is able to prevent exfoliation of the graphene layers and it also prevents further electrolyte decomposition after the initial cycles (see more details in chapter 1.6).

1.3.2 Electrochemical Capacitors

Electrochemical capacitors can be classified into two groups, namely electrochemical double layer capacitors (EDLCs) and pseudocapacitors (also called oxide supercapacitors), Figure 6.

EDLCs store their charge physically, which dramatically increases the cycle life compared to batteries as there is no chemical degradation. Therefore, EDLCs show their main advantages in high specific power and very long stable cycle life. These characteristics are excellent for applications which require high power and high reliability. Examples include container trains at harbours, regenerative breaks in cars, emergency doors in air planes, defibrillators or the use for energy conversion in smart grids and also public electric busses where charging occurs at each station.

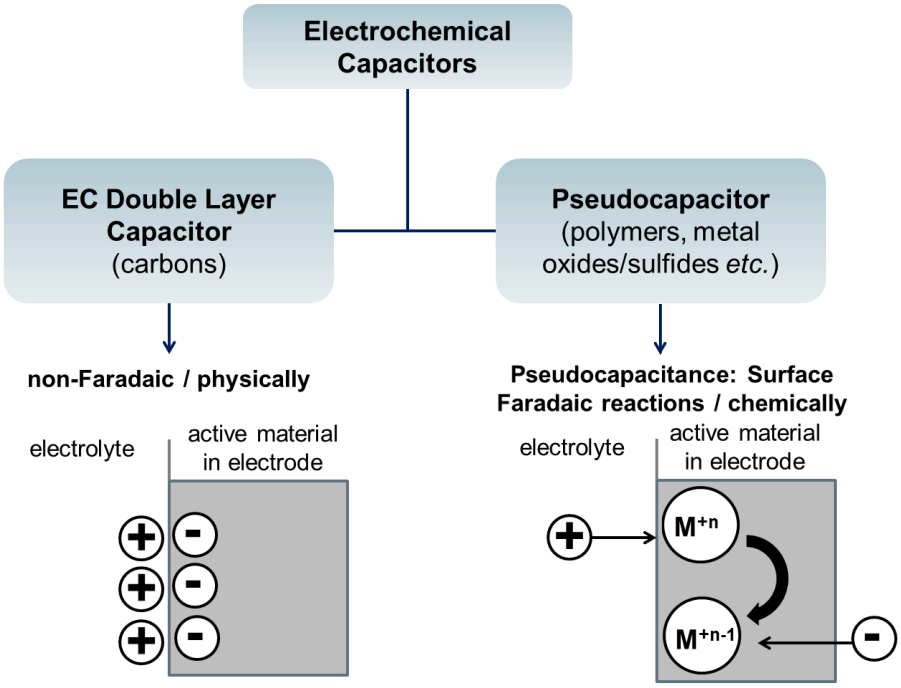

Figure 6: Scheme of possible electrochemical capacitors. The charge storage mechanism can be divided in two main characteristics, e.g. physically stored charged for EDLCs and chemically stored charge for pseudocapacitors.

In 1957 Becker patented a system using a high specific surface area carbon, coated on a metallic current collector [9]. This system provided a very high capacitance. This behaviour could be explained by the known idea of the Helmholtz double layer. Ions move during charge to each electrode with reversed charge and form a double layer at each high surface area electrode. During discharge, ions diffuse back into the electrolytic system as a result of the entropic force. Therefore, the charge is stored only electrostatically via charge separation at the electrode/electrolyte interface.

The capacitance C of a double layer depends on the surface area A, the effective thickness of the double layer d and the dielectric constant of the electrolyte ε_r and of the vacuum ε_0:

$$C = \varepsilon_r \varepsilon_0 \frac{A}{d} \quad (7)$$

Activated carbons (AC) are widely used as EDLC electrode materials today due to their high surface area (up to 3500 $m^2 g^{-1}$), which drastically increases the double layer capacitance (Equation 7). They also offer low costs, high conductivity and electrochemical stability [10, 11].

The specific energy and specific power are related to the maximum cell voltage V and the series resistant R of the whole cell (Equation 8, 9). The resistance is the total of electrolyte resistance, particle-particle resistance, contact resistance between current collector and active material and the resistance of the electrolyte within pores of the active material [12, 13].

$$E_{max} = \frac{1}{2} C V^2 \quad (8)$$

$$P_{max} = \frac{V^2}{4R} \quad (9)$$

Electrolytes used in commercial EDLCs contain quaternary ammonium salts such as tetraethyl ammonium tetrafluoroborate ($TEABF_4$) in propylene carbonate (PC) or acetonitrile. The advantage of organic electrolytes compared to the aqueous electrolytes is the higher achievable cell voltage. Using aqueous electrolytes limits the cell voltage to 1.2 V, whereas organic electrolyte can typically be used up to 2.7 V [14-16]. But, organic electrolytes tend to have a lower dielectric constant, which results in a lower capacitance (Equation 7). Using ionic liquids (ILs) can increase the electrochemical stability window compared to organic electrolytes [17]. They also have a wide thermal stability, high ionic conductivities, are non-volatile and non-flammable, but it has also disadvantages compared to PC based electrolytes. The conductivity at lower temperatures is much lower and they are also more expensive [17-20]. An alternative

approach is a mixture of ILs and organic solvents [20] or highly concentrated (e.g. NaTFSI) aqueous electrolytes which increases the cell voltage of such systems up to 1.8 V [21].

A new class of high energy oxide supercapacitor electrodes are certain transition metal oxides (e.g. TiO_2, V_2O_5, RuO_2, Fe_3O_4). The charge can be stored via electrochemical Faradaic reactions between the electrode material and ions in the appropriate potential window. This is called pseudocapacitance [5]. When a potential is applied to these materials, fast and reversible Faradaic reactions (redox reactions) take place at the surface. In addition to that, there is of course also some charge storage originating from a Helmholtz double layer. In general, the Faradaic stored charge can be ten to hundred times higher than the Helmholtz double layer charge [22].

Pseudocapacitive materials can be classified as intrinsic and extrinsic. Intrinsic pseudocapacitive materials (RuO_2, MnO_2, Nb_2O_5 etc.) display the features of capacitive charge storage for a wide range of morphologies and particle sizes (surface areas). Extrinsic pseudocapacitive materials (e.g. TiO_2) show high dependence on morphologies and especially particle size (surface area) [23]. In the latter, the bulk materials do not show any pseudocapacitive charge storage and upon nano-sizing (increasing the surface area), the charge storage shifts towards pseudocapacitance due to decreased lithium-ion diffusion at the surface and also within the particle [24].

It should be noted, that any of the aforementioned charge storage devices (with charge storage arising from any surface effects), has a massive drawback of self-discharge [25-27]. This means that the full cell would lose some of its energy in its charged stage over time.

1.3.3 Hybrid Energy Storage Devices and Electrodes

In Table 1, the features of EDLCs and LiBs are compared and summarized. EDLCs are more interesting for applications that require high power and long cycle life, whereas applications, that need high energy, would require the implementation of LiBs. Oxide supercapacitor materials (pseudocapacitive materials) are also high power materials, but they show more charge storage via chemical reactions at the surface, increasing the energy density. Thus, oxide supercapacitor materials show features in-between batteries and EDLCs [28].

Table 1: Comparison of EDLCs and LiBs (data partly derived from https://www.supercaptech.com/battery-vs-supercapacitor, 26/06/2017).

	EDLCs	**LiBs**
charge storage mechanism	physical	chemical
charge time	seconds	minutes
discharge time	seconds	minutes
energy efficiency	>99 %	>95 %
cycle life	>500,000	>1,000 (@ 1 C)
self-discharge (per month)	40-50 %	2 %
specific energy (Wh kg^{-1})	4-10	80-260
specific power (kW kg^{-1})	5-40	1.5
cost per Wh	10-20 US$	1-2 US$
cost per kW	25-50 US$	75-150 US$

The term “hybrid” can be used if two or more technologies are combined in order to get the advantages of these in one. The need for devices offering both high energy and power is getting a more and more important research topic. Therefore, the attributes of LiBs and supercapacitors can be combined in parallel and in series [29], Figure 7.

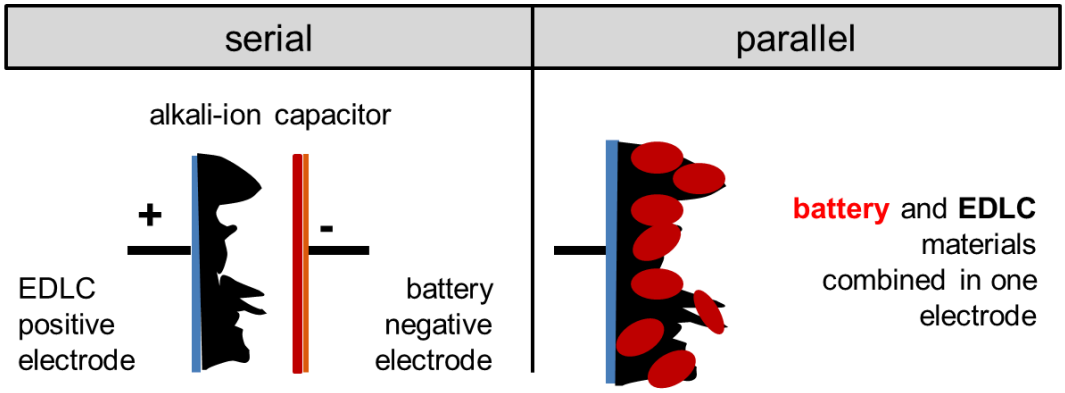

Figure 7: Scheme of possible approaches combining the positive attributes of batteries and electrochemical capacitors. The serial combination includes the use of a LiB and an EDLC electrode material. The parallel combination uses different storage mechanism in one electrode (composite material or simply some nano-sized insertion materials, see chapter 1.5).

The serial combination, e.g. the use of a battery electrode and a double layer capacitive electrode, leads to many advantages. These devices, called asymmetric capacitors, hybrid capacitors or lithium-ion capacitors (LiCs), show a higher specific energy compared to conventional EDLCs and can also display higher power compared to LiBs. Moreover, the cycling stability [30] and rate performance [31, 32] can be improved compared to LiBs. The reason for this behaviour can be found in the high rate capability and high cycle stability of the EDLC electrode [33]. Therefore, the C-rate performance of the cell is mostly related to the performance of the battery electrode in such a device, meaning the C-rate performance is only limited by one electrode material in the system. Another hybrid device is the setup of an AC as the negative electrode and LiB electrode as positive material (e.g. LFP, LCO).

Most current LiCs contain a LiB negative electrode material and an EDLC positive electrode material. The reason for this system is the win of additional full cell voltage, because AC can be easily used in the full width of the electrochemical stability window of the organic electrolyte

(up to 4.4 V vs. Li/Li^+). Common AC electrode active materials in EDLCs are still limited by the electrolyte decomposition at low applied potentials for carbonate-based electrolytes [15]. Using negative electrode materials with low de/lithiation potentials vs. Li/Li^+ should lead to much higher cell voltages when the electrolyte is stable in this system (up to 4.4 V [34]). Published systems include the use of graphite [31, 32, 35], soft carbon [36-38], hard carbon [39], and many more for full cell LiCs with AC on the positive electrode side. Beside graphites or amorphous carbons also other negative electrode materials such as lithium titanate (LTO), lithium vanadium phosphate [40] or Fe_2O_3 [41] were investigated for LiCs .

The parallel combination deals often with the use of composite electrode materials. These may contain two different active materials. Electrodes containing LiB and EDLC electrode materials are one example, as they store the charge chemically and physically. In Equation 9, the leading role of the cell resistance on the power performance was pointed out. The reduction of the electronic resistance of the electrode material was achieved through adding AC leading to far improved rate capability [42]. Cericola et al. showed improved rate capabilities for the composite electrode material based on $LiMn_2O_4$ and AC compared to each active material on its own [29]. Böckenfeld et al. proposed a composite electrode based on LFP and AC [43]. Finally, a parallel combination can be simply reached through nano-sizing various known insertion negative electrode materials. The idea behind is activating extrinsic supercapacitor materials (insertion battery materials) and will be introduced in chapter 1.5. Therefore, it is even possible to make hybrid devices with hybrid electrodes (e.g. nano-sized insertion materials as negative electrode versus AC as positive electrode). Herein, each group of electrode materials for LiBs will to be introduced first.

1.4 Electrode Materials for LiBs

For LiBs, high energy densities can be achieved via a high cell voltage. This includes a high potential vs. Li/Li^+ for the positive electrode material and a low potential vs. Li/Li^+ for the negative electrode material. In Figure 8, different potentials for each positive electrode material are presented. Lithium iron phosphate (LFP) is non-toxic and shows excellent rate capabilities, but compared to it, lithium cobalt oxide (LCO) and nickel cobalt manganese oxide (NCM) are electrochemically active at higher operating potentials. Another approach for higher energy density cells is the increase of the specific capacity. This specific capacity can be calculated based on Equation 5 (chapter 1.2). Today, developing high capacity positive electrode materials is still a big challenge. Positive electrode materials can theoretically deliver up to 350 mAh g^{-1} (lithium vanadium oxides). On the negative electrode side, much higher theoretical specific capacity materials are under investigation. As long the positive electrodes cannot deliver higher capacities, the potential energy win is limited if high capacity negative electrode materials are used. This is simply due to the fact that more positive electrode material (which is often also more expensive) would be needed to balance the full cell energy storage.

There are many examples for possible new negative electrode materials beside the commonly used graphite (372 mAh g^{-1}), such as conversion materials (e.g. transition metal oxides like Fe_2O_3 1,007 mAh g^{-1}; Fe_3O_4 926 mAh g^{-1}), alloying materials (group IV elements such as Si 3572 mAh g^{-1}; Sn 993 mAh g^{-1}) or lithium metal (3,840 mAh g^{-1}). Conversion and alloying materials tend to suffer from large structural changes including massive volume expansion during cycling, which leads to high capacity losses and generally low cycle stability. Lithium metal as negative electrode material still shows high safety risks due to dendritic lithium formation and electrolyte destruction. The latter seems to be partly solved with the inclusion of ionic liquids.

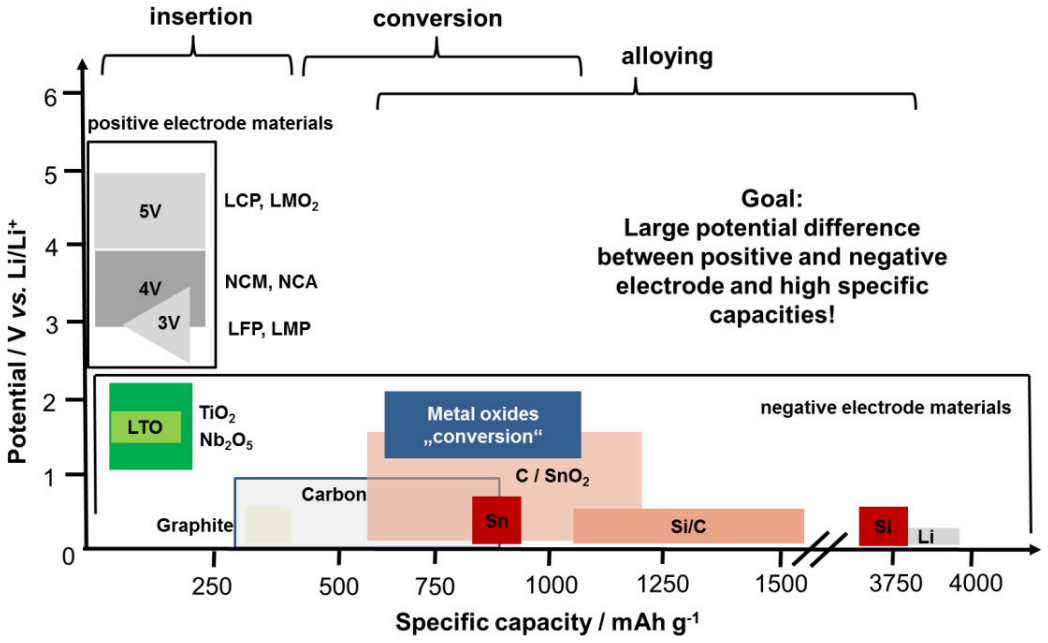

Figure 8: Current investigated and established electrode materials for LiBs (modified taken from [44]).

High specific energy and high power are key characteristics for various battery applications. Some applications need high energy and some need high power (and some need simultaneously both). While the energy density of the battery is the product of the specific capacity and the overall cell voltage, the power density is the measure of the rate at which energy can be stored and released from a system.

Towards high energy negative electrode materials. High energy density can be achieved both via a high cell voltage and high specific capacities (see chapter 1.2, Equation 6). As shown later, the highest energy negative electrode materials are alloying and conversion materials. These can store far more lithium-ions compared to insertion materials, simply due to the ability of massive structural changes during reversible lithiation, and they often show a far lower operating potential compared to transition metal oxide based insertion materials.

Towards high power negative electrode materials. High power can be described as the maximum stored charge even at very high C-rates (Figure 9). The C-rate is correlated to the theoretical capacity of each electrode material. A C-rate of 1C corresponds to an applied current to fully charge the electrode material within 1 h. Therefore, charging or discharging at 2C corresponds to 30 min and C/2 to 2 h. As an example, a LFP electrode has an active material mass loading of 2 mg. The theoretical capacity is 170 mAh g^{-1}. So for 1 C the applied current is 0.34 mA. Slow reactions including massive structural changes are not optimized for high power performances (but it is still questionable what smallest possible particle size might do in future), which also explains why insertion materials are generally far more suitable for usage as high power electrodes at the moment. These materials show very low structural changes upon lithiation and have a very high cycle life.

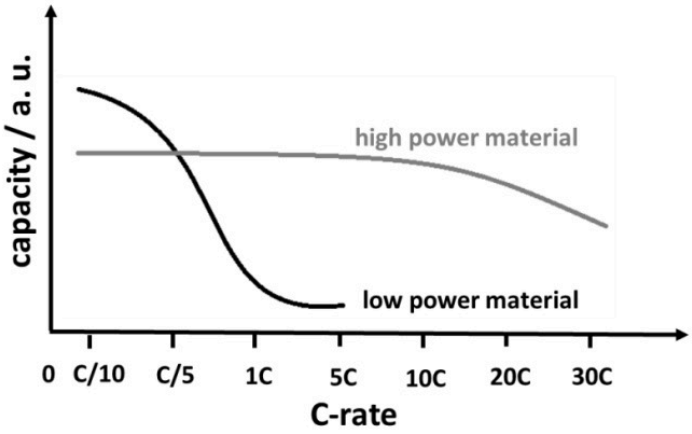

Figure 9: Schematic plot of the capacity versus C-rate for high and low power materials.

The total amount of stored charge for such high surface area metal oxides can be separated into Faradaic contribution of the lithium-ion insertion process, pseudocapacitance (Faradaic charge-transfer process with surface atoms) and the non-Faradaic contribution from the double layer charging. Wang et al. reported an increase of stored charge via pseudocapacitance and a decrease

of stored lithium-ions inserted into the structure at higher applied current rates. This effect was shown to increase with reduced crystallite size and higher surface area [24]. Thus, some insertion battery materials tend to act more like oxide supercapacitor materials at highest applied current rates (fast charging/discharging).

Figure 9 shows a scheme of the general performance of a high power and low power electrode material. A high power electrode material has to possess high solid-state ion diffusivity, high electrical conductivity, minimized solid-state path lengths for ion transport, minimized path lengths for electron transport and finally a high electrode/electrolyte surface area [45], (Figure 10). According to this, low particle sizes and high surface areas favour the high power performance of an electrode material.

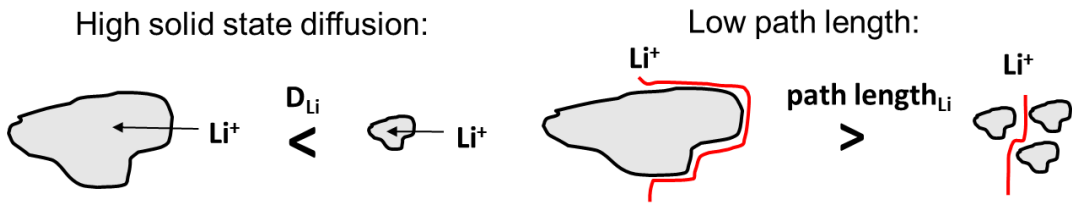

Figure 10: Exemplary presentation of the solid state diffusion and path length in electrode materials.

Guo et al. made a comprehensive review about benefits of nano-sized particles for high power LiBs [46]. Solid-state diffusion of lithium-ions within the electrode materials can be expressed as the mean diffusion (or charge storage) time (t_{mean}). t_{mean} is related to the diffusion coefficient D and the diffusion length L, Equation 10:

$$t_{mean} = \frac{L^2}{2D} \tag{10}$$

Therefore, two approaches can be taken for fast charging/discharging. One can either drastically increase the ion diffusion D or decrease the diffusion length L. Improved diffusion can be related to doping, that can widen the lithium-ion paths within the structure. Such approaches are quite challenging as the optimum dopant atom and amount needs to be investigated. Less challenging seems to be the simple approach of nano-sizing for decreased solid-state diffusion. Guo et al. further pointed out, that a reduction of L from 10 mm (typical size of some commercial electrode materials) to 100 nm can drastically reduce t_{mean} from 5000 to 0.5 s (material with $D = 10^{-10}$ cm^2 s^{-1}, which is a typical value of electrode materials) [46]. The effects are huge, explaining the efforts of R&D in the field of nano-sized electrode materials for LiBs. In the following section, different classes of negative electrode materials will be presented. Insertion materials can be seen as high power and conversion/alloying materials as high energy materials. In addition to this (considering an appropriate mass loading and no additives within the electrode network), insertion materials have very high cycle lives, but low theoretical capacities (low structural changes), whereas conversion/alloying materials have low cycle lives but high theoretical capacities (high structural changes), see Figure 11.

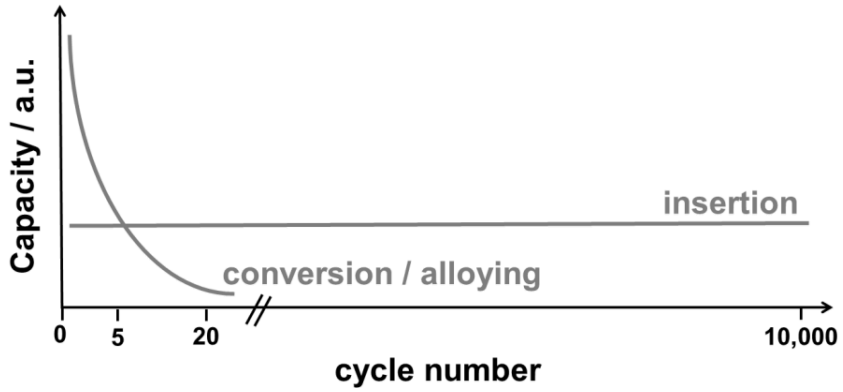

Figure 11: Scheme for comparison of insertion versus conversion/alloying materials. Insertion materials are stable but show low specific capacity whereas conversion/alloying materials show low stability but high specific capacity.

In 2005, Sony developed its Nexelion battery using a negative electrode material mainly composed of a Sn/Co/C composite synthesised by a high energy mechanical milling process [47]. Not only composite materials, but also nano-sized particles and nano-structured materials have been suggested to alleviate the mechanical strain generated due to the volume change as the lithium-ions are inserted into and extracted from the host electrode materials [48, 49]. This development reflects the idea of composites for high cycle life and high capacity electrode materials, see also various commercially available Si/grahite based LiB cells.

1.4.1 Insertion Materials

The general, lithium-ion insertion into a transition metal oxide MO_x is presented in Equation 11 (note that this reaction is also possible for sulphides, phosphates etc.). Characteristic for this process is a high cycle life, high safety but low or medium capacity.

$$MO_x + yLi^+ + ye^- \leftrightarrow Li_yMO_x \quad (11)$$

The term insertion can be used for the reversible lithiation in 1D-olivine (e.g. LFP, rutile TiO_2), 2D-layered (e.g. graphite, layered titanate) and 3D-spinel (e.g. LTO, LMO) structures, whereas the term intercalation is specifically only applicable for 2D layers (Figure 12).

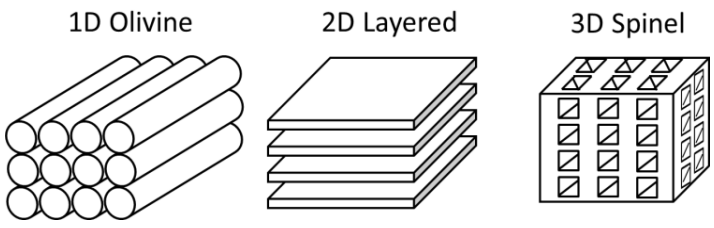

Figure 12: Structures of insertion materials (1D, 2D, 3D).

Insertion materials are ionic/electronic conductors. The ionic transport of the host insertion material is enabled by providing diffusion channels for the lithium-ions and inter-connections of interstitial sites. The electronic transport results from the overlapping of the d orbitals of the (transition) metal. These metals also enable charge compensation during lithiation and delithiation due to its reduction and oxidation, respectively.

There are two processes of lithium-ion insertion. One is a mono-phase homogenous process, where the lithium-ion insertion does not affect the host structure and causes only minimal structural changes (see graphite). The second one is a bi-phase process, where structural rearrangement may involve either a simple reorganization of the lithium-ions within the interstitial sites or the displacement of the transition metal or even the deformation of the anionic sub lattice (see LFP, rutile TiO_2).

Graphite as benchmark negative electrode. The low intercalation/deintercalation potential vs. Li/Li^+ of graphite and the high cycle stability have led to its use as negative electrode in LiBs. During intercalation the graphene layers shift to the favoured AA stacking and the interlayer distance increases around 10 % [50]. These structural changes are far lower compared to alloying and conversion reactions (up to 300 %). Graphite is relatively inexpensive, has a high specific theoretical capacity of 372 mAh g^{-1} and operates at relatively low potentials (range of 0.3 to 0.1 V vs. Li/Li^+). However, formation of a SEI at the surface is necessary to stabilise the negative electrode material, and poor rate retention at applied currents >5 C [30, 51-53]. Due to kinetic limitations during the intercalation of lithium-ions between the graphene layers [32], graphite can suffer in terms of safety, e.g. lithium plating and dendrites can be formed, which can lead to short circuits [54].

Titanates as alternative to graphite. Titanium oxide based materials are very interesting for lithium-ion based electrochemical energy storage systems since their insertion operating potential is in the range 1.0 to 2.5 V vs. Li/Li^+, giving higher safety (no risk of lithium dendrite formation). TiO_2 (ca. 168 mAh g^{-1} for anatase TiO_2) and LTO (175 mAh g^{-1}) offer good sustainability, low cost, low risk to the environment, high cell safety, low capacity loss, high power capability and a very high cycle life due to minimal volume and structural changes during cycling [55]. However, the higher operational potential window dramatically decreases the specific energy of a full cell [56, 57]. Therefore, titanium oxide based LiB materials are the first choice, if power performance, cycle stability, cost or safety are needed parameters. Anatase TiO_2 is very easy to synthesize, which explains the commercial interest in it for electrochemical energy storage devices [24, 58-63]. Anatase TiO_2 has a body centred space group $I4_1/amd$, which is comprised of TiO_6 octahedra sharing two adjacent edges with two other octahedral so that planar double chains are formed [64]. The diffusion of lithium-ions is very facile along a diffusion path connecting the octahedral interstitial sites [65]. 0.5 mol of lithium-ions can be stored per 1.0 mol anatase TiO_2, which is accompanied with a symmetry transformation towards orthorhombic $Pmn2_1$ space group [66] and a unit cell increase along the *b*-axis (decrease along the *c*-axis) which overall expands the unit cell volume by only 4 % [67]. The $Ti^{3+/4+}$ redox reactions take place at ca. 1.6 V vs. Li/Li^+ during lithiation and ca. 2.0 V vs. Li/Li^+ during delithiation.

1.4.2 Conversion Materials

In 2000, Poizot et al. investigated various metal oxides (such as CoO and FeO) as negative electrode materials and measured very high capacities of 700 mAh g^{-1} [68]. It could be shown that during charge the metal oxide was fully converted to its metallic state. Because of this behaviour, these new electrode materials were called conversion materials. The M_aX_b [M = metallic cation, X = anion (S, N, P, O, F)] is reduced to its metallic form surrounded by a gel-like lithium compound Li_nX (see Equation 12 and Figure 13).

$$M_aX_b + (b \cdot n)Li^+ \leftrightarrow aM + b\,Li_nX \qquad (12)$$

One reason for the reversibility (similar amount of lithium-ions are stored and released in the electrode material during cycling) is the enhanced surface energy of the nano-dispersed transition metal particles after reduction (these might have a catalytic effect) [69]. Different from oxides and sulfides, the main exception is fluoride, which reacts at high values close to 3.0 V vs. Li/Li^+, which makes it a candidate for positive electrode materials [70].

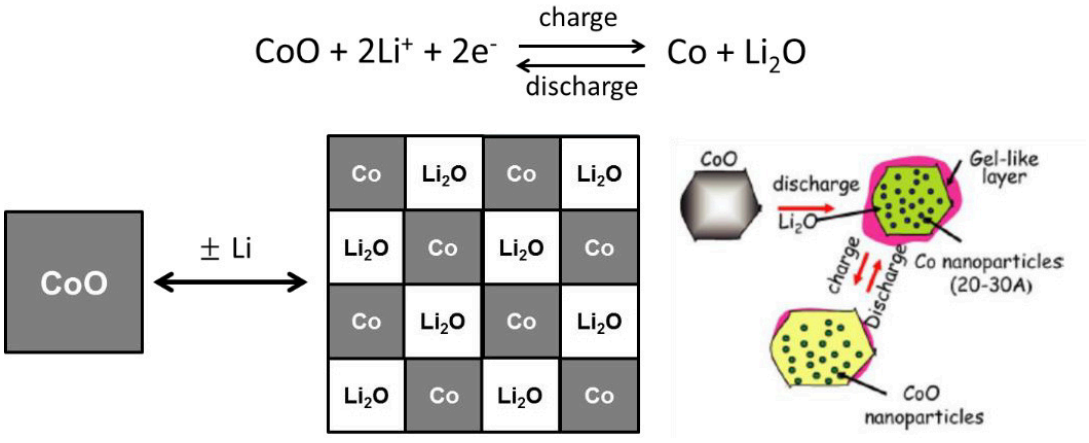

Figure 13: Schematic presentation of the lithiation/delithiation of CoO particles. During the first discharge step a gel-like layer is transformed next to metallic Co particles and Li_2O (modified taken from [71]).

The range of possible conversion materials is very large and has been widely explored. Fe_2O_3 (1007 mAh g^{-1}) and Fe_3O_4 (926 mAh g^{-1}) have high theoretical capacities, are non-toxic and environmentally friendly, highly abundant and inexpensive, which is why these are very interesting candidates for future negative electrode materials in LiBs. However, many of these materials suffer from poor voltage hysteresis and large volume changes upon cycling (causing morphological/structural changes in the negative electrode network) which is observed as large capacity fading [72]. A voltage hysteresis can be understood as a significant shift of the electrochemical potential activity from low potentials during lithiation towards high potentials during delithiation for the negative electrode side (Figure 14).

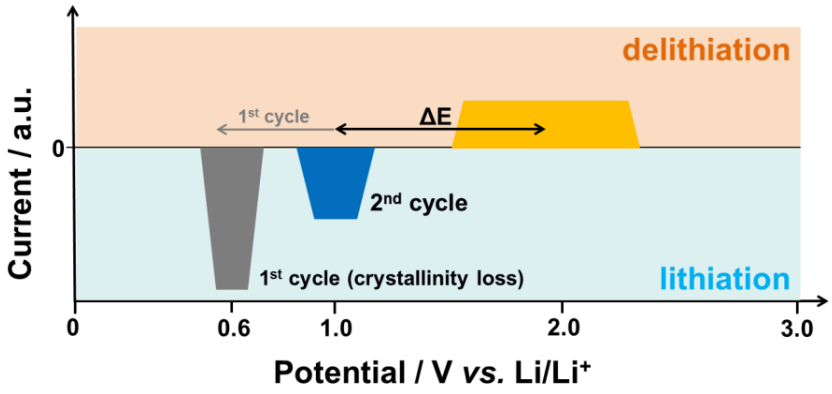

Figure 14: Scheme for representation of the voltage hysteresis (ΔE) during lithiation and delithiation and also showing the impact of crystallinity loss for such conversion materials (scheme herein refers to iron oxides).

In Figure 14, the initial cycling data for the first two cycles of a general conversion material like iron oxides is presented. During initial lithiation, the voltage hysteresis is even higher because the activation energy is higher. The crystalline material undergoes drastic structural changes, which causes additional lithium-ion losses due to irreversible lithiation sites within the structure. For iron and cobalt oxides, the initial voltage hysteresis can be around 1.7 V, which is far higher

compared to graphite with <0.1 V and silicon with <0.5 V. Once the materials becomes amorphous, the lithiation potential changes towards 1.0 V vs. Li/Li^+ for iron and cobalt oxides giving an average voltage hysteresis of ca. 1.3 V. Simply explained, the input energy is far higher than the output energy for such systems, which limits its practical implementation [73, 74].

As mentioned before, conversion materials undergo high structural changes through irreversibly loss of crystallinity, rendering them amorphous after the first cycle, which results in large irreversible capacity losses. Some of these pure negative electrode materials also display low intrinsic conductivity, which limits their use in rechargeable LiBs. Traditionally, the use of a high wt% of conductive additives in the printed electrodes (ca. 30-40 wt% [75, 76]) or conductive carbon shells on particles [77-80], have been used in an attempt to both buffer the huge volume changes observed upon cycling (Figure 15) and enhance the poor electronic conductivity of conversion materials [81].

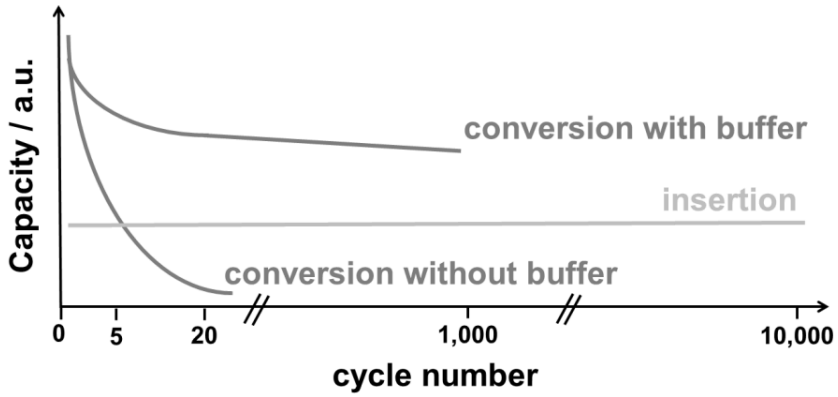

Figure 15: Comparison of cycle stability of conversion material with or without using a buffer.

Using large amounts of carbon is not ideal since it reduces the volumetric energy density. There is a drawback of metal particle agglomeration at the fully lithiated stage. Therefore, nano-sizing

such materials is used as a strategy to increase the cycle life and the reversibility of the back reaction towards the metal oxide. But with all promising achievements in terms of improving the cycle stability of this class of materials, the practical relevance of these results remains to be proven as particle reorganization and volume changes upon cycling are still challenging. Moreover, there is still no convincing strategy to overcome the large voltage hysteresis. Thus the practical application in a commercial device is still highly questionable [74].

1.4.3 Alloying Materials

The high interest in alloying materials is due to the high capacity compared to other negative electrode materials (Figure 16). Alloying materials show much higher theoretical capacities (e.g. Si 3572 mAh g^{-1} and Sn 993 mAh g^{-1} [82]) compared to graphite (372 mAh g^{-1}) and other insertion materials (e.g. TiO_2 and LTO ca. 170 mAh g^{-1}). The high capacity and the low operating potential, result in higher energy densities.

$$M + zLi^+ + ze^- \leftrightarrow Li_zM \quad (13)$$

$$M_xO_y + 2yLi^+ + 2ye^- \rightarrow xM + yLi_2O \quad (14)$$

The main alloying materials such as Sn, Si, Sb and Al undergo drastic structural changes upon lithiation since the maximum amount of lithium-ions can be up to z = 15 (for Si), Equation 13. Some materials such as SnO_2 or ZnO need to be reduced initially via conversion towards its metallic state (Equation 14). However, alloying materials show large irreversible capacity loss during the initial cycles due to high structural changes (similar to conversion materials, movement from crystalline to amorphous phase) and high capacity fading (poor cycle life) during lithiation and delithiation, i.e. >300 % volume change during lithiation for Sn [83, 84]. These large volume changes deform the electrode material, which can be followed by active

material loss due to disconnection from the negative electrode network. Several groups used very low mass loadings/high conductive agent electrodes, a thin film or excessive carbon loading to overcome this issue [82, 85].

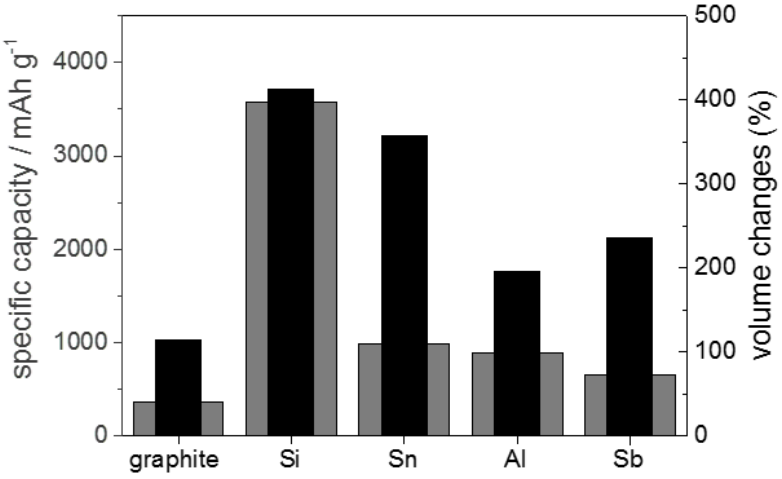

Figure 16: The gravimetric capacity (grey) of a number of electrochemically active metal elements with their volume changes (black) during lithiation [86].

These approaches, however, include less active material within the electrode network limiting the energy density of the full cell. Additionally, the SEI formation on alloying negative electrode material appears to be a dynamic process of breaking and reforming due to the constant volume changes of the alloying particles during cycling which results in constant irreversible loss of active lithium-ions. The thickness of SEI films and the amount of salt-degradation products have been observed to increase with the cycling number [87]. Nano-sizing these materials seem to be a key factor to decrease the defects in the electrode slurry, decrease the agglomeration and also increase the kinetics for higher lithium-ion diffusion in order to prevent trapping of lithium in the alloying host.

The cycle life needs to be drastically increased. Ideas are the combination of an inactive buffer-matrix like graphitic carbon around alloying materials, an active host-matrix such as TiO_2 (which increases the energy density) or the use of highly porous alloying materials. The idea is to start cycling directly from the second cycle of a highly crystalline alloying material. Several studies have shown that this can dramatically increase the cycle life [82, 88, 89].

1.4.4 Combinations of Insertion / Alloying / Conversion Materials

Since insertion materials show high cycle stability but low capacity and conversion / alloying materials show high capacity but low cycle stability, there has been huge interest to combine these two classes of materials. More details and examples can be found later in chapter 5.

Without considering the stability, many researchers have attempted to find highest possible capacities via mixed conversion and alloying materials. Bresser et al. presented a comprehensive summary and comparison of synergies of combined alloying and conversion materials in their review [90]. Palacin et al. still see problems with these classes of materials due to large voltage hysteresis issues remaining unsolved [74]. This should suggest caution when reading all the papers about high capacity negative electrode materials including charge storage mechanism via conversion and alloying materials, as the cell voltage is decreased as soon as the conversion materials are introduced into the negative electrode system. More details can be found in chapter 5.

1.4.5 Tin Dioxide – An Alloying and Conversion Material?

SnO_2 has attracted interest as a negative electrode in lithium-ion batteries because it is relatively inexpensive, easy to produce, non-toxic and shows high capacities [91-102]. For a very long time, SnO_2 was believed to undergo only alloying reactions during cycling resulting to a theoretical capacity of 782 mAh g^{-1} [103-105]. There was some discrepancy in the materials performance especially after nano-sizing, with delithiation capacities up to 1200 mAh g^{-1} [101]. This questioned the origin of the extra capacity, which is not fully answered to date. The electrochemical performance of SnO_2 for LiBs needs to be understood first, Figure 17.

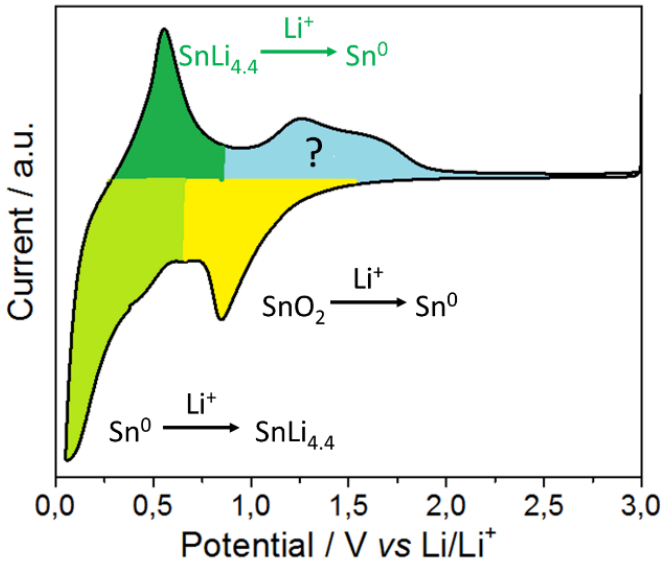

Figure 17: Typical cyclic voltammetry profile showing the lithiation (yellow, green) and delithiation (dark green, blue) regions when nano SnO_2 is cycled as a positive electrode versus lithium metal.

The conversion of SnO_2 towards metallic Sn during initial lithiation causes extreme structural and volume changes (see also Equation 14). During further lithiation, up to 4.4 mol of lithium-ions are stored in the metallic Sn at low potentials (see Equation 13) and this reaction is considered fully reversible. There has been considerable disagreement regarding the reversibility

of the conversion process shown (back reaction towards Sn^{4+}); some researchers suggest this reaction is irreversible (i.e. Sn remains in its metallic state) [103-105], whilst other researchers claim it is (partly) reversible ($Sn^{0}\rightarrow Sn^{2+/4+}$) [106-108]. As shown in Figure 17, there is clearly additional electrochemical activity in the range 0.8 to 2.0 V vs. Li/Li^{+}. This potential region has been investigated further by many groups to date (blue area in Figure 17). In an attempt to show the reversible formation of Sn^{4+}, ex-situ X-ray photoelectron spectroscopy (XPS) measurements [107, 109] and ex-situ high resolution-transmission electron microscopy (HR-TEM) studies [109, 110] were used after the first delithiation step at ca. 3.0 V vs. Li/Li^{+}. Conversely, Lee et al. suggested that the origin of this increased capacity could be mainly found in the electrochemical activity of $LiOH/LiH/LiO_2$ [111]; such species were also believed to be responsible for the additional storage capacities observed for RuO_2 (generated due to the presence of H_2O which led to electrochemically active LiOH in the sample) [112].

Therefore, a convincing comprehensive proof of a reversible conversion reaction is still missing to date (although, there are many pieces of evidence).

1.5 Pseudocapacitive Battery Materials

Pseudocapacitive battery materials can be seen as hybrid electrode materials, as they combine the attributes of supercapacitor and battery materials. There are many extrinsic oxide supercapacitor materials (e.g. TiO_2, VO_2, layered titanate), which show battery-like behaviour for the bulk and increasing oxide supercapacitor-like behaviour with increasing surface area.

For low surface area and well defined electrode materials made from suitable candidates, the insertion process occurs at defined potentials vs. Li/Li^+ (Nernst behaviour, Equation 3); however, for nano-sized versions of the same materials, these potentials can vary considerably [113]. In Figure 18, the charge storage profile for potentiodynamic and galvanostatic electrochemical testing (for a negative electrode) is presented. For bulk electrode materials, the diffusion-limited (battery-like) insertion process is potential dependent for each material, whereas for nano-sized high surface area electrode materials, the charge is stored by surface effects (oxide supercapacitor-like) which results in potential semi-dependent charge storage [23].

The surface effects can be defined as a mixture of physical double-layers and pseudocapacitive fast Faradaic surface reactions [15]. For the pseudocapacitive process, the amount of charge (ΔQ) from Faradaic charge transfer processes depends on the change in applied potential (ΔE). The derivative $d(\Delta Q)/d(\Delta E)$ is equivalent to capacitance, and therefore the amount of stored charge is “linearly” proportional to the applied potential [114]. As batteries show relatively high energy density, and oxide supercapacitors tend to show high power performance, nano-sizing known LiB electrode materials may be one solution for high power and high energy LiBs.

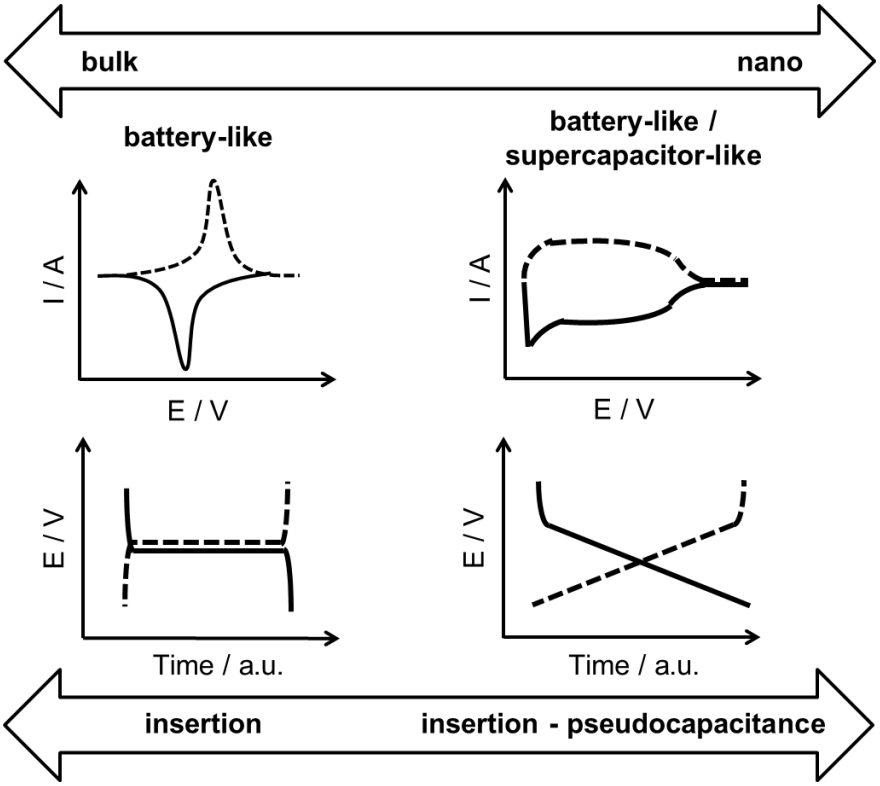

Figure 18: Comparison of the electrochemical manifestation of different charge storage mechanisms for potentiodynamic and galvanostatic measurements. The bulk negative electrode material stores the charge via lithium-ion insertion. A drastic decrease of particle size results in a shift to oxide supercapacitor-like behaviour (more stored charge via surface effects) [115].

Overall, one important goal of research is the marrying of the positive attributes of batteries (e.g. high capacity and energy density) with those of oxide supercapacitors (e.g. high power density). Metal oxides (such as titanates [24], Nb_2O_5 [116], vanadium oxides [117-119], RuO_2 [120] etc.) have been actively investigated as candidate materials for such a purpose, as they have been shown to store charge through lithium-ion insertion (battery-like), as well as fast Faradic reactions on the surface of the materials (pseudocapacitance and Helmholtz double-layer capacitance).

1.5.1 Pseudocapacitance Insertion – Impact of Surface Area and Defects

High power nano-sized insertion materials often show increased defects on the surface and within the crystal due to the very small particle size. Such defects drastically influence the de-/lithiation performance and processes by shifting the thermodynamics and improving the kinetics.

Okubo et al. investigated various nano-crystalline LCO materials for LiBs and could see a large impact of the particle size and surface area on the electrochemical performance [121]. With increasing surface area (decreasing crystallite size), the stored charge decreased (which is similar to the idea of supercapacitors and batteries, where power and energy are inversely related). The slope of the discharge curve of the bulk materials was more rectangular (Figure 19a), meaning LCO undergoes a phase transformation during a redox reaction. With increasing surface area, there was increased charge storage via surface effects, which contributed to a more slope-like discharge curve. The site energy for intercalated lithium-ions is expected to take on a range of values due to the structural disorder for the layers near the surface (Figure 19b), which can also include a higher number of defects and larger inter-layer spacing in the surface layers.

As a result of the higher number of lithium-ion sites near the surface, the power performance (electrochemical performance at higher rates) was superior for 17 nm crystals compared to bulk 200 nm crystals [23, 121]. This was a landmark report, demonstrating the benefits of nano-sizing towards better power performance.

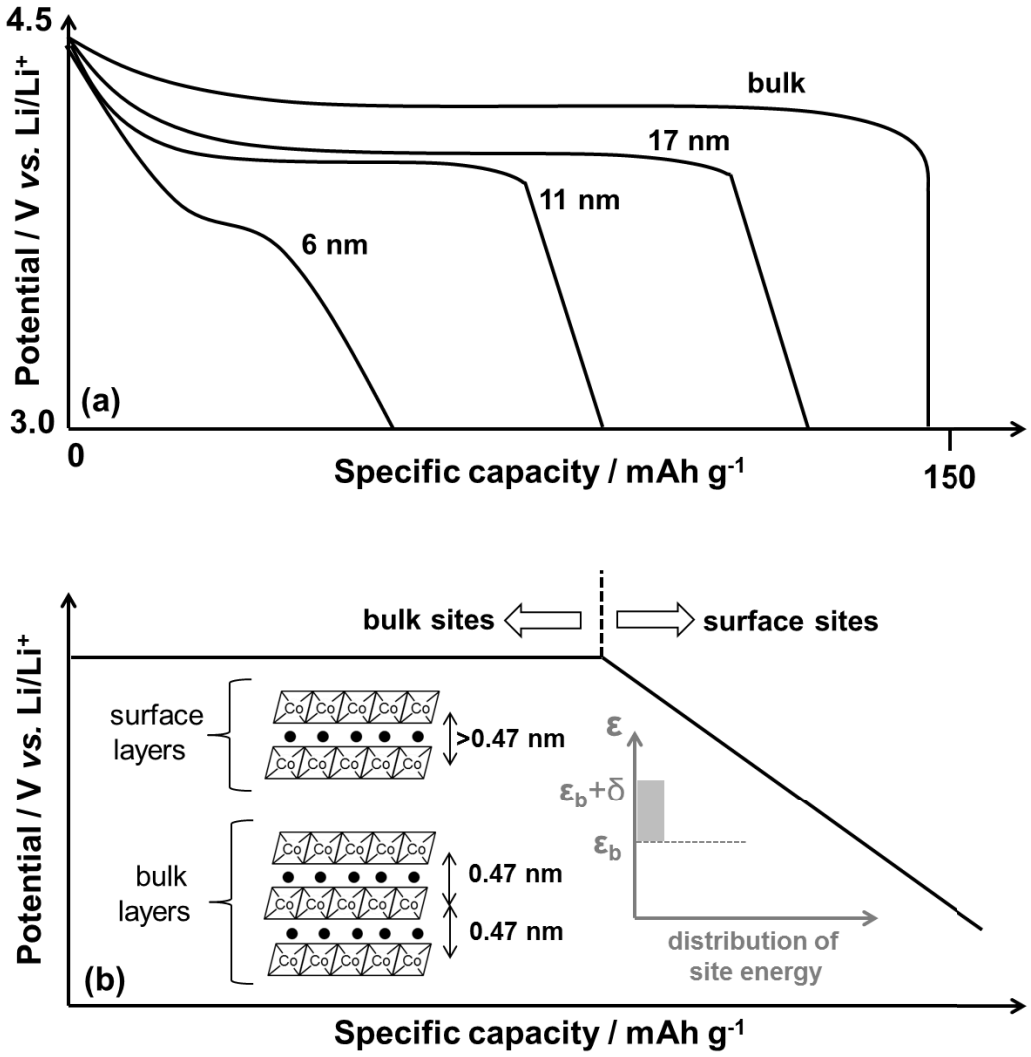

Figure 19: (a) Crystallite size dependence of the second discharge curve for LCO with various crystallite sizes. (b) Expected discharge curve for nano-crystalline LCO. The inset shows the structures within the particle together with the dispersed distribution of the site energy (modified taken from [121]).

Amorphous insertion electrode materials have been increasingly considered as possible high energy and high power electrode materials for lithium-ion and sodium-ion batteries [122], either for the negative [123-125] or the positive electrode [126, 127]. Interestingly, for the negative electrode side, it was possible to use materials such as V_2O_5 [123, 125] and $Li_4Ti_5O_{12}$ [124] in the potential range of 0.05 to 3.0 V vs. Li/Li^+. For each of these reports, the enhanced

electrochemical performance was explained to be due to higher ionic diffusion (larger access of lithium-ions from the electrolyte into the host and opening of diffusion pathways) in the amorphous phase compared to the crystalline counterpart. Moreover, Oh et al. observed that a wider operational potential window was likely due to a wider variety of electrochemically non-equivalent lithium-ion storage sites; vacant lattice sites can provide both cation and anion vacancies, whilst void spaces, cluster gaps or interstitial sites can also be present in this regard [125]. For similar materials (surface areas of 80 m^2 g^{-1} [123] and 15 m^2 g^{-1} [125] for a V_2O_5 aerogel), the shape of potentiodynamic and galvanostatic data plots can be described as a mixture of battery-like and oxide supercapacitor-like behaviour [123-125].

1.5.2 Niobium Pentoxide for High Power LiBs

Niobium pentoxide (Nb_2O_5) is an ideal high power electrode material in LiBs, as it is relatively inexpensive, environmentally benign and stable in a wide range of temperature and pH conditions [116, 128, 129]. The lithium-ion insertion and extraction process for crystalline Nb_2O_5 can be described with: $xLi^+ + xe^- + Nb_2O_5 \leftrightarrow LixNb_2O_5$, where $x \leq 2$ (corresponding to 200 mAh g^{-1}). In comparison to Nb_2O_5 in LiBs, graphite electrodes can suffer from low power density [52, 53]. The specific capacity of crystalline Nb_2O_5 (200 mAh g^{-1}) is relatively modest compared to other materials like lithium metal, Si, Sn, graphite (3860, 3572, 993, 372 mAh g^{-1}, respectively), but Nb_2O_5 has the potential to deliver high power densities due to its high rate performance (combination of lithium-ion intercalation and fast charge storage arising from surface effects), including charge/discharge times of only a few seconds [116, 128-130]. Density functional theory (DFT) analysis by Ganesh et al. showed that the defined high-rate intercalation pseudocapacitative behaviour in this material is due to local charge-transfer at all adsorption sites (leading to high energy), open channels that reduce the diffusion barrier for lithium-ions to

hop between these (leading to high power) and the lack of first-order phase transformation upon lithiation/delithiation (leading to higher capacitive charge storage) [131]. Therefore, different from other materials, Nb_2O_5 shows pseudocapacitive behaviour also within the bulk which is why the charge storage is generally defined as pseudocapacitance intercalation [23]. Several groups have reported the electrochemical performance of Nb_2O_5 in LiBs [128-130, 132-139], and have shown promising high power performances in the potential range 1.2 (or 1.0) to 3.0 V vs. Li/Li^+. Pioneering work by Dunn et al., suggested that high rate charge storage in these and similar materials was mainly due to a mixture of intercalation and pseudocapacitive processes and that charge storage in Nb_2O_5 was greatest for the orthorhombic phase [116, 129]. Surprisingly, this material is rarely reported in a wider potential window (i.e. down to near 0.05 V vs. Li/Li^+).

1.5.3 Layered Titanates for High Power LiBs

Titanium-based materials have shown reasonable specific capacity (e.g. anatase TiO_2 = 168 mAh g^{-1} and $Li_4Ti_5O_{12}$ = 175 mAh g^{-1}) [55], low irreversible capacity loss during the first cycles, high power capability and a very high cycle life, due to minimal volume and structural change in the material during cycling. However, many of these titanium-based electrode materials have a narrow operational potential window, which can substantially limit the specific energy of a full cell, limiting the utility of these materials in certain applications [56, 140].

Due to kinetic limitations during the intercalation of lithium-ions between the graphene layers [32], graphite can suffer in terms of safety, e.g. lithium plating and dendrites can be formed, which can lead to short circuits [54] and poor rate retention at applied currents >10C [30, 51-53].

Layered titanates possess a very large interlayer spacing (ca. 0.8 nm; compared to ca. 0.34 nm for graphite), which drastically improves the high power performances due to higher ionic diffusion. Therefore, layered titanates can be used as electrode material in high power LiBs [141, 142]. By making nano-sized layered titanates, it may be possible to improve the kinetics of lithium-ion intercalation/deintercalation, by greater access of the ions to the entrance sites between the layers as a result of increased surface area to volume ratio. A simplified scheme of the layered titanate showing also the lithium sites between the layers can be found in Figure 20.

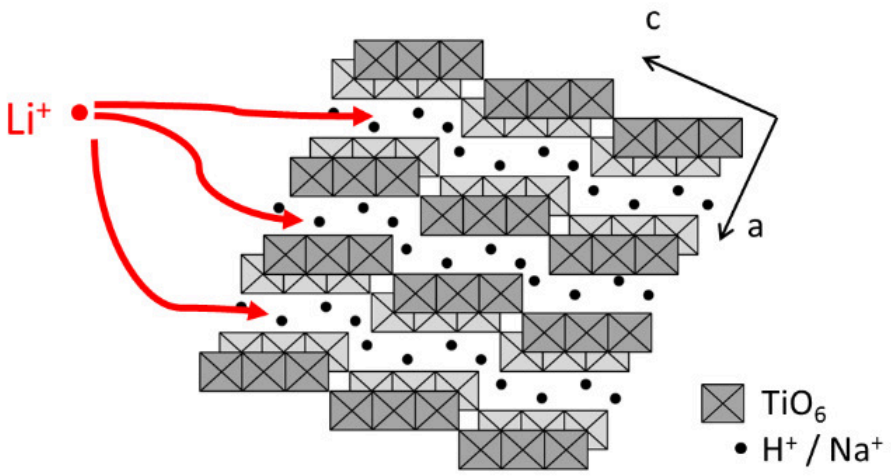

Figure 20: Scheme of main lithiation direction for layered titanates (herein $Na_2Ti_3O_7$).

In the literature, a number of reports on layered titanate electrode materials processed into half cells were cycled at relatively low potentials vs. Li/Li^+ [143-148]. In these reports, applied currents <1.6 A g^{-1} are normally applied at relatively low operating potentials. Moreover, to date the question remains: What is the origin of the stored charge at lower potentials than 1 V vs. Li/Li^+ since the $Ti^{3+/4+}$ redox pair should be active around 1.55 V vs. Li/Li^+?

1.5.4 Vanadium Dioxides for High Power LiBs

Vanadium dioxide (VO_2) is of particular interest due to its low cost and relatively high theoretical capacity of 320 mAh g^{-1} combined with excellent electronic conductivity (key property for high power performance) [149, 150].

Since pseudocapacitance is somehow related to the surface area for most materials, nano-sizing such materials would be expected to lead to enhanced high power performance. Fan et al. investigated vertically aligned VO_2(B) nano-belt forests in the potential range 1.5 to 3.5 V vs. Li/Li^+ and reached an incredibly high capacity of 100 mAh g^{-1} at an applied current of 27 A g^{-1}. In this case, a 3D VO_2 forest inside an Ni foam, was used as an electrode, with a VO_2(B) mass loading of 1 to 2 mg cm^{-2}. The reason for these excellent results could be found in high electronic conductivity and in a shift of charge storage mechanism towards oxide supercapacitor-like behaviour. The same authors also showed that even at a very low rate of 0.1 A g^{-1}, the capacitance contribution to overall charge storage was >20 % [119]. VO_2(B) was concluded to undergo mainly charge storage via insertion processes in the potential range of 0.05 to 3.0 V vs. Li/Li^+, which was confirmed via ex-situ XRDs of the electrode material. These XRDs showed pattern and pattern intensity shifts, which is characteristic for charge storage via insertion (conversion or alloying mechanisms would result in an amorphous phase) [151].

This class of materials is another example for negative electrode materials, where charge storage can arise at lower potentials than usually expected. To date, there is no convincing conclusion why it is possible. Interestingly, most of these vanadium based materials show high power performances, which promotes further investigation of pseudocapacitive charge storage.

1.6 Solid Electrolyte Interphase (SEI)

As stated earlier, the development of a stable SEI was the key development for the use of graphite in LiBs, because many organic electrolytes are not stable at low potentials. Therefore, the SEI layer acts as a protection layer, which prevents further electrolyte decomposition after the initial cycles and it also is able to prevent exfoliation of the graphene layers.

A general organic liquid based electrolyte for lithium-ion batteries (also used within this thesis) consists of a low viscosity solvent (e.g. DMC or DEC, low viscosity but low dielectric constant) and a high dielectric constant solvent (e.g. EC or PC, high dielectric constant but high viscosity). Such a combination is used, as it should combine several aspects including high ionic conductivity, low vapour point, high dielectric constant (enabling the dissolution of lithium-ion salts) and also the ability of SEI formation, as this layer is crucial for a high cycle stability of LiBs. EC and $LiPF_6$ made their way into commercial LiBs since these two are known to form an effective SEI [152].

There are far more electrolyte additives in the electrolyte that might help improvements towards better performance or even stability. Moreover, today's commercial LiBs are sometimes polymer-based because these tend to be more stable during cycling and in a wider temperature range, are easier to process and often also safer.

The electrolyte used herein tended to form a stable SEI at low potentials vs. Li/Li^+. This SEI layer is an electronic insulator, but a lithium-ion conductor, so the growth of the SEI layer is expected to terminate at a certain thickness. For any negative electrode active material surface, an increased surface area shows far higher lithium-ion loss due to the initial decomposition of the lithium-ion salt at the surface, forming several layers (see Figure 21).

These layers can be classified as inorganic and organic layers. Inorganic compounds include compounds such as Li_2O, LiOH, LiF and $LiCO_3$. Recently, it has been shown that such a layer can be even another charge reservoir, where lithium-ions can be reversibly stored and released [112, 153]. Such investigations are quite sensitive since the SEI layer is made of several compounds and is also very thin (hundreds of Å). More research is needed to understand the chemical reactions and also the role of the negative electrode surface area, surface groups and their properties.

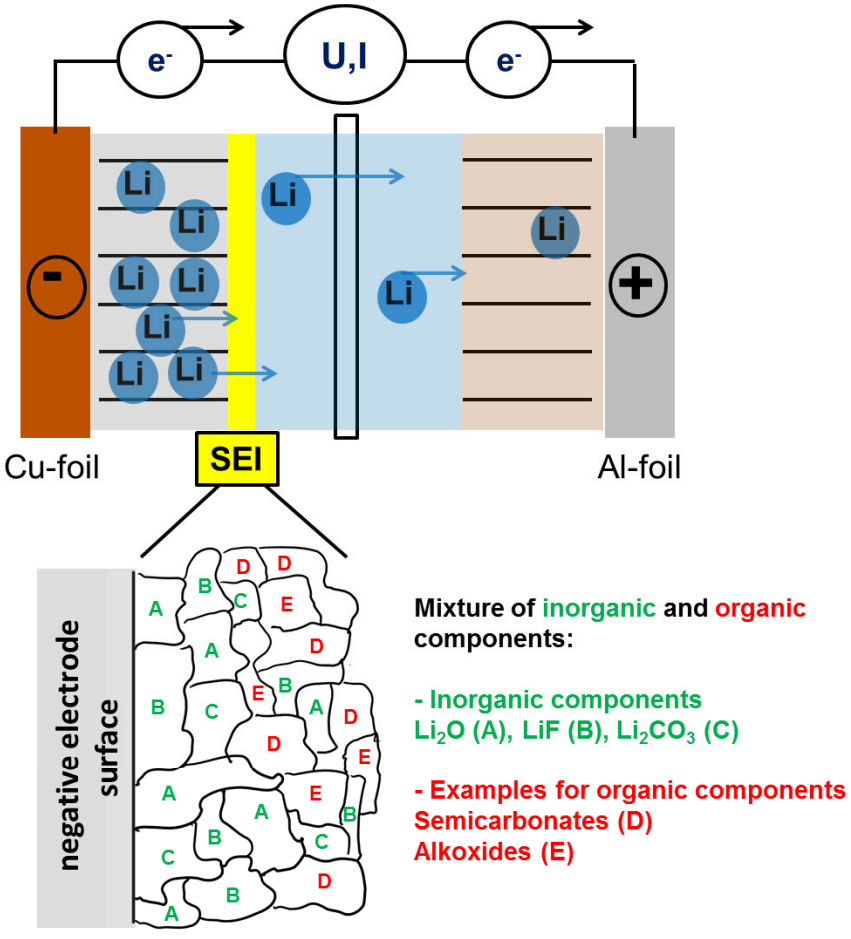

Figure 21: Scheme of an SEI layer showing different layers of inorganic and organic decomposition compounds. The inorganic layer is closer to the negative electrode surface area followed by an organic layer which each are products of $LiPF_6$ and EC reactions during the initial cycles [154].

Overall, a SEI layer is very important for the negative electrode when cycling down to low potentials. It should contribute to cell safety, be highly ion-conductive also for cycling at higher rates, be protective against further electrolyte decomposition and the formation process is associated with a minimum of irreversible material (electrode and electrolyte), charge losses and side reactions including gas evolution. The SEI layer properties should be electronically insulating, which should decrease further electrolyte decomposition. It should show a uniform morphology and chemical composition for a homogeneous current distribution and show good mechanical strength and flexibility for possible volume changes during charge/discharge. E.g. if the SEI layer is not flexible, further electrolyte decomposition would be accompanied with each lithiation due to cracks within the layer. This would also drastically increase the cell resistance during cycling (a thick SEI increases the impedance) [152].

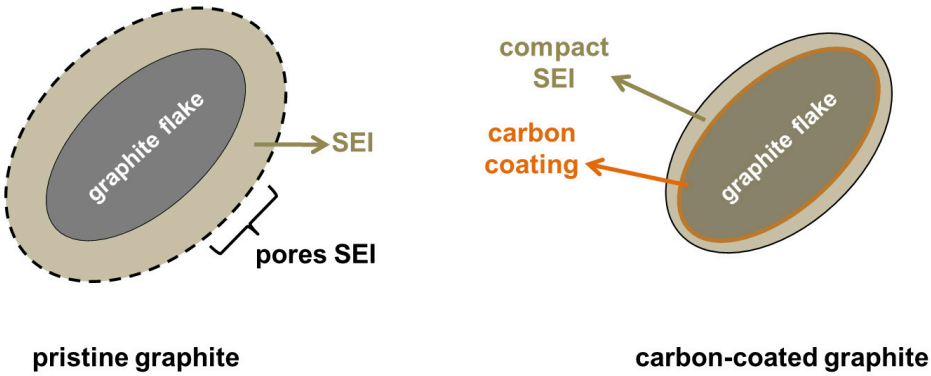

Figure 22: Simplified model to show the SEI on pristine and carbon-coated graphite, modified taken from [155].

It should be clear, why nanosized transition metal oxides are a questionable choice for use as negative electrode materials (at low potentials). With increasing surface area, the SEI layer formation increases (%) resulting in far increased lithium-ions losses in irreversible interstitial sites and electrolyte decomposition [60, 156]. Such a system is very hard to balance for a full cell LiB. Moreover, many nanosized transition metal oxides have been shown to be unable to

form a stable SEI (e.g. conversion materials [81], alloying materials [48, 82, 83] and even insertion materials [156]), meaning electrolyte decomposition is more or less a continuous process for such materials during cycling. There are attempts to improve each, the irreversible capacity loss during the first cycle and Coulombic efficiency. Learning from research for graphite, it was proposed that carbon-coating would drastically decrease the irreversible capacity loss [157-159]. This was referred to a far more compact SEI layer on such a defective and spherical carbon surface [155], Figure 22. Carbon-coating drastically reduces the amount of the overall SEI layers meaning less electrolyte destruction and this approach might be promising also for coating with transition metal oxides (see industrial attempts with LTO). It would be interesting to investigate various surfactants as alternative coating at the surface of the negative electrode material, since these might also be able to contribute to a more compact and stable SEI.

Electrolyte additives are known to contribute to an improved SEI formation, which include vinylene carbonate (VC) and many more [160]. The mechanism of the polymerizable additives towards SEI formation is based on an electrochemically induced polymerization. The radical anion forms an insoluble and stable product as the preliminary SEI nuclei. Electrochemically, this type of additive is very effective since the electron transfer is only involved in the first step [160].

Overall, a stable SEI for the negative electrode site is mandatory. The formation is still investigated worldwide. Continuous SEI formation during cycling is a challenging problem as it limits the power performance and is also responsible for continuous capacity loss. Within this thesis, none of the above points was used to improve the initial irreversible capacity loss and Coulombic efficiency, because the focus was set on other research questions. However, all these strategies might be adapted for future research projects.

1.7 Advantages and Disadvantages of "going nano" for LiBs

With respect to the use of nano-materials for electrodes, there are many advantages and simultaneous disadvantages regarding the use of those.

Disadvantages. One disadvantage is the problem of the toxicity. The consequences of nano-sized materials on human beings and also on the environment are still not fully known, but it is clear that there might be concerns [161, 162]. Another major disadvantage of nano-particles is the more complicated synthesis, with difficulties including reliability, size/morphology control and costs. It will be later shown that the "bottom up" synthesis via a continuous hydrothermal route could be one of other synthesis methods to overcome this issue [163, 164]. For battery applications, nano-sized materials still suffer from high costs (often due to the synthesis), low tap density and a high number of side reactions catalysed by the high surface area. The atoms at the surface are less coordinated compared to atoms in the bulk material, which leads to differing chemical and physical behaviour, like a higher catalytic effect or cation dissolution. Many scientific reports showed a low cycle life due to loss of contact between the particles or material degradation due to transition metal dissolution (e.g. for LFP or Mn-based materials). This is still a big problem for the use of nano-materials as active materials for electrodes especially with higher mass loading [165]. Moreover, the high electrolyte/electrode surface area can lead to more side reactions with the electrolyte, resulting in a higher irreversible capacity loss of up to 80 % during the first cycles (see chapter 3). A proper electrode network is very important for the electrochemical performance. Therefore, nano-sized materials can suffer in maintaining interparticle contact, which is essential for the electronic conductivity. Finally, nano-materials decrease the volumetric energy density compared to the same microsized material.

Advantages. The interest in nano-materials has substantially increased during the past years. As an example, many technologies can profit from "going-nano" by minimizing the operative materials (i.e. computer, surface coatings, solar cells, batteries). Some electrochemical reactions do not take place within bulk materials, but it could be shown that going-nano can make microsized electrochemically inactive materials an active electrode material. Jaio et al. used mesoporous β-MnO_2 in nano-scale (with highly ordered pore structure and highly crystalline walls) as positive electrode insertion material. A large amount of lithium-ions could be stored within the nano-sized material, whereas the bulk material showed no lithium-ion insertion [166], which was similar to the findings for rutile TiO_2 [167, 168]. Going-nano also leads to higher power due to the higher lithium-ion diffusion, reduction of the path length and to higher electron transfers [169]. The energy of the band gap increases and the energy levels of each bands are quantized, which changes the electronic behaviour [170]. As mentioned before, insertion/intercalation materials benefit from nano-sizing in terms of high power performances because of the higher surface to volume ratio, which means more active pathways for lithium-ion storage sides are present. This increases the high rate capability, because the lithium-ion diffusion into the particle core and between the particles is higher. The higher surface area also increases the additional stored charge via pseudocapacitance for some transition metal oxides, which can drastically improve the rate performance. For alloying and conversion materials, nano-sizing is even mandatory because the volume expansion is buffered in a far more efficient way.

1.8 Synthesis Methods of Nano-Materials

In general, there are two ways of making nano-sized materials. One is called “top down” and the other “bottom up”. “Top down” is the stepwise decomposition of the bulk material into nano-scale (e.g. grinding). “Bottom up” is the direct synthesis of nano-particles beginning with atoms or molecules (Figure 23). This “bottom up” approach will be further introduced as there are several synthesis methods.

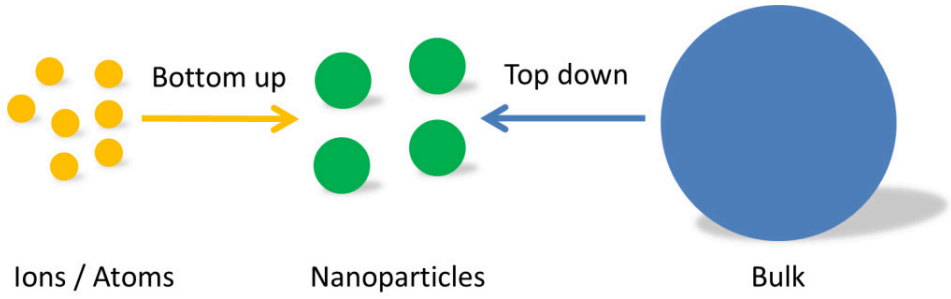

Figure 23: Illustration of the bottom up and top down synthesis approaches.

Precipitating nano-particles from a solution of chemical compounds can be classified into five categories including electrospinning, co-precipitation, micro-emulsions, sol-gel and hydrothermal synthesis. Electrospinning is an effective and inexpensive bottom-up nano-fabrication technique for the synthesis of one dimensional fibre from sol-gel solutions. These fibres are made of nano-particles with controllable morphology [171]. A strong electric field is applied to the tip of a capillary containing the sol-gel solution. A continuous fine jet of solution is ejected from the capillary and moves through an electric field to deposit on a collector. The elongation of the charged droplet expelled from the tip of the needle is caused by electrostatic repulsions experienced in the bends of the lengthening droplet into a fibre which creates the nanometre-scale diameters [171].

Co-precipitation involves the simultaneous occurrence of a nucleation, growth, coarsening and agglomeration processes. The products are in general insoluble and require the use of a metal salt solution, a base ($NaBH_4$, NaOH, $N_2H_2 \cdot H_2O$) and a stabilizing agent. If the parameters such as temperature, reaction time, pH, stabilizing agent, base and choice of salt are made, the reaction is fully reproducible. Nowadays, co-precipitation processes are widely used to produce mainly nano-sized metals, but also metal oxides, organics and pharmaceuticals [172]. Micro-emulsions use a thermodynamic stabile, isotropic dispersion of two non-mixable solutions (i. e. water and oil) and micelles. The micelles are stabilized by a boundary surface of surfactants. Each micelle stores a metal salt and reducing agent (like the way of co-precipitation) or metal salt and precipitation agent. The micelles form a short-lived dimer and the contents of the micellar cores are exchanged. This way, the system of a micelle can be described as a nano-reactor for the formation of nano-particles [173, 174]. A sol-gel process is a wet-chemical technique that uses either a chemical solution (sol) or colloidal particles (sol for nano-scale particle) to produce an integrated network (gel) during the drying process. The sol is a result of a condensation and hydrolysis reaction [175].

1.8.1 Hydrothermal Methods

Hydrothermal synthesis offers many advantages over conventional and non-conventional synthesis methods. It can be used to produce powders, fibres, single crystals, monolithic ceramic bodies, and coatings on metals, polymers, and ceramics [176-178]. Because hydrothermal synthesis takes place in the sealed container, the volatilization of the solvents used in the process is minimal or even negligible. The particle size and morphology can be controlled [179], the yield is often very high, the purity is sometimes even higher than its precursors [180] and the variety of possible synthesized materials is endless. There are only a few less energy consuming

synthesis alternatives to hydrothermal methods and the overall energy consumption is lower as complicated mixing, milling or calcination steps can be omitted. Therefore, hydrothermal methods are considered environmentally friendly due to water being the used solvent, minimal energy consumption and generally high yields.

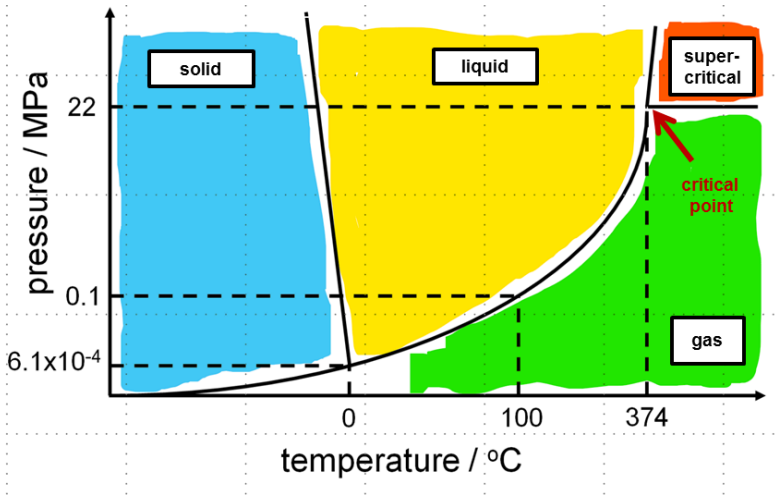

Figure 24: Phase diagram of water.

Hydrothermal reactions can be defined as a process of synthesising ceramic materials directly from homogenous solution or heterogeneous mixtures at defined temperatures (typically >100 °C) and pressures (>1 bar) [176, 181]. In contrast to solvothermal synthesis methods, a hydrothermal synthesis uses water as main solvent. It typically uses moderate temperatures of 100 to 220 °C (subcritical water) at autogenous pressure. Crystal growth under hydrothermal conditions requires a reaction vessel called an autoclave. An autoclave is a closed thick-walled steel cylinder with a hermetic seal which must withstand high temperatures and pressures for prolonged periods of time. The applied temperature and filling factor are key parameters to control the synthesis, as these change the solvent properties. In order to understand hydrothermal reactions, these solvent properties under differing temperature and pressure parameters are introduced.

In Figure 24, a phase diagram of water is presented via a pressure versus temperature plot. Above 374 °C and 22 MPa (critical point), the water is in a supercritical state, which means the distinction between gas and liquid disappears, leading to a substance that can behave simultaneously like a liquid and a gas. Hydrothermal methods usually are in a subcritical state due to the applied temperature with typically <220 °C. Because of the increased temperature and pressure in the autoclave during a hydrothermal reaction, the density, ionic product, dielectric constant and viscosity of solvents change, which drastically impacts the synthesis reaction [182].

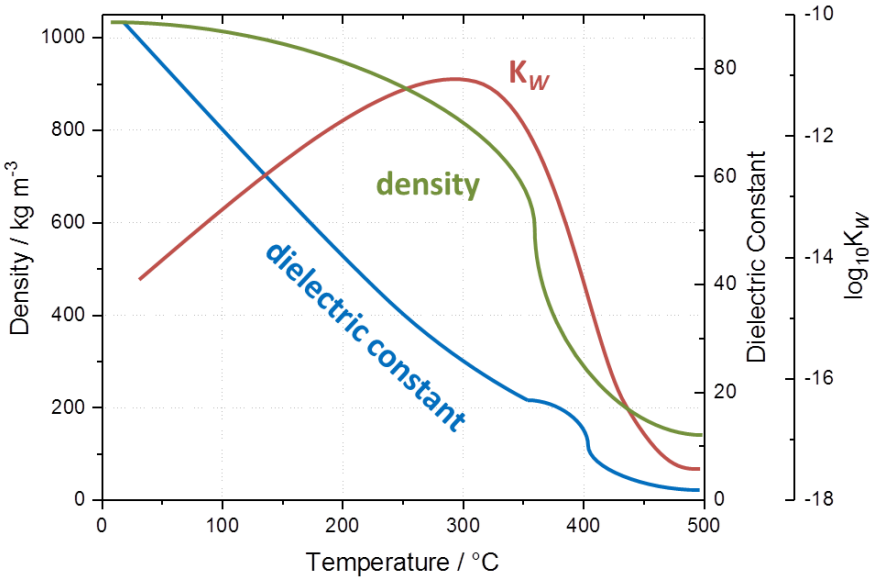

Figure 25: Density, dielectric constant and ionic product of water at 30 MPa as a function of temperature (simplified scheme modified taken from [182]).

Figure 25 shows how the density, dielectric constant and ionic product ($\boldsymbol{K_w}$) of water change with temperature (pressure is set constant at 30 MPa). The density and dielectric constant of water decrease with increasing temperature. When the dielectric constant decreases, the properties of water change to those similar to non-polar solvents, allowing dissolution of non-

polar chemicals. This causes changes in reactivity, solubility and diffusivity of the reactants, which are often either insoluble or unreactive. This change in the dielectric constant and solubility is believed to be one of the driving factors for nanoparticle nucleation in hydrothermal systems [183].

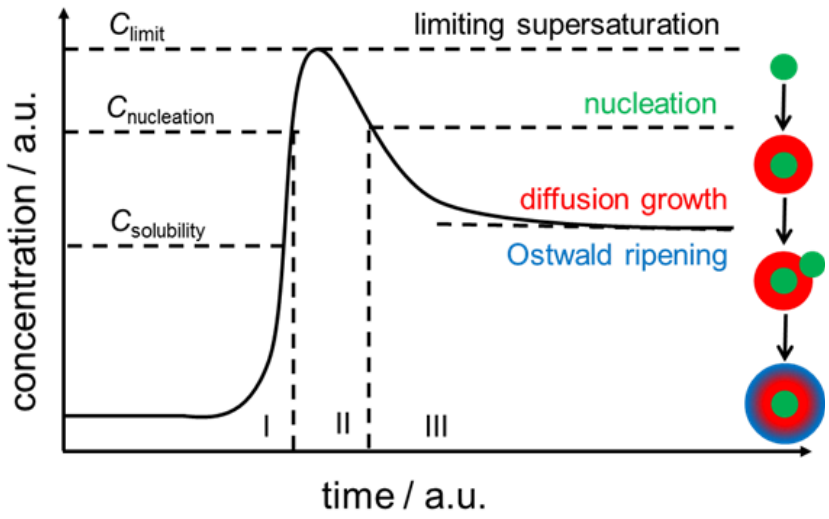

Figure 26: LaMer model of particle nucleation and growth (modified taken from [184]).

The reaction times of traditional hydrothermal reactions in an autoclave can take from a few hours up to several days. In Figure 26, a nucleation and particle growth scheme is presented via a concentration versus time plot. With more reaction time, particle growth is favoured resulting in larger particle sizes and lower surface area. Thus, hydrothermal methods might enable the synthesis of nano-particles, but clearly the diffusion growth and Ostwald ripening might limit obtaining smallest single crystalline particles with narrow size distribution. This requires a hydrothermal synthesis method that enables nucleation driven reactions and very short reaction times. One possibility can be the use of a continuous hydrothermal flow synthesis (CHFS).

1.8.2 Introduction to Continuous Hydrothermal Flow Synthesis

CHFS allows a very short reaction time (seconds and less than seconds), enabling drastic control of particle morphology and size variation, which is usually very narrow [185, 186]. There are many nano-materials that can be synthesized including oxides, sulphides, phosphates etc., doped materials, composites, materials with differing morphology, carbon-coated materials and many more. CHFS is a relatively green process for nano-particle synthesis, the slurries (metal salts diluted in DI water) are easy to handle and the precursors are generally inexpensive. The applied temperatures are still quite moderate (<450 °C) and the yields are often in the range 70 to 99 % [187, 188]. Thus, this method can also be considered as environmentally friendly due to the used solvent and precursors, the moderate temperature and high yield. Additionally, the CMTG-group is also able to carry out high-through put CHFS with 65 samples per day, enabling the possibility of fast, reliable synthesis of libraries. A summary of all advantages of using CHFS for materials discovery and synthesis is given in Figure 27.

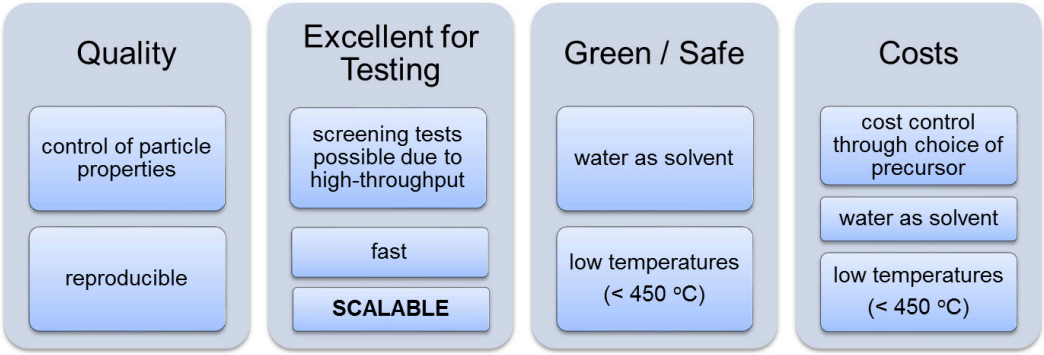

Figure 27: Summary of all advantages of CHFS processes.

CHFS enables a fair comparison of the real impact of the dopant, because most other materials properties such as surface area, crystallinity, water content etc., may not always change due to the short reaction times. Therefore, CHFS is useful for library synthesis with screening tests, e.g. if the optimum conductivity or energy storage performance needs to be found for a class of

materials [189, 190]. Most importantly, the method is reproducible and also scalable. In Figure 28, the two general reactors at UCL are presented. The lab scale reactor is used for materials discovery and promising materials are synthesized at the pilot plant under scaled up conditions with production rates of up to 1 kg per hour. Despite all the advantages, halide ions tend to cause corrosion in the steel mixers and pipes, limiting the precursors that can be used. Moreover, the precursors are preferred to be water soluble.

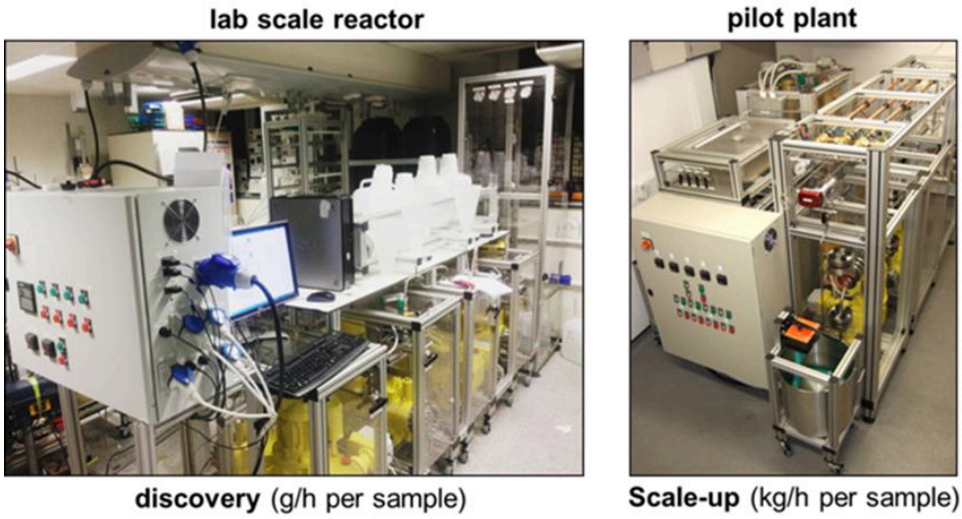

Figure 28: Photos showing a lab scale reactor for materials discovery (left) and a pilot plant for scaling up (right), which are each based at UCL.

In the CHFS process at UCL, a feed of supercritical water (above the critical point of water with T_C = 374 °C and P_C = 22.1 MPa), is rapidly mixed in an engineered mixer [191], with a metal salt/base aqueous precursor feed (at ambient temperature and the same pressure) resulting in rapid formation of nano-particle oxides in aqueous solution (Figure 29).

The nucleation dominated reaction occurs as a result of the metal salts being supersaturated upon mixing. The particles are formed via hydrolysis (Equation 15) and dehydration (Equation 16) reactions of hydrothermal syntheses leading to the formation of metal oxides (L = ligand).

Clearly, the number of intermediate steps during synthesis is often far more complex and this is a simplified model.

Hydrolysis: ML_x (aq.) + $xH_2O \rightarrow M(OH)_x$ (s) + xHL (15)

Dehydration: $M(OH)_x$ (s) $\rightarrow MO_{x/2}$ (s) + x/2 H_2O (16)

Figure 29: General scheme of the CHFS synthesis method.

Shortly after passing the reactor, the nanoparticle slurry gets cooled down within the process enabling very short reaction times (seconds or minutes). These short reaction times limit Ostwald ripening, one main advantage compared to conventionel batch hydrothermal synthesis methods. The nanoparticle slurry is collected at the end of the process in a beaker. The cleaned particles (via dialysis) can be obtained as a wet solid and then freeze-dried to retain maximum surface area.

Why supercritical water (and not subcritical like in many traditional hydrothermal methods)? When the metal salt precursor is mixed with supercritical water, a rapid hydrolysis of the metal salt happens due to the change in the ionic product K_w which can be defined with Equation 17:

$$K_w = [H^+][OH^-] \quad (17)$$

K_w is ca. 10^{-14} mol^2 dm^{-6} under ambient conditions, with the individual concentrations of $[H^+]$ and $[OH^-]$ being ca. 10^{-7} mol dm^{-3}, and it decreases to 10^{-11} mol^2 dm^{-6} at the critical point, with the individual concentrations of $[H^+]$ and $[OH^-]$ being ca. 3.2 x 10^{-6} mol dm^{-3}. Thus, the

individual concentrations of [H^+] and [OH^-] increase by a factor of 30 when the precursor solution is mixed with supercritical water. This change of conditions of the ionic product provides a highly hydrolysing environment. Moreover, supercritical water has a very different density compared to subcritical water. At 20 °C and 101.325 mPa (standard conditions) the density of water is about 1000 kg m^{-3} and decreases down to 322 kg m^{-3} at the supercritical point (ca. 500 kg m^{-3} for subcritical water). Moreover, the dielectric constant of water also undergoes changes when it reaches its supercritical point. Under standard conditions, water can be described as a polar liquid ($\varepsilon = 80$), it shows a high ability to dissolve ionic solids and is mixable with other polar liquids. The dielectric constant of water decreases at higher temperatures. This decrease changes the solubility of other chemical materials in this medium. The change in the dielectric constant (at 374°C and 22 MPa, $\varepsilon = 5$) and the resulting behaviour of solubility is believed to be the driving factor for particle nucleation [183, 192].

CHFS uses short reactions times in addition to nucleation driven conditions. By achieving this fast burst of nucleation, there are minimal particle size discrepancies, thus limiting Ostwald ripening. This gives a narrow particle size distribution, with the possibility of size control by varying reaction times and parameters such as temperature, pressure, precursor type and concentration etc. [193]. The high synthesis temperature is usually sufficient to obtain crystalline precipitates [194].

There are many ways of mixing the supercritical water in flow with the precursor solution (see an example in Figure 30). Since the variety of mixers is far more complex, only the mixer used within this thesis is introduced. For further information, the reader might be referred to the latest review of Darr et al. [195].

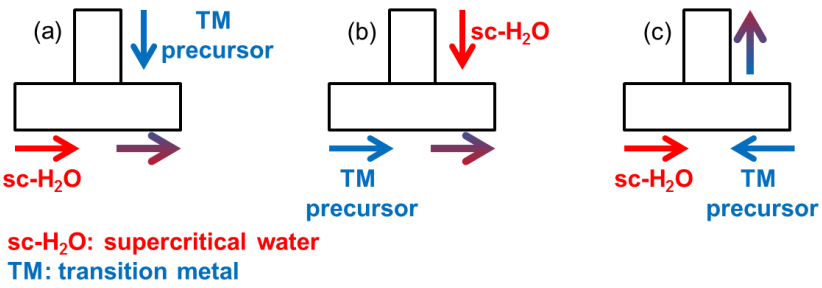

Figure 30: Design of simplified T-piece mixers (modified taken from Kawasaki et al. [196]).

Note: Many CHFS studies in literature report different particle properties (e.g. size, size distribution, morphology, etc.), even though the reaction conditions appear to be similar. This is often a result of differing mixing conditions as shown by Denis et al. for cobalt oxides [197]. The mixer used at UCL is a so-called confined jet mixer (CJM), which is patented (U.S. Patent No. 9,192,901; 2015). In Figure 31, a photo and the general design of the CJM is presented. Different from many other mixers, this one uses the strategy of a co-current mixing. This prevents blockages [191, 198], enabling a safe alternative mixing.

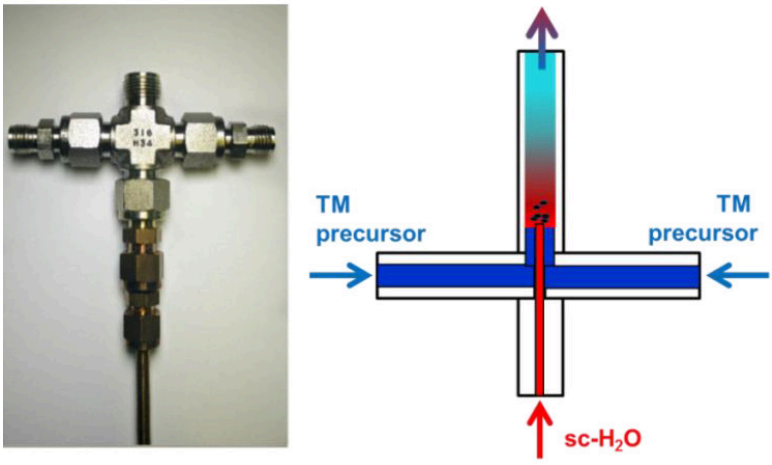

Figure 31: Photo of the used CJM (left) and scheme of the same (right).

1.9 Aims and Objectives

The CHFS process is a key technology that can be used to synthesize nano-particles with narrow size distribution and high surface area. This can be advantageous for both high power and high energy LiB applications. Within the next chapters, several scientific questions were addressed for high power and high energy LiBs.

Scientific questions for high power LiBs:

(i) Why do some negative insertion materials show charge storage at lower potentials than expected? (chapter 3)

(ii) Are there any benefits of using high amounts of Nb^{5+} as dopant in anatase TiO_2? Can the positive attributes of niobium and titanium oxides be combined in one material? (chapter 4)

Scientific questions for high energy LiBs:

(iii) Does the combination of transition metal oxides with SnO_2 really show any benefits for full cell LiBs in terms of energy density? (chapter 5)

(iv) Can Sn as a dopant in nano-sized negative insertion materials be activated as another charge reservoir within the electrode network? (chapter 6)

2. Experimental Methods

2.1 Experimental Overview for CHFS

In the CHFS process, a supercritical water feed was mixed with an appropriate aqueous metal salt solution at ambient temperature in an engineered mixer. As a result, the corresponding metal oxides were rapidly formed in the process (the chemistry may have included hydrolysis, degradation and dehydration reactions). The as-prepared nanoparticles were collected downstream after in-flow cooling in the process.

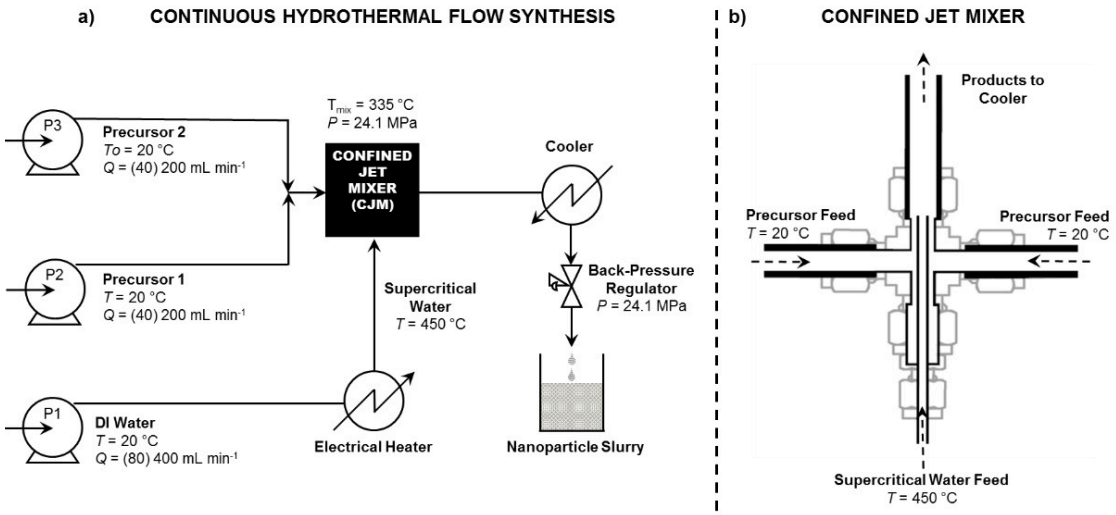

Figure 32: CHFS reactor incorporating a confined jet mixer (CJM). (a) Single-mixer modus: The metal salt (pump P2) and base (pump P3) precursor are mixed together at room temperature and then combined in a supercritical water flow (pump P1) in the CJM. After cooling, the nano-particle slurry is constantly harvested from the exit of the back-pressure regulator. (b) Scheme of the CJM.

The general CHFS reactor is presented in Figure 32 [191, 199-202]. In addition to a single-mixer modus, the synthesis can be performed using a quench of cold water (second CJM placed after the first one), which decreases the reaction time from about 5 sec to less than 1 sec.

Briefly, the laboratory scale process is similar to the pilot plant CHFS process [199, 203] but on ca. 1/5 of the scale. The patented CJM was designed to eliminate blockages under these conditions and facilitate highly turbulent mixing (Reynolds number typically is >5000) [191, 198, 200]. The CJM is essentially an efficient co-current mixing device made from off-the-shelf Swagelok™ fittings that efficiently allows the ambient temperature metal salt solutions to mix with the supercritical water feed to form nanoparticles "in flow" and without blockages. In the lab-scale CHFS process, three identical diaphragm pumps (Primeroyal K, Milton Roy, Pont-Saint-Pierre, France) were used to supply three pressurized (24.1 MPa) feeds. Pump 1 supplied a feed of DI water at a flow rate of 80 mL min^{-1}, which was then heated to 450 °C in flow using a 7 kW electrical water heater. Pump 2 supplied the metal salt precursors at a flow rate of 40 mL min^{-1} and pump 3 supplied DI water or base at a flow rate of 40 mL min^{-1}. The feeds from pumps 2 and 3 were combined at room temperature in a dead volume tee-piece. This precursor mixture was then brought into contact with the flow of supercritical water (co-currently) in the CJM, resulting in a reaction temperature of ca. 335 °C (residence time ca. 5 s).

At the end of the CHFS process, the particle-laden flow was cooled to ca. 40 °C using a pipe-in-pipe counter-current heat exchanger (cooler), before passing through a back-pressure regulator (BPR) and being collected. The resulting nanoparticle-laden slurry was cleaned by allowing the solids to settle by gravity, before dialyzing with DI water (<10 MΩ)

2.1.1 Freeze drying

Freeze-drying is a simple method to remove H_2O from a material without affecting its chemical and physical properties. It is often used for food packaging and agriculture-based industries (e.g. for manure). The material is frozen and the pressure is drastically reduced. This allows the

frozen water to sublimate directly from the solid to the gas phase, rather than melting (see phase diagram for water, Figure 24).

The particles were freeze-dried (Virtis Genesis 35XL) by freezing samples at −60 °C, followed by slow heating under vacuum of <100 mTorr over a period of 24 h. The dried powders were used directly for preparation as electrode inks with no further heat-treatment processing.

2.2 Physical Characterization

2.2.1 Powder X-Ray diffraction (PXRD)

Powder X-ray diffraction is an important and powerful technique to determine or identify the crystal phase of a material. PXRD is non-destructive and it can be used for identification of the crystalline compound, to determine the lattice parameters, type and nature of atoms, to quantify the number of phases (for example the number of layers for graphene) and to calculate the average crystallite size.

The method uses the interaction between the electromagnetic radiation and the electron cloud in the material. If the material is crystalline or partly crystalline, the diffraction pattern is discontinuous, because the interference is ordered. The dependence of the diffraction angle of the X-Ray radiation was first identified by W. L. Bragg in 1913. Bragg showed that the interference of the X-Ray radiation can be considered as the reflection on the lattice planes of the crystal. If the wavelength λ is constant and the inter-planar lattice spacing d is given, reflection only occurs at defined angles (Equation 18), which creates the peaks of the X-ray plot:

$$2d \sin\theta = n\lambda \tag{18}$$

2.2.2 X-ray photoelectron spectroscopy (XPS)

X-ray photoelectron spectroscopy is a quantitative spectroscopic technique that measures the chemical composition at the surface of a material and is based on the photoelectronic effect. It can be used to determine the elemental composition, empirical formula, chemical state and electronic state of the elements, which exist within the surface of a material. It can also do mapping and depth profiling.

An X-ray beam penetrates into the material with a depth of ca. 1 µm and in this entire volume, electrons get excited and emitted. The kinetic energies of the electrons ejected from their orbitals are measured and the patterns of binding energies are a fingerprint of the orbital, element and oxidation state. Useful electron signals are obtained only from a depth of around 10 to 100 Å at the surface. The XPS instrument measures the kinetic energy of all collected electrons. The electron signal includes contributions from both photoelectron and Auger electron lines [204, 205].

2.2.3 Raman spectroscopy

Raman spectroscopy is a contactless analytical materials characterization method which is able to identify and differentiate chemical species. It depends on scattering of light by crystal or molecular lattices. A general Raman spectrometer consists of a monochromatic light source, a sample area with collection optics, a light dispersing unit and a detector.

Interaction between light and material can be described as a collision between a vibrating molecule or lattice and an incident photon from the light source. This collision can be elastic (energy of the photon and energy of the scattered wavelength are the same), which is called Rayleigh-scattering. The collision can also be inelastic, which is called Raman-effect. The energy difference between the inelastic scattered photons and the incident photons is exactly the difference between two energy levels of a molecular vibration (Figure 33). This shift of frequencies is characteristic for each material [206].

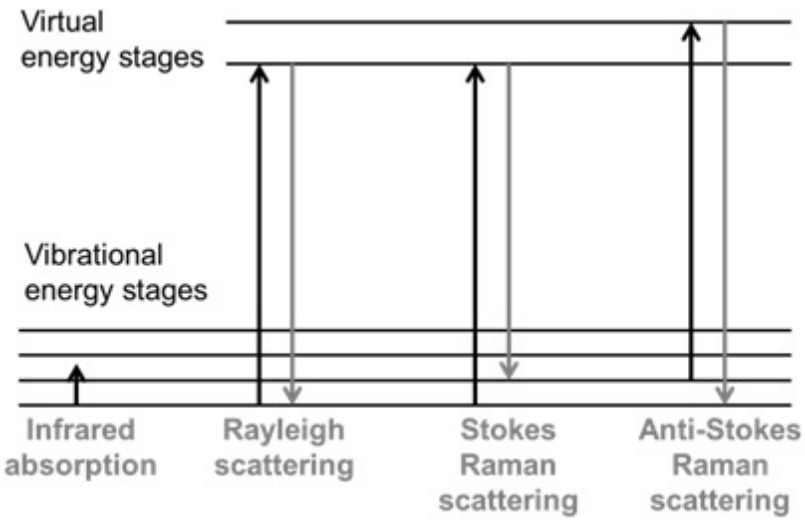

Figure 33: Energy-level diagram showing the states involved in Raman signal.

2.2.4 Scanning electron microscopy (SEM)

Scanning electron microscopy is used to describe the topography and morphology of a surface, which can also be used to determine a particle size. Primary electrons of a focused beam interact with the atoms of the surface of the investigated sample. Secondary electrons (10-50 eV) are generated from this collision between the incoming, primary electrons and the loosely bonded outer electrons of the sample (first nano-meters of the sample).

The topography contrast is given through the yield and angle of detected secondary electrons (Figure 34). More secondary electrons can leave the sample at edges leading to increased brightness at that location [207].

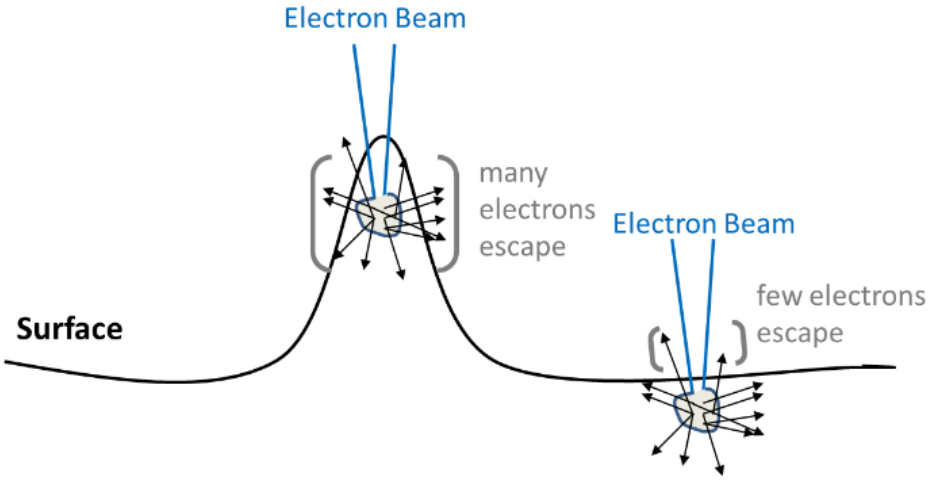

Figure 34: Yield of the secondary electrons dependent on the surface topography.

2.2.5 Transmission electron microscopy (TEM)

TEM is a specific electron microscope, which can give a direct image of an object with the help of an electron beam (with a scale of less than 1 nm). In 1986, Max Knoll and Ernst Ruska won the noble price in physics for the development of this specific microscope in the 1930s. The light source of the microscope in a TEM is replaced by a beam of very fast moving electrons. The investigated sample has to be specially prepared (low concentration on a conductive holder) and held inside a vacuum chamber for improved electron diffusion. Electrons are emitted from the electron gun and illuminate the specimen through a two or three stage condenser lens system. Objective lenses provide the formation of either image or diffraction pattern of the specimen. The electron intensity distribution behind the specimen is magnified with a three or four stage lens system and viewed on a fluorescent screen. The image can be recorded by direct exposure of a photographic emulsion or an image plate or digitally by a CCD camera [208].

2.2.6 Energy Dispersive X-ray Spectroscopy (EDX)

EDX is a simple method to determine the elemental distribution in a sample and is often combined with a TEM or SEM machine. An applied electron beam interacts with the sample, whose emitted X-Rays are specific per element, Figure 35. Such instruments can be also used for elemental mapping of particles, surfaces and other to distinguish the elemental environment for core-shell particles, doped samples etc.

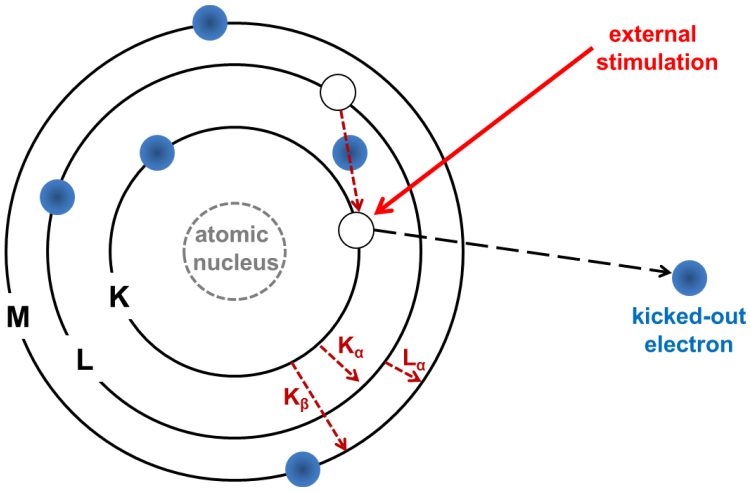

Figure 35: Scheme of an atom for explanation of the principle of EDX.

2.2.7 X-ray fluorescence (XRF)

XRF is a non-destructive analytical technique and is also used to determine the elemental composition of a material. The basic principle behind XRF is when a sample is irradiated by an X-ray beam; an electron is ejected from its lower energy atomic orbit. Similar to EDS (Figure 35), an electron from a higher orbit (energy level) drops to the lower orbit to fill this space and emits a secondary X-ray. The energy of this fluorescent X-ray is characteristic of a particular element, providing the means to qualitatively establish the elemental composition and quantitatively measure the concentration of these elements.

2.2.8 Surface area determination after Brunauer, Emmet and Teller (BET)

BET is a common method to determine the surface area or to investigate the pore size distribution and pore volume of a sample via gas adsorption. Several assumptions, such as multilayer adsorption and energetically homogeneous surfaces, simplify the calculation of the surface area. An adsorption isotherm is determined via measuring the amount of adsorbed gas (N_2) for a wide range of applied pressures at a constant temperature of −196 °C (liquid N_2). The converse desorption isotherm is determined via the measurement of removed gas during reduction of the pressure. Before any measurement, the sample needs to be outgassed [209].

The linear BET equation can be expressed like in Equation 19:

$$\frac{p}{n^a(p^0-p)} = \frac{1}{n_m^a C} + \frac{(C-1)p}{n_m^a C p^0} \tag{19}$$

n^a is the amount of adsorbed gas at the relative pressure p/p_0 and n_m^a is the monolayer capacity (volume of adsorbed gas of a monolayer). C is a constant, related exponentially to the enthalpy of adsorption in the first adsorbed layer and needs to be calculated by measuring the amount of adsorbed gas (nitrogen at 77.3 K) at different pressure ranges ($0.05 < p/p_0 < 0.35$). This measurement gives the slope and y-intercept of Equation 19; meaning, C and n_m^a can be calculated. One nitrogen molecule can be adsorbed (s = 0.162 nm^2 at 77.3 K) per surface unit of the sample and the specific BET surface area SA can be calculated according to Equation 20, where m is the mass in gram of the sample:

$$SA = \frac{n_m^a s N_A}{m} \tag{20}$$

2.2.9 Thermogravimetric analysis (TGA)

TGA is a simple analytical method, which investigates the mass difference of a sample according to applied temperature and time. The investigated sample is placed in an inert holder (e.g. Al_2O_3), that is attached to a weighing machine. The temperature is increased at a constant rate under a defined gas atmosphere and the weight difference is detected. TGA is used to analyse the chemical composition of a sample (e.g. H_2O content) or the chemical reactions (e.g. decomposition) related to applied temperature.

2.3 Electrochemical characterization

2.3.1 Electrode fabrication and testing

A general lithium-ion electrode does not only consist of the active lithium-ion host material. Redox-inactive conductive additives (like carbon black) and a fluorinated [like polytetrafluoroethylen (Teflon) or plyvinylidenfluoride (PVDF)] or non-fluorinated [like styrene-butadiene-rubber (SBR) or carboxymethylcellulose (CMC)] binder polymer are used in addition to the active material. As costs are important parameters, copper and aluminium are used as current collectors. Metallic copper oxidizes above 3.6 V vs. Li/Li^+ and metallic aluminium forms an alloy with lithium-ions below 0.6 V vs. Li/Li^+; consequently, copper is used for low operating potential negative electrode materials and aluminium for high operating potential positive electrodes. Proper processing and mixing of the electrode materials is necessary for an excellent performance in an electrochemical energy storage device. For initial testing, the potential electrode material is processed with conductive additives and a polymeric binder and tested in a coin cell versus lithium metal (Figure 36).

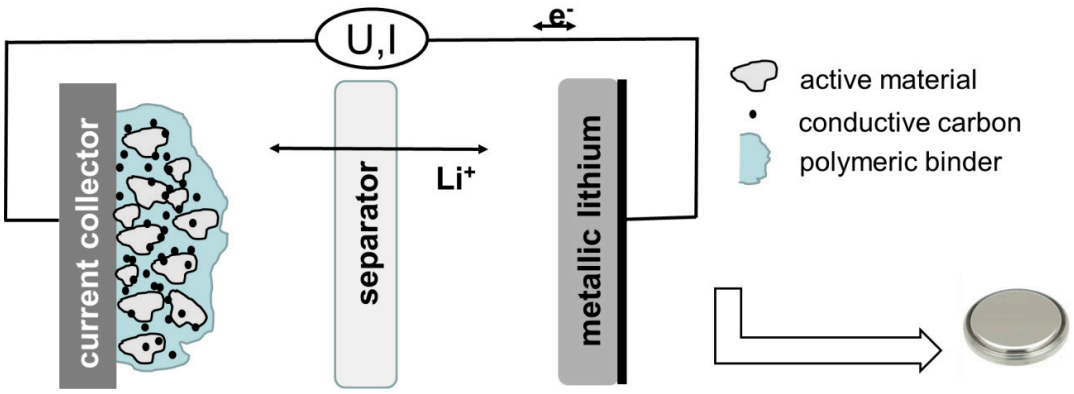

Figure 36: Schematic presentation of the electrochemical testing of an active material in a half cell versus lithium metal.

The as-prepared, freeze-dried samples were directly used to make electrodes, without any post-synthesis heat-treatment. Unless stated otherwise, the slurry for the printed electrode, was prepared with 70 wt% active material, 20 wt% added conductive agent (carbon black, Super P, Alfa Aesar, Heysham, UK) and 10 wt% polyvinylidene fluoride binder (PVDF, PI-KEM, Staffordshire, UK). PVDF was dissolved in NMP (N-methyl-2-pyrrolidone, Sigma Aldrich, St. Louis, USA) for at least 1 hour at room temperature, before adding the active material and conductive agent. The mixtures were milled for 1 hour. A key parameter is highly viscous slurry (honey-like). This enables that only little NMP evaporates, so that the electrode network is very strong with minimal holes and cracks caused by over-drying. The slurry was cast on a copper foil (PI-KEM, Staffordshire, UK) and then dried in an oven at 70 °C (until the electrode was visible "dry"), before being left overnight at room temperature. Electrodes with a diameter of 16 mm were punched out, pressed with 3 tons of force and finally dried overnight at 70 °C. Electrochemical experiments were performed using a two-electrode CR2032-type coin cell, which was assembled in an argon-filled glovebox, with O_2 and H_2O limited below 10 ppm. The counter and reference electrode was lithium metal foil. The separator was a glass microfiber filter (Whatman, Buckinghamshire, UK). A scheme of all components in a coin cell is presented in Figure 37.

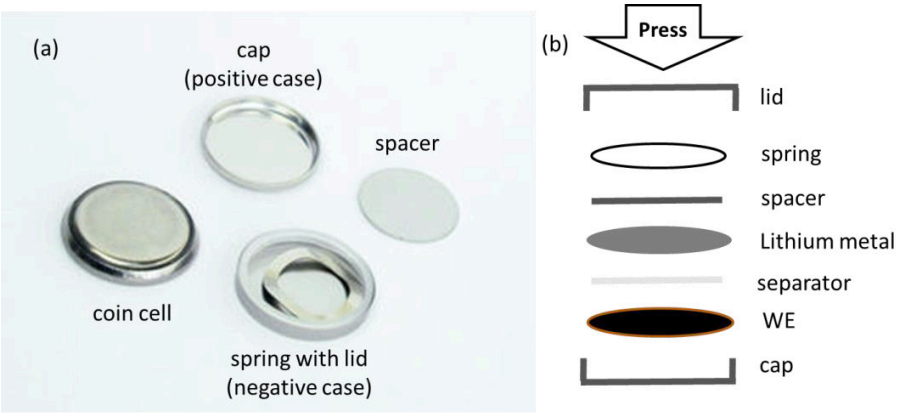

Figure 37: (a) Scheme of the coin cell components and (b) general approach of assembling a half cell.

2.3.2 Cyclic Voltammetry (CV)

Cyclic voltammetry (CV) investigation is a potentiodynamic electrochemical method. The voltage of the working electrode is changed linearly versus time between two potential values and the resulted current is detected (Figure 38). This method helps to determine the potential range where the working electrode is active or, in other words, in which potential range redox, Faradaic or capacitive charge/discharge takes place. Moreover, the crystallinity of a material can be investigated with the width of the recorded peak. Highly crystalline materials show very sharp peaks, while amorphous materials tend to show very broad signals [210].

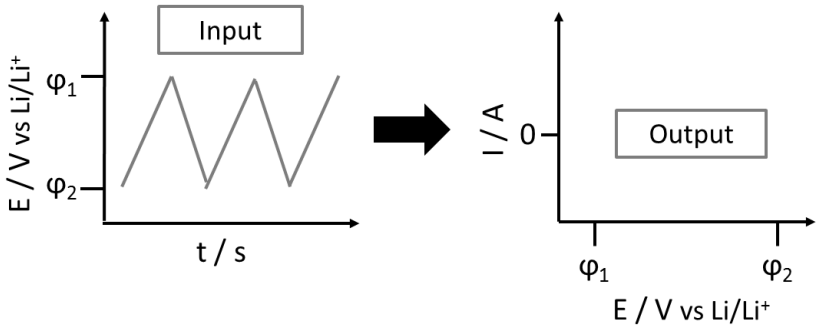

Figure 38: Scheme of the cyclic voltammetry method. A constant scan rate in mV s^{-1} is applied, where the rate switches between two potentials φ_1 and φ_2 (left) and the resulted current I in A is detected (right).

The discharge capacity $Q_{discharge}$ can be calculated with the integral of the current I and the time t (Equation 21).

$$Q_{discharge}[mAh\ g^{-1}] = \int_{t=0}^{t=x} I(t)dt \qquad (21)$$

2.3.3 Galvanostatic measurements

Charge/discharge experiments are used to investigate the cycling stability of the material. Cycling stabilities are very different for electrochemical storage systems (for instance: 1 million cycles for EDLCs and 3,000 cycles for LiBs). Such experiments belong to galvanostatic techniques if a constant current is applied for the working electrode between two cut-off values. For half-cell testing two potentials and for full-cells two voltages are usually chosen. An important factor for an electrode is the Coulombic efficiency η during cycling. This value describes how much capacity is lost during discharge compared to the charge. This value should be as high as possible (>99.9 %) and can be estimated with the following Equation 22:

$$\eta\ [\%] = \frac{Q_{delithiation}[\mathrm{mAh\ g^{-1}}]}{Q_{lithiation}\ [\mathrm{mAh\ g^{-1}}]} \cdot 100 \qquad (22)$$

For half-cell tests, the applied current can be controlled with the reference electrode and the counter electrode is simply the lithium source (Figure 39). For full cell tests, the measurement is more difficult. For this setup the cell must be balanced, which includes a perfect mass ratio between the two electrodes to reach the highest possible cell voltage and to utilize both electrodes in an optimal and safe way.

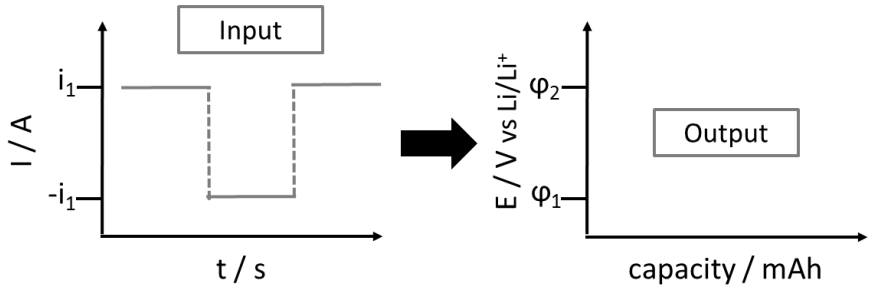

Figure 39: Scheme of the galvanostatic charge/discharge cycling method. A constant current **I** in A is applied, where the setting switches if a certain potential, φ_1 or φ_2, is reached (left) and the resulting capacity in mAh is measured for each charge/discharge step (right).

2.3.4 Electrochemical Impedance Spectroscopy (EIS)

Electrochemical impedance spectroscopy (EIS) is a non-destructive electrochemical method to obtain information about the electronic conductivity of a material. The term “impedance” refers to the frequency dependant resistance towards a current flow of a circuit element (resistor, capacitor, inductor). Therefore, impedance is measured by applying an alternating current potential and measuring the current flow.

Ohm’s law defines the resistance as the ratio between the voltage $U(t)$ and the current $I(t)$ (Equation 23).

$$R = \frac{U(t)}{I(t)} \tag{23}$$

This represents an ideal resistor because the relationship is only limited to one circuit element. An ideal resistor follows Ohm’s law at all current and voltage levels, it is independent of frequency and the alternating current and voltage signals are in phase with each other. This simple concept must be changed to exhibit the more complex behaviours of a real resistor. Like the resistance, impedance represents the ability of an element to resist the current flow, but it is not limited by the above listed properties. The dependency of the frequency f can be expressed for the voltage $U(t)$ and the current $I(t)$ (Equation 24/25). The excitation signal (alternating current potential) $U(t)$ is the potential at the time t, U_0 is the amplitude of the signal and ω the radial frequency ($\omega = 2\pi f$). The responding current $I(t)$ is shifted in phase ϕ.

$$U(t) = U_0 \sin(\omega t) \tag{24}$$

$$I(t) = I_0 \sin(\omega t + \phi) \tag{25}$$

Using Equation 24 and Equation 25, the original Ohm's law can express the impedance Z (Equation 26). The magnitude Z_0 and phase shift ϕ together characterize the impedance.

$$Z = \frac{U(t)}{I(t)} = \frac{U_0 \sin(\omega t)}{I_0 \sin(\omega t + \phi)} = Z_0 \frac{\sin(\omega t)}{\sin(\omega t + \phi)} \tag{26}$$

Euler's relationship (Equation 27) can be used to express the impedance as a complex function $Z(\omega)$ (Equation 28). For this mathematical step, Equation 24/25 are transformed to the complex exponential function, $U(t) = U_0 \exp(i\omega t)$ [211].

$$\exp(i\phi) = \cos(\phi) + i\sin(\phi) \tag{27}$$

$$Z(\omega) = \frac{U(t)}{I(t)} = Z_0 \exp(i\phi) = Z_0(\cos(\phi) + i\sin(\phi)) \tag{28}$$

Equation 28 shows a real and an imaginary part. In the Nyquist plot, the real part is the x-axis and the imaginary part is the y-axis. The values of the y-axis are the negative inverse of the imaginary values. A general Nyquist plot is presented in Figure 40.

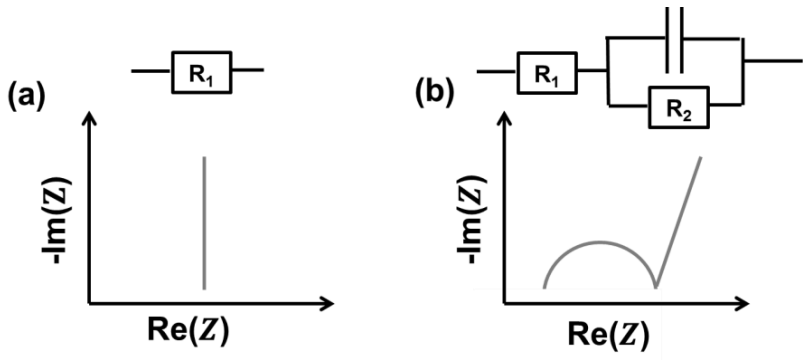

Figure 40: (a) Nyquist plot for an ideal electrochemical device including only a resistor (an ideal supercapacitor should show a Nyquist plot like this) and (b) a lithium-ion half-cell configuration including a capacitor and resistor. R_1 corresponds to the general resistance of the device, electrolyte, current collector etc. whereas R_2 refers to the electrode bulk.

The impedance can be seen as the series (Figure 40a) and parallel (Figure 40b) combination of a capacitor and a resistor. An ideal electrochemical device would show no resistance of the electrodes and the impedance would only be referred to the electrolyte (e.g. an EDLC, scheme in Figure 40a). Unfortunately, beside the electrolyte also other components influence the overall impedance like the inner particle resistance of the electrode active material, the contact between the current collector and the active materials, ion diffusion into the active material, the double layer formation at the surface of the active material or the particle-particle contact. The presented models are very simplified. It is also possible to have more than one semicircle in series or parallel in the plot.

In this work, EIS measurements were performed to compare the different electrode material resistances. It should be noted that the use of coin cells can be problematic. Slight differences of the contact between the separator and electrode can result in a large difference of the measured impedance. Moreover, each coin cell holder is not similar. Therefore, EIS results should be seen more in a qualitative than quantitative way.

2.3.5 Characterization of the charge storage mechanism

As mentioned in the introduction, oxide supercapacitors and batteries can store electric energy but with different charge storage mechanism. Oxide supercapacitor materials store the charge via surface effects and battery materials store the charge via redox reactions within the bulk. As there is a shift towards nano-sized electrode battery materials, there is naturally a shift towards high surface area electrode materials, resulting in increased charge storage via surface effects [24]. The contributions of charge storage arising from insertion or pseudocapacitance need to be quantified at different current ranges. A high power battery electrode material might be classified

as a highly pseudocapacitive insertion material. The charge storage mechanism can be investigated via potentiodynamic and galvanostatic methods.

A scan rate test (potentiodynamic methods) can be carried out to distinguish the charge stored via diffusion-controlled lithium-ion insertion from surface effects. In general, the current in a scan rate experiment can be expressed by a power law (Equation 29), where i is the current (A), a and b are arbitrary coefficients and ν is the potential scan rate (V s^{-1}).

$$i = a\nu^b \tag{29}$$

The coefficient b can be expected to vary in the range 0.5 to 1.0, with a value of 0.5 being characteristic of a diffusion-limited process (charge storage via lithium-ion insertion) and a value of 1.0 for a capacitive process (charge storage via surface capacitive effects). Therefore, to further quantify the different charge storage mechanisms, charge storage via lithium-ion insertion and surface capacitive effects can be calculated using a method that has been described previously in the literature [23, 24, 116, 129, 212]. At a fixed potential, the current response can be seen as a combination of the two aforementioned charge storage mechanisms. The surface capacitive effect (fast kinetics) can be expressed by $k_1\nu$ (b = 1.0), whereas the diffusion-controlled (lithium-ion insertion) contribution can be expressed by $k_2\nu^{\frac{1}{2}}$ (b = 0.5), (Equation 30).

$$i_E = k_1\nu + k_2\nu^{\frac{1}{2}} \tag{30}$$

$$i_E/\nu^{\frac{1}{2}} = k_1\nu^{\frac{1}{2}} + k_2 \tag{31}$$

At a certain potential, the current value was measured for each scan rate. A plot of $i_E/\nu^{\frac{1}{2}}$ versus $\nu^{\frac{1}{2}}$, allows the calculation of k_2 from the y-intercept, and k_1 from the slope of Equation 31. Low scan rates (range of 0.05 to 1 mV s^{-1}) might be chosen as the peak shifts more

at higher applied scan rates [24]. The calculated k_2 value can be used to quantify the amount of charge stored via surface capacitance at each potential. This quantification should be taken with precaution since they give just some indication. More precise measurement methods are needed in the future to explore the real charge storage split.

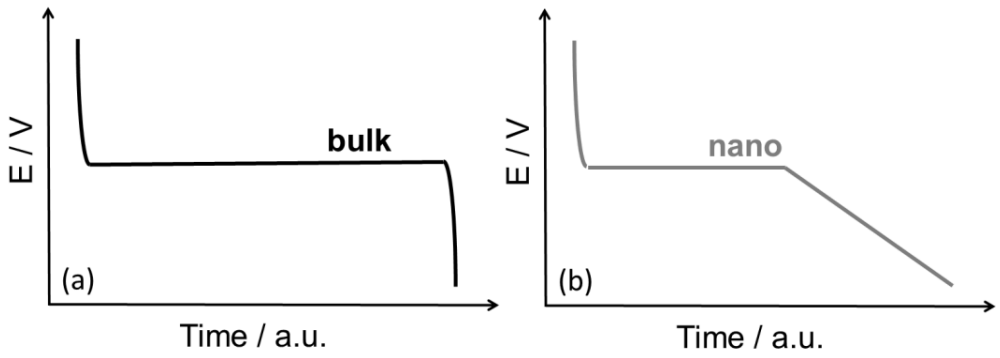

Figure 41: Simplified scheme of charge storage properties of an ideal battery material. (a) Bulk insertion materials show often a constant lithiation / delithiation plateau. (b) Nano-sizing results towards less defined potentials since more active lithium-ion sites with differing binding energies are present.

In Figure 41, a general scheme is presented for other indications of charge storage arising from surface effects which can be easily identified via galvanostatic charge/discharge profiles. Bulk battery materials show very distinct operating potentials whereas with nanosizing, the active sites (or alternative lithium-ion site number) drastically increases which shifts the charge storage behaviour towards oxide supercapacitor-like electrochemical performances. This was seen by many groups for both positive and negative electrodes [23, 60, 213, 214].

3. High Power Negative Electrode Materials for LiBs – Expanding the operational potential window

3.1 Aims

Within this chapter, various insertion-type transition metal oxides were investigated towards their power performance for LiBs and potentially LiCs. The main investigations were set on the electrochemical performance at low potentials vs. Li/Li^+.

3.2 Introduction

Simultaneously achieving high power and high energy is one of the main goals for LiBs. Therefore, pseudocapacitive insertion materials are promising candidates for high power LiBs as they combine the characteristics of alkali-ion battery materials and oxide supercapacitor materials.

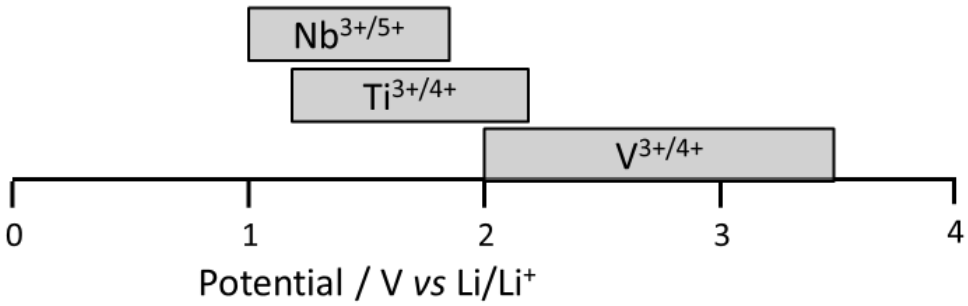

Figure 42: Scheme of the traditional cycling region for $Nb^{3+/5+}$, $Ti^{3+/4+}$ and $V^{3+/4+}$ (each vs. Li/Li^+) due to the known lithium-ion redox activity.

During the past decade, research has mainly focused on the potential range used in conventional LiBs, where the lithium-ion redox reactions should take place, Figure 42. In this chapter, we

additionally investigated whether there was any additional charge storage at lower potential ranges for various metal oxides. Moreover, the influence of the used carbon additive was investigated in a separate section. A major research question was: What happens, if we cycle nano-sized insertion transition metal oxides negative electrodes down to 0.05 V vs. Li/Li^+? Is there any difference in the obtained specific capacity or rate performance?

Nb_2O_5, layered titanate and VO_2 were each synthesized separately using a CHFS process and characterized via a range of analytical techniques including powder X-ray diffraction, X-ray photoelectron spectroscopy, transmission electron microscopy and Brunauer-Emmett-Teller surface area measurements. When testing in a lithium-ion half-cell versus lithium metal, each material was cycled in a wider potential window than that usually applied in the literature (Figure 42). In order to understand the role of the increased operational potential window on the overall electrochemical performance, scan rate tests (chapter 2.3.5) were applied for each material for classification of the electrochemical charge storage properties towards battery-like and oxide supercapacitor-like behaviour (chapter 1.5.4).

3.3 Experimental

3.3.1 Synthesis of the Materials

All nano-particles were synthesized using a laboratory scale CHFS reactor (chapter 2.1).

Nb_2O_5: Pump 2 supplied 0.1 M ammonium niobate (V) oxalate hydrate (Sigma-Aldrich, >99.99 %, Steinheim, Germany) at a flow rate of 40 mL min^{-1} and pump 3 supplied DI water at a flow rate of 40 mL min^{-1}. The feeds from pumps 2 and 3 were combined at room temperature in a dead volume tee-piece. This precursor mixture was then brought into contact with the flow of supercritical water (80 mL min^{-1} heated to 450 °C, reaction temperature of 335 °C, residence time ca. 5 s).

Layered titanate: 0.3 M Titanium(IV) bis(ammonium lactato)dihydroxide solution (TiBALD, 50 wt% in H_2O, Sigma Aldrich, Steinheim, Germany) and 12 M NaOH (Fisher Scientific, Loughborough, UK) were used as precursors. 0.3 M TiBALD was supplied at a flow rate of 40 mL min^{-1} by pump 2. A second feed of 12 M NaOH (precursor 2) was supplied at a flow rate of 40 mL min^{-1} by pump 3. These two precursor feeds were premixed at room temperature in a dead volume tee piece and then brought into contact with a flow of supercritical water (80 mL min^{-1} heated to 450 °C, reaction temperature of 335 °C, residence time ca. 5 s).

VO_2: Ammonium metavanadate (0.1 M, >99 %, Sigma Aldrich, Steinheim, Germany) was mixed with oxalic acid dehydrate (0.2 M, >99 %, Sigma Aldrich, Steinheim, Germany) until the colour changed to blue and used as precursor (V^{5+} to V^{4+}). Four identical diaphragm pumps were used. Pump 1 supplied a flow of supercritical water at a flow rate = 80 mL min^{-1} (heated to 390 °C, reaction temperature of 295 °C). The precursor solution was supplied at a flow rate of 40 mL min^{-1} (pump 2) and premixed at room temperature in a dead volume tee-piece with a second feed of DI water (40 mL min^{-1}, pump 3). These two feeds were brought into contact with

the flow of supercritical water. In order to rapidly cool the newly formed particles, a quench feed of room temperature DI water (pump 4, flow rate = 160 mL min^{-1}) was mixed into the nascent nano-particle product flow at the point just before a pipe-in-pipe cooler (residence time ca. 0.7 s).

3.3.2 Experimental Characterization

PXRD patterns of all samples were obtained on a STOE diffractometer using Mo-Kα radiation (λ = 0.70926 Å) over the 2θ range 2 to 40° with a step size of 0.5° and step time of 20 s (Nb_2O_5) and 30 s (layered titanate, VO_2). XPS measurements were collected using a Thermo Scientific K-alpha spectrometer using Al-Kα radiation and a 128-channel position sensitive detector. The XPS data were processed using CasaXPS™ software (version 2.3.16), the binding energy scales were calibrated using the adventitious C 1s peak at 285.0 eV and the fitting was applied using an appropriate relative sensitivity factor. The size and morphology of the crystallites were determined by TEM using a Jeol JEM 2100 – LaB_6 filament. The system was equipped with a Gatan Orius digital camera for digital image capturing. Samples were prepared by briefly ultrasonically dispersing the powder in ethanol (>99.5 %, EMPLURA, Darmstadt, Germany) and pipetting drops of the dispersed sample on to a 300 mesh copper film grid (Agar Scientific, Stansted, UK). EDX analysis was carried out using an Oxford Instruments X-Ma N80-T Silicon Drift Detector fitted to the TEM and processed using AZtec™ software (error can be up to 1 %). BET surface area measurements were carried out using N_2 in a micrometrics ASAP 2020 Automatic High Resolution Micropore Physisorption Analyzer (Nb_2O_5) or an ASAP 2420 (layered titanate, VO_2). The error for BET was <0.1 m^2 g^{-1}. The samples were degassed at 150 °C (12 h) under vacuum before measurements. Field emission scanning electron microscopy (FE-SEM) images were obtained with a JEOL JSM-6700F microscope operating at 5 kV

accelerating voltage (sample diluted in methanol and then dropped on a pure silicon plate). TGA was performed using a Pyris 1 TGA instrument (Perkin Elmer) under nitrogen with a flow rate of 20 mL min^{-1} in the temperature range 25 to 700 °C with a heating rate of 10 °C min^{-1}. The weighing precision was <0.01 %. Raman spectra were collected with a Renishaw inViaTM Raman microscope (laser λ = 514 nm). The sample was diluted in ethanol and then dropped on a silicon plate.

3.3.3 Electrochemical Testing

Nb_2O_5, layered titanate, VO_2: The electrode mass ratio for Nb_2O_5 or VO_2 was 70:20:10 (active material: carbon additive: binder), whereas it was a 80:10:10 ratio for the layered titanate. The active material loading was in the range 1.0 to 1.5 mg cm^{-2}. Galvanostatic charge/discharge cycling were conducted with 1 M $LiPF_6$ in 3:7 wt% ethylene carbonate/ethyl methylcarbonate (BASF, Ludwigshafen, Germany) as electrolyte using an Arbin Instrument Model BT-2000 battery tester (Caltest Instruments Ltd, Guildford, UK) at room temperature. The specific current rate test was performed using an applied current in the range 0.03 to 10 A g^{-1} in the potential range 0.05 to 3.0 V vs. Li/Li^+. CV measurements were conducted with 1 M $LiPF_6$ in EC/DMC/DEC (1:1:1, v/v) as electrolyte using a galvanostat/potentiostat (PGSTAT302, AUTOLAB, Metrohm, Utrecht, Netherlands).

Carbon Black: The slurry for the electrode was prepared with a content of 90 wt% carbon material (carbon black, Super P, Alfa Aesar, Heysham, UK) and 10 wt% polyvinylidene fluoride (Kynar, ARKEMA). The electrodes had an active material mass loading of 0.7 mg cm^{-2}. The used electrolyte was 1 M $LiPF_6$ in EC/DMC (1:1 v/v, Merck Selectipur LP40, Darmstadt, Germany). C-rate tests were performed using a MACCOR battery tester (Model 4200, Maccor

Inc., Oklahoma, USA) at room temperature. The specific current rates were used in the range 0.05 to 10 A g^{-1} in the potential range 0.05 to 3.0 V vs. Li/Li^+. The electrochemical performance was investigated by CV in the same potential range with a scan rate of 0.2 mV s^{-1} using a galvanostat/potentiostat (PGSTAT302, AUTOLAB, Metrohm, Utrecht, Netherlands).

3.4 Results and Discussion

3.4.1 Characterization Results – Nb_2O_5

Light yellow powder of Nb_2O_5 was obtained with a yield of 90 %. PXRD data revealed large, broad, ill-defined peaks (Figure 43). The data was compared to various Nb_2O_5 ICSD database patterns, and the monoclinic form with space group *C*12/*m*1(12) was found to be the closest reasonable match (similar to PDF 01-074-0312). Overall, there were no distinct phases detected and the PXRD data suggested that the samples were possibly semi-crystalline.

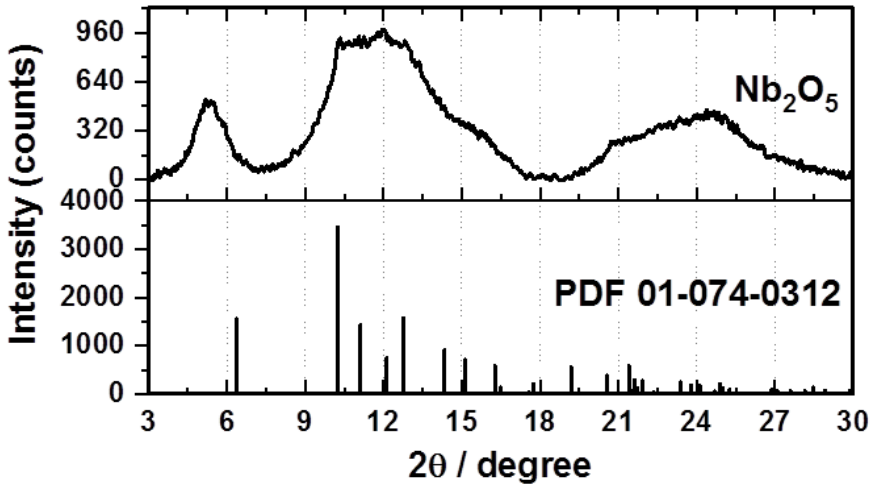

Figure 43: Characterizations of as-made Nb_2O_5: PXRD (Mo-source) patterns showing a semi-crystalline phase.

XPS was used to determine the valence state of the metal ion in the niobium oxide (Figure 44). The Nb 3d level binding energies were 210.6 eV for Nb $3d_{3/2}$ and 207.9 eV for Nb $3d_{5/2}$ with a spin orbit splitting of 2.7 eV, assigned to the core levels of Nb^{5+}. This suggested the niobium was mainly in the 5+ oxidation state.

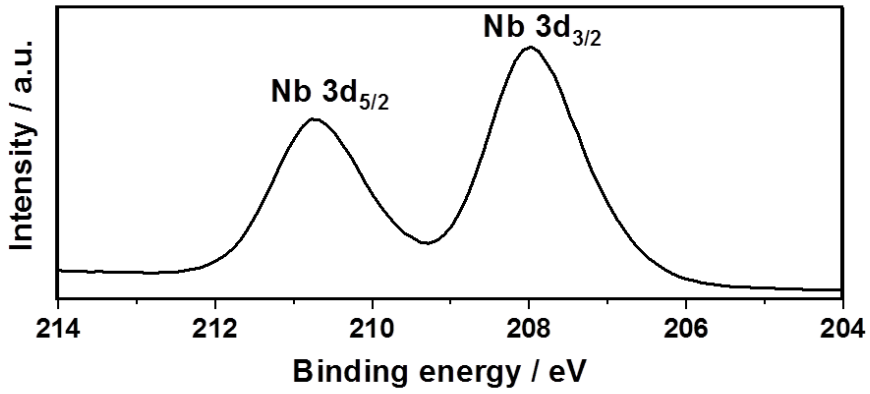

Figure 44: Characterizations of as-made Nb_2O_5: High-resolution XPS spectra showing the Nb 3d binding energies.

TEM images of the sample, revealed very small particles of ca. 7 nm in size that appeared to be semi-crystalline (see Figure 45a,b). There were only a few interlayers detectable for which the observed d-spacing was ca. 0.39±0.04 nm (Figure 45c). Therefore, HRTEM image confirmed also the poorly crystalline nature of the directly synthesized Nb_2O_5. The BET surface area was 158 m^2 g^{-1}.

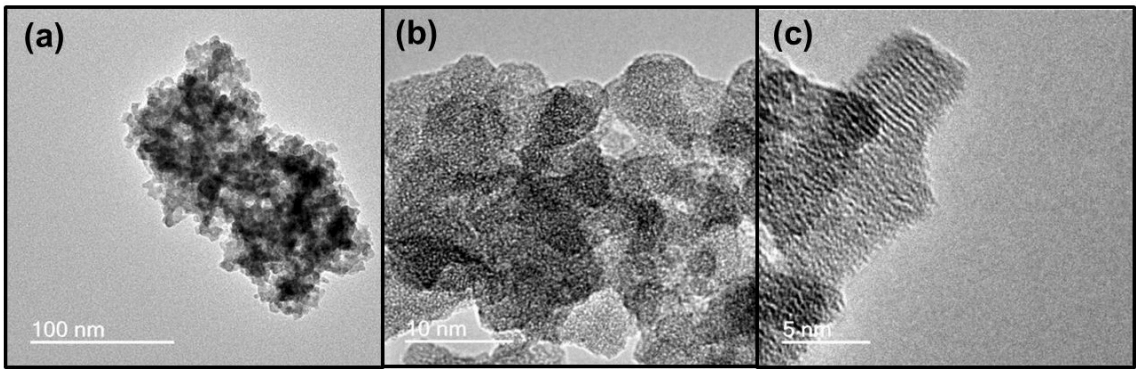

Figure 45: Characterizations of as-made Nb_2O_5: (a)-(b) TEM images showing agglomerates of nano-particles and (c) high resolution TEM showing little evidence of lattice spacing.

3.4.2 Characterization Results – Layered Titanate

The dried titanate sample was obtained as a slightly off-white powder. The materials synthesis was reproduced (except a slightly lower base concentration was used herein) and more characterizations can be found in reference [215]. In Figure 46, the obtained PXRD data for the as-made sample revealed a typical profile of a layered titanate (closest to reference [216], a monoclinic phase with a space group $P2_1/m$). The data revealed an intense peak centred at 4.1°, with other minor peaks at 2θ = 21.6° and 27.2° characteristic of anisotropic layered titanate 2D nano-materials [202, 217]. Several reports have described the crystal structure of these materials as zigzag-layered alkali-trititanates [$(Ti_3O_7)^{2-}$] [147, 148, 218-222], where the alkali metal/hydrogen ions form ionic bonds with TiO_6 octahedra and show very strong interlayer covalent bonding, which stabilizes the structure [219]. The structure can be described as being step layered, with each unit consisting of three edge-sharing octahedra $(Ti_3O_7)^{2-}$, linked by corners. The intense (001) peak in the PXRD pattern at 2θ = 4.1°, was expected due to the extensive sheet-like morphology of the nano-particles (see Figure 20).

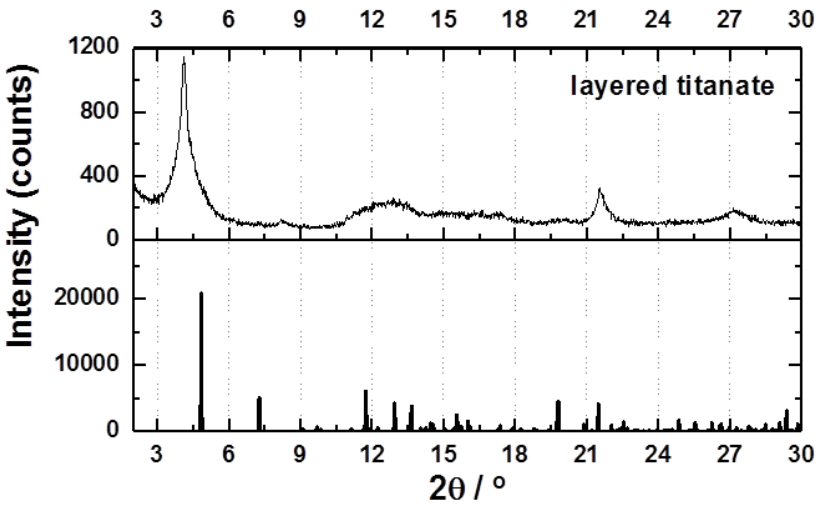

Figure 46: Characterizations of as-made layered titanate: PXRD (Mo-source, reference patterns taken from ref. [216]) data.

XPS was used to determine the valence state of the titanium in the material (Figure 47). The Ti 3d level binding energies were 458.3 eV for Ti $2p_{3/2}$ and 464.1 eV for Ti $2p_{1/2}$ with a spin orbit splitting of 5.8 eV, assigned to the core levels of Ti^{4+}. This suggested the titanium was mainly in the 4+ oxidation state.

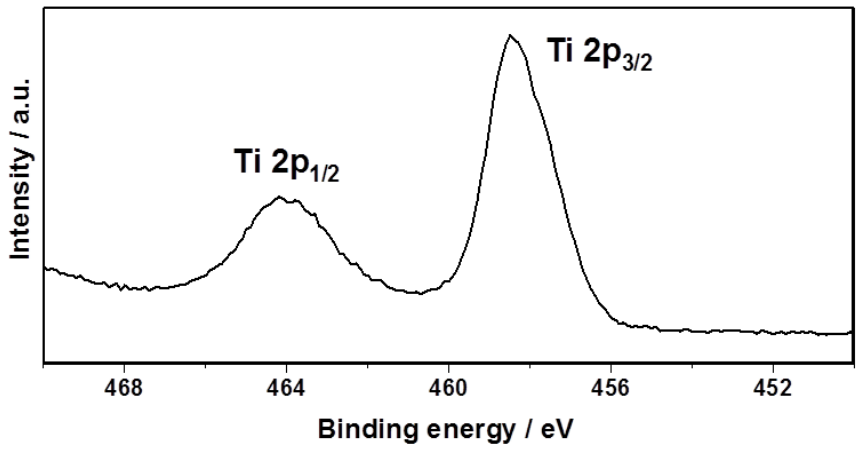

Figure 47: Characterizations of as-made layered titanate: High-resolution XPS spectra showing the Ti 2p binding energies.

Due to the limited resolution of PXRD patterns, Raman spectroscopy was used as a supplementary technique to further confirm the main phase. The Raman spectra of the layered titanate revealed broad bands at 277, 380, 441, 648, 705 and 901 cm^{-1} (Figure 48), which was similar to reported data from literature, but varied slightly because of the differences in particle morphology [147, 223]. The bands below 450 cm^{-1} and in the range 600 to 800 cm^{-1}, were attributed to Na–O bond vibrations and Ti–O stretching vibrations in edge-shared and corner-shared TiO_6 octahedra. Bands at higher frequencies (centred at wavenumbers in the range 800 to 950 cm^{-1}), were assigned to short Ti–O bonds of low coordination. Therefore, the high frequency Raman peaks in the spectrum (*e.g.* 901 cm^{-1}) corresponded to M-O stretches for oxygen atoms coordinated to one titanium atom (at a distance of *ca.* 1.7 Å).

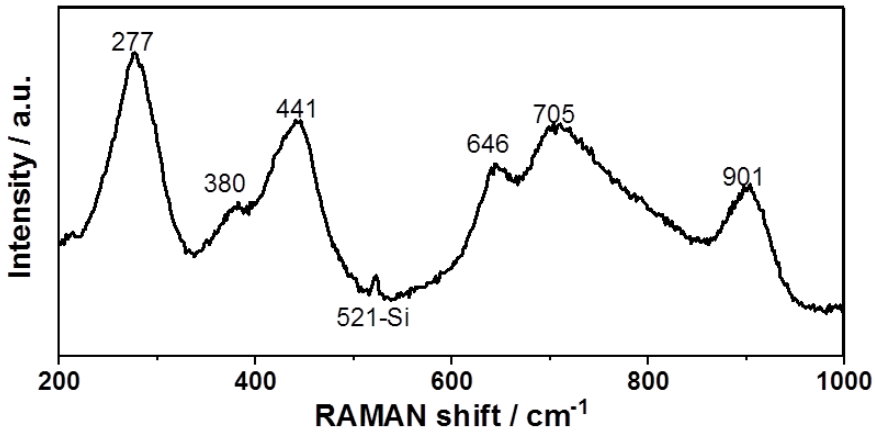

Figure 48: Characterizations of as-made layered titanate: Raman spectrum of the pristine layered titanate. The peak at 521 cm^{-1} is from the silicon plate (sample holder).

It has been reported in the literature that there can often be incomplete sodiation of layered titanates under hydrothermal synthesis conditions [217, 220]. To confirm the composition produced by the reaction, EDX measurements were used to determine the ratio of sodium to titanium atoms in the material (and by implication the amount of protons, which are required for charge balance). This suggested a nominal composition of $H_{1.1}Na_{0.9}Ti_3O_7$ in which both Na^+ and H^+ ions would reside between the anionic layers and provide overall charge balance [220, 221, 224].

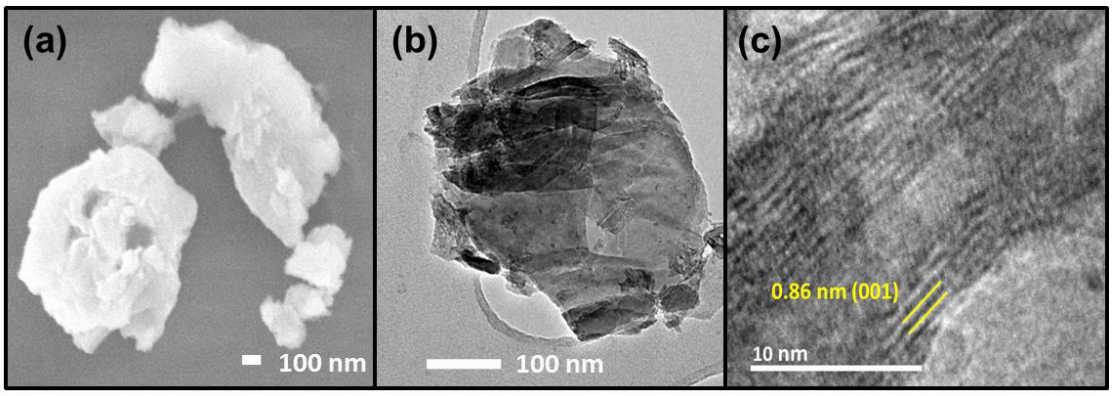

Figure 49: Characterizations of as-made layered titanate: (a) SEM, (b) TEM and (e) high-resolution TEM.

SEM and TEM images confirmed the formation of very thin plate-like nano-sheets of sodium titanate (Figure 49). This is also in agreement with the results of the PXRD measurements, where some crystal orientations in *c*-direction were observed. TEM images showed an interlayer spacing of ca. 0.86 (± 0.07) nm for the (001) planes. Thus, the (001) d-spacing calculated herein, was relatively high for a layered metal oxides. The presence of H_2O groups in the interlayer structure might be expected to widen the interlayer spacing compared to the dehydrated form [147, 221, 224]. The interlayer spacing calculated by TEM imaging, was still lower than the calculated d-spacing from the corresponding powder PXRD data using the Bragg equation and 2θ position for the (001) peak (value = 0.99 nm). This difference is not surprising, as it has been reported elsewhere that the measured d-spacing from TEM data can often be lower than that calculated from the corresponding powder PXRD data [225].

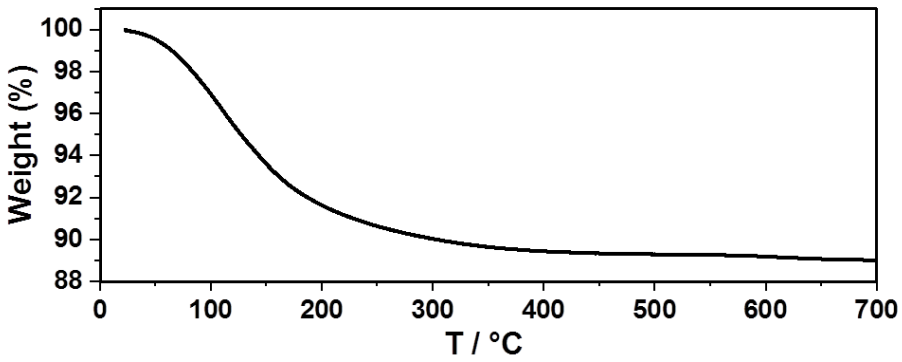

Figure 50: Characterizations of as-made layered titanate: TGA analysis.

Since the (001) d-spacing was quite high, TGA measurements were conducted to obtain the content of weakly associated hydroxyl groups in the crystal (Figure 50). TGA analysis revealed a mass loss of ca. 9 wt% in the temperature range from 25 to 200 °C, which was attributed to the both loss of weakly and strongly associated water. A further mass loss of only ca. 2 wt% (overall loss 11 wt%) was observed in the range 200 to 300 °C, which may be simply due to loss of water from condensation of residual OH groups. Therefore, the large d-spacing for the as-prepared

materials might have been a result of substantial water between the layers. The BET surface area was 79 m^2 g^{-1}.

3.4.3 Characterization Results – VO_2

VO_2 was obtained as dark blue powder. PXRD (Figure 51) of the sample identified a mixture of monoclinic VO_2(M) and metastable VO_2(B) [226, 227], which was published previously by Powell et al. [228]. The material synthesis was reproduced and more details or a comprehensive characterization of the VO_2 based materials used herein can be found in reference [229].

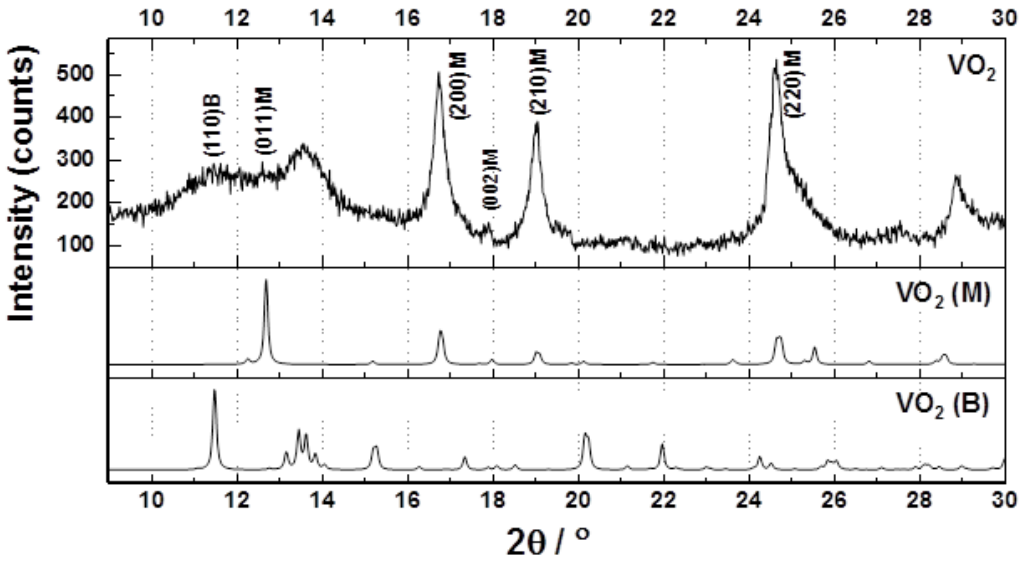

Figure 51: Characterizations of as-made VO_2: PXRD (Mo-source) pattern. The reference pattern were the ICSD 34033 for VO_2(M) and ICSD 73856 for VO_2(B).

The four strongest PXRD peaks corresponded to the (011), (200), (210) and (220) planes of VO_2(M), similar to reference patterns ICSD 34033 and the low-angle peak located at 2θ = 11.6 ° was assigned as the (110) plane of VO_2(B) similar to reference patterns ICSD 73856. There might be evidence for additional diffraction peaks in the region round 10 to 15 °. However, due

to broadening of the (110)B and (011)M diffraction peaks, it was impossible to assign specific diffraction planes and identify any further phases.

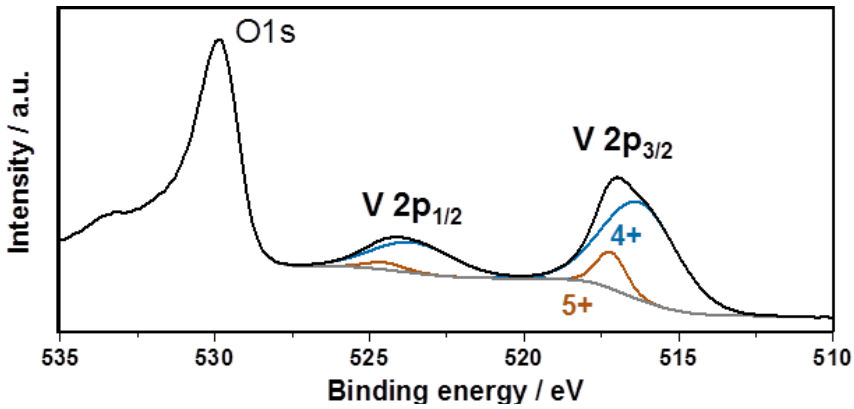

Figure 52: Characterizations of as-made VO_2: High-resolution XPS spectra showing the V2p binding energies.

The XPS data suggested the surface of the sample was composed of V^{4+} and some V^{5+} in an atomic ratio of ca. 84:16 (Figure 52). As there was no detectable impurity phase in the PXRD data, it was concluded that there was most likely some surface oxidation occurring, which is known in the literature, especially for high surface area VO_2 materials [230].

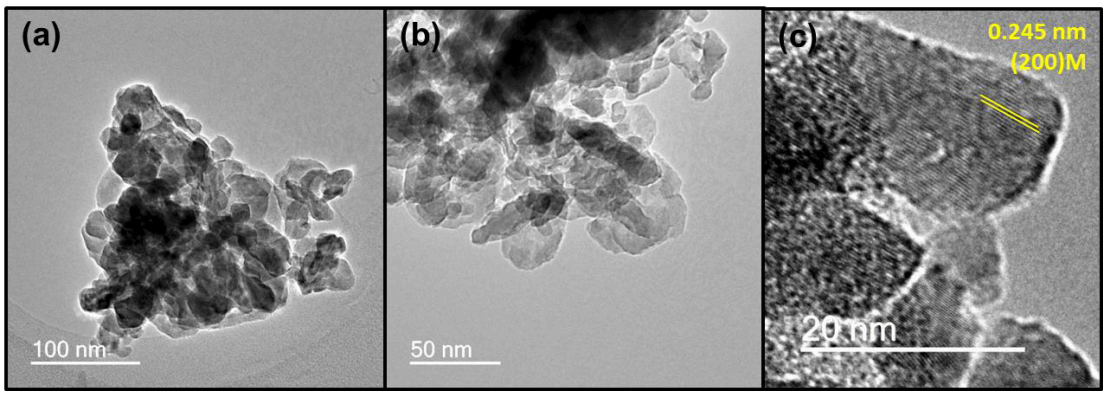

Figure 53: Characterizations of as-made VO_2: (a)-(b) TEM images showing agglomerates of nano-sheet particles and (c) high resolution TEM showing lattice spacing.

TEM images of the nano-material (Figure 53) revealed that the powders were comprised of ca. 40 nm (average) nano-sheets that were only a few atomic layers thick (with few thin rod-like structures). This should also explain some peak intensity and broadening variation in the PXRD data compared to the reference database. Some particles showed lattice fringes with 0.32±0.03 nm matching the (011) inter-planar spacing in VO_2(M) [231]. The BET surface area was 86 $m^2 g^{-1}$, which was quite high compared to other VO_2 materials reported in the literature ranging from 3 to 185 $m^2 g^{-1}$ [150, 226, 232-238].

3.4.4 Understanding the Charge Storage Properties (0.05 – 3.0 V vs. Li/Li^+)

All materials were cycled in a wider potential window than usual. In Figure 47, a scheme is presented to initially investigate the charge storage properties. The CV results and the galvanostatic potential versus capacity plot data were directly compared with battery-like and oxide supercapacitor-like behaviour for potentiodynamic measurements under equivalent conditions.

Interestingly, the electrochemical activity of the Nb_2O_5 active material was evaluated beyond the typical range for the redox couple of $Nb^{3+} \leftrightarrow Nb^{5+}$ (1.2 to 2.1 V vs. Li/Li^+) and the CV profile did not show clear insertion peaks at well-defined potentials vs. Li/Li^+, suggesting the charge storage process occurred via both lithium-ion insertion and surface effects, which was consistent with the observation of a poorly crystalline or amorphous negative electrode material [123-125].For the layered titanate, the measured specific current arising from lithium-ion storage was at lower potentials than typically reported for titanates containing an octahedral oxygen environment in the literature (this work: 0.05 to 3.0 V vs. Li/Li^+, majority of literature: 1.0 to 3.0 V vs. Li/Li^+) [65, 239, 240]. The $Ti^{3+/4+}$ redox couple should be active in the range 1.0 to 2.3 V vs. Li/Li^+ according to the majority of published results for anatase, rutile and brookite TiO_2 [65]. The CV profile and potential versus capacity plot did not show clear insertion peaks at well-defined potentials vs. Li/Li^+, suggesting the charge storage process occurred via both lithium-ion insertion and surface effects.

Similar observations were made for VO_2. The obtained electrochemical data showed some very broad peaks suggesting charge storage arose from lithium-ion insertion and surface effects. This material was also active in a wider potential window compared to published investigations of similar vanadium oxides (ca. 1.5 to 3.0 V vs. Li/Li^+) [150, 232, 234, 235, 241, 242].

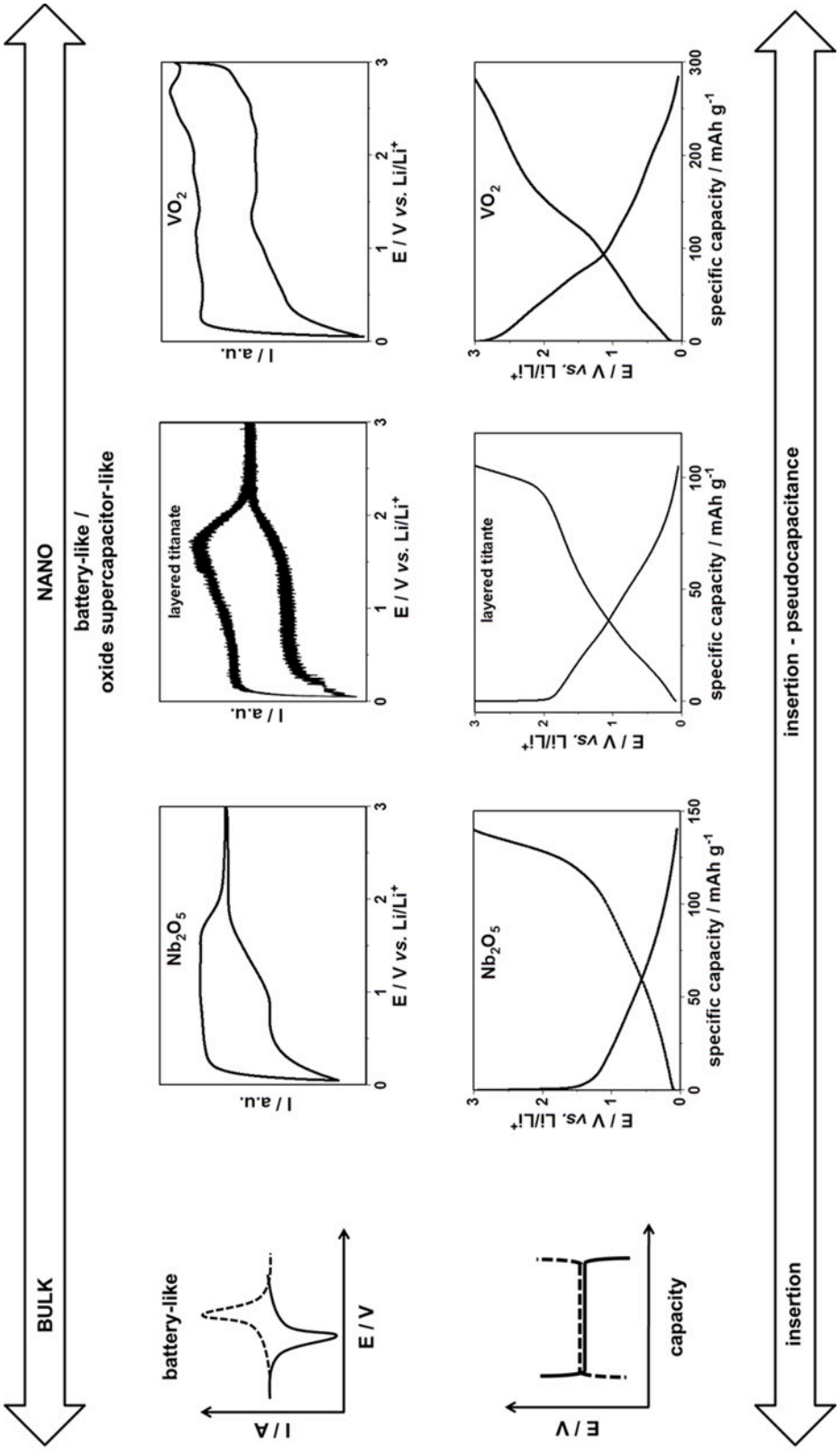

Figure 54: Initial investigation of the charge storage properties for Nb_2O_5, layered titanate and VO_2 in direct comparison to traditional charge storage properties of bulk battery materials and high surface area EDLCs. The CV scan rate was set to 0.1 mV s^{-1} for Nb_2O_5 and layered titante and 0.25 mV s^{-1} for VO_2 (first row). The galvanostatic charge discharge profile (second row) was obtained for the fifth cycle at 500 mA g^{-1}.

Further investigations using potentiodynamic methods via a scan rate test were explored in order to understand the nature of the charge storage (Figure 55a-c). A plot of $i_E/\nu^{\frac{1}{2}}$ versus $\nu^{\frac{1}{2}}$ was used to calculate k_2 from the y-intercept and k_1. The obtained k_1 value was then used to quantify the amount of charge stored via surface effects at each potential. The calculated current that resulted from surface effects was determined for each scan rate, which was then plotted against the overall measured current (see grey area in Figure 55d-f) and used to finally calculate the contribution of stored charge arising from surface effects. The charge storage arising from surface effects at 1 mV s^{-1} was already 42, 49 and 70 % for Nb_2O_5, layered titanate and VO_2, respectively. Thus, calculation of the area, as described in chapter 2.3.5, provided a qualitative indication of the relative contributions from charge stored via surface effects (pseudocapacitance and Helmholtz double-layer charge) and diffusion-limited processes (classical lithium-ion insertion).

Simultaneous charge storage via both diffusion-limited (insertion) and surface effects at the full width of electrochemical potential window of the electrode material has been observed previously for transition metal oxides such as amorphous MoO_3 (200 m^2 g^{-1}) [243], spinel Fe_3O_4 spinel [244] and V_2O_5-anchored carbon nano-tubes [213]. It can be concluded that one reason for the expanded electrochemical activity in a wide potential window might be a shift in the electrochemical performance towards oxide supercapacitor-like behaviour. This might be a side-effect of the high surface area and low crystallinity which each offer a wider variety of electrochemically non-equivalent lithium-ion storage sites (less potential dependent charge storage). Such vacant lattice sites can provide both cation and anion vacancies, whilst void spaces, cluster gaps or interstitial sites can also be present in this regard.

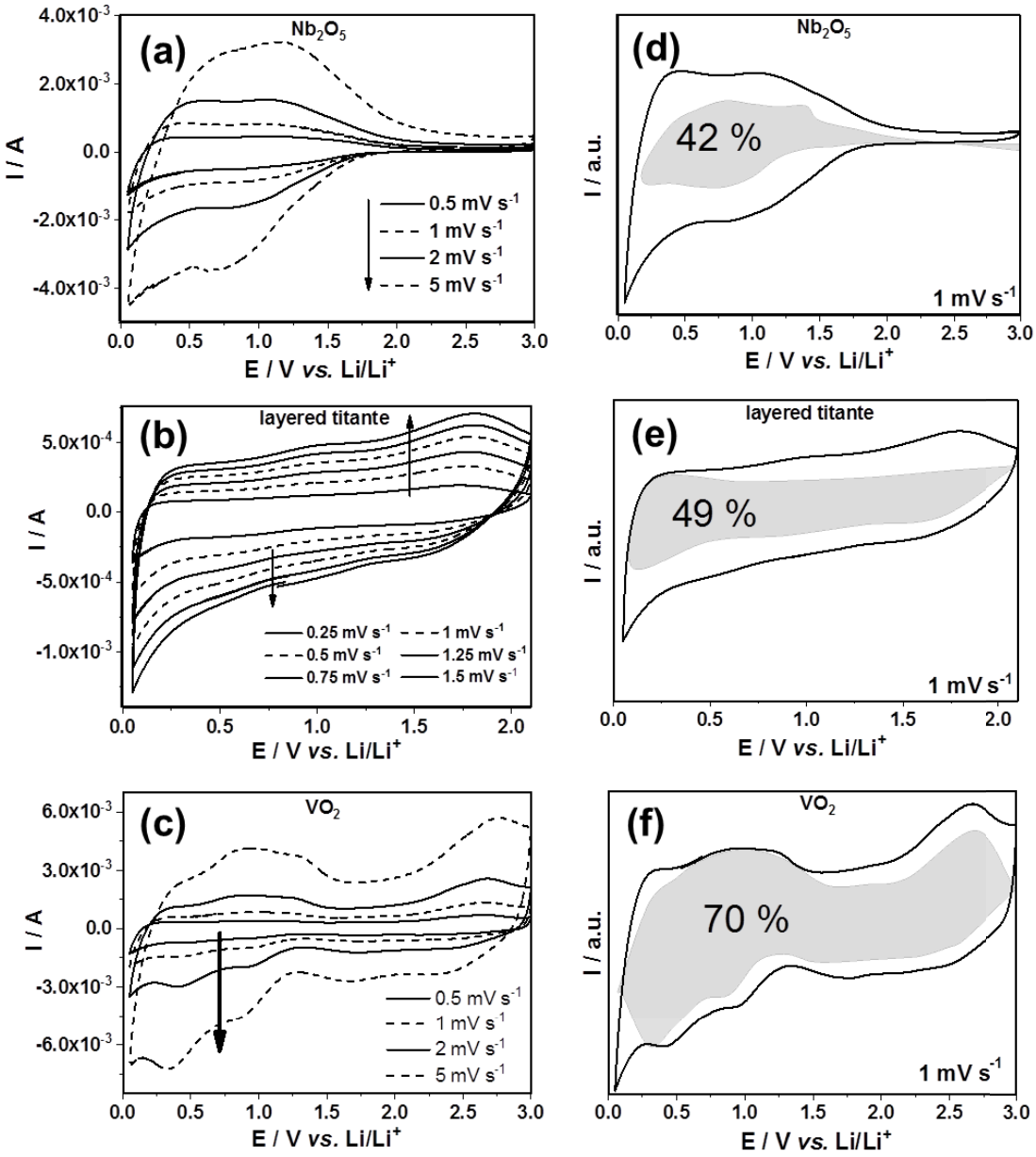

Figure 55: CV data for (a) Nb_2O_5 using scan rate test in the range 0.5 to 5 mV s^{-1} in the potential range 0.05 to 3 V vs. Li/Li^+, (b) layered titanate using scan rate test in the range 0.25 to 1.50 mV s^{-1} in the potential range 0.05 to 2.10 V vs. Li/Li^+ and (c) VO_2 using scan rate test in the range 0.5 to 5 mV s^{-1} in the potential range 0.05 to 3 V vs. Li/Li^+. (d), (e) and (f) corresponding analysis of the current arising from surface effects (grey area) at various potentials (vs. $Li/Li^{+)}$ at 1 mV s^{-1} for Nb_2O_5, layered titanate and VO_2, respectively.

Herein, it was found that each material became more dependent on the surface effects at higher rates (due to diffusion limitations), similar to that seen in nano-crystalline oxide supercapacitor materials [118, 129]. In Figure 56, the charge storage contributions for each material are plotted for two different scan rates. Cycling at 0.5 mV s^{-1} corresponds to a full charge/discharge cycle with 3.3 hours of testing for Nb_2O_5 and VO_2 and to a full cycle with 2.3 hours of testing for layered titanate. Increasing the scan rate to 1 mV s^{-1} halved the cycle times. This showed a direct correlation with the charge storage arising from surface effects. With increasing scan rate (less time for ion diffusion) the charge storage contributions from surface effects were observed to increase. This might be one key parameter for the excellent high power performances of each material.

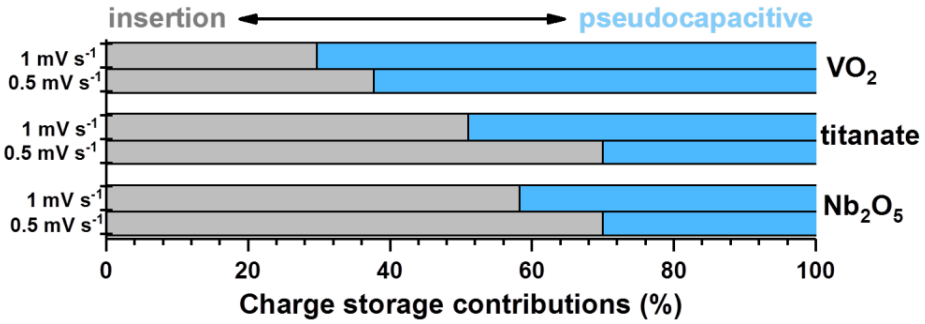

Figure 56: Plot showing relative charge storage contributions from diffusion-controlled processes (insertion, grey) and from surface effects (pseudocapacitance, blue) at scan rates of 0.5 and 1 mV s^{-1}.

Overall, the three materials showed high surface areas and quite poor crystallinity as seen by the PXRD and TEM images. By cycling down to 0.05 V vs. Li/Li^+, these materials are investigated in a potential area, where they would not be expected to be necessarily active. The obtained CV and capacity versus potential plots revealed significant charge storage for all three materials in unconventional potential regions. This was found to be in part due to pseudocapacitive charge storage, which is also believed to be the reason for the excellent high power performance in each

material. In the future, the role of the crystallinity and particle size should be investigated for each material, in order to understand the lithium-ion active sites and charge storage processes during cycling.

3.4.5 General Electrochemical Performance (0.05 – 3.0 V vs. Li/Li^+)

For initial testing, galvanostatic charge/discharge cycling at low currents helped to identify the maximum capacity of a material. In Figure 57, the cycling behaviour at low rates (50 and 30 mA g^{-1}) is presented for Nb_2O_5, layered titanate and VO_2, respectively. The obtained specific capacities were 150, 149 and 300 mAh g^{-1}, respectively. The irreversible capacity loss (Table 2) was very high for all three materials at these current rates (<55 %), which questions directly usage of such materials under these cycling conditions. The high irreversible capacity loss was due to reaction of electrolyte with the carbon additive in the electrode (SEI formation) [147, 245] and also due to the high surface area of the transition metal oxide. Such materials can cause lots of electrolyte destruction especially at lower potentials, where the organic electrolyte is known to be less stable. Moreover, there can be irreversible lithium-ion loss due to structural changes [246] and also due to irreversible reactions with water/hydroxyl-groups.

For an ideal electrode material, the Coulombic efficiency during cycling should be as high as possible. Otherwise, the system would continuously lose lithium-ions, causing an early cell failure. For all high surface area transition metal oxides, the Coulombic efficiency was very low under these cycling conditions (Figure 57, Table 2). Nb_2O_5, layered titante and VO_2 showed an average Coulombic efficiency of 77 %, 60 % and 91 % (for cycle 2 to 20), respectively. The low Coulombic efficiencies might be expected, as a stable SEI for high surface area transition metal oxides, is questionable and was observed before [188, 246, 247], see also [82, 83].

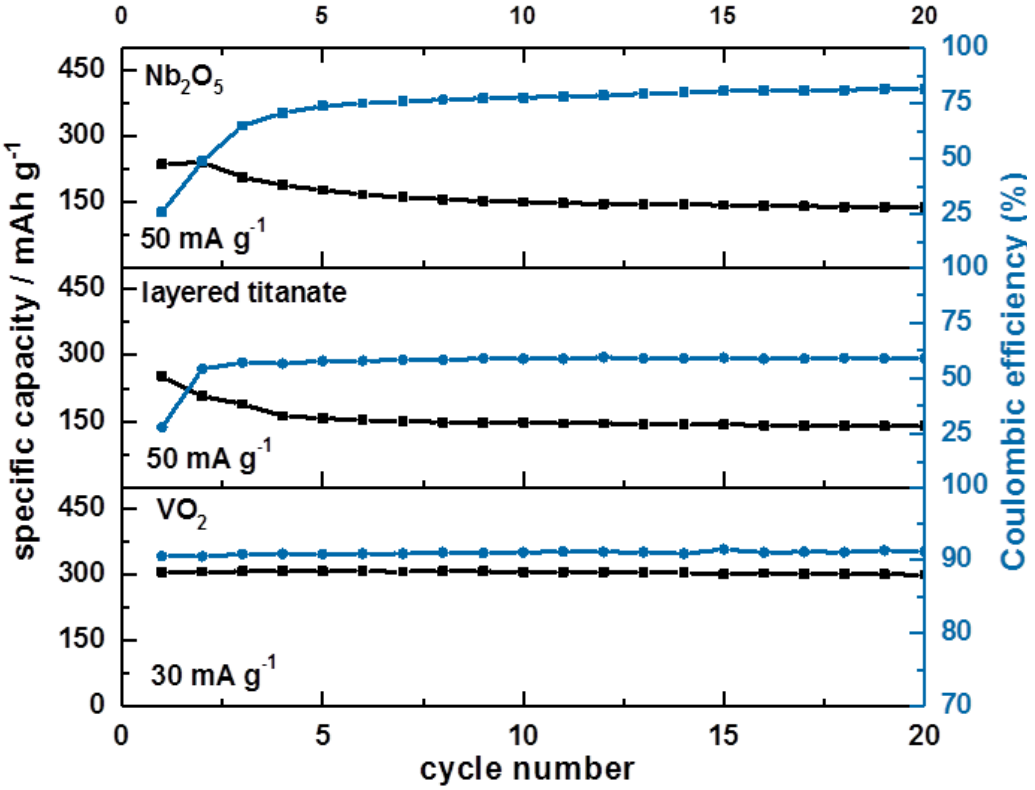

Figure 57: Galvanostatic charge/discharge cycling in the potential range 0.05 to 3 V vs. Li/Li^+ for Nb_2O_5, layered titanate and VO_2 at low current rates. Note: The VO_2 sample was first tested via CV.

In Figure 58, a potential versus capacity plot is presented to identify the origin of the low Coulombic efficiency. For Nb_2O_5 (Figure 58a) and also layered titanate (Figure 58b), the Coulombic efficiency at 500 mA g^{-1}, was close to 100 %, whereas at 50 mA g^{-1}, it was very poor. The origin could be found at low potential vs. Li/Li^+ during lithiation, which could be a direct indication for electrolyte destruction. The use of electrolyte additives might help improve this in the future [248, 249].

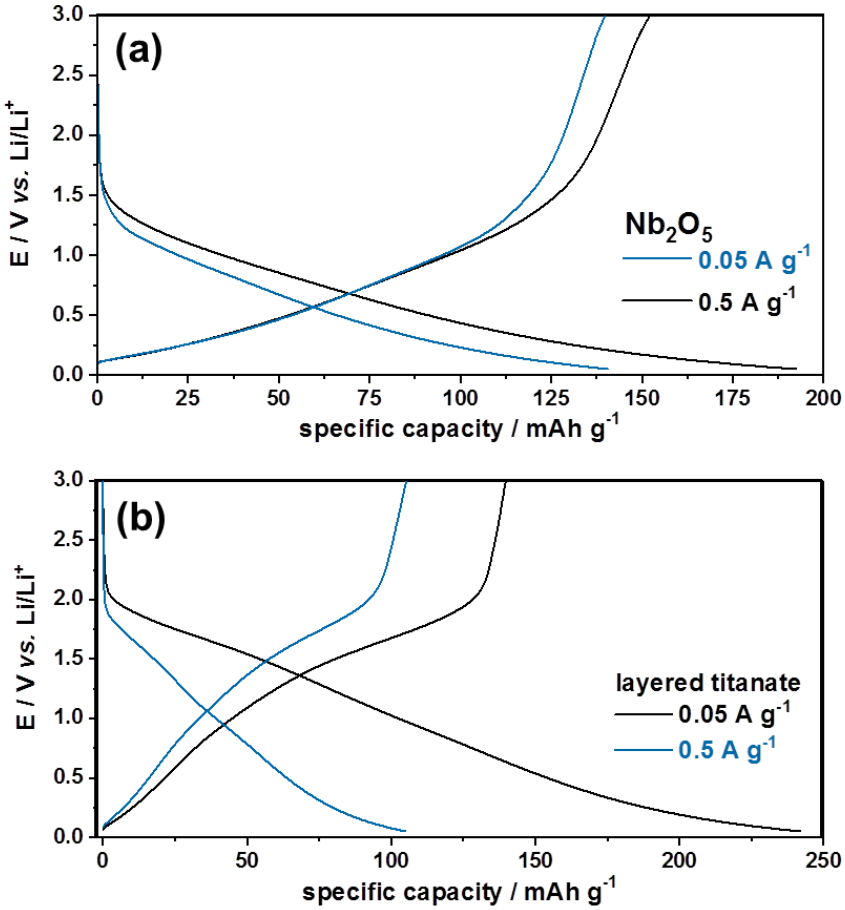

Figure 58: Galvanostatic charge/discharge cycling (5th cycle) in the range 0.05 to 3 V vs. Li/Li^+ at 50 mA g^{-1} and 500 mA g^{-1} for (a) Nb_2O_5 and (b) layered titanate.

Presumably, these materials acted like electrochemical catalysts and the high surface area led to continuous electrolyte destruction. Carbon coating or the use of surfactants might also assist in preventing these degradation processes, as the transition metal oxide surface might be shielded from direct electrolyte contact or a stable SEI might be enabled. Despite all these disadvantages, testing under high power conditions showed promising results (Figure 59). The main obtained specific capacities and cycling data can be found in Table 2.

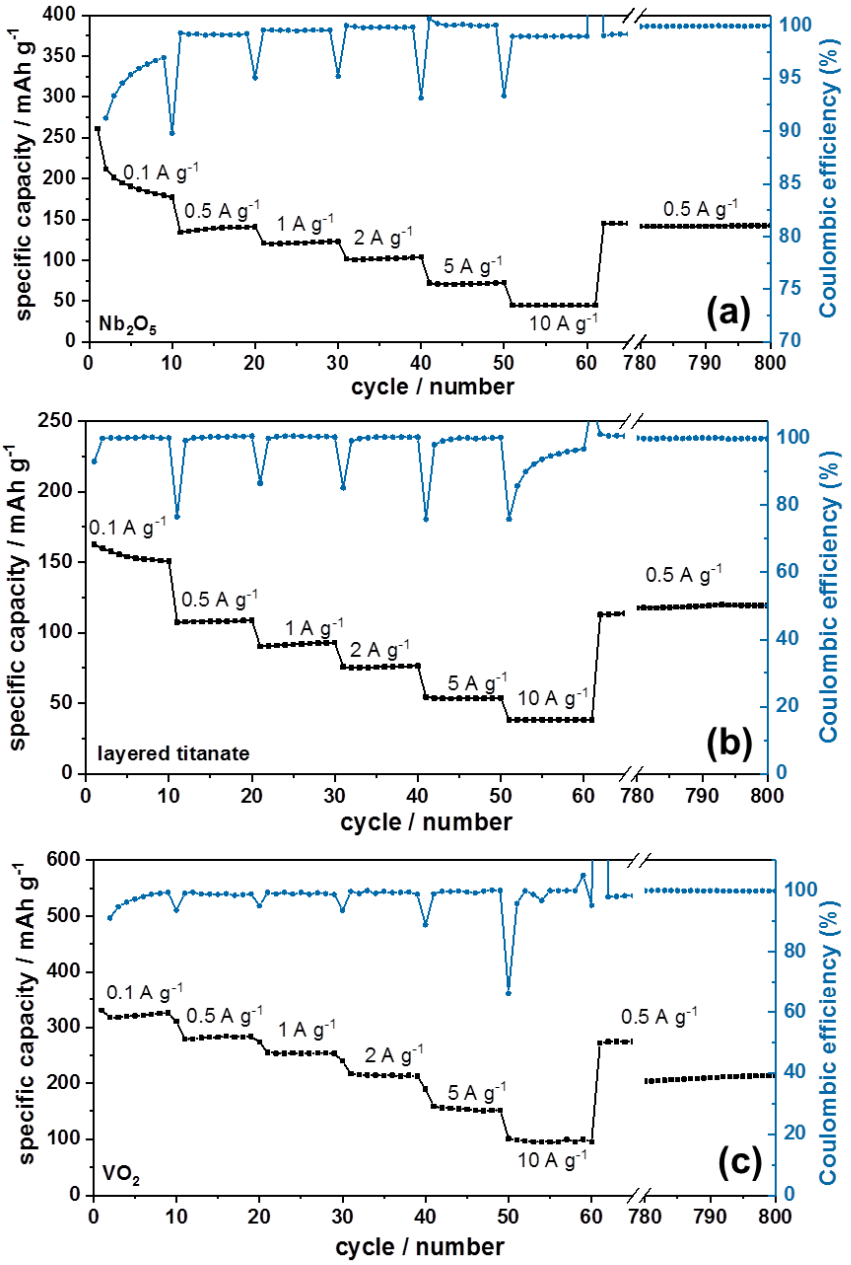

Figure 59: Current rate tests with applied currents in the range 0.1 to 10 A g^{-1} with followed long-term cycling for (a) Nb_2O_5, (b) layered titanate and (c) VO_2.

A C-rate test at various current rates was performed in the applied current range of 0.1 to 10 A g^{-1} (range from testing in several hours to <30 s per charge/discharge as a measured time).

At the lowest applied current of 0.1 A g^{-1}, the specific capacity remained at ca. 180, 155 and 322 mAh g^{-1} for Nb_2O_5, layered titanate and VO_2, respectively. For Nb_2O_5, this was equivalent to 1.8 moles of stored lithium-ions per 1 mole of Nb_2O_5 (theoretical capacity 200 mAh g^{-1}). For the layered titante, this was equivalent to 1.25 moles of stored lithium-ions per 1 mole of $H_{1.1}Na_{0.9}Ti_3O_7$ (theoretical capacity of ca. 192 mAh g^{-1} for storage of 2 moles of lithium-ions per 1 mole of $H_{1.1}Na_{0.9}Ti_3O_7$) and for VO_2, this was equivalent to 1 mol of stored lithium-ions per 1 mole of VO_2 (theoretical capacity 320 mAh g^{-1}).

Clearly, the Coulombic efficiency was far improved (>99.3 %) for all materials at a current rate of 500 mA g^{-1}. At the highest current, the obtained capacities were 43, 38 and 95 mAh g^{-1} (for Nb_2O_5, layered titanate and VO_2, respectively), which were promising values for less than 30 seconds of charge or discharge. This means that charge/discharge within seconds can still give up to 24 % of capacity compared to charge/discharge within several hours. These are high numbers and are most likely related to several reasons (see also following section for more details on the influence of the used carbon black additive). The high power performance can be partially explained in terms of the very high interlayer spacing for the titanate sheets. This increased spacing most likely enhanced ionic diffusion, which is known as one of the limiting factors for high power materials [45]. But overall, the high accessibility of the electrolyte towards the transition metal oxide surface should have enabled drastic increased lithium-ion conductivity, which is one key parameter for high power performances.

Importantly, the C-rate test was followed with a long-term cycling test at a current rate of 500 mA g^{-1} for all materials and showed that 96.5, 105 and 78 % of the initial capacity could be retained after more than 750 cycles for Nb_2O_5, layered titanate and VO_2, respectively. This makes Nb_2O_5 and layered titanate excellent candidate for high power hybrid devices, like hybrid capacitors with a negative battery-like electrode and a positive supercapacitor-like electrode.

This would enable maximum cell voltage and also increased power performance compared to conventional EDLCs.

The slight increasing capacity over time for the layered titanate might relate to some particle cracking (more active lithium-ion sites), which was seen also before for rutile TiO_2 in a different unpublished work. It can be also a result of co-active sodium- and lithium-ions.

Table 2: Summary of the electrochemical performance from the results of Figure 57 and Figure 59.

	Nb_2O_5	**Layered titantate**	**VO_2**
BET surface area	158 m^2 g^{-1}	79 m^2 g^{-1}	87 m^2 g^{-1}
Electrode wt% fraction	70:20:10	80:10:10	70:20:10
Irreversible capacity loss 0.1 A g^{-1}	28 %	23 %	57 %
Coul. eff. at low rate	77 %	60 %	91 %
Coul. eff. at 0.5 A g^{-1}	99.6 %	99.9 %	99.3 %
Spec. capacity at 0.1 A g^{-1}	180 mAh g^{-1}	155 mAh g^{-1}	322 mAh g^{-1}
Spec. capacity at 10 A g^{-1}	43 mAh g^{-1}	38 mAh g^{-1}	95 mAh g^{-1}
Spec. capacity at 0.5 A g^{-1} (cycle 65)	147 mAh g^{-1}	113 mAh g^{-1}	273 mAh g^{-1}
Spec. capacity at 0.5 A g^{-1} (cycle 800)	142 mAh g^{-1}	119 mAh g^{-1}	213 mAh g^{-1}
Capacity retention after 735 cycles	96.5 %	105 %	78 %

Recently, some groups investigated niobium oxides in an expanded potential window. Chen et al. investigated micro-sized, urchin-shaped Nb_2O_5 (0.05 to 3.0 V vs. Li/Li^+) and could see a reversible capacity of 390 mAh g^{-1} after 200 cycles [250]. Most stored charge of 75 % was measured between 1.0 to 3.0 V vs. Li/Li^+ at 50 mA g^{-1}, whereas the used material herein showed ca. 17 % charge storage in the same range at 50 and 500 mA g^{-1}. The difference might be due to higher crystallinity and lower surface area of the microsized, urchin-shaped Nb_2O_5 which both increase the diffusion-limited battery-like behaviour. Ma et al. investigated orthorhombic nano-

sheet Nb_2O_5 (0.01 to 3.0 V vs. Li/Li^+) and could measure a reversible capacity of 225 mAh g^{-1} after 100 cycles at 0.1 A g^{-1} and 105 mAh g^{-1} at the highest applied current of 1 A g^{-1} [251]. The material did not show typical lithiation/delithiation plateaus during cycling and showed also only 9 % charge storage (compared to the overall charge) between 1.0 to 3.0 V vs. Li/Li^+ at 0.1 mA g^{-1}. Unfortunately, no explanation for the expanded potential window was given in either work. Clearly, the particle characteristics (size, morphology) seem to play a crucial role for the electrochemical behaviour.

In a related report to the layered titanate investigations, the electrochemical properties of materials derived from $NaTi_3O_6(OH)\cdot 2H_2O$ with corrugated layered structure consisting of $(Ti_6O_{14})^{4-}$ units with hydrated sodium cations and protons in the interlayer spaces, have been investigated [147]. In that work, heating the material to 600 °C, removed water irreversibly from the $NaTi_3O_6(OH)\cdot 2H_2O$ material and the interlayer distances became smaller. It was reported that the dehydrated form could reversibly intercalate both lithium- and/or sodium-ions and the electrochemical potential profile showed a non-linear sloping dependence with degree of intercalation (when cycling down to 0.05 V vs. Li/Li^+ or vs. Na/Na^+), indicative of a solid-solution mechanism for intercalation. Thus, water removal seemed crucial for such systems and should be done for future applications of layered titanates in alkali-ion batteries. Clearly for layered titanates, the investigations towards high power performances needs further investigations, as the pseudocapacitive charge storage arises already at lower rates for such high surface area titanates.

Wu et al. investigated VO_2(M) with a reversible capacity of 200 mAh g^{-1} at 0.1 A g^{-1} (0 to 3.0 V vs. Li/Li^+) and could see similar potentiodynamic and galvanostatic profiles [252]. The main difference of this bulk material was in the potential range of 1.5 to 3.0 V vs. Li/Li^+, where the typical insertion/extraction peaks were clearly visible. This difference might be due to reduced

surface area, which can be expected to decrease oxide supercapacitor-like and increase battery-like behaviour. The reason for the far higher power performance compared to Nb_2O_5 and layered titanate might be simply due to the fact that VO_2 is an excellent electronic conductor, which is one main feature of high power materials.

Summing up, nano-sized insertion materials like Nb_2O_5, layered titanate and VO_2 can show limitations at low current rates due to continuous electrolyte destruction, but they can also show excellent high power properties with good cycle life. Since each material had carbon black as additive in their electrode network, the next step was to evaluate how the carbon might also contribute to the high power performance. This is investigated in the next section.

3.4.6 The Role of Carbon Black Additive on the Performance of the Overall Electrode

Carbons with high surface area are ideal charge storage materials for high power devices such as lithium-ion capacitors and EDLCs. Moreover, defective carbons (e.g. hard or soft carbons) can also store additional charge via insertion of lithium-ion and at very low potentials via lithium metal plating [36, 37, 253, 254].

Therefore, the specific capacity, which might arise from the carbon additive in the electrode, needed to be further investigated for each investigated electrode. In Figure 60a, the CV of carbon black used in all previous investigated electrodes, is presented at a scan rate of 0.2 mV s^{-1}. During the first cycle, there was an irreversible peak at 0.6 V vs. Li/Li^+, which could be attributed to the SEI formation. The second cycle already showed high reversibility, but clearly the carbon contributed to the additional irreversible capacity loss. There was low Coulombic efficiency at low applied currents, which might indicate lithium plating. This can also further

promote electrolyte destruction (Figure 60b). The obtained capacities were 112 mAh g^{-1} at 0.5 A g^{-1}, 70 mAh g^{-1} at 5 A g^{-1} and 52 mAh g^{-1} at 10 A g^{-1}.

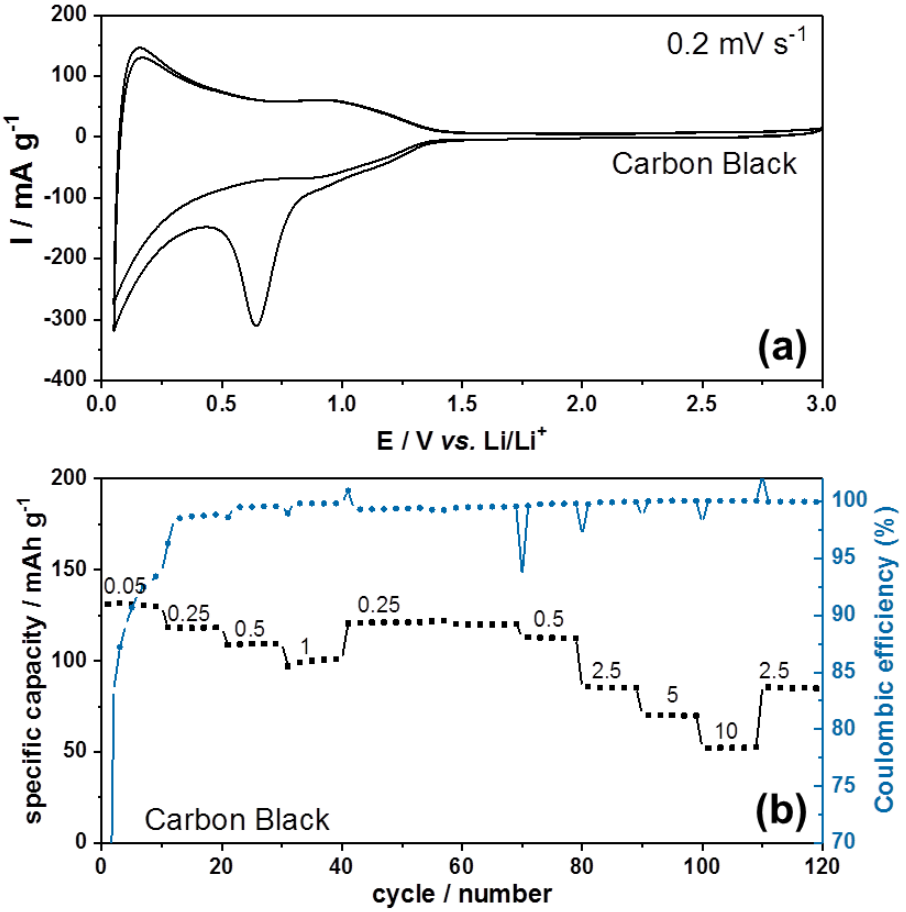

Figure 60: (a) CV at 0.2 mV s^{-1}. (b) C-rate test with corresponding applied currents per cycle in A g^{-1}.

These obtained electrochemical data can be used to calculate the impact of carbon black in each electrode material. The obtained capacities were recalculated with 90 wt% active material (20 or 10 wt% carbon black). In Figure 61 it is shown that, the carbon black impact was clearly quite low. For each the obtained capacities at 0.5 A g^{-1} (10 A g^{-1}), the potential carbon additive charge storage contribution was around 20 (31), 10 (17) and 10 (14) % for Nb_2O_5, layered titanate and VO_2, respectively. These values are still qualitative estimations due to the ex-situ calculation of

the capacity contributions. However, due to the excellent high power properties of the carbon, some of the high power performances of the transition metals might be due to the conductive additive within the electrode (see also the increase of possible contributions with higher rates).

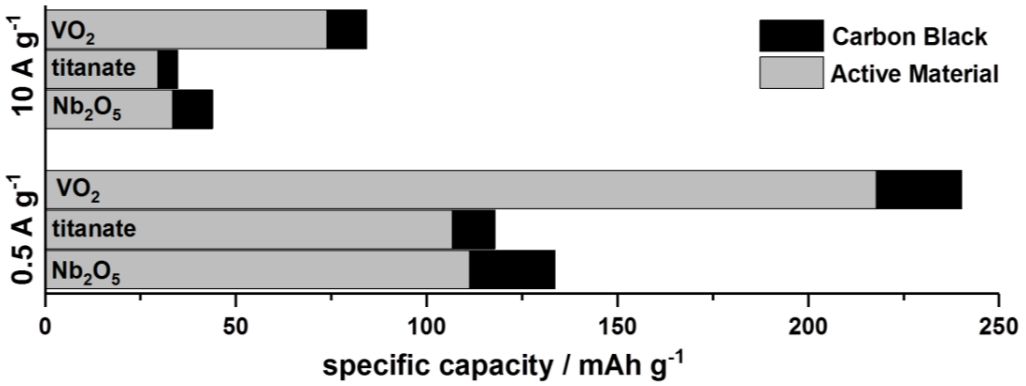

Figure 61: New calculation of the specific capacity and the corresponding specific capacities based on carbon additive and Nb_2O_5, layered titanate and VO_2 for various current rates.

To date, it is not known how the carbon additive and the active material interact. Does the lithium-ion insert into the transition metal first or form a double layer at the carbon surface additive or is there no favoured reaction? Further fundamental research is needed to understand the charge storage properties of such mixed electrode materials. The main finding of this section can be found in the possible increased charge storage contributions of the carbon additive at higher rates.

3.5 Overall Discussion and Outlook

The initial question was: What happens, if less crystalline nano-particles with high surface area insertion materials are cycled down to low potentials vs. Li/Li^+? For Nb_2O_5, layered titanate and VO_2, the crystallinity was quite low and the surface area was >79 $m^2\ g^{-1}$. For these three different classes of insertion materials, it could be shown that each had additional charge storage in potential regions, where it would not be expected to show any reversible electrochemical activity. One driving factor for this might be pseudocapacitive behaviour, which could be a result of nano-sizing and/or low apparent crystallinity (Figure 62). This included that the reversible lithium-ion storage occurred at different occupation sites resulting in different energy levels. The pseudocapacitive charge storage resulted also in excellent power performances for each material. When cycling only for 15 or 30 seconds, the charge storage was still ca. 42, 38 and 95 mAh g^{-1} for Nb_2O_5, layered titanate and VO_2, respectively. There might also have been some charge storage contributions from the carbon additives within the electrode network, but more research is needed to understand this.

For all these materials, it could be shown that the transition metal oxide had a huge drawback of low Coulombic efficiencies at low rates, which might be due to electrolyte destruction caused by the absence of a stable SEI. This also gives a direction, where these materials could be useful for in future, since high energy LiBs would not benefit from any of these materials. Furthermore, carbon coating of the active material might assist shielding the electrolyte from the catalytic surface of the transition metal and also electrolyte additives might assist the formation of a stable ionic conductive SEI during the first cycle.

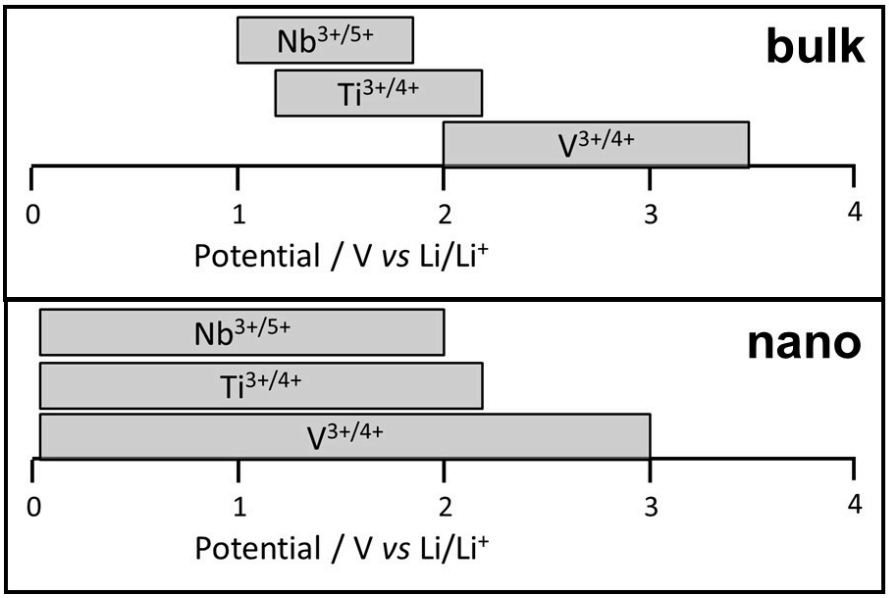

Figure 62: Simplified scheme of the charge storage regions for various bulk and nano-sized insertion materials.

Overall, this chapter shows that there are still a lot of open questions needing to be answered related to the electrochemical performance of nano-sized electrode materials. What is the role of crystallinity and porosity? More tests would be useful to understand this. Example given, Nb_2O_5 could be heat-treated at various temperatures (100, 200, 300, …, 1000 ^{o}C) and the cycling behaviour at low rates should be investigated. This could give a direct answer how the crystallinity controls the lithium-ion active sites and therefore, the operational potential window. This might also answer the question of why the materials show lithium-ion Faradaic reaction at the surface. Moreover, carbon coating should be tested for such materials in order to understand how electrolyte destruction interferes with the obtained charge/discharge signal? For this, an ex-situ carbon coating might be performed with a sucrose and Nb_2O_5 in water suspension, where the sucrose decomposes to amorphous carbon at the surface of the transition metal oxide with increasing temperature (caramelization) [79].

Since self-discharge is a known problem for high power devices, the self-discharge over hours or even longer of such metal oxide electrode materials should be investigated.

As the Coulombic efficiency and cycle life was very high at higher current rates, such materials might be useful as a negative electrode material in a high power hybrid capacitors with an activated carbon positive counter-electrode in the future (EDLC electrode) [31, 32]. As such, it would be expected that by increasing the operational potential window (due to the negative electrode), the energy and power density of the device increases. Especially Nb_2O_5 and layered titante would be excellent candidates, since their operational potential window is quite low (also compared to VO_2). The electrolyte would be similar to those used in conventional LiBs, where charge storage at the positive electrode occurs via double-layer capacitance at the high surface area carbon and charge storage at the negative electrode via pseudocapacitance insertion. Such charge storage might be even more energy efficient, if optimized carbon morphologies (like high surface area and more graphitic, see [31, 32, 35]) would be used as carbon additives. The focus of such devices (negative electrode is battery based and positive electrode is EDLC based) was set so far on LTO versus AC [255] or graphitic carbons (graphite, soft carbon, hard carbon) versus AC [32, 37, 254]. LTO shows a high operating potential vs. Li/Li^+ and graphitic carbons suffer at high rate operations. Therefore, Nb_2O_5 and layered titanate might be exciting alternatives compared to the current investigated hybrid devices.

4. High Power Negative Electrode Materials for LiBs – Combining Niobium and Titanium Oxides

4.1 Aims

Anatase TiO_2 and Nb_2O_5 are known to be excellent high power insertion materials. In an attempt to combine both, 25 at% Nb^{5+} was doped into anatase TiO_2. The doped and undoped materials were fully characterized and evaluated as potential high power materials for LiBs and LiCs.

4.2 Introduction

Titanium dioxide is an ideal negative electrode material to replace graphite as it is safe, inexpensive and environmentally friendly. In comparison to TiO_2, graphite suffers from low power density issues and requires a protective SEI layer to be formed [24, 59, 167, 256-261]. Moreover, TiO_2 has a structure that is stable under long term charge/discharge cycling across a range of C-rates, which can offer superior performance at higher power.

Undoped TiO_2 (anatase) negative electrode materials possess low electronic conductivity due to the wide band gap (ca. 3.0 to 3.4 eV) [262]. It is possible to increase the electronic conductivity of TiO_2 via introduction of dopants (such as Nb^{5+}) into the anatase structure [257, 258, 261, 263]. Fehse et al. showed that the partial density of states (PDOS) of Nb 4d and Ti 3d are similar, but the additional Nb 4d electron pushes the Fermi level from the top of the valence band for undoped TiO_2 to the bottom of the conduction band for Nb-doped TiO_2. The lowest Nb 4d empty states are not in the band gap, but overlap with Ti 3d empty states to form a band in the range 0

to 2 eV. As the Fermi level is located within this band, Nb-doped anatase TiO_2 exhibits metallic conductivity due to the delocalization of this additional Nb 4d electron [258].

High power Nb_2O_5 based electrodes have received much attention due to their ability to rapidly store charge from a combination of lithium-ion insertion/deinsertion and pseudocapacitive charge storage mechanisms [68, 116, 128-130]. It is postulated that there might be also positive contributions in terms charge storage via surface effects if Nb^{5+} is combined with anatase TiO_2, which should improve the high power performance.

In this chapter, the direct and continuous synthesis of undoped and Nb-doped TiO_2 (25 at% dopant) is presented. It is approached that the incorporation of Nb^{5+} in the structure improves the electrochemical performance (compared to undoped TiO_2) at higher charge/discharge rates. The results are described in terms of the impact of doping on electronic conductivity, lithium-ion diffusion kinetics and charge storage properties (via both diffusion controlled and/or surface effects) on timescales of a few minutes or a few seconds.

4.3 Experimental

4.3.1 Synthesis of the Materials

The nano-particles were synthesized using a laboratory scale CHFS reactor (chapter 2.1). TiBALD [Titanium(IV) bis(ammonium lactato)dihydroxide solution, 50 wt% H_2O, Sigma Aldrich, Steinheim, Germany], ammonium niobate(V) oxalate hydrate (Sigma-Aldrich, >99.99 %, Steinheim, Germany) and KOH (Fisher Scientific, Loughborough, UK) were used as aqueous precursors in D.I. Water (10 MΩ). For the synthesis of undoped TiO_2, 0.3 M TiBALD was used as metal salt precursor 1 and DI water was used in place of precursor 2. DI water from pump 1 was heated to 400 °C and mixed with the combined precursor feed, resulting in a

calculated reaction temperature of 305 °C inside the CJM. For the synthesis of Nb-doped TiO_2, 0.4 M TiBALD and 0.1 M ammonium niobate(V) oxalate hydrate were premixed at room temperature and used as metal salt precursor 1. This mixture was then combined in flow with 0.3 M KOH (precursor 2). This combined precursor feed (metal salt plus base) was mixed with the supercritical water flow (heated to 450 °C) to give a mixing temperature of 335 °C in the CJM.

4.3.2 Experimental Characterization

PXRD patterns of the samples were obtained on a STOE diffractometer using Mo-Kα radiation (λ = 0.70926 Å) over the 2θ range 7 to 40° with a step size of 0.5° and step time of 30 s. XPS measurements were collected using a Thermo Scientific™ K-alpha™$^+$ spectrometer using Al-Kα radiation and a 128-channel position sensitive detector. Survey scans were conducted at a pass energy of 150 eV and high resolution scans were conducted at a pass energy of 50 eV for Ti(2p), Nb(3d), O(1s) and C(1s). The XPS spectra were processed using CasaXPS™ software (version 2.3.16) and the binding energy scales were calibrated using the adventitious C 1s peak at 284.5 eV. Backgrounds were subtracted using the Shirley routine [264] and peaks were fitted with an appropriate Gaussian/Lorentzian line shape. Relative concentrations of Ti and Nb within the sample were estimated by measurement of the peak areas of Ti(2p) and Nb(3d) core lines and application of the appropriate relative sensitivity factors. The size and morphology of the crystallites were determined by TEM using a Jeol JEM 2100 – LaB_6 filament. The system was equipped with a Gatan Orius digital camera for digital image capturing. Samples were prepared by ultrasonically dispersing a few mg of the powder in ethanol (>99.5 %, EMPLURA, Darmstadt, Germany) and pipetting drops of the dispersed sample on to a copper film grid (300 mesh – Agar Scientific, Stansted, UK). The average crystallite size was determined by the

average of at least 60 crystallites. EDX analysis was carried out using an Oxford Instruments X-Ma N80-T Silicon Drift Detector fitted to the TEM and processed using AZtec™ software (error can be up to 1 %). BET surface area measurements were carried out using N_2 in a micrometrics ASAP 2020 machine. Prior to analysis, the samples were degassed at 150 °C (12 h) under vacuum before measurements. The error for BET was <0.1 $m^2 g^{-1}$.

4.3.3 Electrochemical Testing

The specific electrode mass loading for each electrode disc with a diameter of 16 mm was in the range of 1.0 to 1.5 mg cm^{-2}. The separator (glass microfiber filters, WHATMAN, Buckinghamshire, UK) was saturated with an organic electrolyte of LiPF6 in 3:7 wt% ethylene carbonate/ethyl methyl carbonate (BASF, Ludwigshafen, Germany). Electrochemical measurements were performed using a 48-channel Arbin Instrument (Caltest Instruments Ltd, Guildford, UK) at room temperature. The electrochemical performance was first investigated by CV in the potential range 1.2 to 2.5 V vs. Li/Li^+ with the scan rate in the range 0.1 mV s^{-1} to 1.0 mV s^{-1}. The specific current rate test was performed by applying various specific currents of 0.1 to 15 A g^{-1} in the potential range of 1.2 to 3 V vs. Li/Li^+.

Electrochemical impedance spectroscopy (EIS) was measured by applying an AC (alternating current) potential (5 mV) across a frequency range of 10 mHz to 500 kHz to an electrochemical cell and then measuring the current response through the cell with a galvanostat/potentiostat (PGSTAT302, AUTOLAB, Metrohm). The cell was assembled with Celgard 2400 separator soaked with 1 M LiPF6 in EC/DMC/DEC (1:1:1, v/v) as electrolyte with a lithium metal counter electrode for this measurement. EIS was performed versus OCV of the pristine cell.

4.4 Results and Discussion

4.4.1 Characterization Results

Undoped TiO_2 and Nb-doped TiO_2 were obtained as white and blue powders, respectively (see Figure 63a). The reaction yield was each above 90 %. The synthesis of anatase TiO_2 via CHFS was reported before; see [195, 202, 265]. The PXRD data confirmed a good match to the pattern for phase pure anatase TiO_2 (tetragonal, space group $I4_1/amd$, ICSD 9852), see Figure 63b. High-quality PXRD data revealed very minor impurity peaks in the Nb-doped TiO_2 sample at $2\theta = 14.4$ and 20.5 °, which is in line with the results from Shin et al. [266]. Due to the low intensity it was not possible to clearly identify the impurity phase. Considering the results from directly synthesized Nb_2O_5 (see previous chapter), it was not very likely, that these impurity peaks belong to a phase of Nb_2O_5.

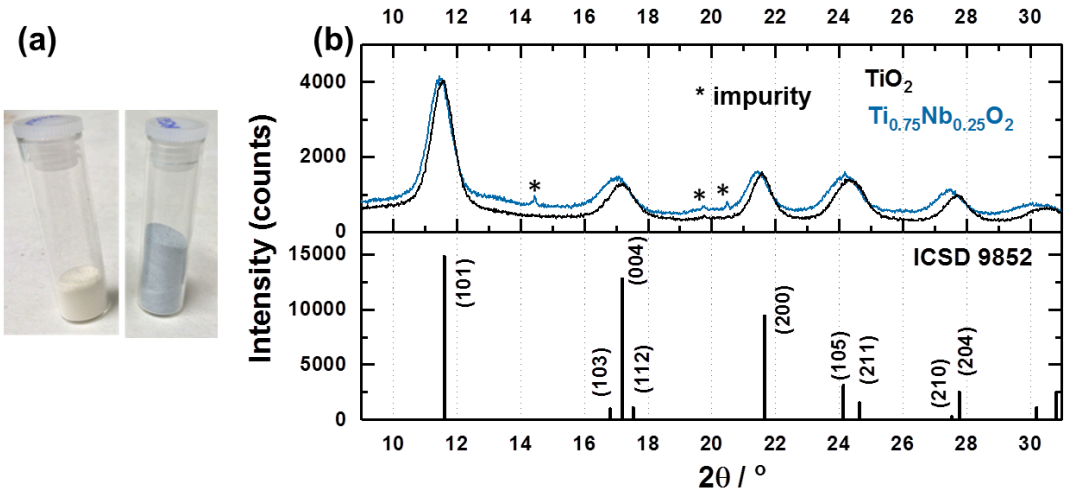

Figure 63: (a) Photograph of the pure (left) and doped (right) dried powder. (b) PXRD (Mo-source) patterns of pure (bottom, black) and Nb-doped anatase TiO_2 (top, blue).

There was a small peak shift to lower 2θ values in the PXRD data for Nb-doped TiO_2 compared to the undoped counterpart, especially at higher angles. This was due to lattice expansion,

resulting from the substitution of larger Nb^{5+} (ionic radius = 0.64 Å) for Ti^{4+} (ionic radius = 0.61 Å) in the TiO_6 octahedra of the anatase structure.

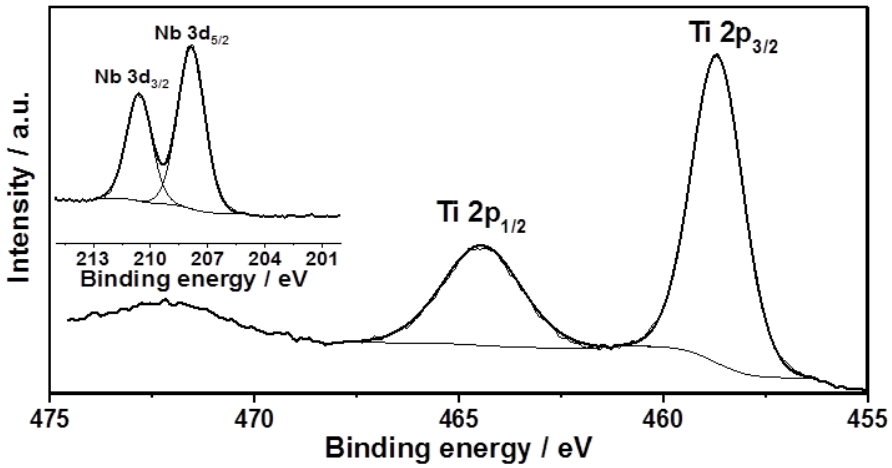

Figure 64: XPS spectra for sample $Ti_{0.75}Nb_{0.25}O_2$: High-resolution spectra oft he Ti 2p and the Nb 3d.

The valence state of the metal ions was determined with XPS for sample $Ti_{0.75}Nb_{0.25}O_2$, see Figure 64. The Nb-3d level binding energies were 210.6 eV (Nb $3d_{3/2}$) and 207.9 eV (Nb $3d_{5/2}$) with a spin orbit splitting of 2.7 eV, which were assigned to the core levels of Nb^{5+}. The Ti 2p level binding energies were 464.9 eV (Ti $2p_{1/2}$) and 459.1 eV (Ti $2p_{3/2}$) with a spin orbit splitting of 5.8 eV, which were assigned to the core levels of Ti^{4+}. No additional Ti peaks were observed within the spectra, suggesting 4+ was the only oxidation state for titanium. Semi-quantitative analysis of the peak areas for the Ti 2p and Nb 3d core lines, estimated the elemental composition at the surface to be 25 at% Nb relative to Ti. Additional EDX measurements suggested a composition of 22.6 ±1.9 at% Nb relative to Ti. Therefore, XPS and EDX measurements showed similar values, which was also in line with the precursor solutions. Together with the results from PXRD, this suggested successful doping of the Nb^{5+} into the anatase structure.

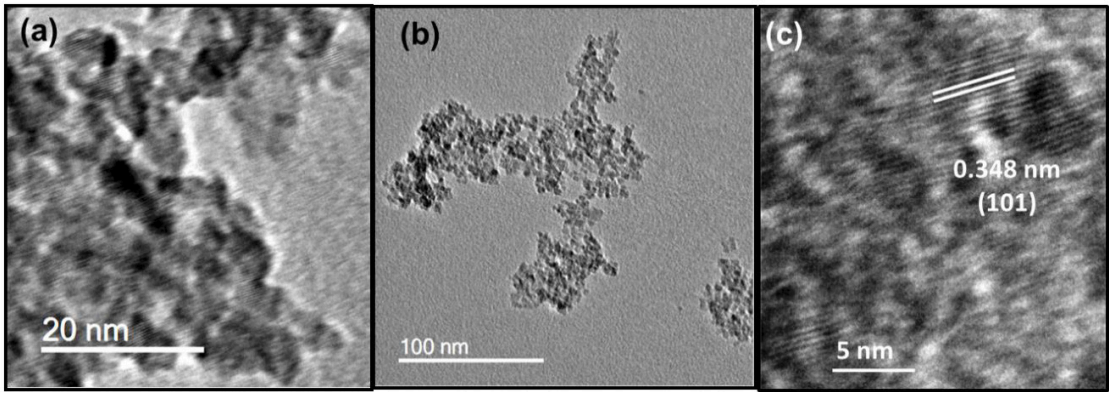

Figure 65: TEM images of (a) TiO_2 and (b) $Ti_{0.75}Nb_{0.25}O_2$. (c) HRTEM image of $Ti_{0.75}Nb_{0.25}O_2$.

TEM images revealed very small spherical particles with narrow size distribution for both undoped and Nb-doped titania (Figure 65). The average crystallite size of undoped and Nb-doped TiO_2 was 4.5 (±0.6) and 4.9 (±0.6) nm (>100 particles sampled). The interlayer spacing for undoped and doped TiO_2 was calculated from relevant TEM images and was found to be 0.34 (±0.01) and 0.35 (±0.01) nm, respectively, which is consistent with expectations for the (101) planes of tetragonal-phase anatase. The BET surface area of the undoped TiO_2 was 288 $m^2 g^{-1}$ and for Nb-doped TiO_2, it was 239 $m^2 g^{-1}$.

4.4.2 Understanding the Charge Storage Properties (1.2 – 3.0 V vs. Li/Li^+)

As stated in the previous chapter, the redox activity of the $Ti^{3+/4+}$ redox couple is generally observed in the potential range of 1.2 to 2.1 V vs. Li/Li^+ for most titanates (except rutile TiO_2, which undergoes drastic structural changes at ca. 1.1 V vs. Li/Li^+ [167]). Initially, the electronic conductivity was investigated for both materials. A potential versus capacity plot, suggested that the overpotential between lithiation and delithiation (current rate 5 A g^{-1}) was higher for the undoped TiO_2 compared to the Nb-doped TiO_2 (Figure 66a), which suggested higher electronic conductivity for the Nb-doped sample.

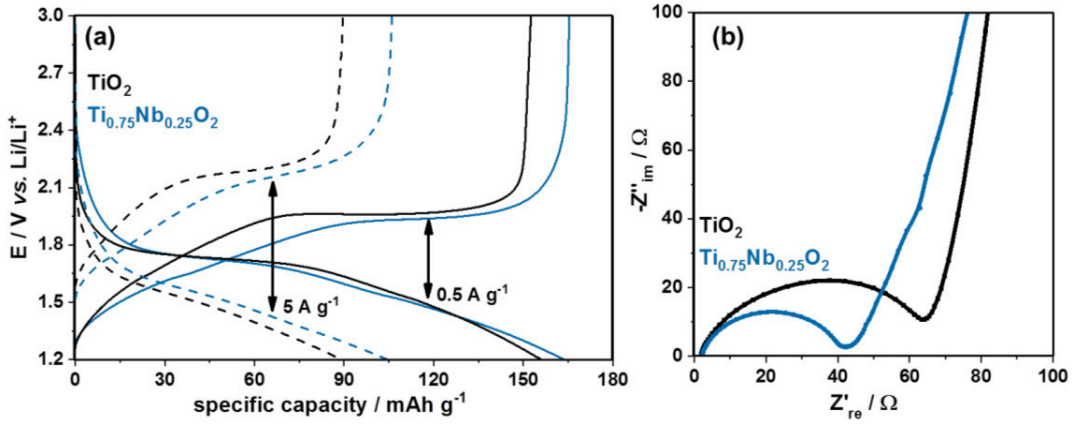

Figure 66: (a) Charge/discharge profile for TiO_2 and $Ti_{0.75}Nb_{0.25}O_2$, showing the potential (vs. Li/Li^+) versus specific capacity (mAh g^{-1}) at applied currents of 0.5 and 5 A g^{-1}, respectively. (b) Electrochemical impedance spectra of pristine coin half cells based on TiO_2 and $Ti_{0.75}Nb_{0.25}O_2$ electrodes.

EIS was performed in order to further investigate the improved performance of Nb-doped TiO_2 at higher current rates (Figure 66b). The EIS results were similar for both samples and each curve could be divided into a high frequency region (a semicircle) and a low frequency region (a straight line). The high-frequency intercept with the real axis (x-axis) represents the Ohmic resistance, which is related to the electrolyte. As both samples were measured under the same conditions, the Ohmic resistance was similar for both. The semicircle at higher frequencies gives some information about the electrode resistance (charge-transfer resistance). As shown in the

Nyquist plot, the general trend was towards lower resistance for the doped sample (ca. 41 Ω) versus the undoped sample (ca. 62 Ω). This suggested higher electronic conductivity for the doped sample, which has been previously observed for other Nb-doped titanium oxides [239, 258, 267].

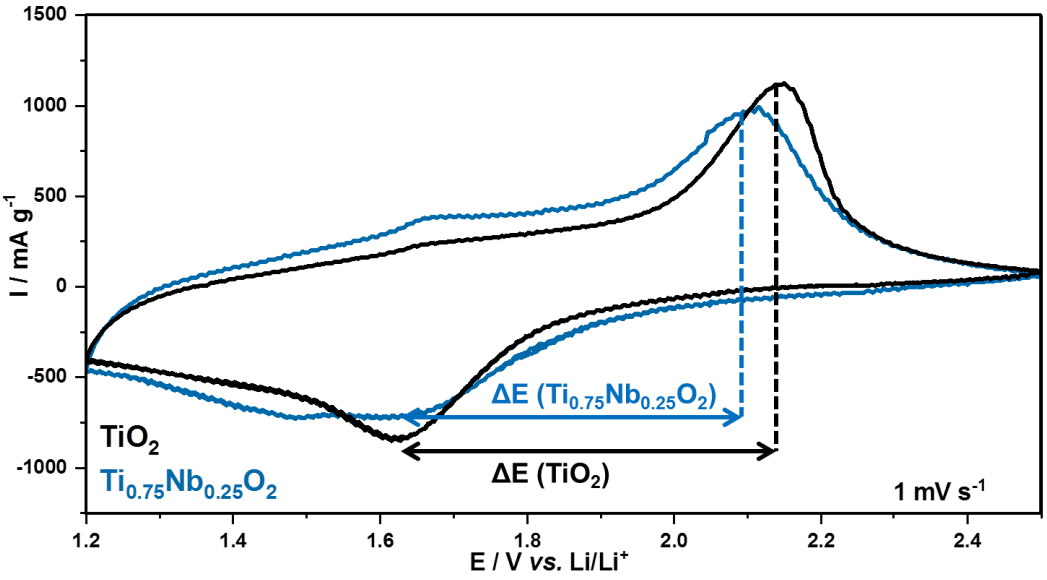

Figure 67: CVs of the undoped and doped titanias at an applied scan rate of 1 mV s^{-1}. The highlighted potential difference (ΔE) corresponds to the $Ti^{3+/4+}$ redox couple.

CVs were carried out to gain a better understanding of the electrochemical performance for the two materials. The specific current response at an applied scan rate of 1 mV s^{-1} is presented in Figure 67. A decrease in peak height was observed with doping of 25 at% Nb into TiO_2 in the characteristic range where Ti^{3+}/Ti^{4+} is active for anatase TiO_2 (1.6 and 2.2 V vs. Li/Li^+), which would have been expected due to the lower titanium-ion concentration. Interestingly, the peak potential for undoped titania exhibited a higher peak shift (difference between the lithiation and delithiation peaks) of 0.52 V compared to the Nb-doped material (peak shift 0.47 V). This gave an indirect indication of better lithium-ion insertion kinetics for the Nb-doped TiO_2 [58, 266,

268], which could be a consequence of higher interlayer spacing for the Nb-doped sample compared to the undoped TiO_2 (see results PXRD). Two further peaks were observed for the Nb-doped TiO_2 at 1.49 and 1.67 V vs. Li/Li^+ for the lithiation and delithiation, respectively. These might correspond to the $Nb^{5+/3+}$ redox couple [116, 130].

A scan rate test was carried out to distinguish the charge stored via diffusion-controlled lithium-ion insertion from surface effects (Figure 68a,b). The calculations were undertaken using the same method as used in chapter 3 (see also chapter 2.3.5). The slight shift of the lithium-ion deinsertion/insertion peak for higher applied scan rates was ignored and the potential value from a sweep rate of 0.5 mV s^{-1} was used as the standard deinsertion/insertion potential. Low scan rates (range of 0.1 to 1 mV s^{-1}) were chosen as the peak shifted more at higher applied rates [24]. The current that resulted from capacitive effects at the surface, was calculated for a scan rate of 0.5 mV s^{-1}, which was then plotted against the overall measured current (grey area in Figure 68c,d). Undoped and doped TiO_2 showed charge storage contributions via surface effects of 50 and 65 % at a scan rate of 0.5 mV s^{-1}, respectively. This is surprising since the doped sample showed a lower BET surface area (288 vs. 239 m^2 g^{-1} for undoped and doped TiO_2, respectively).

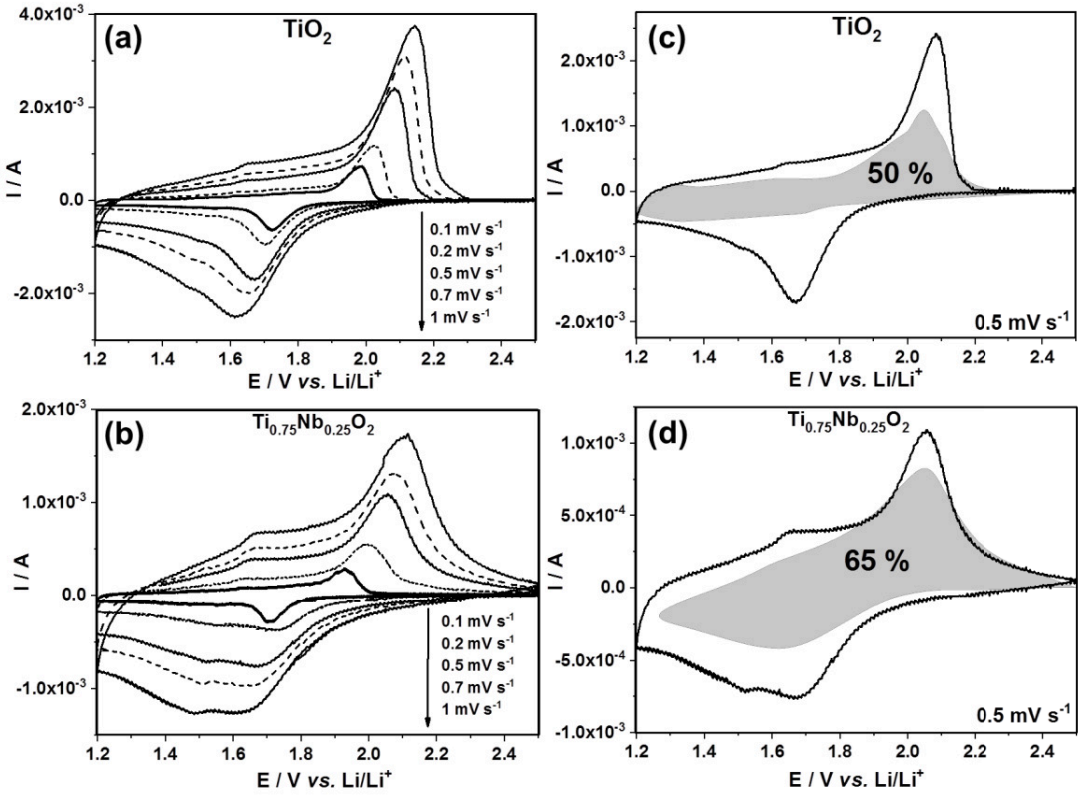

Figure 68: CVs at applied rates in the range of 0.1 to 1 mV s^{-1} (scan rate test) for (a) undoped and (b) doped TiO_2. The calculated current response arising from charge storage via capacitance (grey area) at a scan rate of 0.5 mV s^{-1} is shown for (c) pure TiO_2 and (d) $Ti_{0.75}Nb_{0.25}O_2$.

Thus, the doped titania sample showed higher electronic conductivity, better lithium-ion kinetics, additional charge storage contributions from the Nb-dopant and finally, higher charge storage via surface effects compared to undoped TiO_2.

4.4.3 General Electrochemical Performance (1.2 – 3.0 V vs. Li/Li^+)

Initial Coulombic efficiency from CV testing at 0.05 mV s^{-1} was ca. 73 and 88 % for undoped and doped TiO_2, respectively. Similar to the results obtained in chapter 3, reasons for this might be found in crystal water and interstitial sites from defects, which would each cause additional lithium-ion loss (heat-treatments might be necessary). A main factor is the electrolyte destruction due to SEI formation and this is directly related to the surface area (288 vs. 239 $m^2 g^{-1}$ for undoped and doped TiO_2, respectively).

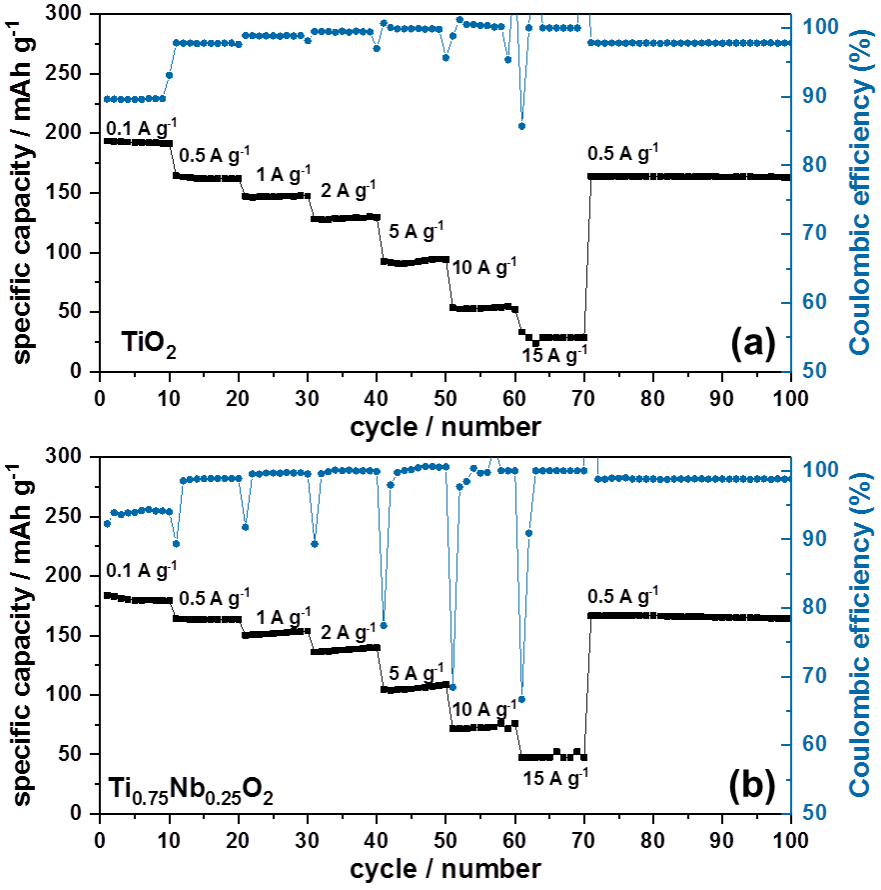

Figure 69: Electrochemical performance plots of specific capacity (mAh g^{-1}) versus cycle number at applied currents in the range of 0.1 to 15 A g^{-1} for (a) TiO_2 and (b) $Ti_{0.75}Nb_{0.25}O_2$.

Galvanostatic cycling tests at various specific current rates were performed from 0.1 to 15 A g^{-1} (considering 1C = 175 mAh g^{-1}, this is equivalent to a C-rate range of ca. 0.5 C to 86 C). It should be mentioned that the C-rate corresponds to the full theoretical charge/discharge within one hour for 1 C, but this relates to the bulk delithiation/lithiation charge storage mechanism, which is typical for a battery material. Undoped and doped TiO_2 showed significant charge storage via surface effects, which are more commonly associated with oxide supercapacitors. Therefore, the C-rate and measured time is given in the following.

The charge storage behaviour fitted well to the galvanostatic charge/discharge cycling results (Figure 69). Diffusion-limited charge storage processes are expected to decrease drastically when the electrode material is electrochemically cycled within seconds (see also previous chapter 3), since the main charge storage mechanism is due to surface effects at these high rates.

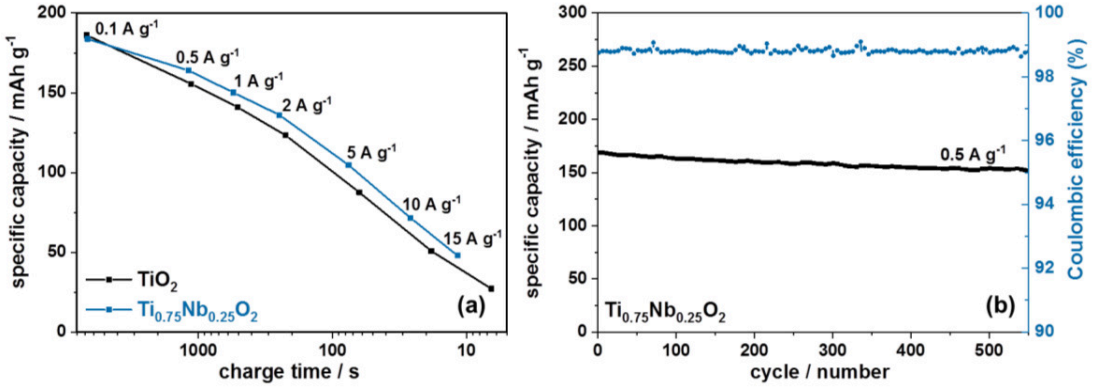

Figure 70: (a) Electrochemical performance plots of specific capacity (mAh g^{-1}) versus delithiation time at applied currents in the range of 0.1 to 15 A g^{-1} for TiO_2 (black) and $Ti_{0.75}Nb_{0.25}O_2$ (blue). b) Long-term cycling stability study at an applied current of 0.5 A g^{-1} for $Ti_{0.75}Nb_{0.25}O_2$.

At the lowest applied current rate, the undoped and Nb-doped TiO_2, showed a specific capacity of 186 mAh g^{-1} and 180 mAh g^{-1}, respectively (C-rate ca. 0.5 C, 6200 s per charge or discharge). At higher currents, the Nb-doped TiO_2 showed superior rate retention compared to its undoped counterpart; at a current rate of 5 A g^{-1} (C-rate ca. 29 C, 65 s per charge or discharge), the

undoped and Nb-doped TiO_2 showed a specific capacity of 88 mAh g^{-1} and 105 mAh g^{-1}, respectively. At the highest applied current of 15 A g^{-1} (C-rate ca. 86 C, ca. 10 s per charge or discharge), the undoped and doped nano-TiO_2 samples showed a specific capacity of 27 and 48 mAh g^{-1}, respectively (Table 3).

A capacity versus charge time plot for each applied current rate is given in Figure 70a. Clearly, both materials show excellent high power characteristics. Since the charge is stored within seconds at higher rates, it should be noted, that there might be problems of self-discharge as seen for many supercapacitors. Herein, the materials were tested without a relaxing time between charge/discharge. For real full cell applications, the potential self-discharge rate should be tested.

Long-term galvanostatic charge/discharge cycling for the Nb-doped sample at a specific current rate of 0.5 A g^{-1} is presented in Figure 70b. The Coulombic efficiency remained >98.7 % and overall a specific capacity retention of ca. 91 % (initial and final value 168 and 153 mAh g^{-1}, respectively) was achieved after 540 cycles. Therefore, the as-prepared nano-sized Nb-doped TiO_2 showed high cycle stability at a current rate of 0.5 A g^{-1}.

Table 3: Summary of the electrochemical performance.

	TiO_2	**$Ti_{0.75}Nb_{0.25}O_2$**
BET surface area	288 m^2 g^{-1}	239 m^2 g^{-1}
Electrode wt% fraction	70:20:10	70:20:10
Intial Coul. eff. 0.1 A g^{-1}	28 %	23 %
Coul. eff. at 0.1 A g^{-1}	90 %	94 %
Coul. eff. at 0.5 A g^{-1}	98 %	99 %
Spec. capacity at 0.1 A g^{-1}	193 mAh g^{-1}	180 mAh g^{-1}
Spec. capacity at 10 A g^{-1}	73 mAh g^{-1}	47 mAh g^{-1}
Spec. capacity at 15 A g^{-1}	54 mAh g^{-1}	30 mAh g^{-1}

In a later report by Shin et al. [266], various dopant concentrations (0, 5, 10, 15, 20 at%) of Nb^{5+} in anatase TiO_2 were investigated for use as negative electrode materials in lithium-ion batteries. The emphasis was set on the electronic and ionic conductivity and the results herein were partly confirmed. In their work, even if the electronic conductivity was highest for the sample with 20 at% Nb in TiO_2, the best performing material was found to be 10 at% Nb-doped anatase TiO_2, which was found to be due to the best compromise in ionic and electronic conductivity. Therefore, 10 at% Nb-doped TiO_2 should be synthesized via CHFS in future.

4.5 Overall Discussion and Outlook

Interestingly, the obtained results suggested that the BET surface area was not the most critical parameter for the high power performance. Although the BET surface area decreased for 18 % with higher Nb-dopant level, the overall stored charge increased when using high power testing conditions. Less dependence of surface area on the high power performance has been observed previously for Nb_2O_5 [129] and MnO_2 [269] negative electrode materials. Overall, Nb-doping into anatase TiO_2 was shown to drastically improve the charge storage at higher current rates. The combined effect of higher electronic conductivity, improved lithium-ion kinetics and higher charge storage via surface effects, benefitted the high power performance for nano-sized Nb-doped TiO_2 compared to the undoped counterpart. For optimum performance, 10 at% Nb-doped TiO_2 should probably be synthesized via CHFS in future, as proposed by Shin et al. [266].

Solid solutions of niobium and titanium oxides for use as high power and stable negative electrode materials in lithium-ion batteries could play a crucial role in future. There are also other ways of combining these two transition metals in a hetero-metallic oxide. In recent reports, titanium niobium oxides (such as $TiNb_2O_7$) were introduced as potential lithium-ion negative electrode materials with exceptional high rate performance, high capacities (up to 300 mAh g^{-1}) and high stability [270-272]. Unfortunately, the synthesis needs very high temperatures (typically above 1000 ^oC) and nano-sizing is challenging to date. It would be interesting to see if CHFS could be used to make such classes of nano-sized titanium niobium oxides for use in alkali-ion batteries. As other transition metal oxides are known to show promising high power performances due to fast Faradaic processes, future studies should investigate the effect of alternative dopants in titania (e.g. Ru, Mn, Fe, Ni, Mo etc., whose corresponding transition metal oxide is known to be highly pseudocapacitive under high current rates) in nano-TiO_2 or other lithium-ion insertion host systems [15].

5. Transition Metal Ion Dopants in SnO_2 – Useful for High Energy LiB Full Cells?

5.1 Aims

SnO_2 is known to be an excellent high capacity negative electrode material for alkali-ion batteries. Unfortunately, it also suffers from high irreversible capacity losses during the first cycle. Herein, SnO_2 was combined with various transition metal dopants in order to improve the initial delithiation capacity. The active potential regions vs. Li/Li^+ were evaluated according to their ability to improve the energy density when used in a full cell LiB.

5.2 Introduction

Recently, many papers have been published in the literature, claiming that the electrochemical performance of SnO_2 could be drastically improved by doping (incorporating) with the following transition metal ions (oxides): Fe [91, 273, 274], Cu [275], Co [107, 276, 277], Co-Ni [98, 278], Zn [279, 280], Ti [281] and Ni [282]. Unfortunately, only a few of these studies named the specific surface area of the doped/composite SnO_2 and the pristine SnO_2, and for some, the surface area of the pristine SnO_2 was even three times smaller compared to the transition metal modified SnO_2 [91, 107]. In 2000, Li et al. emphasized the importance of the surface area for the stability and electrochemical properties of SnO_2 [283]. Overall, doping is often proposed to drastically increase the overall capacity. This statement is conflicting because the doped and undoped SnO_2 tend to show different material's properties (e.g. surface area) and the doped sample is sometimes also carbon coated. Moreover, the calculated capacity is often only based on the metal oxide active material neglecting the contributions from the carbon additive [91].

Herein, the contribution of carbon additives on the electrochemical performance in such high capacity systems is critically discussed. It will be shown, that it is important to take into account the carbon as another charge storage reservoir. Given the range of possible particle properties that affect the charge storage, herein, an attempt was made to understand the true effect of the transition metal dopant on the electrochemical performance of SnO_2. Unlike other works from the literature, a fair comparison was made (similar surface area, doping concentration, water content etc.) with the aim of giving realistic comparisons.

The transition metal dopants were grouped into two classes: redox-inactive and possible redox-active dopants; redox-inactive dopants included Nb, Ti and Zr. Possible redox-active dopants (Fe, Co, Cu, Zn, Mn and Ni) were classified because of the known ability of their metal oxides to undergo conversion (alloying) reactions with lithium-ions [68, 73]. The electrochemical performance of LiB half cells of the as-prepared nano-materials was evaluated via potentiodynamic methods in order to assess the potentials at which redox activity occurs during cycling. It is known that the energy density is related to the voltage multiplied by the charge for an ideal battery; therefore, the wider the potential window, the more energy that can be stored. With this in mind, it was sought to identify the location of the potential peaks for charge and discharge in the doped materials and make qualitative assessments on the likely energy density that would result (particularly if they were to be made into full cells in the future).

Due to the issue, that no effective buffer for the volume expansion during charge/discharge was used, only the first cycle was investigated and long-term cycling tests were not possible (as they would not give credible investigations).

5.3 Experimental

5.3.1 Synthesis of the Materials

All SnO_2 based materials were synthesized with a lab scale CHFS reactor. Potassium stannate trihydrate (99.9 %), titanium oxysulfate (≥29 % Ti as TiO_2), ammonium niobate oxalate hydrate (99.99 %) and zinc nitrate hexahydrate (98 %) were purchased from Sigma-Aldrich, Dorset, UK. Cobalt nitrate hexahydrate (99 %), iron (III) citrate nonahydrate (98 %), copper nitrate trihydrate (99 %) and zirconyl nitrate hydrate (99.5 %) were purchased from Acros Organics, Fisher Scientific, Leicestershire, UK. Manganese nitrate tetrahydrate (98 %) and nickel nitrate hexahydrate (98 %) were purchased from Alfa Aesar, Lancashire, UK. For the synthesis, 0.1 M of Sn salt was used for the production of undoped SnO_2 and 0.09 M of Sn salt mixed together with 0.01 M of the respective transition metal ion salt was used for the production of doped SnO_2. This precursor mixture was mixed with DI water (each 40 mL min^{-1}) and brought into contact with the flow of supercritical water (80 mL min^{-1}, heated to 450 °C, reaction temperature of 335 °C, residence time ca. 5 s), chapter 2.1.

5.3.2 Experimental Characterization

PXRD patterns of all samples were obtained on a STOE diffractometer using Mo-Kα radiation (λ = 0.70926 Å) over the 2θ range 2 to 40° with a step size of 0.5° and step time of 20 s. XPS measurements were collected using a Thermo Scientific K-alpha spectrometer using Al-Kα radiation and a 128-channel position sensitive detector. The XPS data were processed using CasaXPS™ software (version 2.3.16), the binding energy scales were calibrated using the adventitious C 1s peak at 285.0 eV and the fitting was applied using an appropriate relative sensitivity factor. Elemental composition of the samples was determined with an XRF

spectrometer (Rh target, Bruker M4 Tornado). For recording XRF spectra, pellets of the powders were pressed under identical conditions (*ca.* 300 mg, 2 tons of force, 30 s). The error for XRF is lower than 0.1 %. Lattice structural information and particle morphology were examined *via* TEM with a JEOL 2100 TEM. BET surface area measurements were carried out using N_2 in a Micrometrics ASAP 2020 Automatic High-Resolution Micropore Physisorption Analyzer. The samples were degassed at 120 °C (5 h) under vacuum before measurements. The error for BET was <0.1 m^2 g^{-1}. TGA was performed using a TGA Q500 instrument (TA instruments) under nitrogen with a flow rate of 40 mL min^{-1}. The test started from room temperature to 300 °C with a heating rate of 20 °C min^{-1}. The weighing precision was <0.01 %.

5.3.3 Electrochemical Testing

The slurry for all electrode materials was prepared with a content of 80 wt% active materials, 10 wt% conductive agent and 10 wt% PVDF. Another set of electrodes of undoped SnO_2 were prepared with a ratio of 50:40:10 and carbon black electrodes were fabricated with a ratio of 90:10. The mixtures were combined in a high shear mixer (model THINKY ARE-310, Thinky, CA, USA) using three cycles of mixing for 2 min duration at 2000 rpm (each cycle was followed by a defoaming step of 10 s at 2200 rpm). The doctor bladed electrodes were dried in an oven at 70 °C for 1 hour, pressed with 800 kg of force and then left overnight at room temperature. Electrodes with a diameter of 15.0 mm were punched out, dried 12 hours at 70 °C and then overnight under vacuum. The electrodes had an active material mass loading of 1.5 ±0.5 mg cm^{-2}. The separator was saturated with 120 µL of 1 M $LiPF_6$ in ethylene carbonate / dimethyl carbonate (1:1 v/v, Merck Selectipur LP40, Darmstadt, Germany). The electrochemical performance was investigated by CV between 0.05 to 3.0 V vs. Li/Li^+ with a scan rate of

0.1 mV s^{-1} using a galvanostat/potentiostat (PGSTAT302, AUTOLAB, Metrohm, Utrecht, Netherlands).

5.4 Results and Discussion

5.4.1 Characterization Results

All materials were obtained as powders with different colours according to the dopant used (Figure 72). The synthesis of SnO_2 via CHFS was reported before; see [284, 285].

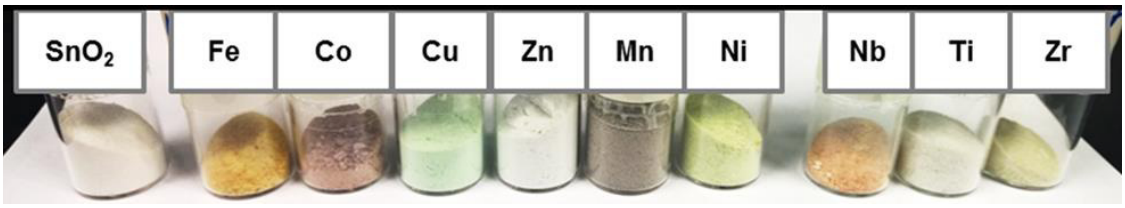

Figure 71: Photo showing the colour of the doped SnO_2 nano-particles compared to undoped SnO_2.

PXRD data for the samples revealed tetragonal SnO_2 (space group *P*42/*mnm*, PDF 41-1445) as the main phase with no implications of impurity peaks (Figure 72). Moreover, the broad peaks (normalized herein for a better comparison) indicated similar nano-sized crystallites for all samples.

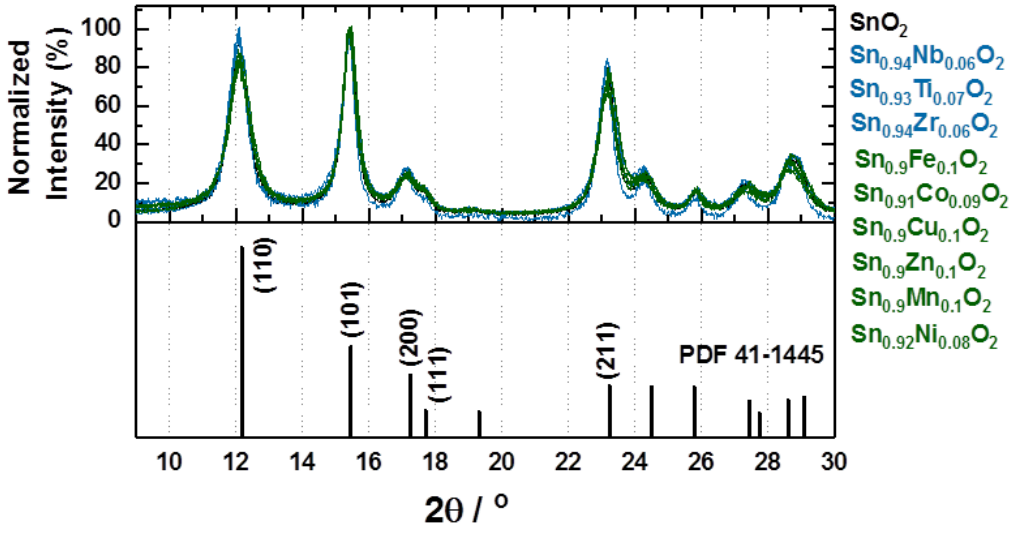

Figure 72: PXRD patterns [Mo-source, normalized to the (101) peak intensity] for potential redox-inactive (blue) and redox-active (green) dopants in SnO_2 and undoped SnO_2 (black) in the 2θ range 9 to 30°.

XRF measurements showed that the dopant concentration was in the range of 6 to 10 at%. The colour change in the samples, XRF results and the PXRD results, all suggested that successful doping had been achieved with no phase separation.

It is known that nano-materials are often hygroscopic and that such water can result in the formation of LiOH which can affect the electrochemical performance of negative electrode materials such as SnO_2 [111, 112]. Consequently, TGA measurements were undertaken on all nano-materials (Figure 73) to assess water contents. A weight loss of ca. 3 wt% due to weakly associated water, was observed for all the nano-materials in the temperature range 25 to 120 °C [286] (with no more than 4 wt% loss overall up to a temperature of 300 °C). Considering that the electrodes were heated (70 °C) and dried overnight under vacuum (via the glove box) to remove water, it is safe to suggest there should have been <1 wt% water in the active materials as used in the half cell configuration.

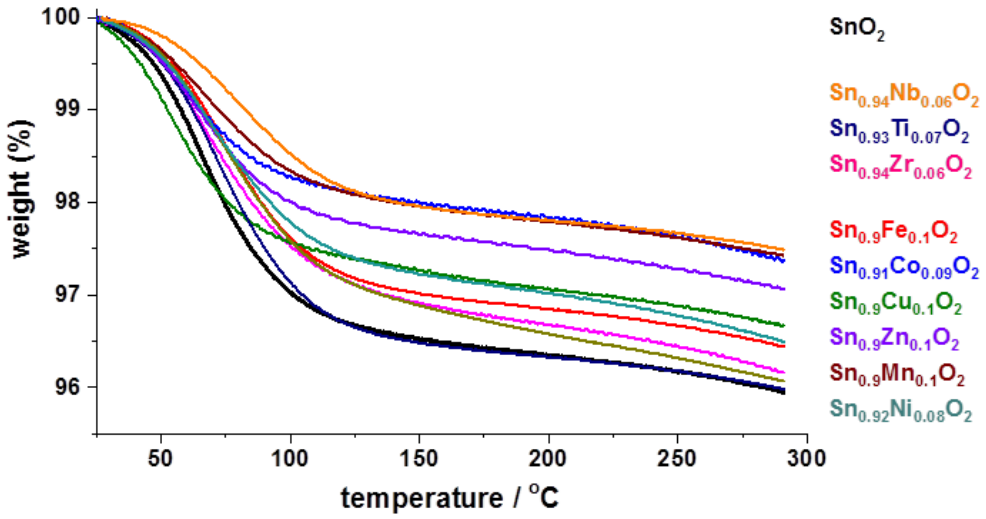

Figure 73: TGA measurements for all samples in the temperature range 25 to 300 °C.

The high-resolution XPS spectrum of the Sn 3d region for undoped SnO_2 (Figure 74) revealed two peaks corresponding to the binding energies for Sn 3d5/2 at 486.1 and Sn 3d3/2 at 494.5 eV, which were assigned to Sn^{4+} and were observed in similar range for all doped materials.

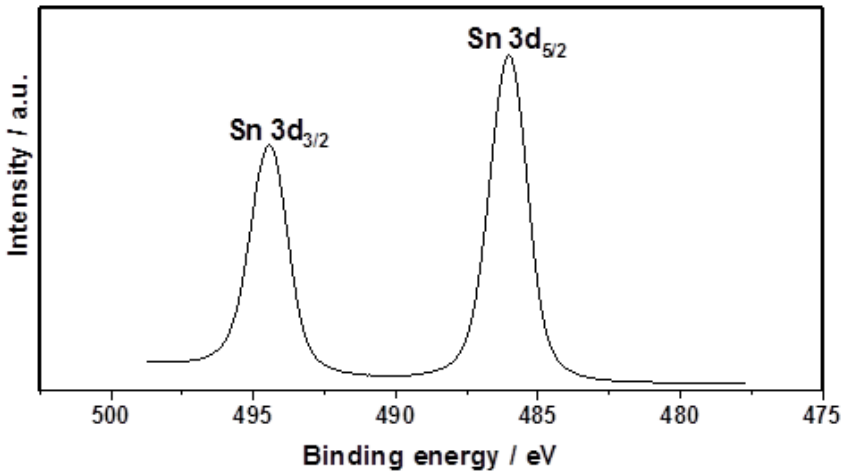

Figure 74: High-resolution XPS spectra of the Sn 3d region for undoped SnO_2.

The XPS spectra for all dopants are presented in Figure 75. For sample $Sn_{0.9}Fe_{0.1}O_2$, the Fe 2p3/2 peak could be best fitted with two components with a minor one at 710.7 eV and a major one at 715.3 eV, which were ascribed to Fe^{2+} and Fe^{3+}, respectively (Figure 75a). For sample $Sn_{0.91}Co_{0.09}O_2$, the spin-orbit splitting was 15.9 eV for the Co 2p3/2 peak at 781.1 eV and Co 2p1/2 peak at 797.0 eV, which is indicative of Co^{2+} as the main oxidation state [287] (Figure 75b). For sample $Sn_{0.9}Cu_{0.1}O_2$, there were two peaks detected corresponding to Cu 2p3/2 at 933.3 eV and Cu 2p1/2 at 953.1 eV, with spin-orbit splitting of 19.8 eV, indicative of Cu^{2+} (Figure 75c). For sample $Sn_{0.9}Zn_{0.1}O_2$, two split peaks were measured at 1021.6 eV and 1044.7 eV with a spin-orbit splitting of 23.1 eV indicative of Zn^{2+} (Figure 75d). For sample $Sn_{0.9}Mn_{0.1}O_2$, the Mn 3s region could not be investigated due to an overlap with the Sn 4p peaks. There were two peaks at 641.4 eV (major) and 644.9 eV (minor) for the Mn 3p3/2, which shows that Mn^{2+} was mainly present with some Mn^{3+} (Figure 75e). For sample $Sn_{0.92}Ni_{0.08}O_2$, the peaks

at 855.8 and 873.3 eV represent the Ni^{2+} state (2p3/2 and 2p1/2, respectively), Figure 75f. The Ti 2p binding energies were 463.4 eV (Ti 2p1/2) and 457.7 eV (Ti 2p3/2), with a spin-orbit splitting of 5.7 eV; these peaks were assigned to the core levels of Ti^{4+} (Figure 75g).

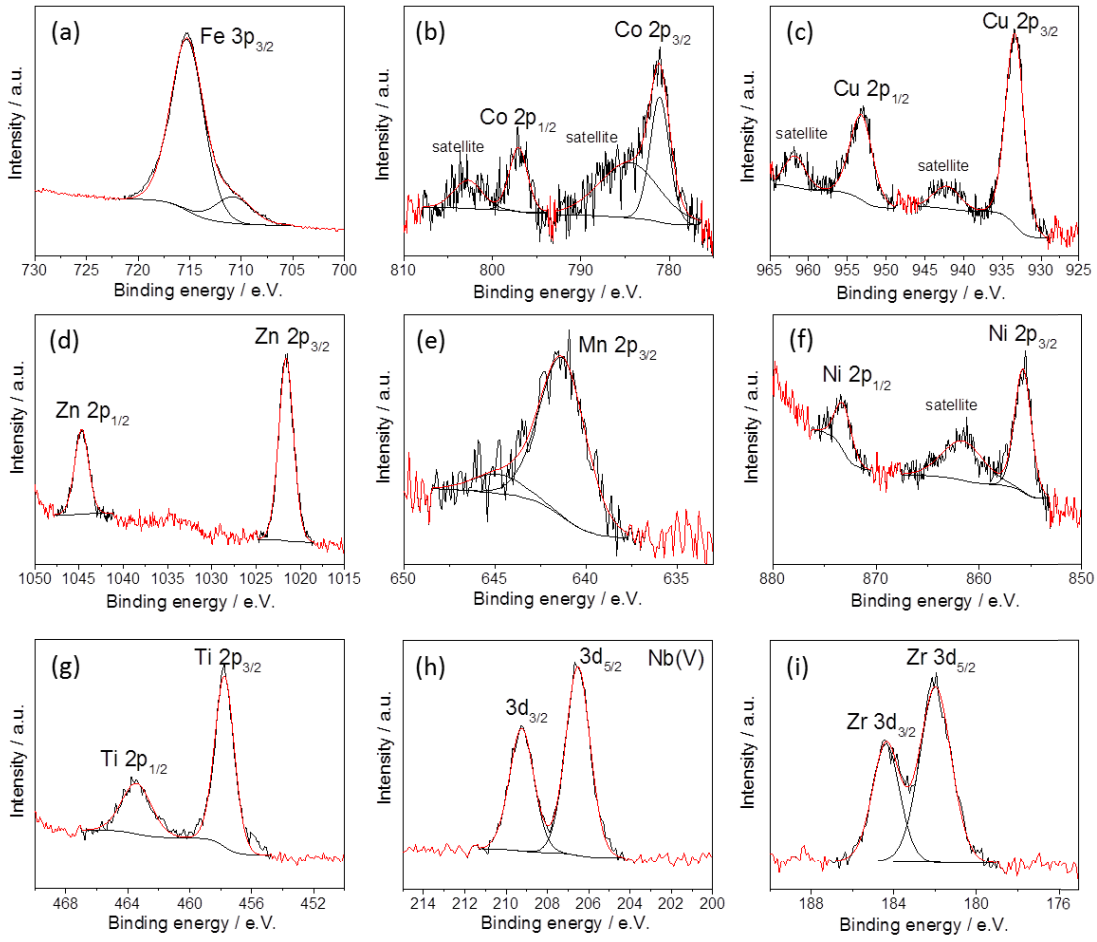

Figure 75: High-resolution XPS spectra of the splitting energies for (a) Fe 3p3/2, (b) Co 2p, (c) Cu 2p, (d) Zn 2p, (e) Mn 2p3/2, (f) Ni 2p, (g) Ti 2p, (h) Nb 3d and (i) Zr 3d orbitals. Each plot of the transition metal XPS spectra corresponds to the transition metal doped SnO_2 material.

For sample $Sn_{0.94}Nb_{0.06}O_2$, the Nb-3d level binding energies were 209.3 eV (Nb 3d5/2) and 206.6 eV (Nb 3d3/2) with a spin-orbit splitting of 2.7 eV, which was due to the presence of Nb^{5+}

(Figure 75h). For sample $Sn_{0.94}Zr_{0.06}O_2$, there were two peaks with binding energies of 182.0 and 184.4 eV that correspond to Zr 3d3/2 and Zr 3d5/2, respectively, and were representative of Zr^{4+} (Figure 75i). The oxidation state of the metal-ions in the precursors did not change (except partly for Fe and Mn) during the synthesis and therefore, all doped transition metals remained (mainly) in the same oxidation state as their precursor solution (Table 4).

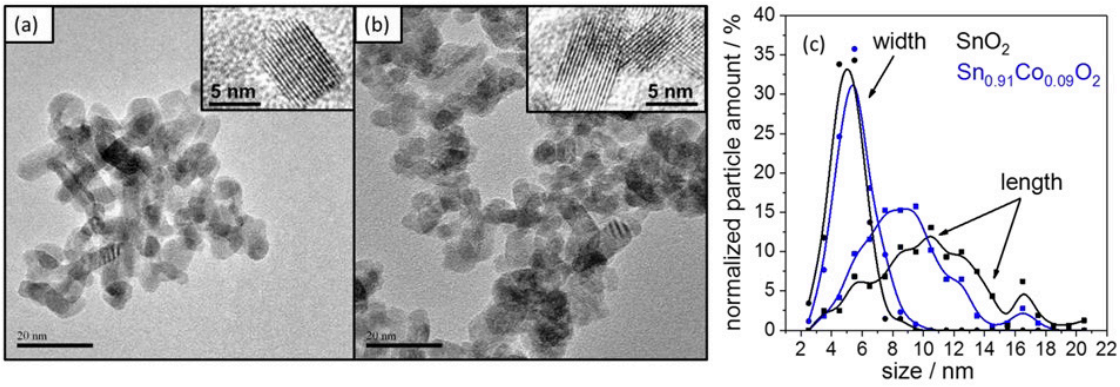

Figure 76: TEM images of (a) undoped SnO_2 (bar = 20 nm) and (b) $Sn_{0.91}Co_{0.09}O_2$ (bar = 20 nm). HRTEM inset is shown on the top right of each figure (bar = 5 nm). (c) Normalized particle amount plotted for the size parameters width and length (>150 particles sampled).

The morphology, size and crystallinity were examined by TEM (Figure 76). The particles had a rod-like and spherical morphology, appeared to be slightly aggregated and were mono-crystalline. The inset in Figure 76a and 66b revealed an interlayer spacing of ca. 0.34±0.03 nm (110) for both undoped SnO_2 and $Sn_{0.91}Co_{0.09}O_2$. The undoped SnO_2 appeared to show more rod-like particles compared to Co-doped SnO_2, which showed more spherical particles (Figure 76c). The average measured crystallite sizes were in a similar range for both undoped SnO_2 (mean particle length 10.6 nm, mean particle width 5.0 nm; >150 particles sampled) and $Sn_{0.91}Co_{0.09}O_2$ (mean particle length 8.7 nm, mean particle width 5.5 nm; >150 particles sampled), which is in line with the similar surface areas of ca. 95.1 and 99.6 $m^2\ g^{-1}$ for undoped and Co-doped SnO_2,

respectively. The BET surface areas of all SnO_2 based nanoparticle samples were in the range 85.4 to 123.3 $m^2 g^{-1}$, see Table 4.

Overall, the CHFS process facilitated the synthesis of various as-prepared doped SnO_2 materials with similar surface area, water content, crystallinity and dopant concentration. The oxidation state of the dopant was controlled by the choice of precursor in solution. Thus, for electrochemical investigations versus lithium metal in a half-cell configuration, the effects of the dopant transition metal on the electrochemical properties could be compared without considering any significant differences in the surface area, crystallinity or water content.

Table 4: Characterization details for the as-synthesized undoped and doped SnO_2 materials. The colour is given based on Figure 71, the dopant concentration was obtained via XRF, the oxidation state of the dopant was identified with XPS measurements, the water content via TGA and the surface area was obtained via BET surface area measurements.

Sample name	**Colour**	**Dopant conc. / at%**	**Ox. state dopant**	**H_2O content / wt%**	**Surface area / $m^2 g^{-1}$**
SnO_2	white	0	-	<1	95.1
$Sn_{0.94}Nb_{0.06}O_2$	light yellow	5.8	5+	<1	112.5
$Sn_{0.93}Ti_{0.07}O_2$	white	7.3	4+	<1	110.8
$Sn_{0.94}Zr_{0.06}O_2$	light grey	6.1	4+	<1	98.0
$Sn_{0.9}Fe_{0.1}O_2$	yellow	9.9	2+/3+	<1	123.1
$Sn_{0.91}Co_{0.09}O_2$	brown	8.9	2+	<1	99.6
$Sn_{0.9}Cu_{0.1}O_2$	light green	10.4	2+	<1	102.0
$Sn_{0.9}Zn_{0.1}O_2$	white	9.8	2+	<1	98.4
$Sn_{0.9}Mn_{0.1}O_2$	dark brown	9.6	4+	<1	85.4
$Sn_{0.92}Ni_{0.08}O_2$	light green	8.2	2+	<1	99.8

5.4.2 The Role of Carbons in SnO_2 Electrode Networks

For a stable SnO_2 based negative electrode, significant levels of carbons (introduced via carbon coating, graphene, carbon black etc.) are often used to compensate for the extreme volume expansions that occur during cycling, e.g. typically less than 63 wt% of SnO_2 active material in the printed electrode has been used [91-102, 288-290]. Therefore, the specific capacity was measured in using 50 wt% undoped SnO_2 in order to ascertain the baseline electrode performance with this level of carbon present. In Figure 77, the CV is plotted for undoped SnO_2 and the contributions of the carbon black, were calculated based on similar measurements with pure carbon black electrodes (see blue area Figure 77).

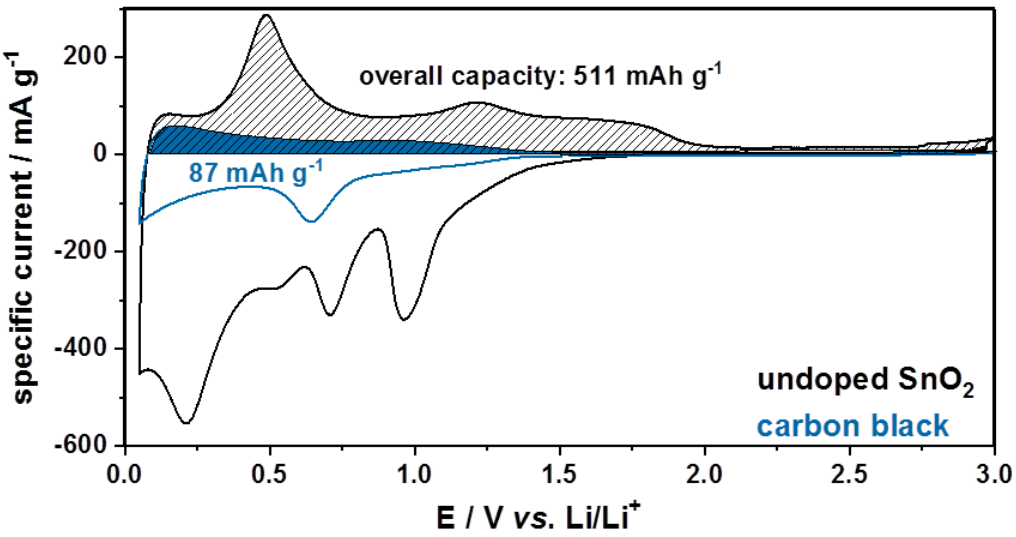

Figure 77: CV at a scan rate of 0.1 mV s^{-1} for undoped SnO_2. The electrode loading was 50 wt% SnO_2, 40 wt% carbon and 10 wt% PVDF.

Pure SnO_2 underwent two types of lithiation processes, namely the initial conversion to Sn metal and Li_2O at 0.96 V vs. Li/Li^+ and the alloying reaction of the Sn metal with lithium-ions towards Li_xSn ($0 \leq x \leq 4.4$) at ca. 0.22 V vs. Li/Li^+. There was an additional peak at 0.70 V vs. Li/Li^+ which was due to SEI formation on the carbon additive; for more information see the

comparison with carbon black electrode (chapter 3.4.6) and also the results from Fransson et al. [291]. During delithiation, the Li_xSn compound dealloyed at 0.50 V vs. Li/Li^+ and also showed additional redox activity at higher potentials (>1.0 V vs. Li/Li^+). As shown herein, the additional charge/discharge activity of the carbon additive was not negligible, since >87 mAh g^{-1} could be released during delithiation. This meant that from the overall specific capacity of 511 mAh g^{-1}, ca. 17 % of the delithiation capacity could have been due to the carbon. If only the delithiation capacity is calculated based on undoped SnO_2 (no contributions from the carbon assumed), the specific capacity would be 986 mAh g^{-1}.

There are many carbon modifications which often differ in the degree of graphitization, changing the overall charge storage properties. As an example, hard carbons show specific capacities of up to 800 mAh g^{-1} [253, 292]. Carbon black used herein is not comparable to the carbon-coatings used in the literature, since the obtained capacities are <200 mAh g^{-1} at low rates and the graphitization degree differs. Therefore, the impact of any carbon additive might be even higher in literature than shown herein. It should be noted that many transition metals (e.g. Fe or Ni) are known to catalyse the graphitization of amorphous carbon at higher temperature [293] meaning that even for doped and undoped samples, the charge storage properties of the carbon-coating is expected to differ.

Clearly, the electrochemical lithiation/delithiation in a carbon/active material composite electrodes is still not fully understood and an exact determination of the individual capacity contributions of each material in the composite is not possible. With this in mind, only 10 wt% carbon content electrodes were used for further electrochemical testing as to minimize the additional electrochemical contributions from it.

5.4.3 Electrochemical Performance Evaluation of the doped SnO_2 materials via Cyclic Voltammetry

The CVs for samples $Sn_{0.94}Nb_{0.06}O_2$, $Sn_{0.93}Ti_{0.07}O_2$ and $Sn_{0.94}Zr_{0.06}O_2$ (redox-inactive dopants) versus SnO_2 are presented in Figure 78. The lithiation and delithation activity was lower at all potentials for the doped materials compared to the undoped SnO_2, showing no beneficial input of the dopant on the capacity performance. Similar to these results, no capacity improvement at low currents has been previously reported in the literature for Ti-doped SnO_2, when similar surface areas were used with 21 $m^2\ g^{-1}$ for undoped SnO_2 and 26 $m^2\ g^{-1}$ Ti-doped SnO_2 [281].

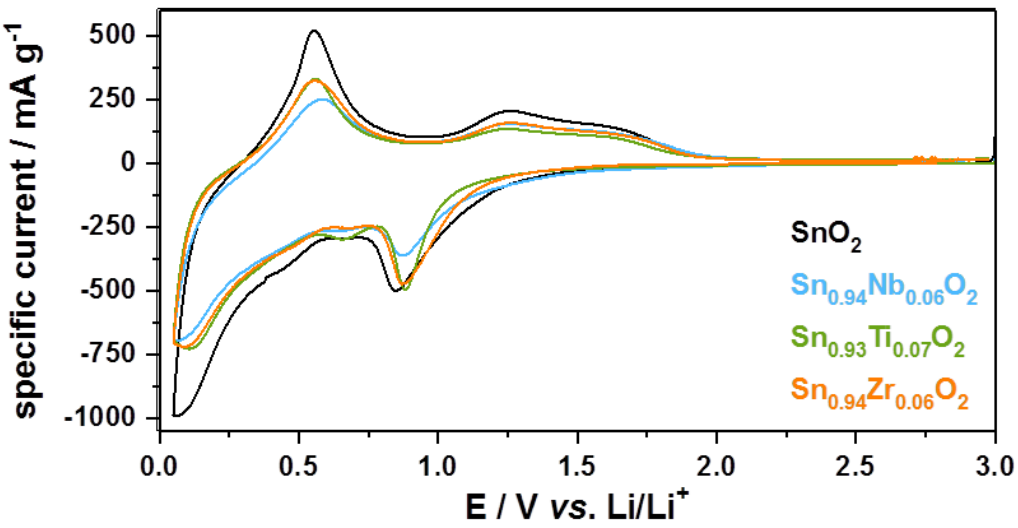

Figure 78: CVs at a scan rate of 0.1 mV s^{-1} for all expected redox-inactive dopants. The electrode loading was 80 wt% SnO_2, 10 wt% carbon and 10 wt% PVDF.

The CV results of all possible redox-active dopants are shown in Figure 79. These dopants might have the potential to (partially) undergo a conversion reaction themselves.

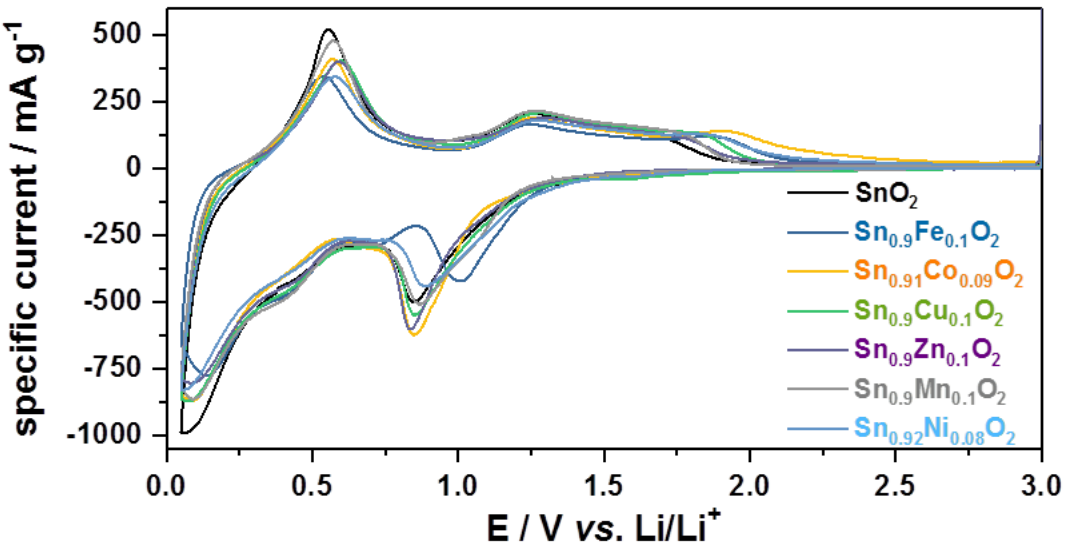

Figure 79: CVs at a scan rate of 0.1 mV s^{-1}. Illustration of all CVs for possible redox-active dopants. The electrode loading wt% ratio was 80:10:10 for the SnO_2, carbon and PVDF, respectively.

In Figure 80, the lithiation peaks are presented via a specific current versus potential plot and the corresponding specific lithiation capacities are given in Table 5. Pure SnO_2 underwent two lithiation steps, namely the initial conversion towards Sn metal and Li_2O at ca. 0.85 V vs. Li/Li^+ and the alloying reaction of the Sn metal with lithium-ions towards Li_xSn ($0 \leq x \leq 4.4$) at ca. 0.1 V vs. Li/Li^+. These potentials for the conversion and alloying reactions were lower than those shown in Figure 77. This might be due to increased electrode resistance caused by the relatively low carbon content in the majority of the electrodes. All samples showed two lithiation peaks, although the alloying peak was less strong for the doped samples compared to the undoped counterpart, which could be attributed to the lower concentration of Sn atoms in the materials. The conversion peak was higher for the majority of the redox-active dopants (except for Ni and Fe), which might correspond to the initial reduction of CoO [68, 294], CuO [295], ZnO [296] and Mn_2O_3 [297]. Moreover, $Sn_{0.9}Mn_{0.1}O_2$ showed a shoulder around 0.4 V vs. Li/Li^+ which might be related to the Mn in the sample [297]. NiO can be active at ca. 1.0 V vs. Li/Li^+ [298], which may be so with the results herein, since the first lithiation peak was broader

compared to the undoped SnO_2. Sample $Sn_{0.9}Fe_{0.1}O_2$ showed a broader lithiation peak at ca. 1.0 V and a second smaller one at ca. 0.6 V vs. Li/Li^+. Overall, these results may be an indication that all "conversion-type" dopants remained (partly) electrochemically active during cycling.

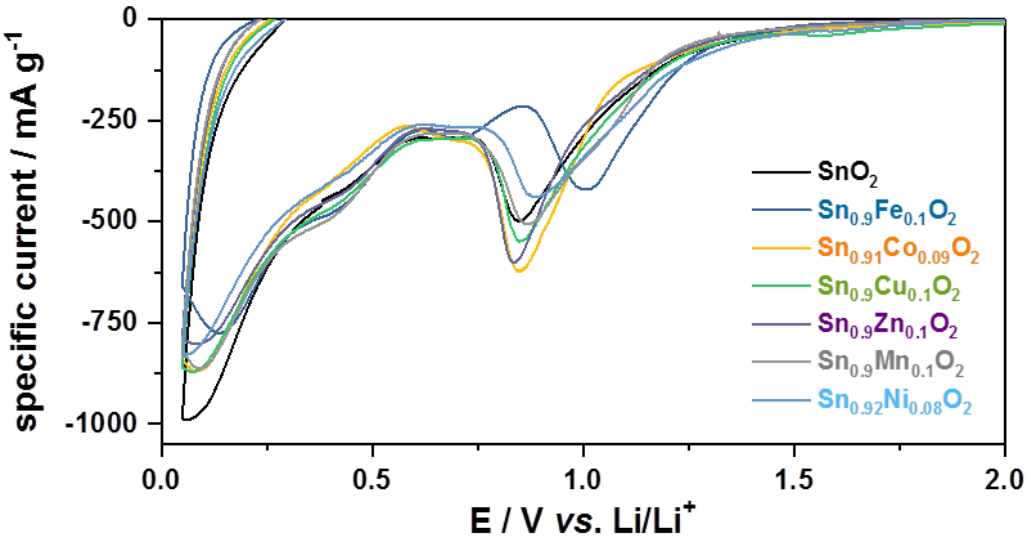

Figure 80: CVs at a scan rate of 0.1 mV s^{-1} with focus on the lithiation performance for all samples based on potential redox active dopants in comparison to undoped SnO_2. The electrode loading wt% ratio was 80:10:10 for the SnO_2, carbon and PVDF, respectively.

The first lithiation capacities were all in the range of ca. 1165 to 1324 mAh g^{-1}. As there were many potential contributions in addition to the SnO_2 activity for these capacities (e.g. SEI formation and possible electrochemical activity of the dopant), the origin of all lithiation contributions is not further discussed in detail hereafter.

In Figure 81, the delithiation performance was plotted for all SnO_2 samples doped with possible redox active dopants. The undoped SnO_2 showed the highest measured current for the dealloying peak at ca. 0.55 V vs. Li/Li^+, which can again be explained with the highest concentration of Sn atoms of any sample. Overall, there was no observed capacity win for any sample during delithiation until 1.5 V vs. Li/Li^+. However, there was a capacity win for all (potential) redox

active dopants at potentials higher than 1.7 V vs. Li/Li^+, which might be explained by the additional delithiation reactions from the conversion of the doped transition metal. CuO based electrode materials might have been expected to show additional delithiation activity at 2.5 V vs. Li/Li^+ [295], which was not observed herein and was also not observed for other Cu/Sn oxide composite negative electrode materials [275, 299, 300]. Overall, the samples with Fe, Co and Ni, clearly showed the largest capacity wins at higher potentials.

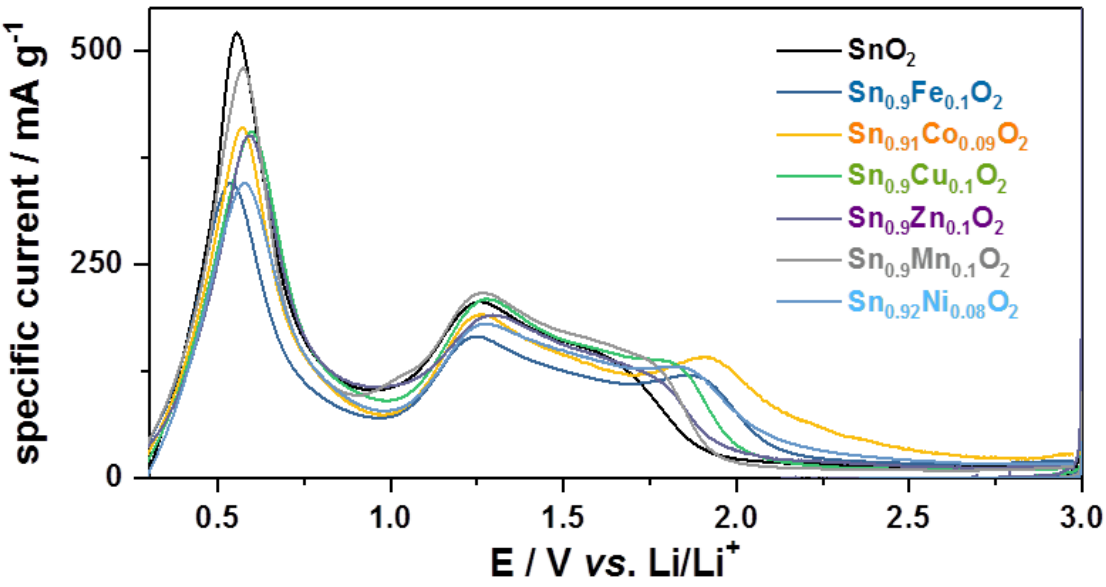

Figure 81: CVs at a scan rate of 0.1 mV s^{-1}, focus on the delithiation performance for all samples based on potential redox active dopants in comparison to undoped SnO_2. The plot highlights that for all materials, there is a capacity loss at lower potentials and a capacity win at higher potentials. The electrode loading wt% ratio was 80:10:10 for the SnO_2, carbon and PVDF, respectively.

In Figure 82, the delithiation performance is summarized in a scheme with the data from sample $Sn_{0.91}Co_{0.09}O_2$. All SnO_2 based materials containing dopants that might be redox-active, showed a capacity loss relative to undoped SnO_2 at lower potentials (<1.2 V vs. Li/Li^+), but a capacity win at higher potentials (>1.7 V vs. Li/Li^+). Similar results were obtained recently for molybdenum tin oxide composites, which showed a higher capacity compared to undoped SnO_2,

but additional delithiation processes occurred at higher potentials [301]. Herein, $Sn_{0.9}Cu_{0.1}O_2$ and $Sn_{0.9}Mn_{0.1}O_2$ showed slightly higher delithiation capacities compared to undoped SnO_2. Overall, taking into account the samples are all of similar surface areas and crystallinity, sample $Sn_{0.91}Co_{0.09}O_2$ outperformed the undoped SnO_2 and all other samples in terms of Coulombic efficiency and specific capacity (Table 5). This is unsurprising given the current interest in Co-Sn oxides in the literature [107, 276, 277, 302-305] and would explain the current commercial and academic interest in composite C-Sn-Co negative electrodes, e.g. in Nexelion batteries from Sony (where the wt% ratio of graphite:Sn:Co is typically 50:25:25) [47].

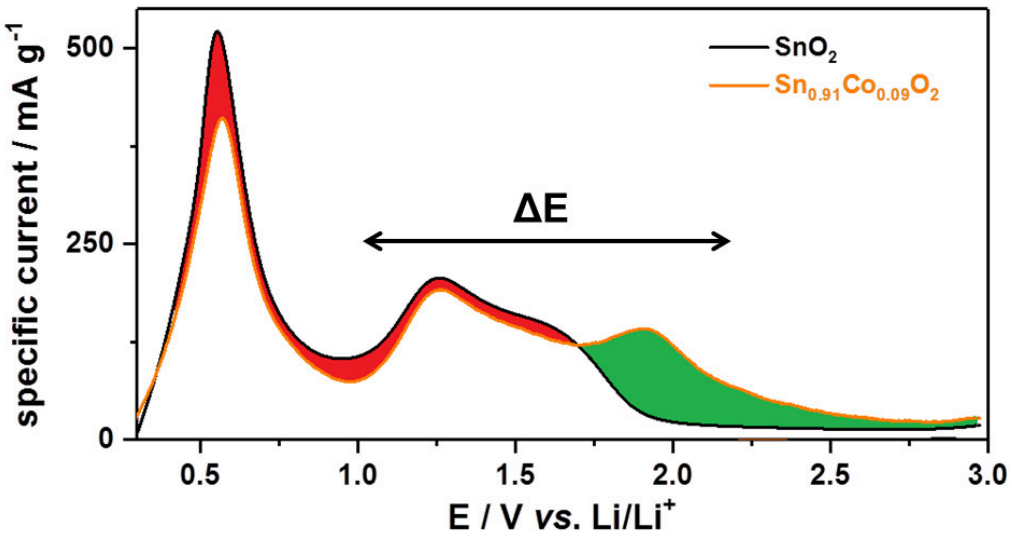

Figure 82: A schematic plot with the capacity loss shown in the red area and gain in the green area.

The question remains as to whether such mixed conversion and alloying materials would be expected to offer gains in terms of energy density if they were evaluated in full cells. Meister et al. recently investigated various types of lithium-ion battery full cells and showed that for all investigated negative active materials (Si/C vs. graphite vs. soft carbon vs. $ZnFe_2O_4$), energy inefficiency was mainly caused by a voltage hysteresis between the charge and discharge curve [306]. As stated before, the energy density of the full cell might be simply understood as the

mathematical product of full cell voltage and specific capacity. This, in turn, means that a slight capacity win for a composite material (herein especially $Sn_{0.9}Cu_{0.1}O_2$) might not give a larger energy density compared to undoped SnO_2, since a high cell voltage is sacrificed through the voltage hysteresis at the same time.

Table 5: All dopants were split into two groups, namely redox-active (possible conversion reaction ability) and inactive dopants (else). The calculated capacities are based on the measured CVs for the first cycle.

Sample name	Expected dopant reactivity	Lithiation capacity / mAh g^{-1}	Delithiation capacity / mAh g^{-1}	Coul. Eff. / %
SnO_2	-	1299.8	812.2	62.5
$Sn_{0.94}Nb_{0.06}O_2$	redox inactive	960.4	633.2	65.9
$Sn_{0.93}Ti_{0.07}O_2$		1061.2	600.8	56.6
$Sn_{0.94}Zr_{0.06}O_2$		1066.0	628.1	58.9
$Sn_{0.9}Fe_{0.1}O_2$	redox active	1283.2	753.9	58.8
$Sn_{0.91}Co_{0.09}O_2$		1199.7	952.9	79.4
$Sn_{0.9}Cu_{0.1}O_2$		1314.7	838.9	63.8
$Sn_{0.9}Zn_{0.1}O_2$		1256.8	800.7	63.7
$Sn_{0.9}Mn_{0.1}O_2$		1323.8	845.8	63.9
$Sn_{0.92}Ni_{0.08}O_2$		1164.7	802.5	68.9

Overall, it was observed that if the material's properties of doped SnO_2 were similar to the undoped one, the benefits (towards high energy full cells) of doping might not be as evident as proposed by many reports in the literature. This is a key investigation, since many researchers claim improved performances for doped SnO_2. There can be an improvement due to simultaneous changes in crystallinity, surface area etc. If these parameters are all similar, like herein, we could clearly show that the advantages are not as evident. In particular, there are often more disadvantages considering improvements towards energy density. The dopant could have

an impact on the cycle stability and rate capability. However, no effective buffer was used herein limiting credible investigations. For such a study, carbon/SnO_2 composites might be used, where the undoped and doped materials show again similar materials properties.

5.5 Overall Discussion and Outlook

Various doped SnO_2 nano-materials were compared as potential negative electrode materials for LiBs. These nano-sized SnO_2 materials were synthesized with similar surface area, water content and dopant concentration in a single step, by using a continuous hydrothermal synthesis route. Under these conditions, it was possible to investigate the potential location (vs. Li/Li^+) of the charge storage and release when the materials were cycled in a coin cell (versus lithium metal). This showed that the overall capacity win of some materials might not be beneficial for the full cell and that many dopants actually worsen the energy performance of SnO_2, which is different from what is claimed by many other authors in the literature. Overall, the general concept of using mixed alloying/conversion for full cell LiBs is questionable until the problem of the huge voltage hysteresis for conversion materials can be overcome.

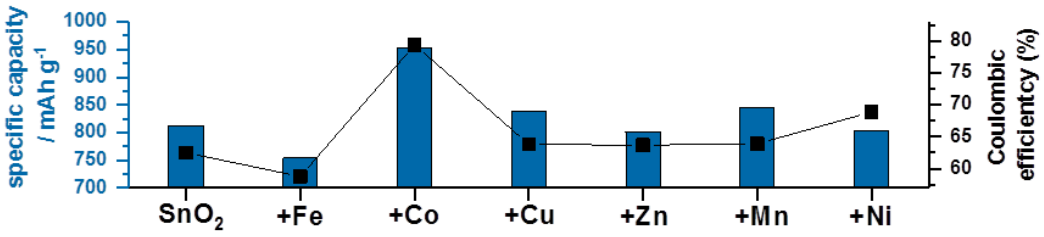

Figure 83: Delithiation capacity (left, blue) and Coulombic efficiency (right, black) for undoped SnO_2 and SnO_2 dopant with potentially redox-active transition metals. The data is obtained from the first cycle of the CVs.

The Coulombic efficiency and specific capacity were obtained from CV experiments. Redox-inactive dopants did not contribute to the capacity, which is why the main focus was set on potential redox-active dopants (Figure 83). Only the sample with 9 wt% Co was observed to significantly increase the delithiation capacity from 812 mAh g^{-1} for undoped SnO_2 to 953 mAh g^{-1} with also far increased Coulombic efficiency of 79.4 % (62.5 % for undoped SnO_2). This is also in line with the usage of Sn/Co/C negative electrodes in Sony's Nexelion batteries.

This chapter was also a good example of how the CHFS process can facilitate a better investigation compared to batch hydrothermal or related synthesis methods. The short reaction time and nucleation driven conditions, enabled a synthesis of particles with similar materials properties. Thus, a comprehensive study with fair comparisons was possible. This can be used for various other examples for LiB electrode materials like optimized doping concentrations of various dopants in LFP [189, 307] or simply the optimum atomic ratio of NCA and NMC positive electrode materials for LiBs.

There are currently many researchers, trying to implement alloying-type Zn-based materials in LiBs as the negative electrode (Zn as alloying material shows also electrochemical activity at low potentials) [90]. The whole approach taken herein might be indeed repeated for zinc oxides to answer the question which dopant might really improve the electrochemical performance of ZnO. Such investigations can also be conducted for sodium-ion batteries as the chemistry of this battery is quite similar to LiBs.

6. Stable, High Energy Negative Electrode Materials for LiBs - Combinations of Insertion and Alloying Materials

6.1 Aims

Insertion materials show excellent cycle life but low specific capacities. Sn-based compounds show high specific capacities and low cycle life. Therefore, Sn as alloying material and TiO_2, Nb_2O_5 and VO_2 as insertion materials were combined via doping in order to gain medium capacity and medium cycle life.

6.2 Introduction

A number of reports in the literature have sought to develop complex materials or nano-composites, which display a combination of different charge storage mechanisms e.g. both insertion and conversion/alloying reactions [140, 308]. It is envisaged that such materials can provide a balance between moderate structural changes and reasonably high capacities, which should prolong cycle life stability. In the first section, the role of different concentrations of Sn-dopant in anatase TiO_2 on the electrochemical performance in negative electrodes for LiBs, is discussed. This idea was used for two other insertion electrode materials for a general proof of concept. All materials were synthesized in a single step and were used without any further heat-treatment.

Sn-doped TiO_2: A range of phase-pure (anatase) TiO_2 (~5 nm) and Sn-doped TiO_2 nano-particle powders with the formula $Ti_{1-x}Sn_xO_2$ (where x = 0, 0.06, 0.11 and 0.15) were synthesized using a lab scale CHFS reactor. Charge/discharge cycling tests are carried out in two different potential

ranges of 3.0 to 1.0 V vs. Li/Li^+ and also a wider range of 3.0 to 0.05 V vs. Li/Li^+. In the narrower potential range, the undoped TiO_2 nano-particles displayed superior electrochemical performance compared to all the Sn-doped titania crystallites. In the wider potential range, the Sn-doped samples performed better than undoped TiO_2. The reasons for these results were investigated and the special role of Sn as dopant was evaluated.

Sn-doped Nb_2O_5 and Sn-doped VO_2: A series of nano-sized tin-doped metal oxides of niobium(V) and vanadium(IV), were directly synthesized using a pilot scale CHFS process (herein >65 g h^{-1} production rate). All tin-doped nano-materials showed higher specific capacities compared to their undoped metal oxide counterparts and the increased charge storage could be said to originate from the electrochemical activation of the tin dopant as an alloying material.

6.3 Experimental

6.3.1 Synthesis of the Materials

Different concentrations of Sn-doped TiO_2 were synthesized with a lab scale reactor. The materials for comparison of Sn-doped Nb_2O_5 and VO_2 materials were synthesized using the pilot plant CHFS reactor (chapter 2.1).

Sn-doped TiO_2: For the metal salt feed, the precursor solution of a mixture of acidified titanium oxysulphate hydrate ($TiOSO_4$: 29 wt% TiO_2 and 17 wt% H_2SO_4, Sigma Aldrich, Steinheim, Germany) and tin(IV) sulphate ($SnSO_4$ 97 %, Acros Organics, Geel, Belgium) were combined to give a total metal ion concentration of 0.0625 M. The titanium salt was used with a concentration of 0.0625, 0.06, 0.575 and 0.055 M, whereas for the last three concentrations, the tin salt concentration was set to 0.0025, 0.005 and 0.0075 M, respectively. These concentrations

corresponded to a nominal precursor Sn at% of 0, 4, 8 and 12 %. However, the samples were labelled according to actual at% of Sn measured via EDX, i.e. the actual formulas of TiO_2, $Ti_{0.94}Sn_{0.06}O_2$, $Ti_{0.89}Sn_{0.11}O_2$, $Ti_{0.85}Sn_{0.15}O_2$, i.e. corresponding to 0, 6, 11, and 15 at% Sn, respectively. The base concentration was kept constant throughout all experiments at 0.0703 M. This precursor mixture was then brought into contact with the flow of supercritical water (heated to 400 °C, reaction temperature of 305 °C, residence time ca. 6 s).

Sn-doped Nb_2O_5 and Sn-doped VO_2: 0.1 M Ammonium niobate(V) oxalate hydrate (Sigma-Aldrich, >99.99 %, Steinheim, Germany) was used for the synthesis of the niobium oxides. Ammonium metavanadate (0.1 M, >99 %, Sigma Aldrich, Steinheim, Germany) was mixed with oxalic acid dehydrate (0.2 M, >99 %, Sigma Aldrich, Steinheim, Germany) until the colour changed from yellow to dark blue and then used as metal salt V^{4+} precursor solution for the vanadium oxides synthesis [228]. Tin(IV) sulphate (97 %, Acros Organics, Geel, Belgium) was used as Sn^{4+} precursor in concentrations of 0.02 M and 0.013 M for the synthesis of $Nb_{1.66}Sn_{0.34}O_5$ and $V_{0.8}Sn_{0.2}O_2$, respectively.

Nano-sized transition metal oxides were synthesized using a pilot-scale CHFS reactor utilizing a CJM [191]. A stream of cold DI water was pumped (via pump 1 at 400 mL min^{-1}) and heated in flow to well above its critical temperature (heated to 450 °C at 24.1 MPa). In this case, the ambient temperature metal salt precursor and DI water or base were first premixed in flow in a low volume T-piece (0.25" internal diameter) at ambient temperature using pumps 2 and 3, respectively (both at 200 mL min^{-1}). This combined metal salt/base aqueous precursor feed mixture (at 400 mL min^{-1}) entered into the side arms of the CJM, where it rapidly mixed with the inner supercritical water feed, forming a turbulent jet. The reaction slurry had a residence time of ca. 6.5 s after which time it was then cooled in flow.

6.3.2 Experimental Characterization

PXRD patterns of the samples were obtained on a STOE diffractometer using Mo-Kα radiation (λ = 0.70926 Å), over the 2θ range 2 to 35° with a step size of 0.5° and step time of 20 s. PXRD patterns of the vanadium oxides were obtained on a Bruker D4 diffractometer using Cu-Kα radiation (λ = 1.54178 Å) over the 2θ range of 20 to 80° with a step size of 0.05° and a step time of 2 s. XPS measurements were collected using a Thermo Scientific™ K-alpha™$^{+}$ spectrometer using Al-Kα radiation and a 128-channel position sensitive detector. Survey scans were conducted at an energy of 150 eV and high resolution region scans were conducted at 50 eV. The XPS spectra were processed using CasaXPS™ software (version 2.3.16). The binding energy scale was calibrated by a C 1s peak at 285.0 eV. Backgrounds were subtracted using the Shirley routine [264] and peaks were fitted with an appropriate Gaussian/Lorentzian line shape. Relative concentrations of the transition metals within the sample were estimated by measurement of the peak areas of the core lines and application of the appropriate relative sensitivity factors. The size and morphology of the crystallites were determined by transmission electron microscopy (TEM) using a Jeol JEM 2100 – LaB_6 filament. The system was equipped with a Gatan Orius digital camera for digital image capturing. Samples were prepared by briefly ultrasonically dispersing a few mg of the powder in ethanol (>99.5 %, EMPLURA, Darmstadt, Germany) and pipetting drops of the dispersed sample on to a copper film grid (300 mesh – Agar Scientific, Stansted, UK). The average crystallite size was determined by the average of at least 150 crystallites with ImageJ software. EDX analysis was carried out using an Oxford Instruments X-Ma N80-T Silicon Drift Detector fitted to the TEM and processed using AZtec™ software (error can be up to 1 %). BET surface area measurements were carried out using N_2 in a micrometrics ASAP 2420 instrument (titanium based samples) or a micrometrics ASAP 2020 instrument (else). The samples were degassed at 150 °C (12 h) under vacuum before measurements. The error for BET was <0.1 $m^2 g^{-1}$.

6.3.3 Electrochemical Testing

Sn-doped TiO_2: The electrodes had active material mass loadings in the range of ca. 1 to 4 mg cm^{-2}. The organic electrolyte was $LiPF_6$ in 3:7 wt% ethylene carbonate/ethyl methyl carbonate (BASF, Ludwigshafen, Germany). All electrochemical measurements were performed using a 48-channel Arbin Instrument (Caltest Instruments Ltd, Guildford, UK) at room temperature. The electrochemical performance was first investigated by CV in the potential range 0.05 to 3.0 V vs. Li/Li^+ with a scan rate of 0.05 mV s^{-1}. Galvanostatic charge/discharge cycling was followed in the range 1.0 to 3.0 V and also in the range 0.05 to 3.0 V vs. Li/Li^+ at various current rates.

Sn-doped Nb_2O_5 and VO_2: The electrodes had an active material mass loading of 1.7 ±0.2 mg cm^{-2} and 1.0 ±0.2 mg cm^{-2} for $Nb_{1.63}Sn_{0.34}O_5$ and $V_{0.8}Sn_{0.2}O_2$, respectively. The used electrolyte was 1 M $LiPF_6$ in EC/DMC (1:1 v/v, Merck Selectipur LP40, Darmstadt, Germany). C-rate tests and long-term cycling tests were performed using a Maccor battery tester (Model 4200, Maccor Inc., Oklahoma, USA) at room temperature. The specific current rates were set between an applied current of 0.1 to 2.0 A g^{-1} in the potential range 0.05 to 3.0 V vs. Li/Li^+. The electrochemical performance was investigated by CV in the same potential range with a scan rate of 0.1 mV s^{-1} using a galvanostat/potentiostat (PGSTAT302, AUTOLAB, Metrohm, Utrecht, Netherlands).

6.4 Results and Discussion

6.4.1 Characterization Results – Sn-doped TiO_2

The as-prepared undoped nano-TiO_2 sample was collected as white powder with yield >85 % while Sn doping changed the colour to light yellow. PXRD data for all samples suggested anatase TiO_2 (ICSD 9852) as main phase, Figure 84. There were no additional peaks in the PXRD patterns (e.g. such as those for SnO_2 or other impurities). Upon doping, there was a slight shift in peak positions (<0.1 °) towards lower angles, e.g. (004) and (200), which might be explained with the slightly larger ionic radius of doped Sn^{4+} (0.069 nm) compared to Ti^{4+} (0.0606 nm).

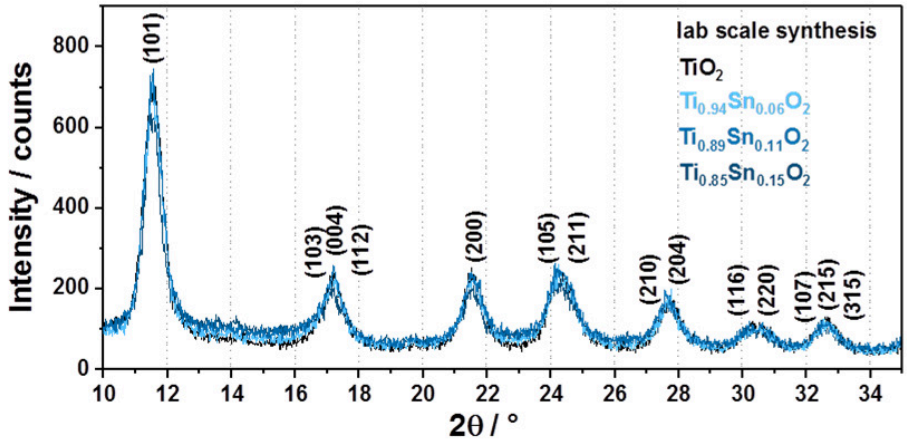

Figure 84: Sn-doped anatase TiO_2 synthesized with a CHFS lab scale reactor: PXRD patterns of undoped anatase TiO_2, $Ti_{0.94}Sn_{0.06}O_2$, $Ti_{0.89}Sn_{0.11}O_2$ and $Ti_{0.85}Sn_{0.15}O_2$.

XPS analysis of the as-prepared $Ti_{0.85}Sn_{0.15}O_2$ sample is presented in Figure 85. The high-resolution spectrum of Ti 2p showed the binding energies for Ti $2p_{3/2}$ at 458.2 and Ti $2p_{1/2}$ at 464.0 eV, which were assigned to Ti^{4+} in the titania [309]. The high-resolution spectrum of Sn 3d showed peaks corresponding to the binding energies of Sn $3d_{5/2}$ at 486.4 and Sn $3d_{3/2}$ at 494.8 eV, which were assigned to Sn^{4+} [310]. For each sample, the ratio of Ti to Sn was investigated with the high-resolution Ti 2p and Sn 3d spectra. The doping content x of Sn in

$Ti_{1-x}Sn_xO_2$ increased with higher tin loading during synthesis: $Ti_{0.94}Sn_{0.06}O_2$ (suggested as 11.5 %), $Ti_{0.89}Sn_{0.11}O_2$ (suggested as 18.8 %), $Ti_{0.85}Sn_{0.15}O_2$ (suggested as high as 26.5 %). These differences are understandable when one considers that XPS is a surface technique and given that these Sn doped phases are metastable forms and possess very high surface areas, it is highly likely that the larger Sn^{4+} cations prefer to be nearer to the surface of these very small crystallites (or simply, the nucleation of anatase TiO_2 is favoured within this synthesis system). EDX measurements suggested Ti:Sn ratios for the samples of 94:6 $Ti_{0.94}Sn_{0.06}O_2$, 89:11 for $Ti_{0.89}Sn_{0.11}O_2$ and 85:15 for $Ti_{0.85}Sn_{0.15}O_2$. Therefore, XPS and EDX measurements suggested successful incorporation of Sn^{4+} into the nano-particles, with the actual Sn at% increasing as the concentration of the Sn precursor was increased during the synthesis.

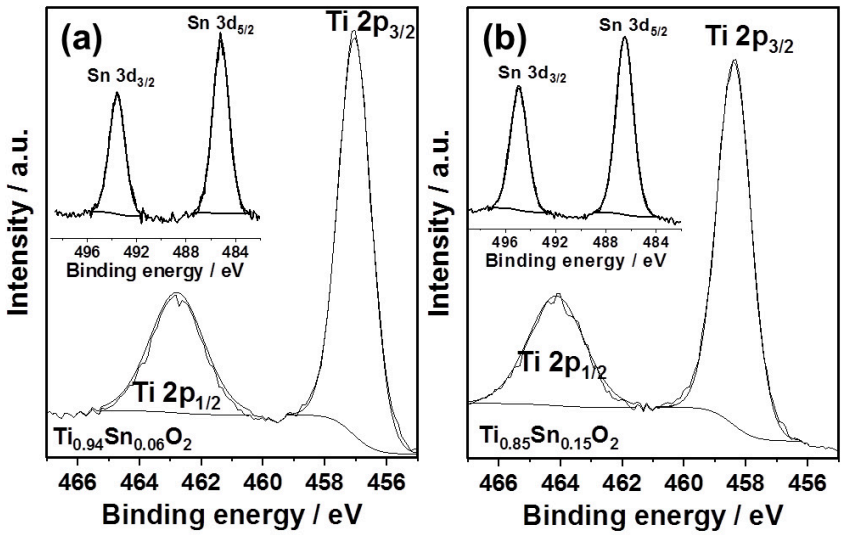

Figure 85: XPS spectra for the (a) $Ti_{0.96}Sn_{0.04}O_2$ and (b) $Ti_{0.85}Sn_{0.15}O_2$ samples with high-resolution Ti 2p and Sn 3d spectra.

In Figure 86, the obtained TEM images are presented. The average crystallite size (sampled from the size of 150 crystals) increased with higher Sn doping, from ca. 4.0 nm for the pure TiO_2 to ca. 5.4 nm for $Ti_{0.85}Sn_{0.15}O_2$. Another indication for the substitution of Ti^{4+} atoms by the dopant

in the crystal structure is a slight increase of the d-spacing of 0.345 nm (TiO_2), 0.347 nm ($Ti_{0.94}Sn_{0.06}O_2$), 0.349 nm ($Ti_{0.89}Sn_{0.11}O_2$) and 0.353 nm ($Ti_{0.85}Sn_{0.15}O_2$), which was consistent with the (101) planes of a tetragonal-phase anatase (please note the systematic error around ±0.03 nm). The BET surface areas of the samples decreased with higher Sn doping content [TiO_2 (245 $m^2 g^{-1}$), $Ti_{0.94}Sn_{0.06}O_2$ (230 $m^2 g^{-1}$), $Ti_{0.89}Sn_{0.11}O_2$ (208 $m^2 g^{-1}$), and $Ti_{0.85}Sn_{0.15}O_2$ (178 $m^2 g^{-1}$)] corresponding to the increase of the average crystallite size with more Sn, which was confirmed via TEM images.

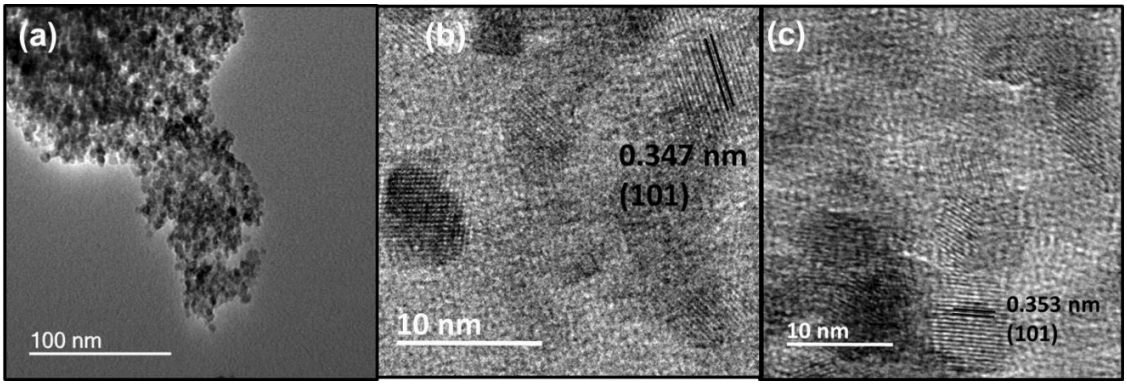

Figure 86: TEM images of undoped anatase TiO_2 (a), $Ti_{0.89}Sn_{0.11}O_2$ (b) and $Ti_{0.85}Sn_{0.15}O_2$ (c).

6.4.2 Characterization Results – Sn-doped Nb_2O_5 (pilot plant synthesis)

Undoped Nb_2O_5 and $Nb_{1.66}Sn_{0.34}O_5$ (yield >90 %, production rate ca. 130 g h^{-1}) were collected as free flowing powders after freeze drying and directly used for further investigation. The doped niobia powder was slightly yellow. Each material was investigated via PXRD, Figure 87. No evidence of a separate phase such as SnO_2 phase was detected in the patterns for the as-prepared nano-powder. The PXRD data reflections were very broad, which indicated a small sized, semi-crystalline material, as seen before in chapter 3.

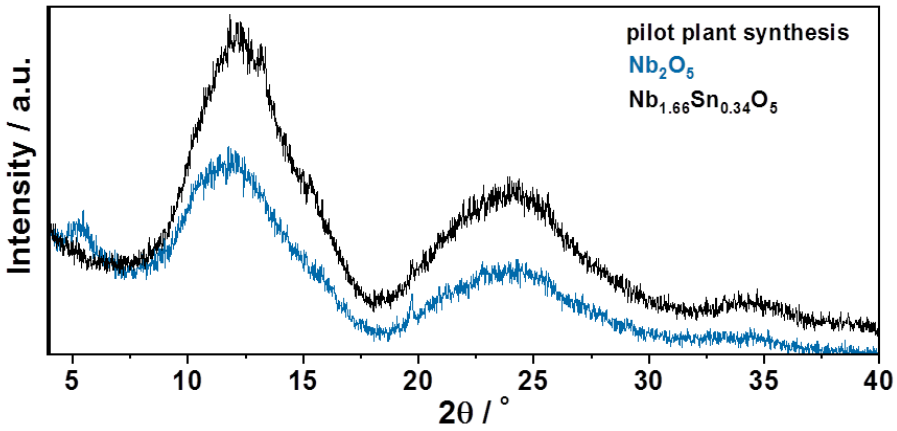

Figure 87: Materials characterization of $Nb_{1.66}Sn_{0.34}O_5$ synthesized with the pilot plant CHFS. PXRD (Mo-source) data patterns.

EDX measurement analysis of the sample suggested a homogenous distribution of the Sn in the sample and suggested a Sn:Nb atomic ratio of 17:83, which was slightly higher compared to the results on the surface of the material obtained by XPS (15.7:84.3). XPS measurements (Figure 88) showed only Nb^{5+} and Sn^{4+} as oxidation states since each spectrum showed a typical two-peak structure (2d5/2, 2d3/2 for Sn; 3d5/2, 3d3/2 for Nb) due to the spin–orbit splitting.

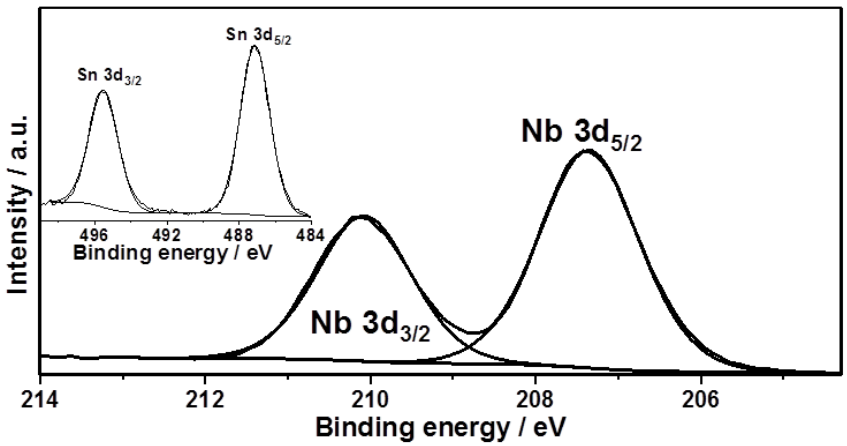

Figure 88: XPS spectra in the tin 3d and niobium 3d region.

The particle morphology for $Nb_{1.66}Sn_{0.34}O_5$ predominantly consisted of nano-particles with a defective "spherical" morphology of ca. 15 nm in size, Figure 89a. According to HRTEM images, there were no detectable interlayer d-spacings, which were attributed to the highly defective structure (Figure 89b). The BET surface area was 183 $m^2 g^{-1}$ for undoped Nb_2O_5 and 167 $m^2 g^{-1}$ for $Nb_{1.66}Sn_{0.34}O_5$.

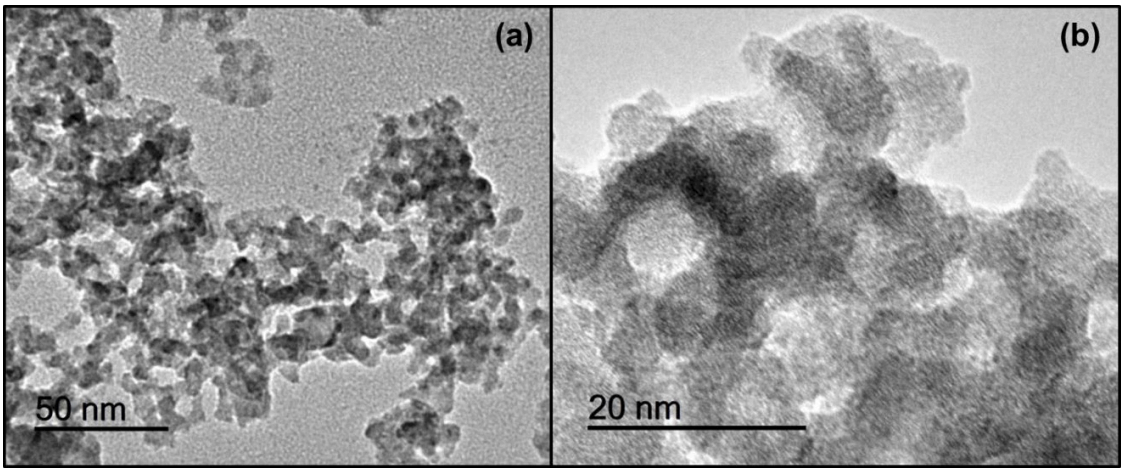

Figure 89: (a) TEM image of $Nb_{1.66}Sn_{0.34}O_5$ and (b) HRTEM images showing no interlayer spacing.

6.4.3 Characterization Results – Sn-doped VO_2 (pilot plant synthesis)

$V_{0.8}Sn_{0.2}O_2$ and undoped VO_2 (each non-optimised yield >56 %, production rate ca. 65 g h^{-1}) were collected as free flowing powders after freeze drying and directly used for further investigations. The doped vanadia powder was dark blue in colour. The yield was low for the doped and undoped vanadium dioxide synthesis as it was not optimized in this first attempt and can be increased in the future by the use of an appropriate base or an alternative precursor that is less soluble [191].

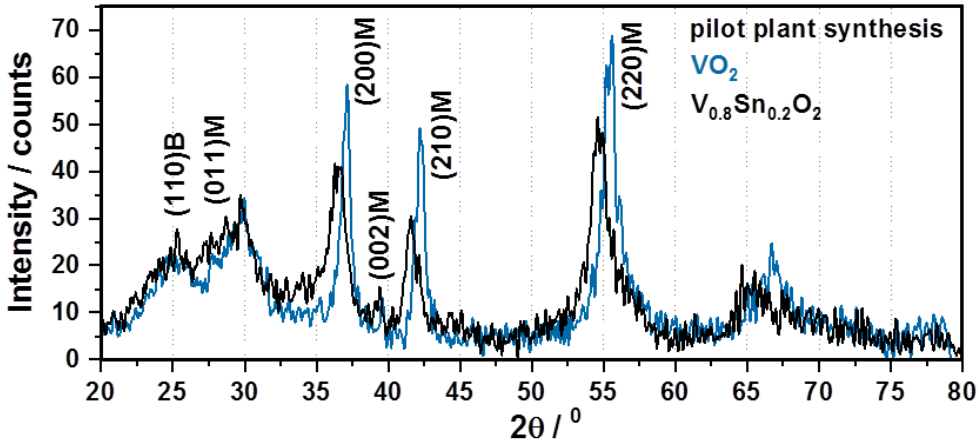

Figure 90: Materials characterization of $V_{0.8}Sn_{0.2}O_2$ synthesized with the pilot plant CHFS. PXRD (Cu-source) data patterns (for comparison, undoped VO_2 synthesized with the pilot plant is also plotted).

Both materials were investigated via PXRD, Figure 90. No evidence of a separate phase such as SnO_2 phase was detected in the patterns of sample $V_{0.8}Sn_{0.2}O_2$. There was no indication of any V_2O_5 phase; however, the patterns were very broad and suggested a mixture of monoclinic VO_2(M) and metastable VO_2(B) phase. Within this study, a higher mixing temperature was used compared to the previous study (chapter 3) on the synthesis of VO_2 (335 vs. 305 °C). Thus, the sample appeared to contain relatively less of the metastable low temperature VO_2(B) phase [247].

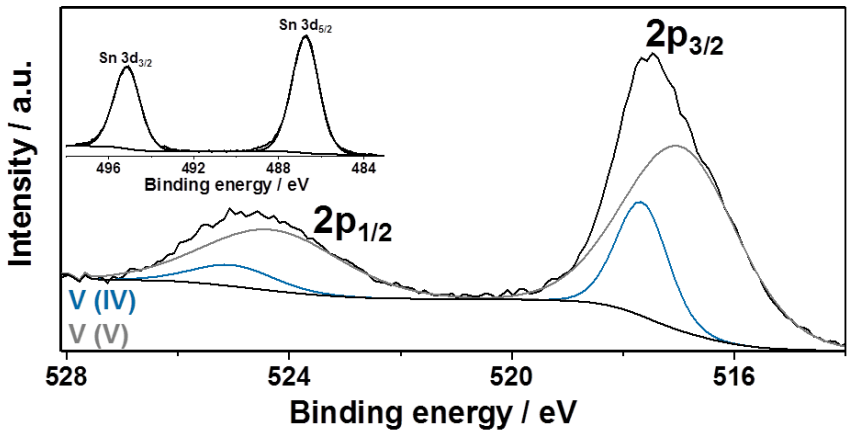

Figure 91: XPS spectra of the tin 3d and vanadium 2p region for sample $V_{0.8}Sn_{0.2}O_2$.

The XPS data suggested the surface of the sample was composed of Sn^{4+}, V^{4+} and some V^{5+} in an atomic ratio of 20:61:18, respectively (Figure 91). As there was no detectable impurity phase in the PXRD data, it was concluded that surface oxidation had occurred [230].

For $V_{0.8}Sn_{0.2}O_2$, the particle morphology predominantly consisted of a mixture of defective spherical particles as well as thin sheets with lengths less than 1 µm, see SEM imaging in Figure 92c. EDX measurements on the surfaces of either the sheets or the defective spheres, suggested a Sn:V atomic ratio of 20.5:79.5, which was consistent with the results obtained by XPS investigations.

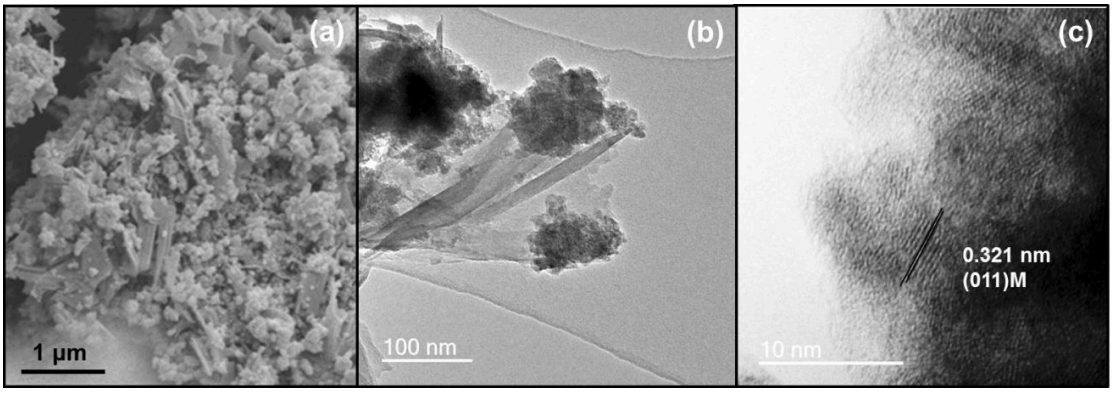

Figure 92: Materials characterization of $V_{0.8}Sn_{0.2}O_2$ synthesized with the pilot plant CHFS. (a) SEM image, (b) TEM image of the particles and (c) HRTEM images showing the interlayer spacing for the doped VO_2 sample.

SEM and TEM images revealed also mixed particle morphologies of defective spherical particles as well as thin sheets (Figure 92a,b). HRTEM measurements gave detected interlayer spacing of 0.321±0.03 nm that might correspond to the (011) plane of VO_2(M), Figure 92c. The BET surface area was 22 $m^2 g^{-1}$ for undoped VO_2 and 24 $m^2 g^{-1}$ for $V_{0.8}Sn_{0.2}O_2$.

6.4.4 Electrochemical performance - Sn-doped TiO_2

CVs at a scan rate of 0.05 mV s^{-1} in the range of 0.05 to 3.0 V vs. Li/Li^+, are presented in Figure 93. A pair of cathodic and anodic peaks were observed in the potential range 1.5 and 2.3 V vs. Li/Li^+, relating to lithium-ion insertion into and extraction from the interstitial octahedral site of anatase TiO_2. For sample $Ti_{0.85}Sn_{0.15}O_2$ (Figure 93a), there was also an additional broad oxidation peak at 0.5 V vs. Li/Li^+. Comparison of all samples in the potential range 0.05 to 3.0 V vs. Li/Li^+ showed an increasing lithiation activity at low potentials and delithiation activity at 0.5 V vs. Li/Li^+ with higher Sn at%. This was due to the electrochemical activation of the Sn dopant resulting in additional activity due to the alloying reaction towards Li_xSn. Thus, after the first cycle, it was suggested that these doped materials might form a nano-composite of Sn and TiO_2 in the electrode matrix. This might allow buffering of the volume expansion resulting from the alloying reaction (largely active below 1.0 V vs. Li/Li^+) with the less expansive TiO_2 (active in the range of ca. 1.0-3.0 V vs. Li/Li^+).

As the surface area decreased with higher Sn-loading, the initial capacity loss due to the SEI formation may be expected to decrease. The general trend herein showed that with higher Sn-loading, the initial irreversible capacity loss from CV tests increased (from 363 mAh g^{-1} for the pure TiO_2 to 467 mAh g^{-1} for $Ti_{0.85}Sn_{0.15}O_2$). This was another indication of the electrochemical activation of Sn-dopants towards additional alloying reactions, as these alloying processes are known to undergo high irreversible capacity losses during the first cycle. Therefore, cycling in a wider potential range towards 0.05 V vs. Li/Li^+ most likely favoured the formation of Li_xSn alloy (where $0<x\leq4.4$), see [311, 312].

Overall, it could be suggested that the elemental Sn behaved like a separate Sn alloying material phase during subsequent cycling.

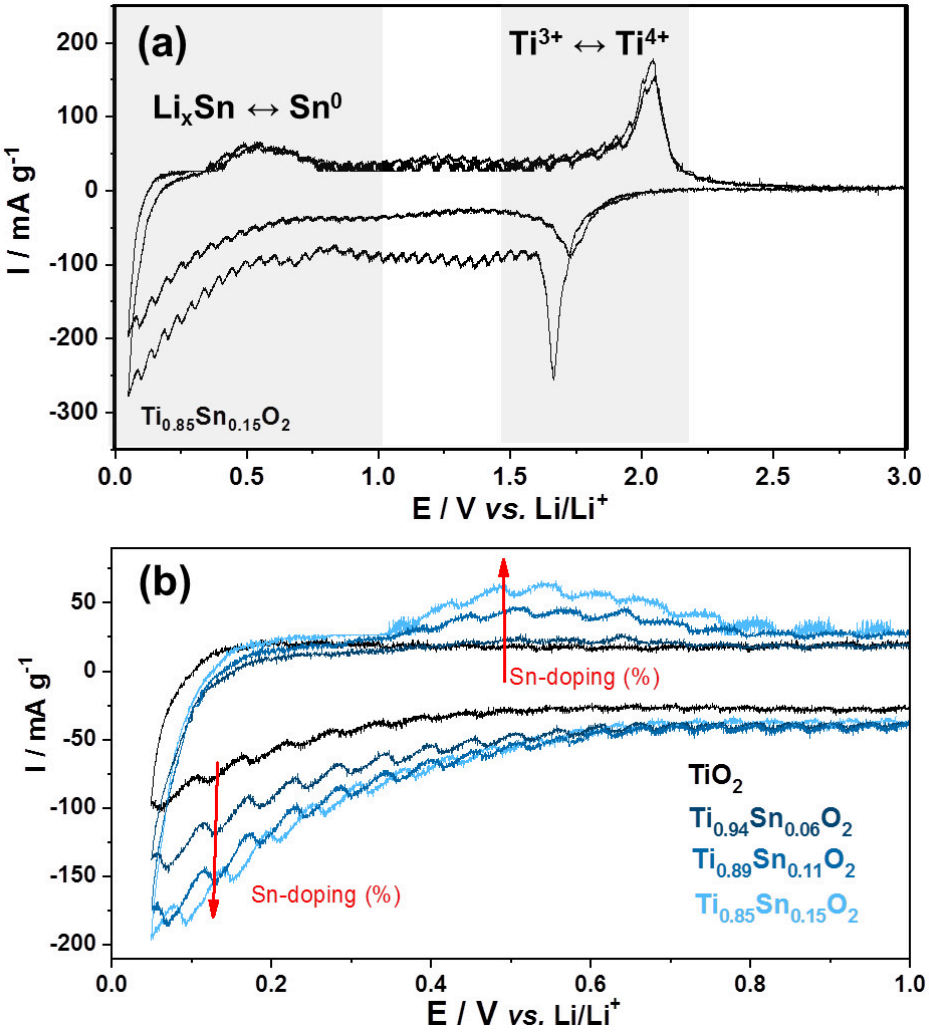

Figure 93: (a) CV for the as-prepared nano-powder in the potential range of 0.05 and 3.0 V vs. Li/Li^+ at an applied scan rate of 0.05 mV s^{-1} for $Ti_{0.85}Sn_{0.15}O_2$. (b) CVs of the 2nd cycle for all materials showing an increase of the de-/alloying peak with higher Sn loading.

For initial comparison, the influence of Sn-doping on the electrochemical performance was investigated via a C-rate tests in the range 1.0 to 3.0 V vs. Li/Li^+ (Figure 94). The results showed that with increasing Sn-doping (and therefore, with less amount of redox-active TiO_2), the overall specific capacity decreased as might be expected. Considering the decrease in surface area and increase of crystallite size, the C-rate retention did not benefit from Sn-doping because a larger crystallite size could be expected to decrease the ionic diffusion (conductivity), and limit

the material as a high power negative electrode, as shown be Wang et al. [24]. At 1.5 A g^{-1}, the obtained capacities were 140, 88, 64 and 56 mAh g^{-1} for undoped anatase TiO_2, $Ti_{0.94}Sn_{0.06}O_2$, $Ti_{0.89}Sn_{0.11}O_2$ and $Ti_{0.85}Sn_{0.15}O_2$, respectively.

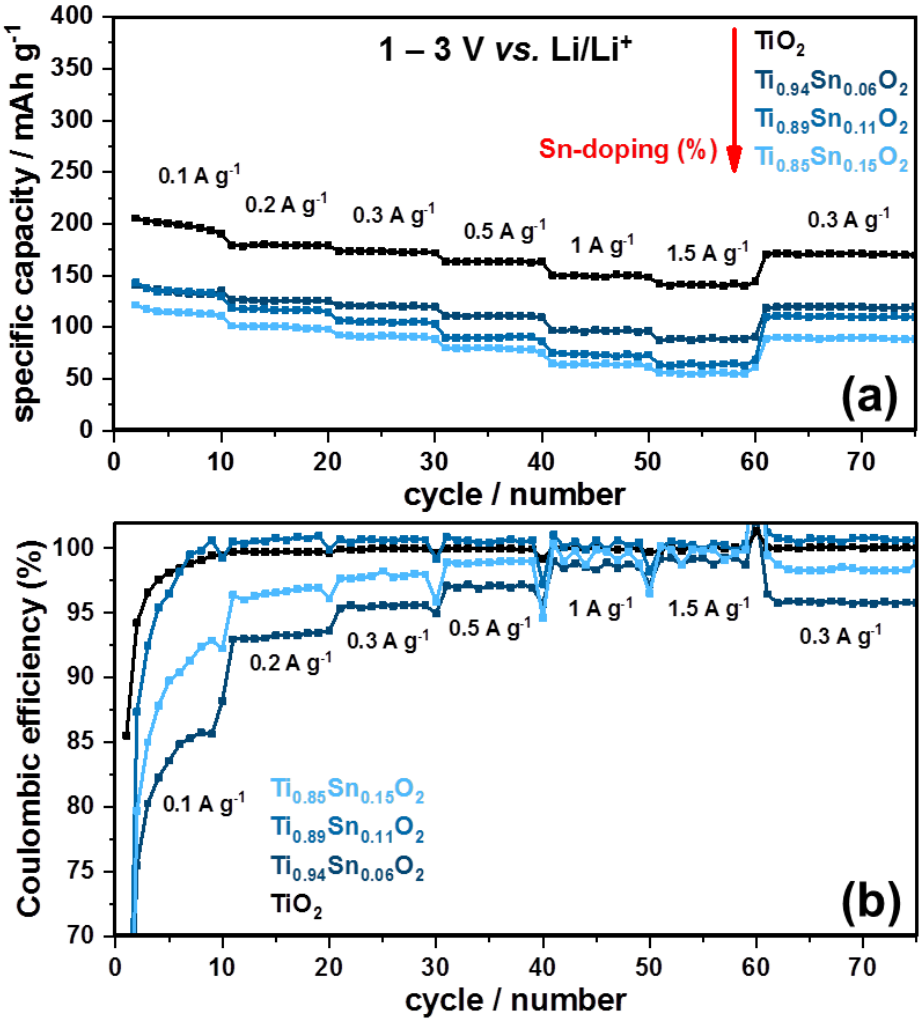

Figure 94: (a) Plots of specific capacity versus cycle number for variable current rate tests of all samples in the potential range 1.0 to 3.0 V vs. Li/Li^+ with (b) corresponding Coulombic efficiency.

After the initial C-rate tests in the range 1.0 to 3.0 V vs. Li/Li^+, the potential window was expanded to 0.05 V vs. Li/Li^+. The main benefit from this was in the electrochemical activation

of the Sn doped in the anatase, which thereafter is expected to form a separate phase after the initial activation (as seen in Figure 93). For C-rate tests with wider potential window (Figure 95), greater Sn-doping increased the specific capacity. At an applied current of 100 mA g^{-1}, the $Ti_{0.85}Sn_{0.15}O_2$ sample showed a steady capacity loss with an average capacity of ca. 350 mAh g^{-1}, whereas undoped TiO_2 showed only a capacity of ca. 240 mAh g^{-1}.

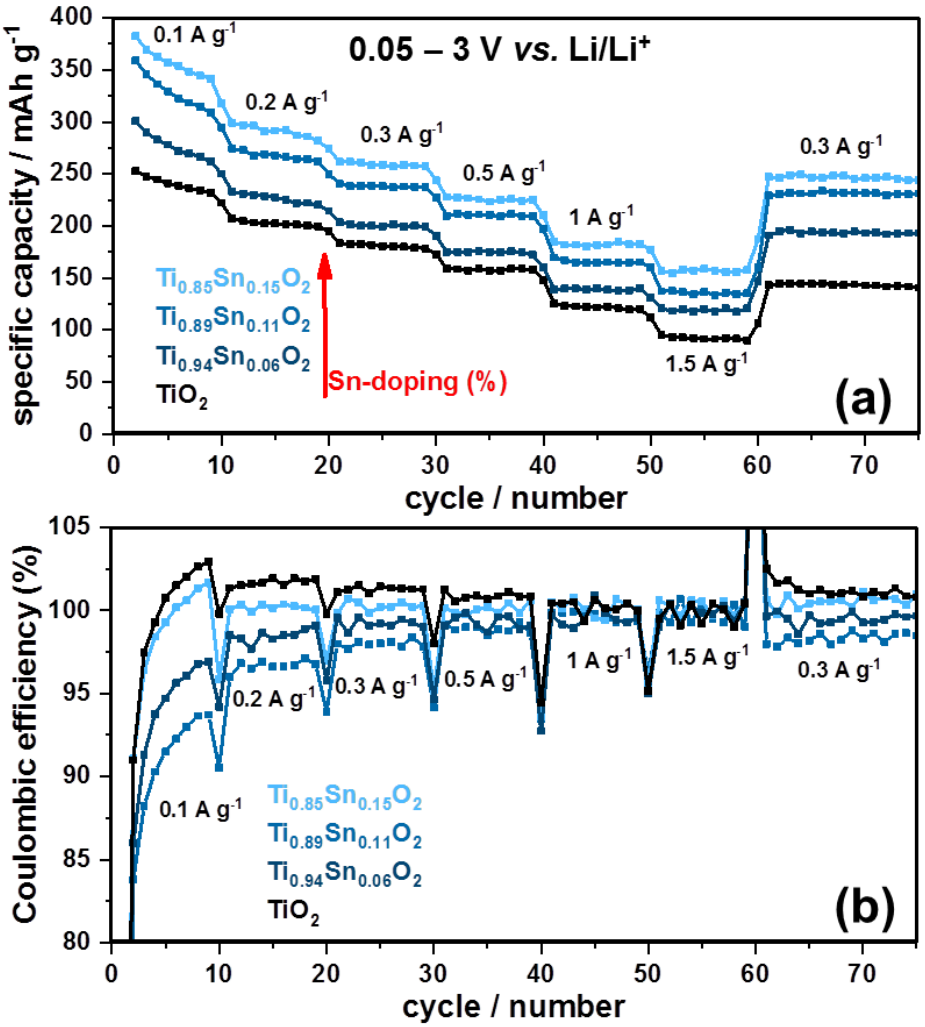

Figure 95: (a) Plots of specific capacity versus cycle number. Variable current rate tests of all samples in the potential range 0.05 to 3 V vs. Li/Li^+ with (b) corresponding Coulombic efficiency.

A potential versus capacity plot for cycling tests at low currents is presented in Figure 96. In the potential range 1.0 to 3.0 V vs. Li/Li^+, the Sn-dopant remained electrochemically inactive and

did not appear to contribute to the stored charge of the electrode material. Therefore, with increasing Sn content within the sample, the obtained specific capacity of the titanate decreased (Figure 96a). When the potential window was widened to the range 0.05 to 3.0 V vs. Li/Li^+, the Sn dopant drastically improved the electrochemical capacity through additional charge storage at lower potentials (Figure 96b).

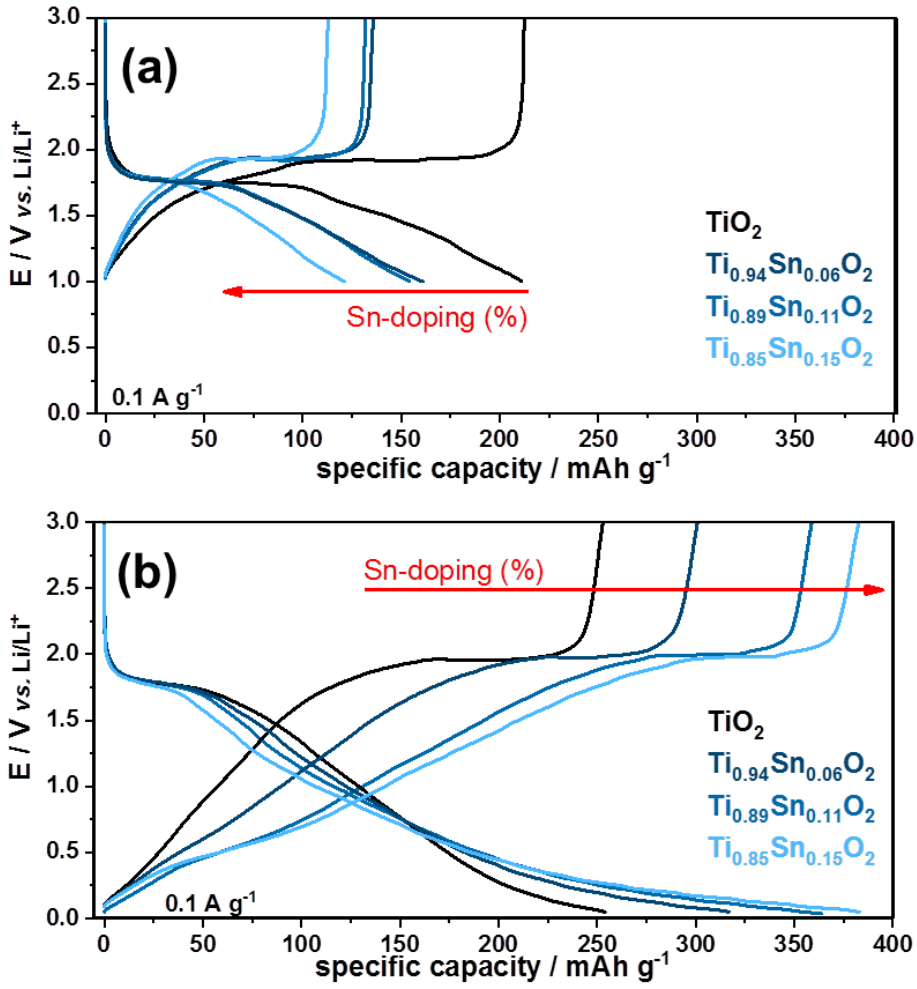

Figure 96: Potential versus specific capacity plots (third cycle of the C-rate test) for nano-TiO_2 and the Sn-doped titania at a constant applied current of 100 mA g^{-1}. (a) in the potential range of 1.0 to 3.0 V vs. Li/Li^+ and (b) in the potential range of 0.05 to 3.0 V vs. Li/Li^+.

The effect of electrochemically active Sn-dopants in TiO_2 was also investigated previously. Wang et al. investigated mesoporous Sn-doped TiO_2 thin films as negative electrode materials. They showed that 6 at% Sn could be doped into the TiO_2 and although the Sn was doped in the structure, the Sn remained active in the same potential ranges (1.0 to 0.05 V vs. Li/Li^+ for lithiation and 0.5 V vs. Li/Li^+ for delithiation), which also contributed to a higher irreversible capacity loss during the first cycle and higher capacities during cycling, e.g. compared to the pure TiO_2 (101 mAh g^{-1}) the doped material exhibited a capacity of 253 mAh g^{-1} at an applied current of 85 mA g^{-1} [313]. The same behaviour was shown for literature reports on tin titanate nano-tubes where a synergistic effect of combining the advantages of "TiO_2" in terms of cycle life and "SnO_2" in terms of specific capacity was observed [314]. For a 27 at% Sn-doped TiO_2, a specific capacity of 240 mAh g^{-1} was obtained over 300 cycles (compared to 168 mAh g^{-1} of the pure TiO_2) at an applied current of 250 mA g^{-1} [314]. Both reports included CV measurements, which showed high current peaks at low potentials (0 to 0.5 V vs. Li/Li^+), which was due to the formation of Li_xSn, and a characteristic peak at 0.5 V vs. Li/Li^+ for the delithiation of the alloy. Therefore, it was suggested that during the first reduction cycle (at low potential) the Sn^{4+} in the anatase structure was reduced to a separate phase of elemental tin (Sn^0) with Li_2O being irreversibly formed (as suggested in a report by Wang et al. [315] and which could be a reason for the higher irreversible capacity loss). At lower potentials, this Sn^0 was then lithiated in the range 1.0 to 0.05 V vs. Li/Li^+.

Pure SnO_2 is very unstable when used as negative electrode material for LiBs and its specific capacity decays quite soon during cycling. Herein, more than 75 cycles were performed with nearly no decay. Thus, increased capacity with simultaneous good cycle life was reached through using these combined insertion and alloying materials. In the next sections, it is investigated, whether this behaviour also applies to other nano-sized insertion materials.

6.4.5 Electrochemical performance - Sn-doped Nb_2O_5

Figure 97 shows the CV data for undoped and Sn-doped Nb_2O_5; where an irreversible minor peak was observed at ca. 0.6 V vs. Li/Li^+ for both materials, which was due to the reaction of the electrolyte with the carbon additive in the electrode (SEI formation), see chapter 3.4.6 [147, 245]. For the $Nb_{1.66}Sn_{0.34}O_5$, the electrochemical activity of the active material, was extended beyond the typical range for the redox couple of $Nb^{5+} \leftrightarrow Nb^{3+}$ and the CV profile did not show clear insertion peaks at well-defined potentials vs. Li/Li^+, which was consistent with the previous results for negative electrode nano-materials with high surface area, see chapter 3.

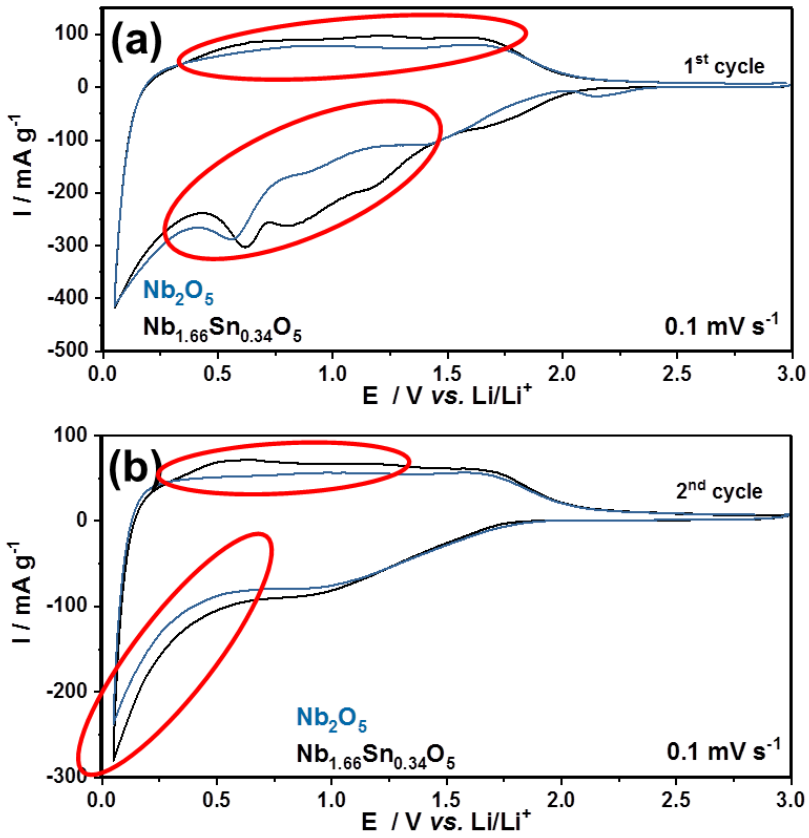

Figure 97: CVs at 0.1 mV s^{-1} of doped and undoped Nb_2O_5 synthesized with the pilot plant showing the first (a) and second (b) cycle. The red circles highlight the redox activity regions of interest.

In Figure 97a, the first cycle is presented where an increased redox-activity was observed for the doped sample in the range 1.2 to 0.7 V vs. Li/Li^+ during lithiation and in the range 0.4 to 1.7 V vs. Li/Li^+ during delithiation, which each presumably corresponded to the initial conversion reation of Sn^{4+} to Sn^0 and dealloying reaction of the Li_xSn, respectively. Since the undoped Nb_2O_5 showed a higher BET surface area compared to the doped sample (183 $m^2 g^{-1}$ for undoped Nb_2O_5 and 167 $m^2 g^{-1}$ for $Nb_{1.66}Sn_{0.34}O_5$), the initial alloying reaction might not have resulted in an clear increase in current at low potentials. The undoped Nb_2O_5 had a higher surface area compared to the doped counterpart and therefore, higher SEI formation and irreversible lithium-ion losses on defective sites were expected. The second cycle gave already a clearer view on the redox-activity. The doped sample showed increased redox-activity in the potential region of the de-/alloying reaction of the dopant. Thus, it could be shown, that also for Nb_2O_5, the Sn-dopant could be electrochemically activated at low potentials (Figure 97b).

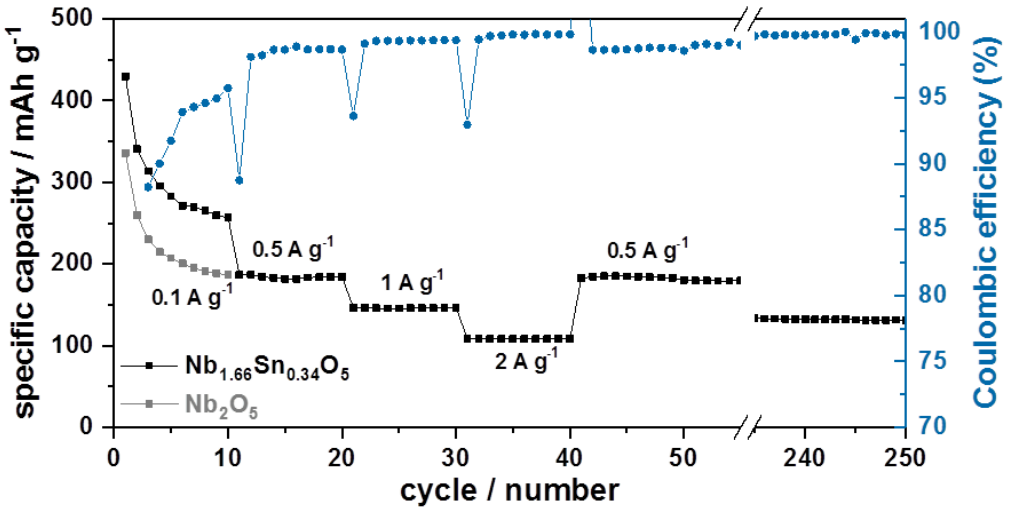

Figure 98: Plot of specific capacity (left y-axis) and Coulombic efficiency (right y-axis) versus cycle number. Variable current rate tests for Nb_2O_5 and $Nb_{1.66}Sn_{0.34}O_5$ (each synthesized using the CHFS pilot plant) in the potential range 0.05 to 3.0 V vs. Li/Li^+.

Undoped Nb_2O_5 had a specific capacity of 191 mAhg^{-1} and $Nb_{1.66}Sn_{0.34}O_2$ was 272 mAh g^{-1} (at 0.1 A g^{-1}). The specific capacities of $Nb_{1.66}Sn_{0.34}O_5$ at different current rates were 181 mAh g^{-1} at 0.5 A g^{-1}, and 110 mAh g^{-1} at 2 A g^{-1}, Figure 98. The Coulombic efficiency was <95 % at 0.1 A g^{-1}, >98.5 % at 0.5 A g^{-1} and >99.4 % at higher current rates. The capacity remained quite stable during the following cycles at 0.5 A g^{-1} with a capacity retention of 86 % (from 178 to 154 mAh g^{-1}). The cycle stability was slightly less than that reported in the previous study for Nb_2O_5 where a retention of 98.6 % was observed after 800 cycles at the same current rate [188]. The decreased stability might be also due to the effects of alloying of Sn component in the materials, which can lead to significant local structural and volume changes that affect microstructure, giving deleterious effects on capacity retention.

6.4.6 Electrochemical performance - Sn-doped VO_2

For the $V_{0.8}Sn_{0.2}O_2$ electrode material testing in half cells, the CV profile was not very well defined at each potential, which was likely to be due to the material being mixed phase VO_2 [247]. In the potential range of 2.0 to 3.0 V vs. Li/Li$^+$, there were two reversible minor peaks, which could be attributed to lithium-ion insertion into VO_2 [316, 317], but overall, as for the niobium oxide based materials, the charge storage could be largely defined as being "pseudocapacitive with some insertion" [188, 247], Figure 99. Pure VO_2 synthesized with the CHFS pilot plant showed a virtual identical CV profile as the analogous material synthesized with the lab scale reactor, chapter 3.4.4.

In comparison to the undoped VO_2, the CV of the Sn-doped VO_2 material showed a delithiation peak at 0.55 V vs. Li/Li$^+$ (tentatively assigned to the dealloying reaction), Figure 99b. There was an important difference in the CV for $V_{0.8}Sn_{0.2}O_2$, which was not seen for the other two doped

materials (TiO_2 and Nb_2O_5) or the undoped VO_2; which was an additional delithiation peak at 1.18 V vs. Li/Li^+. This peak at 1.18 V vs. Li/Li^+ may relate to the back reaction towards $Sn^{2+/4+}$ and would be comparable to the CV peak of highly dispersed SnO_2 in a very conductive electrode network, as reported recently by Shen et al. [99], Srinivasan et al. [318] and Liang et al. [94]. Though, more evidence is needed in future to fully confirm this suggestion for the $V_{0.8}Sn_{0.2}O_2$ sample. This peak remained stable after five cycles of testing, showing a stable additional capacity win (Figure 99b).

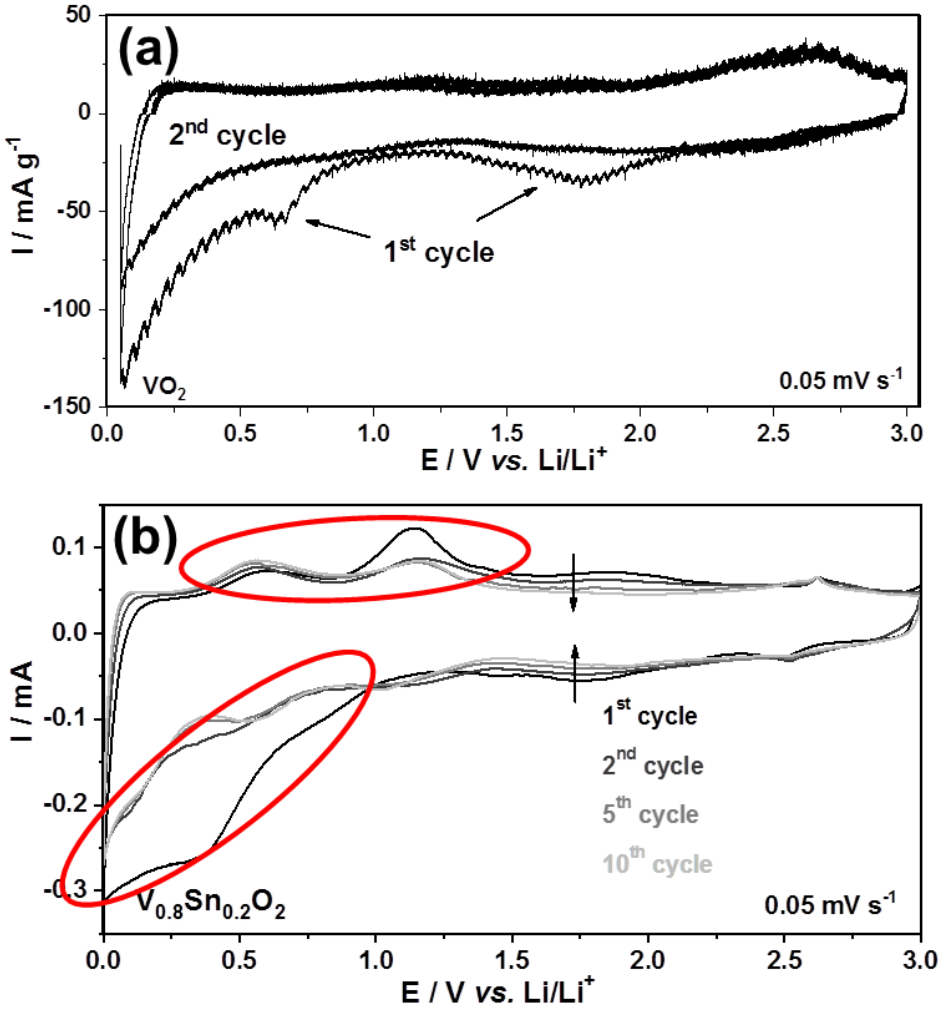

Figure 99: CVs at 0.05 mV s^{-1} of (a) VO_2 (data obtained with an ARBIN battery tester) and (b) $V_{0.8}Sn_{0.2}O_2$. The red marks highlight the redox activity differences.

The C-rate test for $V_{0.8}Sn_{0.2}O_2$ is presented in Figure 100, with obtained capacities of 673 mAh g^{-1} at 0.1 A g^{-1}, 607 mAh g^{-1} at 0.5 A g^{-1} and 515 mAh g^{-1} at 2 A g^{-1}. These were far higher than undoped VO_2, which had a specific capacity of 255 mAh g^{-1} at 0.1 A g^{-1}. The Coulombic efficiency was <97 % (after 4 cycles) at 0.1 A g^{-1} and >99.5 % at higher currents. The capacity remained relatively unstable during the subsequent 100 cycles at 0.5 A g^{-1}, with capacity retention of 71 %, going from 608 to 432 mAh g^{-1}.

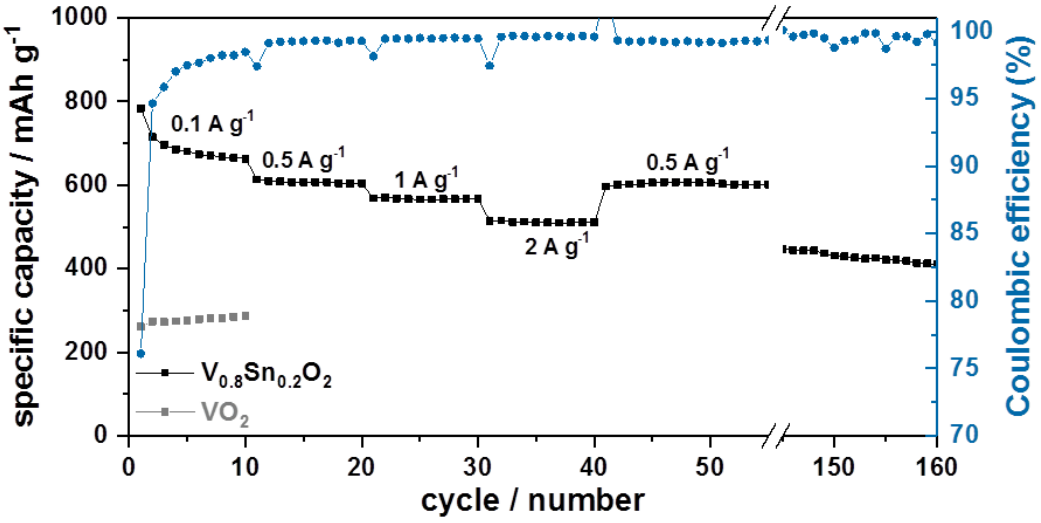

Figure 100: Plot of specific capacity (left y-axis) and Coulombic efficiency (right y-axis) versus cycle number. Variable current rate tests for VO_2 and $V_{0.8}Sn_{0.2}O_2$ (each synthesized with the pilot plant) in the potential range 0.05 to 3.0 V vs. Li/Li^+.

Considering that the Sn-atoms in the VO_2-based materials remained electrochemically active during cycling, the limited cycle stability might be due to significant contributions from alloying of the Sn component in the materials, which can lead to significant local volume changes that affect microstructure (giving deleterious effects on capacity retention) and that normally give huge capacity decay during cycling [319, 320]. Overall, it could be concluded that the use of Sn-atoms in nano-sized insertion transition metal oxides, can increase the specific capacity because of the electrochemical activity of the Sn^{4+}, and that V^{4+}-based materials might show a (partial) back reaction towards SnO_x. VO_2 is an excellent electronic conductor and a good matrix element for alloying based materials that has been noted in previous reports by Reddy et al. [321-323]. The electronic properties of VO_2 might have benefitted increased electron transport, which is one driving force for the conversion reaction [324, 325].

The question remains, why the doped vanadate showed such a higher capacity compared to the undoped counterpart, namely 422 mAh g^{-1}. The theoretical additional capacity for $V_{0.8}Sn_{0.2}O_2$ arising from alloying and conversion reactions is 299 mAh g^{-1} (= 1493 mAh g^{-1} x 0.2). Thus, the Sn^{4+} atoms in the $V_{0.8}Sn_{0.2}O_2$ sample might undergo a back reaction of the conversion reaction. In any case, the value of 422 mAh g^{-1} is higher than 299 mAh g^{-1}; therefore, the additional charge storage might also arise from other mechanisms, e.g. reactive Li_2O/LiOH/LiH layers, which were most likely formed during the first lithiation [111, 112, 326]. Another reason for the increase in capacity may be due to the ability of the nano-sized materials to accommodate more lithium-ions in surface or defect sites (this could happen as soon the Sn^{4+} forms the secondary phase and separates from the host lattice after the first cycle). Large increases in surface area can benefit lithium-ion storage [327, 328], e.g. as shown in this section, where undoped VO_2 (22 m^2 g^{-1}) showed a specific capacity of 255 mAh g^{-1}, whereas higher surface area undoped VO_2 (87 m^2 g^{-1}) showed a specific capacity of 350 mAh g^{-1} (each tested at 100 mA g^{-1}, chapter 3.4.3). Therefore, the overall charge storage mechanism, in particular for sample $V_{0.8}Sn_{0.2}O_2$, is quite complex and would warrant further detailed in-situ or post-cycling investigation in the future.

Thus, Sn-doped nanosized VO_2 was the third example showing increased specific capacity due to the electrochemical activation of the Sn-dopant.

6.5 Overall Discussion and Outlook

Initially it was observed, that incorporation of Sn into nano-sized TiO_2, increases the specific capacity with increasing Sn loading due to an electrochemical activation of the Sn dopant at lower potentials vs. Li/Li^+. This led to the question whether this might be generally true for nano-sized transition metal oxides. The tests showed that the incorporation of Sn into various insertion nano-materials (differing in their transition metal oxidation state) can increase the specific capacity due to additional alloying reactions (Figure 101).

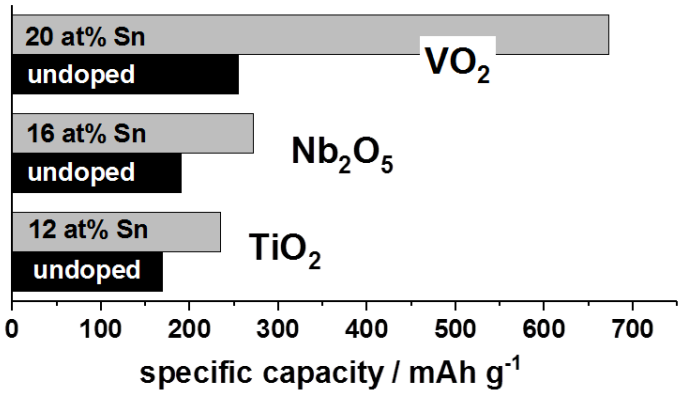

Figure 101: Specific capacities for various nano-sized insertion materials when they are undoped and Sn-doped. The capacity data for TiO_2 is taken from [329]. All materials were synthesized with the pilot plant with production rates of >65 g h^{-1}.

The low Coulombic efficiencies for $Ti_{0.85}Sn_{0.15}O_2$, $Nb_{1.66}Sn_{0.34}O_5$ and $V_{0.8}Sn_{0.2}O_2$ at low rates were similar to the results from chapter 3 and could be expected, because a stable SEI for high surface area transition metal oxides is questionable and was also observed before [188, 246, 247], see also [82, 83]. Electrolyte additives [248, 249] or even carbon coating for an effective electrolyte shielding might help improve this further in the future.

Considering, that these materials can be made easily under scaled-up conditions in a single step, the results show a huge advantage compared to conventional Sn-based materials which require

often several synthesis steps. The driving force for this electrochemical behaviour remains unclear and extensive studies would be needed to understand the Sn-activation (DFT calculations might help here). Another open question is the additional capacity in the vanadium oxide sample. The vanadate system is very complex which asks for in-situ investigations in future. Such investigations might include in-situ XPS for the exact redox activity at various potentials.

In general, an ideal system might be the doping of Sn into thin nano-sheet insertion materials, so that the Sn can break out of the sheet, forming a secondary phase. Thus, the volume expansions during lithiation might be best buffered through these remaining sheets (Figure 102).

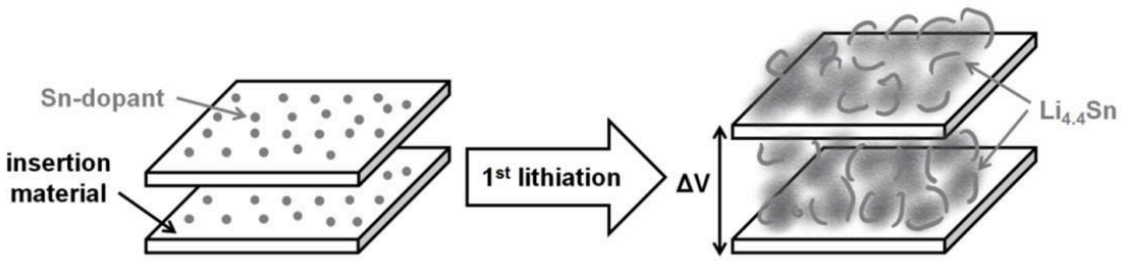

Figure 102: Proposed scheme for ideal Sn-doped insertion materials.

There are other possible ways in which Sn-based materials could be mixed with other carbons or transition metal oxides, which may offer different results, e.g. core/shell [330], carbon/alloying [110, 331], hollow nano-spheres [332], and many more [308]. The benefit of the approach used herein, is in the scalability and ease of the synthesis process in a single step. Furthermore, these initial results are promising because they describe a material capable of combined insertion and alloying charge storage processes that has high stability compared to alloying materials and high capacities compared to insertion materials.

7. Conclusions and Future Directions

All materials were made with a single step synthesis using a CHFS reactor and no further processing was applied. This shows a huge advantage compared to many other synthesis methods, which often use several synthesis steps. Overall, there were four main findings within this thesis:

In chapter 3, it could be concluded that nano-sizing insertion materials can drastically change the charge storage properties. This might be a reason for a widened operational potential window when these negative electrode materials are cycled down to 0.05 V vs. Li/Li^+. It is notable that different classes of materials showed the same effect. Namely, Nb_2O_5, layered titanate and VO_2 each showed a drastic shift towards oxide supercapacitor-like behaviour even at lower current rates. Similarities of these materials included a high BET surface area and also quite low crystallinity. These materials might be an excellent choice for hybrid devices in future, where a negative pseudocapacitive battery material electrode is combined with an EDLC carbon electrode for maximum power and compromised energy density. This study also shows that the focus on crystalline materials for insertion electrode applications in alkali-ion batteries might be expanded to defective structures. Such defects may promote high power performance and also show differing charge storage behaviours. DFT studies on the influence of crystallinity for various insertion materials (like herein Nb_2O_5, layered titanate and VO_2) might help to understand the impact of defects on the charge storage behaviour towards high power and high energy performances in future. Clearly, there is still much room for understanding the role of such high surface area insertion materials for use in hybrid devices.

Chapter 4 gave an easy and impressive example, how the high power performance of anatase TiO_2 can be improved. High loadings of 25 at% Nb^{5+} could be successfully incorporated into the

anatase TiO_2, which was shown by a peak shift in the PXRD and further XPS and EDX analyses. Incorporation of niobium was beneficial for high rate retentions which were shown to be due to kinetic improvements, higher electronic conductivity and higher charge storage via surface effects. In future, 10 at% Nb-doped TiO_2 should be synthesized or even a single phase titanium niobium oxide (like $TiNb_2O_7$), as each were shown to give excellent high power performances for alkali-ion batteries. It would be interesting to see, what CHFS could do for the synthesis of nano-sized $TiNb_2O_7$.

The high performance for all materials in chapter 3 and 4 were given without measuring potential self-discharge. This would include that the materials would get lithiated and an inactive step would be included (meaning, no current or potential control is further applied for a certain amount of time). It would be very important to understand the "quality" of the charge for a better evaluation for use in high power hybrid devices in future.

Chapter 5 gives a good example how the CHFS reactor can be used to answer a scientific question. In this case, the question dealt with the real role of a transition metal ion dopant in SnO_2 on the electrochemical performance. Many publications in literature showed a drastic improvement with doping, although many other material's properties also changed during doping and processing (including surface area, crystallinity, carbon coating). Therefore, many parameters changed simultaneously with doping which does not help illuminate the real impact of the dopant. CHFS can be used to control the general materials properties (particle size, crystallinity, dopant concentration etc.), so that a realistic role of the dopant can be obtained compared to the undoped or other doped SnO_2. It could be shown that for most dopants, the general capacity performance is not useful towards high energy LiBs. This is clearly a far different result compared to most suggestions from the literature. In future, it is hoped to understand the role of the cobalt ion in SnO_2. The same approach taken herein might be also

useful for sodium-ion batteries. Moreover, there are other alloying materials like ZnO and silicon, which might show the same effect with cobalt incorporation. It is essential to increase the cycle stability, which might be done in-situ with addition of carbon like a coating or graphene during the continuous hydrothermal process.

In chapter 6, it was shown that doping Sn into various nano-sized insertion materials can drastically increase the stored capacity when the Sn is activated at lower potentials. This is a simple approach, as these materials can be made with various synthesis methods in a single step. Moreover, the materials were made under scaled-up conditions with a production rate of up to 200 g h^{-1}. In future, it might be interesting to focus on insertion materials with a sheet-like morphology. The Sn-dopant might form then a secondary phase between these layers during initial lithiation. Moreover, extensive studies are needed to understand why the Sn-dopant can be activated and also if all dopants get activated or only the ones closer to the surface?

All materials herein showed the drawback of high irreversible capacity losses during the first cycle or even at lower rates. Thus, it would be essential to drastically improve this for practical use in future. Solutions might include additives in the electrolyte, carbon coating or even the use of surfactants as SEI stabilizing agents.

I. References

[1] Z. Yang, J. Zhang, M.C. Kintner-Meyer, X. Lu, D. Choi, J.P. Lemmon, J. Liu, *Chemical Reviews,* **111** (2011) 3577-3613.

[2] M. Reich, P.M. Vasconcelos, *Elements,* **11** (2015) 305-310.

[3] M. Winter, R.J. Brodd, *Chemical Reviews,* **104** (2004) 4245-4270.

[4] J.R. Miller, A.F. Burke, *The Electrochemical Society Interface,* **17** (2008) 53.

[5] Y. Zhang, H. Feng, X. Wu, L. Wang, A. Zhang, T. Xia, H. Dong, X. Li, L. Zhang, *International Journal of Hydrogen Energy,* **34** (2009) 4889-4899.

[6] J.M. Tarascon, M. Armand, *Nature,* **414** (2001) 359-367.

[7] Y. Nishi, *Journal of Power Sources,* **100** (2001) 101-106.

[8] C. Glaize, S. Genies, Lithium batteries and other electrochemical storage systems, *John Wiley & Sons*, (2013).

[9] H.E. Becker, U.S. Patent No. 2,800,616 (1957).

[10] J. Gamby, P.L. Taberna, P. Simon, J.F. Fauvarque, M. Chesneau, *Journal of Power Sources,* **101** (2001) 109-116.

[11] M. Galinski, K. Babeł, K. Jurewicz, *Journal of Power Sources,* **228** (2013) 83-88.

[12] M. Gaberscek, J. Moskon, B. Erjavec, R. Dominko, J. Jamnik, *Electrochemical and Solid-State Letters,* **11** (2008) A170-A174.

[13] S. Dsoke, X. Tian, C. Täubert, S. Schlüter, M. Wohlfahrt-Mehrens, *Journal of Power Sources,* **238** (2013) 422-429.

[14] H.Y. Lee, J.B. Goodenough, *Journal of Solid State Chemistry,* **144** (1999) 220-223.

[15] P. Simon, Y. Gogotsi, *Nature Materials,* **7** (2008) 845-854.

[16] S. Pohlmann, A. Balducci, *Electrochimica Acta,* **110** (2013) 221-227.

[17] V. Ruiz, T. Huynh, S.R. Sivakkumar, A.G. Pandolfo, *RSC Advances,* **2** (2012) 5591-5598.

[18] M. Montanino, M. Moreno, F. Alessandrini, G.B. Appetecchi, S. Passerini, Q. Zhou, W.A. Henderson, *Electrochimica Acta,* **60** (2012) 163-169.

[19] M. Armand, F. Endres, D.R. MacFarlane, H. Ohno, B. Scrosati, *Nature Materials,* **8** (2009) 621-629.

[20] R.S. Kühnel, N. Böckenfeld, S. Passerini, M. Winter, A. Balducci, *Electrochimica Acta,* **56** (2011) 4092-4099.

[21] D. Reber, R.-S. Kuhnel, C. Battaglia, *Sustainable Energy & Fuels,* **1** (2017) 2155-2161.

[22] G. Wang, L. Zhang, J. Zhang, *Chemical Society Reviews,* **41** (2012) 797-828.

[23] V. Augustyn, P. Simon, B. Dunn, *Energy & Environmental Science,* **7** (2014) 1597-1614.

[24] J. Wang, J. Polleux, J. Lim, B. Dunn, *The Journal of Physical Chemistry C,* **111** (2007) 14925-14931.

[25] B.E. Conway, W. Pell, T. Liu, *Journal of Power Sources,* **65** (1997) 53-59.

[26] T. Liu, W. Pell, B. Conway, *Electrochimica Acta,* **42** (1997) 3541-3552.
[27] B. Ricketts, C. Ton-That, *Journal of Power Sources,* **89** (2000) 64-69.
[28] B.E. Conway, *Journal of the Electrochemical Society,* **138** (1991) 1539-1548.
[29] D. Cericola, P. Novák, A. Wokaun, R. Kötz, *Electrochimica Acta,* **56** (2011) 8403-8411.
[30] J.-H. Kim, J.-S. Kim, Y.-G. Lim, J.-G. Lee, Y.-J. Kim, *Journal of Power Sources,* **196** (2011) 10490-10495.
[31] S.R. Sivakkumar, A.S. Milev, A.G. Pandolfo, *Electrochimica Acta,* **56** (2011) 9700-9706.
[32] S.R. Sivakkumar, J.Y. Nerkar, A.G. Pandolfo, *Electrochimica Acta,* **55** (2010) 3330-3335.
[33] A.G. Pandolfo, A.F. Hollenkamp, *Journal of Power Sources,* **157** (2006) 11-27.
[34] W.J. Cao, J.P. Zheng, *Journal of The Electrochemical Society,* **160** (2013) A1572-A1576.
[35] S.R. Sivakkumar, A.G. Pandolfo, *Electrochimica Acta,* **65** (2012) 280-287.
[36] M. Schroeder, Lithium-Ion batteries and capacitors: Towards safer electrochemical energy storage, *Institut für Physikalische Chemie - Westfälischen Wilhelms-Universität Münster* (2013).
[37] M. Schroeder, M. Winter, S. Passerini, A. Balducci, *Journal of The Electrochemical Society,* **159** (2012) A1240-A1245.
[38] M. Schroeder, M. Winter, S. Passerini, A. Balducci, *Journal of Power Sources,* **238** (2013) 388-394.
[39] W.J. Cao, J.P. Zheng, *Journal of Power Sources,* **213** (2012) 180-185.
[40] N. Böckenfeld, A. Balducci, *Journal of Power Sources,* **235** (2013) 265-273.
[41] A. Brandt, A. Balducci, *Electrochimica Acta,* **108** (2013) 219-225.
[42] X. Sun, X. Zhang, B. Huang, H. Zhang, D. Zhang, Y. Ma, *Journal of Power Sources,* **243** (2013) 361-368.
[43] N. Böckenfeld, R.S. Kühnel, S. Passerini, M. Winter, A. Balducci, *Journal of Power Sources,* **196** (2011) 4136-4142.
[44] R. Marom, S.F. Amalraj, N. Leifer, D. Jacob, D. Aurbach, *Journal of Materials Chemistry,* **21** (2011) 9938-9954.
[45] P.V. Braun, J. Cho, J.H. Pikul, W.P. King, H. Zhang, *Current Opinion in Solid State and Materials Science,* **16** (2012) 186-198.
[46] Y.G. Guo, J.S. Hu, L.J. Wan, *Advanced Materials,* **20** (2008) 2878-2887.
[47] J. Wolfenstine, J. Allen, J. Read, D. Foster, *DTIC Document*, 2006.
[48] C.-M. Park, J.-H. Kim, H. Kim, H.-J. Sohn, *Chemical Society Reviews,* **39** (2010) 3115-3141.
[49] http://www.sony.net/SonyInfo/News/Press/200502/05-006E/index.html (01/02/2014).
[50] M. Winter, K. C.; Besenhard, J. O., Lithium Batteries - Science and Technology, *Kluwer Academic Publisher* (2004).
[51] F. Ding, W. Xu, D. Choi, W. Wang, X. Li, M.H. Engelhard, X. Chen, Z. Yang, J.-G. Zhang, *Journal of Materials Chemistry,* **22** (2012) 12745-12751.
[52] N. Cuesta, A. Ramos, I. Cameán, C. Antuña, A.B. García, *Electrochimica Acta,* **155** (2015) 140-147.

[53] K.-J. Kim, T.-S. Lee, H.-G. Kim, S.-H. Lim, S.-M. Lee, *Electrochimica Acta,* **135** (2014) 27-34.

[54] D. Aurbach, E. Zinigrad, Y. Cohen, H. Teller, *Solid State Ionics,* **148** (2002) 405-416.

[55] M.V. Reddy, G.V. Subba Rao, B.V.R. Chowdari, *Chemical Reviews,* **113** (2013) 5364-5457.

[56] V. Etacheri, R. Marom, R. Elazari, G. Salitra, D. Aurbach, *Energy & Environmental Science,* **4** (2011) 3243-3262.

[57] D. Deng, M.G. Kim, J.Y. Lee, J. Cho, *Energy & Environmental Science,* **2** (2009) 818-837.

[58] B. Hao, Y. Yan, X. Wang, G. Chen, *ACS applied materials & interfaces,* **5** (2013) 6285-6291.

[59] K. Zhu, Q. Wang, J.-H. Kim, A.A. Pesaran, A.J. Frank, *The Journal of Physical Chemistry C,* **116** (2012) 11895-11899.

[60] J.Y. Shin, D. Samuelis, J. Maier, *Advanced Functional Materials,* **21** (2011) 3464-3472.

[61] M.L. Sushko, K.M. Rosso, J. Liu, *The Journal of Physical Chemistry C,* **114** (2010) 20277-20283.

[62] J. Chen, L. Yang, Y. Tang, *Journal of Power Sources,* **195** (2010) 6893-6896.

[63] H. Lindström, S. Södergren, A. Solbrand, H. Rensmo, J. Hjelm, A. Hagfeldt, S.-E. Lindquist, *The Journal of Physical Chemistry B,* **101** (1997) 7717-7722.

[64] C. Howard, T. Sabine, F. Dickson, *Acta Crystallographica Section B: Structural Science,* **47** (1991) 462-468.

[65] Z. Yang, D. Choi, S. Kerisit, K.M. Rosso, D. Wang, J. Zhang, G. Graff, J. Liu, *Journal of Power Sources,* **192** (2009) 588-598.

[66] R. Cava, D. Murphy, S. Zahurak, A. Santoro, R. Roth, *Journal of Solid State Chemistry,* **53** (1984) 64-75.

[67] G. Sudant, E. Baudrin, D. Larcher, J.-M. Tarascon, *Journal of Materials Chemistry,* **15** (2005) 1263-1269.

[68] P. Poizot, S. Laruelle, S. Grugeon, L. Dupont, J.M. Tarascon, *Nature,* **407** (2000) 496-499.

[69] Y.-M. Kang, M.-S. Song, J.-H. Kim, H.-S. Kim, M.-S. Park, J.-Y. Lee, H.K. Liu, S.X. Dou, *Electrochimica Acta,* **50** (2005) 3667-3673.

[70] T. Li, Z.X. Chen, X.P. Ai, Y.L. Cao, H.X. Yang, *Journal of Power Sources,* **217** (2012) 54-58.

[71] J.-M. Tarascon, S. Grugeon, M. Morcrette, S. Laruelle, P. Rozier, P. Poizot, *Comptes Rendus Chimie,* **8** (2005) 9-15.

[72] M.R. Palacin, *Chemical Society Reviews,* **38** (2009) 2565-2575.

[73] J. Cabana, L. Monconduit, D. Larcher, M.R. Palacín, *Advanced Materials,* **22** (2010) E170-E192.

[74] L. Croguennec, M.R. Palacin, *Journal of the American Chemical Society,* **137** (2015) 3140-3156.

[75] X.-H. Ma, X.-Y. Feng, C. Song, B.-K. Zou, C.-X. Ding, Y. Yu, C.-H. Chen, *Electrochimica Acta,* **93** (2013) 131-136.

[76] J. Zhang, Y. Sun, Y. Yao, T. Huang, A. Yu, *Journal of Power Sources,* **222** (2013) 59-65.

[77] H.S. Kim, S.G. Kwon, S.H. Kang, Y. Piao, Y.-E. Sung, *Electrochimica Acta,* **136** (2014) 47-51.

[78] Y.S. Hu, R. Demir-Cakan, M.M. Titirici, J.O. Müller, R. Schlögl, M. Antonietti, J. Maier, *Angewandte Chemie - International Edition,* **47** (2008) 1645-1649.

[79] F. Mueller, D. Bresser, E. Paillard, M. Winter, S. Passerini, *Journal of Power Sources,* **236** (2013) 87-94.

[80] C. Wang, G. Shao, Z. Ma, S. Liu, W. Song, J. Song, *Electrochimica Acta,* **130** (2014) 679-688.

[81] A. Kraytsberg, Y. Ein-Eli, *Journal of Solid State Electrochemistry,* (2017) 1-17.

[82] W.-J. Zhang, *Journal of Power Sources,* **196** (2011) 13-24.

[83] S. Goriparti, E. Miele, F. De Angelis, E. Di Fabrizio, R. Proietti Zaccaria, C. Capiglia, *Journal of Power Sources,* **257** (2014) 421-443.

[84] A.R. Kamali, D.J. Fray, *Reviews on Advanced Materials Science,* **27** (2011) 14-24.

[85] L. Ji, Z. Lin, M. Alcoutlabi, X. Zhang, *Energy & Environmental Science,* **4** (2011) 2682-2699.

[86] P.N. Kumta, J. Maranchi, M. Datta, Patent No. WO2005076389 A9, (2005).

[87] H. Zhao, Z. Zhu, C. Yin, H. Guo, D.H.L. Ng, *Materials Chemistry and Physics,* **110** (2008) 201-205.

[88] K. Nishikawa, K. Dokko, K. Kinoshita, S.-W. Woo, K. Kanamura, *Journal of Power Sources,* **189** (2009) 726-729.

[89] H.p. Zhao, C.y. Jiang, X.m. He, J.g. Ren, *Journal of Power Sources,* **184** (2008) 532-537.

[90] D. Bresser, S. Passerini, B. Scrosati, *Energy & Environmental Science,* **9** (2016) 3348-3367.

[91] F. Mueller, D. Bresser, V.S.K. Chakravadhanula, S. Passerini, *Journal of Power Sources,* **299** (2015) 398-402.

[92] G. Zhou, D.-W. Wang, L. Li, N. Li, F. Li, H.-M. Cheng, *Nanoscale,* **5** (2013) 1576-1582.

[93] Y. Liu, X. Yan, J.-L. Lan, D. Teng, Y. Yu, X. Yang, *Electrochimica Acta,* **137** (2014) 9-16.

[94] J. Liang, X.Y. Yu, H. Zhou, H.B. Wu, S. Ding, X.W.D. Lou, *Angewandte Chemie International Edition,* **53** (2014) 12803-12807.

[95] X. Wang, X. Cao, L. Bourgeois, H. Guan, S. Chen, Y. Zhong, D.M. Tang, H. Li, T. Zhai, L. Li, *Advanced Functional Materials,* **22** (2012) 2682-2690.

[96] M. Ara, V.R. Chitturi, S.O. Salley, K.S. Ng, *Electrochimica Acta,* **161** (2015) 269-278.

[97] X. Zhou, L. Yu, X.W.D. Lou, *Advanced Energy Materials,* **6** (2016) 1600451.

[98] X. Xu, S. Chen, C. Xiao, K. Xi, C. Guo, S. Guo, S. Ding, D. Yu, R.V. Kumar, *ACS Applied Materials & Interfaces,* **8** (2016) 6004-6010.

[99] L. Shen, F. Liu, G. Chen, H. Zhou, Z. Le, H.B. Wu, G. Wang, Y. Lu, *Journal of Materials Chemistry A,* **4** (2016) 18706-18710.

[100] F.M. Hassan, Z. Chen, A. Yu, Z. Chen, X. Xiao, *Electrochimica Acta,* **87** (2013) 844-852.

[101] K. Zhao, L. Zhang, R. Xia, Y. Dong, W. Xu, C. Niu, L. He, M. Yan, L. Qu, L. Mai, *Small,* **12** (2016) 588-594.

[102] B. Huang, X. Li, Y. Pei, S. Li, X. Cao, R.C. Massé, G. Cao, *Small,* **12** (2016) 1945-1955.

[103] J.S. Chen, Y.L. Cheah, Y.T. Chen, N. Jayaprakash, S. Madhavi, Y.H. Yang, X.W. Lou, *The Journal of Physical Chemistry C,* **113** (2009) 20504-20508.

[104] M.S. Park, Y.M. Kang, G.X. Wang, S.X. Dou, H.K. Liu, *Advanced Functional Materials,* **18** (2008) 455-461.

[105] Y.-D. Ko, J.-G. Kang, J.-G. Park, S. Lee, D.-W. Kim, *Nanotechnology,* **20** (2009) 455701.

[106] R. Demir-Cakan, Y.-S. Hu, M. Antonietti, J. Maier, M.-M. Titirici, *Chemistry of Materials,* **20** (2008) 1227-1229.

[107] Y. Wang, Z.X. Huang, Y. Shi, J.I. Wong, M. Ding, H.Y. Yang, *Scientific Reports,* **5** (2015) 9164.

[108] D. Mhamane, V. Aravindan, D. Taneja, A. Suryawanshi, O. Game, M. Srinivasan, S. Ogale, *Composites Science and Technology,* **130** (2016) 88-95.

[109] Z. Chen, M. Zhou, Y. Cao, X. Ai, H. Yang, J. Liu, *Advanced Energy Materials,* **2** (2012) 95-102.

[110] X. Guo, X. Fang, Y. Sun, L. Shen, Z. Wang, L. Chen, *Journal of Power Sources,* **226** (2013) 75-81.

[111] S.-Y. Lee, K.-Y. Park, W.-S. Kim, S. Yoon, S.-H. Hong, K. Kang, M. Kim, *Nano Energy,* **19** (2016) 234-245.

[112] Y.-Y. Hu, Z. Liu, K.-W. Nam, O.J. Borkiewicz, J. Cheng, X. Hua, M.T. Dunstan, X. Yu, K.M. Wiaderek, L.-S. Du, *Nature Materials,* **12** (2013) 1130-1136.

[113] P. Simon, Y. Gogotsi, B. Dunn, *Science Magazine,* **343** (2014) 1210-1211.

[114] B.E. Conway, Electrochemical supercapacitors: Scientific Fundamentals and Technological Applications, *Springer Science & Business Media* (2013).

[115] M. Lübke, A. Sumboja, I. Johnson, D.J. Brett, P.R. Shearing, Z. Liu, J.A. Darr, *Electrochimica Acta,* **192** (2016) 363-369.

[116] V. Augustyn, J. Come, M.A. Lowe, J.W. Kim, P.-L. Taberna, S.H. Tolbert, H.D. Abruña, P. Simon, B. Dunn, *Nature Materials,* **12** (2013) 518-522.

[117] L.T. Anh, A.K. Rai, T.V. Thi, J. Gim, S. Kim, E.-C. Shin, J.-S. Lee, J. Kim, *Journal of Power Sources,* **243** (2013) 891-898.

[118] E. Khoo, J. Wang, J. Ma, P.S. Lee, *Journal of Materials Chemistry,* **20** (2010) 8368-8374.

[119] G. Ren, M.N.F. Hoque, X. Pan, J. Warzywoda, Z. Fan, *Journal of Materials Chemistry A,* **3** (2015) 10787-10794.

[120] S. Ardizzone, G. Fregonara, S. Trasatti, *Electrochimica Acta,* **35** (1990) 263-267.

[121] M. Okubo, E. Hosono, J. Kim, M. Enomoto, N. Kojima, T. Kudo, H. Zhou, I. Honma, *Journal of the american chemical society,* **129** (2007) 7444-7452.

[122] E. Uchaker, G. Cao, *Chemistry–An Asian Journal,* **8** (2015) 1608-1617.

[123] A. Moretti, M. Secchiaroli, D. Buchholz, G. Giuli, R. Marassi, S. Passerini, *Journal of The Electrochemical Society,* **162** (2015) A2723-A2728.

[124] Z. Yu, G. Zhu, H. Xu, A. Yu, *Energy Technology,* **2** (2014) 767-772.

[125] O.B. Chae, J. Kim, I. Park, H. Jeong, J.H. Ku, J.H. Ryu, K. Kang, S.M. Oh, *Chemistry of Materials,* **26** (2014) 5874-5881.

[126] E. Uchaker, Y.-Z. Zheng, S. Li, S.L. Candelaria, S. Hu, G. Cao, *Journal of Materials Chemistry A,* **2** (2014) 18208-18214.

[127] Y. Fang, L. Xiao, J. Qian, X. Ai, H. Yang, Y. Cao, *Nano letters,* **14** (2014) 3539-3543.

[128] J. Come, V. Augustyn, J.W. Kim, P. Rozier, P.-L. Taberna, P. Gogotsi, J.W. Long, B. Dunn, P. Simon, *Journal of The Electrochemical Society,* **161** (2014) A718-A725.

[129] J.W. Kim, V. Augustyn, B. Dunn, *Advanced Energy Materials,* **2** (2012) 141-148.

[130] M. Wei, K. Wei, M. Ichihara, H. Zhou, *Electrochemistry Communications,* **10** (2008) 980-983.

[131] A.A. Lubimtsev, P.R. Kent, B.G. Sumpter, P. Ganesh, *Journal of Materials Chemistry A,* **1** (2013) 14951-14956.

[132] H. Nakazawa, K. Sano, T. Abe, M. Baba, N. Kumagai, *Journal of Power Sources,* **174** (2007) 838-842.

[133] M. Wei, Z.-m. Qi, M. Ichihara, H. Zhou, *Acta Materialia,* **56** (2008) 2488-2494.

[134] A.L. Viet, M.V. Reddy, R. Jose, B.V.R. Chowdari, S. Ramakrishna, *The Journal of Physical Chemistry C,* **114** (2009) 664-671.

[135] A.L. Viet, M. Reddy, R. Jose, B. Chowdari, S. Ramakrishna, *The Journal of Physical Chemistry C,* **114** (2009) 664-671.

[136] H. Luo, M. Wei, K. Wei, *Materials Chemistry and Physics,* **120** (2010) 6-9.

[137] H. Wen, Z. Liu, J. Wang, Q. Yang, Y. Li, J. Yu, *Applied Surface Science,* **257** (2011) 10084-10088.

[138] A. Le Viet, M.V. Reddy, R. Jose, B.V.R. Chowdari, S. Ramakrishna, *Electrochimica Acta,* **56** (2011) 1518-1528.

[139] X. Wang, C. Yan, J. Yan, A. Sumboja, P.S. Lee, *Nano Energy,* **11** (2015) 765-772.

[140] D. Deng, M.G. Kim, J.Y. Lee, J. Cho, *Energy & Environmental Science,* **2** (2009) 818-837.

[141] J. Li, Z. Tang, Z. Zhang, *Chemistry of Materials,* **17** (2005) 5848-5855.

[142] J. Li, Z. Tang, Z. Zhang, *Chemical Physics Letters,* **418** (2006) 506-510.

[143] J. Liu, X. Li, M. Cai, R. Li, X. Sun, *Electrochimica Acta,* **93** (2013) 195-201.

[144] C. Hua, X. Fang, Z. Wang, L. Chen, *Electrochemistry Communications,* **32** (2013) 5-8.

[145] W. Chen, Z. Zhou, H. Liang, L. Shao, J. Shu, Z. Wang, *Journal of Power Sources,* **281** (2015) 56-68.

[146] X. Luan, Y. Wang, *Journal of Materials Science & Technology,* **30** (2014) 839-846.

[147] M. Shirpour, J. Cabana, M. Doeff, *Energy & Environmental Science,* **6** (2013) 2538-2547.

[148] M. Shirpour, J. Cabana, M. Doeff, *Chemistry of Materials,* **26** (2014) 2502-2512.

[149] M.J. Powell, P. Marchand, C. Denis, J.C. Bear, J.A. Darr, I.P. Parkin, *Nanoscale,* **44** (2015) 18686-18693.

[150] C. Niu, J. Meng, C. Han, K. Zhao, M. Yan, L. Mai, *Nano Letters,* **14** (2014) 2873-2878.

[151] G. He, L. Li, A. Manthiram, *Journal of Materials Chemistry A,* **3** (2015) 14750-14758.
[152] J. Vetter, P. Novák, M.R. Wagner, C. Veit, K.C. Möller, J.O. Besenhard, M. Winter, M. Wohlfahrt-Mehrens, C. Vogler, A. Hammouche, *Journal of Power Sources,* **147** (2005) 269-281.
[153] S.J. Rezvani, R. Gunnella, A. Witkowska, F. Mueller, M. Pasqualini, F. Nobili, S. Passerini, A.D. Cicco, *ACS applied materials & interfaces,* **9** (2017) 4570-4576.
[154] E. Peled, D. Golodnitsky, G. Ardel, *Journal of The Electrochemical Society,* **144** (1997) L208-L210.
[155] C. Natarajan, H. Fujimoto, K. Tokumitsu, A. Mabuchi, T. Kasuh, *Carbon,* **39** (2001) 1409-1413.
[156] M. Wagemaker, F.M. Mulder, *Accounts of Chemical Research,* **46** (2013) 1206-1215.
[157] H.-Y. Lee, J.-K. Baek, S.-W. Jang, S.-M. Lee, S.-T. Hong, K.-Y. Lee, M.-H. Kim, *Journal of power sources,* **101** (2001) 206-212.
[158] M. Yoshio, H. Wang, K. Fukuda, T. Umeno, T. Abe, Z. Ogumi, *Journal of Materials Chemistry,* **14** (2004) 1754-1758.
[159] N. Ohta, K. Nagaoka, K. Hoshi, S. Bitoh, M. Inagaki, *Journal of Power Sources,* **194** (2009) 985-990.
[160] S.S. Zhang, *Journal of Power Sources,* **162** (2006) 1379-1394.
[161] M. Bundschuh, F. Seitz, R.R. Rosenfeldt, R. Schulz, *PLoS ONE,* **7** (2012) e48956.
[162] C. Buzea, Pacheco, II, K. Robbie, *Biointerphases,* **2** (2007) MR17-71.
[163] P.G. Bruce, B. Scrosati, J.-M. Tarascon, *Angewandte Chemie International Edition,* **47** (2008) 2930-2946.
[164] A.S. Arico, P. Bruce, B. Scrosati, J.-M. Tarascon, W. van Schalkwijk, *Nature Materials,* **4** (2005) 366-377.
[165] S. Ramdon, B. Bhushan, *Journal of Power Sources,* **246** (2014) 219-224.
[166] F. Jiao, P.G. Bruce, *Advanced Materials,* **19** (2007) 657-660.
[167] Y.S. Hu, L. Kienle, Y.G. Guo, J. Maier, *Advanced Materials,* **18** (2006) 1421-1426.
[168] E. Baudrin, S. Cassaignon, M. Koelsch, J.P. Jolivet, L. Dupont, J.M. Tarascon, *Electrochemistry Communications,* **9** (2007) 337-342.
[169] S. Goriparti, E. Miele, F. De Angelis, E. Di Fabrizio, R. Proietti Zaccaria, C. Capiglia, *Journal of Power Sources* **257** (2014) 421-443.
[170] Y. Gogotsi, *ACS Nano,* **8** (2014) 5369-5371.
[171] C.F. Armer, M. Lübke, M. Reddy, J.A. Darr, X. Li, A. Lowe, *Journal of Power Sources,* **353** (2017) 40-50.
[172] A.H. Lu, E.e.L. Salabas, F. Schüth, *Angewandte Chemie International Edition,* **46** (2007) 1222-1244.
[173] J. Lopez Perez, M. Lopez Quintela, J. Mira, J. Rivas, S. Charles, *The Journal of Physical Chemistry B,* **101** (1997) 8045-8047.
[174] B.K. Paul, S.P. Moulik, *Current Science,* **80** (2001) 990-1001.

[175] I.A. Rahman, V. Padavettan, *Journal of Nanomaterials,* **2012** (2012) 8.

[176] A. Rabenau, *Angewandte Chemie International Edition in English,* **24** (1985) 1026-1040.

[177] G. Demazeau, *Journal of Materials Chemistry,* **9** (1999) 15-18.

[178] A. Kafizas, C.W. Dunnill, I.P. Parkin, *Journal of Materials Chemistry,* **20** (2010) 8336-8349.

[179] S.D. Burnside, V. Shklover, C. Barbé, P. Comte, F. Arendse, K. Brooks, M. Grätzel, *Chemistry of Materials,* **10** (1998) 2419-2425.

[180] M.-A. Einarsrud, T. Grande, *Chemical Society Reviews,* **43** (2014) 2187-2199.

[181] R. Roy, *Journal of Solid State Chemistry,* **111** (1994) 11-17.

[182] A.A. Peterson, F. Vogel, R.P. Lachance, M. Froling, J.M.J. Antal, J.W. Tester, *Energy & Environmental Science,* **1** (2008) 32-65.

[183] T. Adschiri, Y.-W. Lee, M. Goto, S. Takami, *Green Chemistry,* **13** (2011) 1380-1390.

[184] V.K. LaMer, R.H. Dinegar, *Journal of the American Chemical Society,* **72** (1950) 4847-4854.

[185] J.A. Darr, M. Poliakoff, *Chemical Reviews,* **99** (1999) 495-542.

[186] Z. Zhang, S. Brown, J.B. Goodall, X. Weng, K. Thompson, K. Gong, S. Kellici, R.J. Clark, J.R. Evans, J.A. Darr, *Journal of Alloys and Compounds,* **476** (2009) 451-456.

[187] M. Lübke, I. Johnson, N.M. Makwana, D. Brett, P. Shearing, Z. Liu, J.A. Darr, *Journal of Power Sources,* **294** (2015) 94-102.

[188] M. Lübke, A. Sumboja, I.D. Johnson, D.J. Brett, P.R. Shearing, Z. Liu, J.A. Darr, *Electrochimica Acta,* **192** (2016) 363-369.

[189] I.D. Johnson, M. Loveridge, R. Bhagat, J.A. Darr, *ACS Combinatorial Science,* **11** (2016) 665-672.

[190] D.P. Howard, P. Marchand, L. McCafferty, C.J. Carmalt, I.P. Parkin, J.A. Darr, *ACS Combinatorial Science,* **19** (2017) 239-245.

[191] R.I. Gruar, C.J. Tighe, J.A. Darr, *Ind. Eng. Chem. Res.,* **52** (2013) 5270-5281.

[192] T. Adschiri, Y. Hakuta, K. Sue, K. Arai, *Journal of Nanoparticle Research,* **3** (2001) 227-235.

[193] P.W. Dunne, A.S. Munn, C.L. Starkey, T.A. Huddle, E.H. Lester, *Philosophical Transactions of the Royal Society A,* **373** (2015) 20150015.

[194] K. Byrappa, S. Ohara, T. Adschiri, *Advanced Drug Delivery Reviews,* **60** (2008) 299-327.

[195] J.A. Darr, J. Zhang, N.M. Makwana, X. Weng, *Chemical Reviews,* **117** (2017) 11125-11238.

[196] S.-I. Kawasaki, K. Sue, R. Ookawara, Y. Wakashima, A. Suzuki, Y. Hakuta, K. Arai, *The Journal of Supercritical Fluids,* **54** (2010) 96-102.

[197] C.J. Denis, C.J. Tighe, R.I. Gruar, N.M. Makwana, J.A. Darr, *Crystal Growth & Design,* **9** (2015) 4256-4265.

[198] J. Darr, C.J. Tighe, R. Gruar, US Patent No. 9,192,901, (2015).

[199] C.J. Tighe, R.Q. Cabrera, R.I. Gruar, J.A. Darr, *Industrial & Engineering Chemistry Research,* **52** (2013) 5522-5528.

[200] M. Chen, C.Y. Ma, T. Mahmud, J.A. Darr, X.Z. Wang, *The Journal of Supercritical Fluids,* **59** (2011) 131-139.

[201] X. Lu, M. Yu, G. Wang, T. Zhai, S. Xie, Y. Ling, Y. Tong, Y. Li, *Advanced Materials,* **25** (2013) 267-272.

[202] Z. Zhang, S. Brown, J.B.M. Goodall, X. Weng, K. Thompson, K. Gong, S. Kellici, R.J.H. Clark, J.R.G. Evans, J.A. Darr, *Journal of Alloys and Compounds,* **476** (2009) 451-456.

[203] M. Chen, C.Y. Ma, T. Mahmud, J.A. Darr, X.Z. Wang, *The Journal of Supercritical Fluids,* **59** (2011) 131-139.

[204] P. Van der Heide, X-ray photoelectron spectroscopy: An introduction to principles and practices, *John Wiley & Sons*, (2011).

[205] J.M. Hollander, W.L. Jolly, *Accounts of Chemical Research,* **3** (1970) 193-200.

[206] Colthup, Norman. Introduction to infrared and Raman spectroscopy. *Elsevier*, (2012).

[207] A. Khursheed, Scanning electron microscope optics and spectrometers, *World Scientific*, (2011).

[208] L. Reimer, Transmission electron microscopy: physics of image formation and microanalysis, *Springer*, (2013).

[209] J.B. Condon, Surface area and porosity determinations by physisorption: measurements and theory, *Elsevier*, (2006).

[210] Bard, Allen J., and Larry R. Faulkner, Fundamentals and applications. *Electrochemical Methods* **2** (2001).

[211]http://www.gamry.com/application-notes/basics-of-electrochemical-impedance-spectroscopy, (2017).

[212] T.C. Liu, W. Pell, B. Conway, S. Roberson, *Journal of the Electrochemical Society,* **145** (1998) 1882-1888.

[213] M. Sathiya, A. Prakash, K. Ramesha, J.M. Tarascon, A. Shukla, *Journal of the American Chemical Society,* **133** (2011) 16291-16299.

[214] A. Eftekhari, *Journal of Power Sources,* **343** (2017) 395-411.

[215] Z. Zhang, J.B. Goodall, S. Brown, L. Karlsson, R.J. Clark, J.L. Hutchison, I. Rehman, J.A. Darr, *Dalton Transactions,* **39** (2010) 711-714.

[216] O.V. Yakubovich, V.V. Kireev, *Crystallography Reports,* **48** (2003) 24-28.

[217] Q. Chen, W. Zhou, G. Du, L.-M. Peng, *Advanced Materials,* **14** (2002) 1208-1211.

[218] P. Senguttuvan, G. Rousse, V. Seznec, J.-M. Tarascon, M.R. Palacín, *Chemistry of Materials,* **23** (2011) 4109-4111.

[219] Y. An, Z. Li, H. Xiang, Y. Huang, J. Shen, *Central European Journal of Physics,* **9** (2011) 1488-1492.

[220] K. Kiatkittipong, A. Iwase, J. Scott, R. Amal, *Chemical Engineering Science,* **93** (2013) 341-349.

[221] D. Yang, Z. Zheng, Y. Yuan, H. Liu, E.R. Waclawik, X. Ke, M. Xie, H. Zhu, *Physical Chemistry Chemical Physics,* **12** (2010) 1271-1277.

[222] L. Wang, T. Zhang, Q. Qi, J. Hu, Y. Zeng, G. Lu, *Materials Letters,* **63** (2009) 903-904.

[223] H. Liu, D. Yang, Z. Zheng, X. Ke, E. Waclawik, H. Zhu, R.L. Frost, *Journal of Raman Spectroscopy,* **41** (2010) 1331-1337.

[224] D. Yang, Z. Zheng, H. Liu, H. Zhu, X. Ke, Y. Xu, D. Wu, Y. Sun, *The Journal of Physical Chemistry C,* **112** (2008) 16275-16280.

[225] W. Chen, X. Guo, S. Zhang, Z. Jin, *Journal of Nanoparticle Research,* **9** (2007) 1173-1180.

[226] E. Baudrin, G. Sudant, D. Larcher, B. Dunn, J.-M. Tarascon, *Chemistry of Materials,* **18** (2006) 4369-4374.

[227] J.-H. Son, J. Wei, D. Cobden, G. Cao, Y. Xia, *Chemistry of Materials,* **22** (2010) 3043-3050.

[228] M.J. Powell, P. Marchand, C. Denis, J. Bear, J. Darr, I. Parkin, *Nanoscale,* **7** (2015) 18686-18693.

[229] M.J. Powell, VO_2 thin films and nanoparticles, from chemical vapour deposition and hydrothermal synthesis, for energy efficient applications, *UCL (University College London)*, 2015.

[230] J. Parker, *Physical Review B,* **42** (1990) 3164.

[231] T. Yao, L. Liu, C. Xiao, X. Zhang, Q. Liu, S. Wei, Y. Xie, *Angewandte Chemie,* **125** (2013) 7702-7706.

[232] C. Nethravathi, C.R. Rajamathi, M. Rajamathi, U.K. Gautam, X. Wang, D. Golberg, Y. Bando, *ACS Applied Materials & Interfaces,* **5** (2013) 2708-2714.

[233] M.E. Spahr, P. Stoschitzki-Bitterli, R. Nesper, O. Haas, P. Novák, *Journal of The Electrochemical Society,* **146** (1999) 2780-2783.

[234] C. Nethravathi, B. Viswanath, J. Michael, M. Rajamath, *Carbon,* **50** (2012) 4839-4846.

[235] L. Mai, Q. Wei, Q. An, X. Tian, Y. Zhao, X. Xu, L. Xu, L. Chang, Q. Zhang, *Advanced Materials,* **25** (2013) 2969-2973.

[236] M. Xue, H. Chen, J. Ge, J. Shen, *Microporous and Mesoporous Materials,* **131** (2010) 37-44.

[237] S. Pavasupree, Y. Suzuki, A. Kitiyanan, S. Pivsa-Art, S. Yoshikawa, *Journal of Solid State Chemistry,* **178** (2005) 2152-2158.

[238] J.M. Won, Y.N. Ko, J.-K. Lee, Y.C. Kang, *Electrochimica Acta,* **156** (2015) 179-187.

[239] B. Tian, H. Xiang, L. Zhang, Z. Li, H. Wang, *Electrochimica Acta,* **55** (2010) 5453-5458.

[240] Y.-Q. Wang, L. Gu, Y.-G. Guo, H. Li, X.-Q. He, S. Tsukimoto, Y. Ikuhara, L.-J. Wan, *Journal of the American Chemical Society,* **134** (2012) 7874-7879.

[241] Q. Zhao, L. Jiao, W. Peng, H. Gao, J. Yang, Q. Wang, H. Du, L. Li, Z. Qi, Y. Si, Y. Wang, H. Yuan, *Journal of Power Sources,* **199** (2012) 350-354.

[242] X. Tian, X. Xu, L. He, Q. Wei, M. Yan, L. Xu, Y. Zhao, C. Yang, L. Mai, *Journal of Power Sources,* **255** (2014) 235-241.

[243] T. Brezesinski, J. Wang, S.H. Tolbert, B. Dunn, *Nature Materials,* **9** (2010) 146-151.

[245] A. Rudola, K. Saravanan, C.W. Mason, P. Balaya, *Journal of Materials Chemistry A,* **1** (2013) 2653-2662.

[246] M. Lübke, P. Marchand, D.J. Brett, P. Shearing, R. Gruar, Z. Liu, J.A. Darr, *Journal of Power Sources,* **305** (2016) 115-121.

[247] M. Lübke, N. Ding, M.J. Powell, D.J. Brett, P.R. Shearing, Z. Liu, J.A. Darr, *Electrochemistry Communications,* **64** (2016) 56-60.

[248] K. Abe, H. Yoshitake, T. Kitakura, T. Hattori, H. Wang, M. Yoshio, *Electrochimica Acta,* **49** (2004) 4613-4622.

[249] L. Chen, K. Wang, X. Xie, J. Xie, *Journal of Power Sources,* **174** (2007) 538-543.

[250] H. Lu, K. Xiang, N. Bai, W. Zhou, S. Wang, H. Chen, *Materials Letters,* **167** (2016) 106-108.

[251] L. Wang, B. Ruan, J. Xu, H.K. Liu, J. Ma, *RSC Advances,* **5** (2015) 36104-36107.

[252] Y. Shi, S.-L. Chou, J.-Z. Wang, H.-J. Li, H.-K. Liu, Y.-P. Wu, *Journal of Power Sources,* **244** (2013) 684-689.

[253] E. Buiel, J.R. Dahn, *Electrochimica Acta,* **45** (1999) 121-130.

[254] M. Schroeder, M. Winter, S. Passerini, A. Balducci, *Journal of Power Sources,* **238** (2013) 388-394.

[255] D. Cericola, P. Novák, A. Wokaun, R. Kötz, *Journal of Power Sources,* **196** (2011) 10305-10313.

[256] S. Hu, H. Wang, J. Cao, J. Liu, B. Fang, M. Zheng, G. Ji, F. Zhang, Z. Yang, *Materials Letters,* **62** (2008) 2954-2956.

[257] Y. Wang, B.M. Smarsly, I. Djerdj, *Chemistry of Materials,* **22** (2010) 6624-6631.

[258] M. Fehse, S. Cavaliere, P.E. Lippens, I. Savych, A. Iadecola, L. Monconduit, D.J. Jones, J. Rozière, F. Fischer, C. Tessier, L. Stievano, *The Journal of Physical Chemistry C,* **117** (2013) 13827-13835.

[259] L. Wu, D. Buchholz, D. Bresser, L. Gomes Chagas, S. Passerini, *Journal of Power Sources,* **251** (2014) 379-385.

[260] J. Qiu, S. Li, E. Gray, H. Liu, Q.-F. Gu, C. Sun, C. Lai, H. Zhao, S. Zhang, *The Journal of Physical Chemistry C,* **118** (2014) 8824-8830.

[261] H. Usui, S. Yoshioka, K. Wasada, M. Shimizu, H. Sakaguchi, *ACS Applied Materials & Interfaces,* **7** (2015) 6567-6573.

[262] A.G. Dylla, G. Henkelman, K.J. Stevenson, *Accounts of Chemical Research,* **46** (2013) 1104-1112.

[263] J.-H. Jeong, D.-w. Jung, E.W. Shin, E.-S. Oh, *Journal of Alloys and Compounds,* **604** (2014) 226-232.

[264] D. A. Shirley, *Physical Review B,* **5** (1972) 4709-4714.

[265] Z. Zhang, J.B.M. Goodall, D.J. Morgan, S. Brown, R.J.H. Clark, J.C. Knowles, N.J. Mordan, J.R.G. Evans, A.F. Carley, M. Bowker, J.A. Darr, *Journal of the European Ceramic Society,* **29** (2009) 2343-2353.

[266] J.-Y. Shin, J.H. Joo, K.K. Adepalli, D. Samuelis, J. Maier, *Physical Chemistry Chemical Physics,* **18** (2016) 8963-8970.
[267] S. Lee, J.H. Noh, H.S. Han, D.K. Yim, D.H. Kim, J.-K. Lee, J.Y. Kim, H.S. Jung, K.S. Hong, *The Journal of Physical Chemistry C,* **113** (2009) 6878-6882.
[268] J. Wang, Y. Zhou, Y. Hu, R. O'Hayre, Z. Shao, *Journal of Materials Science,* **48** (2013) 2733-2742.
[269] O. Ghodbane, J.-L. Pascal, F. Favier, *ACS Applied Materials & Interfaces,* **1** (2009) 1130-1139.
[270] C. Jo, Y. Kim, J. Hwang, J. Shim, J. Chun, J. Lee, *Chemistry of Materials,* **26** (2014) 3508-3514.
[271] H. Park, H.B. Wu, T. Song, U. Paik, *Advanced Energy Materials,* **5** (2015).
[272] K. Tang, X. Mu, P.A. van Aken, Y. Yu, J. Maier, *Advanced Energy Materials,* **3** (2013) 49-53.
[273] W. Xie, S. Li, S. Wang, S. Xue, Z. Liu, X. Jiang, D. He, *ACS Applied Materials & Interfaces,* **6** (2014) 20334-20339.
[274] D.-J. Ryu, H.-W. Jung, S.-H. Lee, D.-J. Park, K.-S. Ryu, *Environmental Science and Pollution Research,* **15** (2016) 15015-15022.
[275] B. Lu, H. Wang, R. Hu, L. Yang, J. Liu, J. Liu, M. Zhu, *Materials Letters,* **185** (2016) 9-12.
[276] N. Wan, X. Lu, Y. Wang, W. Zhang, Y. Bai, Y.-S. Hu, S. Dai, *Scientific Reports,* **6** (2016) 18978.
[277] X. Zhang, X. Huang, X. Zhang, L. Xia, B. Zhong, T. Zhang, G. Wen, *Electrochimica Acta,* **222** (2016) 518-527.
[278] G. Gao, H.B. Wu, S. Ding, X.W.D. Lou, *Small,* **11** (2015) 432-436.
[279] F. Belliard, P. Connor, J. Irvine, *Ionics,* **5** (1999) 450-454.
[280] N. Feng, L. Qiao, D. Hu, X. Sun, P. Wang, D. He, *RSC Advances,* **3** (2013) 7758-7764.
[281] H. Wang, L. Xi, J. Tucek, Y. Zhan, T.F. Hung, S.V. Kershaw, R. Zboril, C.Y. Chung, A.L. Rogach, *Nanoscale,* **5** (2013) 9101-9109.
[282] Q. Zhu, P. Wu, J. Zhang, W. Zhang, Y. Zhou, Y. Tang, T. Lu, *ChemSusChem,* **8** (2015) 131-137.
[283] N. Li, C.R. Martin, B. Scrosati, *Electrochemical and Solid-State Letters,* **3** (2000) 316-318.
[284] G.-w. Chu, Q.-h. Zeng, Z.-g. Shen, H.-k. Zou, J.-f. Chen, *Chemical Engineering Journal,* **253** (2014) 78-83.
[285] Z. Fang, H. Assaaoudi, R.I. Guthrie, J.A. Kozinski, I.S. Butler, *Journal of the American Ceramic Society,* **90** (2007) 2367-2371.
[286] J. Zhu, Z. Lu, S.T. Aruna, D. Aurbach, A. Gedanken, *Chemistry of Materials,* **12** (2000) 2557-2566.
[287] T.J. Chuang, C.R. Brundle, D.W. Rice, *Surface Science,* **59** (1976) 413-429.
[288] M.S.A. Sher Shah, J. Lee, A.R. Park, Y. Choi, W.-J. Kim, J. Park, C.-H. Chung, J. Kim, B. Lim, P.J. Yoo, *Electrochimica Acta,* **224** (2017) 201-210.
[289] Y. Li, Y. Zhao, C. Ma, Y. Zhao, *Electrochimica Acta,* **218** (2016) 191-198.
[290] L. Chen, X. Ma, M. Wang, C. Chen, X. Ge, *Electrochimica Acta,* **215** (2016) 42-49.
[291] L. Fransson, T. Eriksson, K. Edström, T. Gustafsson, J.O. Thomas, *Journal of Power Sources,* **101** (2001) 1-9.

[292] E. Buiel, A.E. George, J.R. Dahn, *Journal of The Electrochemical Society,* **145** (1998) 2252-2257.
[293] D. Zhai, H. Du, B. Li, Y. Zhu, F. Kang, *Carbon,* **49** (2011) 725-729.
[294] D. Li, L.-X. Ding, S. Wang, D. Cai, H. Wang, *Journal of Materials Chemistry A,* **2** (2014) 5625-5630.
[295] W. Yang, J. Wang, W. Ma, C. Dong, G. Cheng, Z. Zhang, *Journal of Power Sources,* **333** (2016) 88-98.
[296] G.-L. Xu, Y. Li, T. Ma, Y. Ren, H.-H. Wang, L. Wang, J. Wen, D. Miller, K. Amine, Z. Chen, *Nano Energy,* **18** (2015) 253-264.
[297] K. Zhong, X. Xia, B. Zhang, H. Li, Z. Wang, L. Chen, *Journal of Power Sources,* **195** (2010) 3300-3308.
[298] C. Chen, P.J. Perdomo, M. Fernandez, A. Barbeito, C. Wang, *Journal of Energy Storage,* **8** (2016) 198-204.
[299] X. Zhu, H. Shi, J. Yin, H. Zhu, Y. Zhou, Y. Tang, P. Wu, T. Lu, *RSC Advances,* **4** (2014) 34417-34420.
[300] H. Wang, X. Du, X. Jiang, Y. Chai, X. Yang, R. Yuan, *Chemical Engineering Journal,* **313** (2017) 535-543.
[301] D. Cao, H. Wang, B. Li, C. Li, S. Xie, A.L. Rogach, C. Niu, *Electrochimica Acta,* **216** (2016) 79-87.
[302] X. Shi, H. Song, A. Li, X. Chen, J. Zhou, Z. Ma, *Journal of Materials Chemistry A,* **12** (2017) 5873-5879.
[303] W.-S. Kim, Y. Hwa, H.-C. Kim, J.-H. Choi, H.-J. Sohn, S.-H. Hong, *Nano Research,* **7** (2014) 1128-1136.
[304] C. Chen, Q. Ru, S. Hu, B. An, X. Song, X. Hou, *Electrochimica Acta,* **151** (2015) 203-213.
[305] Y. Cao, L. Zhang, D. Tao, D. Huo, K. Su, *Electrochimica Acta,* **132** (2014) 483-489.
[306] P. Meister, H. Jia, J. Li, R. Kloepsch, M. Winter, T. Placke, *Chemistry of Materials,* **28** (2016) 7203-7217.
[307] I.D. Johnson, E. Blagovidova, P.A. Dingwall, D.J. Brett, P.R. Shearing, J.A. Darr, *Journal of Power Sources,* **326** (2016) 476-481.
[308] H. Wang, H. Huang, C. Niu, A.L. Rogach, *Small,* **11** (2015) 1364-1383.
[309] G.S. Herman, Y. Gao, *Thin Solid Films,* **397** (2001) 157-161.
[310] D. Barreca, S. Garon, E. Tondello, P. Zanella, *Surface Science Spectra,* **7** (2000) 81-85.
[311] C. Zhang, X. Peng, Z. Guo, C. Cai, Z. Chen, D. Wexler, S. Li, H. Liu, *Carbon,* **50** (2012) 1897-1903.
[312] X. Zhu, Y. Zhu, S. Murali, M.D. Stoller, R.S. Ruoff, *Journal of Power Sources,* **196** (2011) 6473-6477.
[313] Y. Wang, M. Xu, Z. Peng, G. Zheng, *Journal of Materials Chemistry A,* **1** (2013) 13222-13226.

[314] H. Wang, L. Xi, J. Tucek, C. Ma, G. Yang, M.K. Leung, R. Zboril, C. Niu, A.L. Rogach, *ChemElectroChem,* **1** (2014) 1563-1569.

[315] Y. Wang, Z.X. Huang, Y. Shi, J.I. Wong, M. Ding, H.Y. Yang, *Scientific Reports,* **5** (2015) 9164.

[316] W. Zhang, L. Shi, K. Tang, Y. Yu, *Chemistry Letters,* **41** (2012) 104-106.

[317] N.A. Chernova, M. Roppolo, A.C. Dillon, M.S. Whittingham, *Journal of Materials Chemistry,* **19** (2009) 2526-2552.

[318] N.R. Srinivasan, S. Mitra, R. Bandyopadhyaya, *Physical Chemistry Chemical Physics,* **16** (2014) 6630-6640.

[319] J. Chen, H. Hou, Y. Yang, W. Song, Y. Zhang, X. Yang, Q. Lan, X. Ji, *Electrochimica Acta,* **164** (2015) 330-336.

[320] D. Bresser, G.-T. Kim, E. Binetti, M. Striccoli, R. Comparelli, S. Seidel, D. Ozkaya, M. Copley, P. Bishop, E. Paillard, S. Passerini, *Journal of Power Sources,* **294** (2015) 406-413.

[321] M. Reddy, V. Khai, B. Chowdari, *Solid State Ionics,* **268** (2014) 277-281.

[322] M. Reddy, G.S. Rao, B. Chowdari, *Journal of Materials Chemistry,* **21** (2011) 10003-10011.

[323] B. Das, M. Reddy, G.S. Rao, B. Chowdari, *Journal of Solid State Electrochemistry,* **15** (2011) 259-268.

[324] F. Wang, R. Robert, N.A. Chernova, N. Pereira, F. Omenya, F. Badway, X. Hua, M. Ruotolo, R. Zhang, L. Wu, *Journal of the American Chemical Society,* **133** (2011) 18828-18836.

[325] L. Li, F. Meng, S. Jin, *Nano Letters,* **12** (2012) 6030-6037.

[326] D. Aurbach, *Journal of Power Sources,* **89** (2000) 206-218.

[327] W.J. Borghols, M. Wagemaker, U. Lafont, E.M. Kelder, F.M. Mulder, *Chemistry of Materials,* **20** (2008) 2949-2955.

[328] K.T. Lee, J. Cho, *Nano Today,* **6** (2011) 28-41.

[329] M. Lübke, D. Howard, C.F. Armer, A.J. Gardecka, A. Lowe, M. Reddy, Z. Liu, J.A. Darr, *Electrochimica Acta,* **231** (2017) 247-254.

[330] J.Y. Liao, A. Manthiram, *Advanced Energy Materials,* **4** (2014) 14.

[331] Y. Xu, Q. Liu, Y. Zhu, Y. Liu, A. Langrock, M.R. Zachariah, C. Wang, *Nano Letters,* **13** (2013) 470-474.

[332] J.S. Chen, L.A. Archer, X.W.D. Lou, *Journal of Materials Chemistry,* **21** (2011) 9912-9924.

II. List of Figures

III. List of Tables